



NUCLEAR WASTE
MANAGEMENT
ORGANIZATION

SOCIÉTÉ DE GESTION
DES DÉCHETS
NUCLÉAIRES

NWMO-FORM-AD-0008-R001

Contractor Document Approval Cover Sheet
File with Contractor Document. Security Class: Internal Use

Title: 3D GEOPHYSICAL FORWARD AND INVERSION MODELLING OF THE REVELL BATHOLITH AND SURROUNDING GREENSTONE BELT		External Document No.: SGL-IR-Ignace-2020	Revision: 001
Company Name: <i>Sander Geophysics Limited (SGL)</i>			
NWMO Document No.: APM-REP-01332-0270	Revision: R000	NWMO P.O. No.: PO_2000315	
Date Submitted: <i>2020/10/20</i>		Page: 119	

**3D GEOPHYSICAL FORWARD AND INVERSION MODELLING OF THE REVELL BATHOLITH AND
SURROUNDING GREENSTONE BELT**

NWMO Authorization

Accepted By: *Aaron DesRoches* Date: October 20, 2020

Aaron DesRoches
Senior Scientist (Geophysics)

Approved by: *Sarah Hirschorn* Date: October 20, 2020

Sarah Hirschorn
Director Geoscience

Associated with NWMO-STD-AD-0001, Standards for Controlled Documents



Issue Date: October, 2020

3D GEOPHYSICAL FORWARD AND INVERSION MODELLING OF THE REVELL BATHOLITH AND SURROUNDING GREENSTONE BELT

Prepared for:

Nuclear Waste Management Organization (NWMO)

by:

Sander Geophysics Limited (SGL)



**NWMO REPORT NUMBER:
APM-REP-01332-0270**

Signatures



Martin Bates, Ph.D., P.Ge



Derek Kouhi, M.Sc., P.Ge



Martin Mushayandevu, Ph.D., P.Ge

Executive Summary

This technical report documents the results of 3D geophysical forward and inverse modelling of the Revell batholith and surrounding Raleigh Lake and Bending Lake greenstone belt to assist in assessing the suitability of the Ignace area to safely host a deep geological repository (Golder, 2015).

The objective of this project is to produce a 3D geophysical model of the Revell batholith created by forward and inverse modelling of airborne magnetic and gravity data constrained by known geological, geophysical and petrophysical information provided by NWMO.

The aeromagnetic data used for 3D geophysical modelling was generated by merging a magnetic airborne survey data acquired by Sander Geophysics (SGL) in 2014 with airborne survey data acquired by Fugro Airborne Surveys (Fugro) in 2000-2001 (Data Set 1107d-Revision 1, OGS, 2011). The SGL dataset was flown with a 100 m line spacing at an average height of 98 m above the ground and the Fugro data set was obtained with a line spacing of 200 m and a magnetic sensor height of approximately 73 m above the ground. The merging of the data sets entailed some reprocessing of the data. The difference in the acquisition dates called for a reconciliation of the International Geomagnetic Reference Field (IGRF) correction and the difference in acquisition heights called for a reconciliation for the height difference between the magnetic sensors in the two surveys.

The gravity data used were generated by merging airborne gravity data acquired by SGL in 2014 with ground gravity measurements obtained by the Geological Survey of Canada (GSC) between 1944 and 2018. The merging processes entailed reprocessing the GSC gravity data using SGL gravity correction standards (SGL, 2015) in order to ensure that the data sets were compatible.

The Digital Elevation Model (DEM) terrain grid used was created by merging data from three sources with different resolutions. A 1 m spatial resolution LiDAR coverage acquired by ATLIS Geomatics covered most of the area. This was extended with a combination of terrain survey data, acquired by SGL in 2014 from altimeter measurements and GPS data and one arc-second resolution Shuttle Radar Topography Mission (SRTM) data.

An updated bedrock geology map and geological database for the northern portion of the Revell batholith (Parmenter et al., 2020) was used to build the model. The associated database had structural information with foliation trends and, in some instances, foliation strikes and dips. The foliation in the greenstones surrounding the Revell batholith display systematic variations, which have been used to infer the average dips of the contacts between the greenstones and the batholith. Petrophysical data in the form of magnetic susceptibility and density measurements were sourced from NWMO, Ontario Geological Survey (OGS), and Geological Survey of Canada (GSC), and were used to constrain the 3D geophysical models.

A model extending 31.4 km north-south and 30.7 km east-west was selected covering the central and northern portion of the Revell batholith. It incorporates most of a low gravity anomaly associated with the Revell batholith. A model depth of 4 km below sea level was deemed appropriate based on preliminary 2D modelling in the Phase 2 report (SGL, 2015) and updated 2D modelling as part of this study.

The 3D models were created using GeoModeller© software (Intrepid Geophysics©). A 3D geology model based only on the interpolation of surface bedrock geology data was created as a starting point. This was then improved by 3D forward modelling of the gravity data and incorporating the results from the 2D profile forward modelling. This improved model was then used as the starting model for the 3D inversion models. Gravity data was inverted for first, followed by magnetic inversions and lastly, joint gravity and magnetic inversions.

The report provides results of forward modelling and inversion of gravity and magnetic data to estimate the shape, depth, thickness and the distribution of geological units within the batholith.

The final model created incorporates 4 rock units for the Revell batholith; 1) an oval-shaped feldspar megacrystic granite rock unit in the central portion of the batholith, 2) biotite granite to granodiorite rocks which underlie most of the northern, central and southern portions of the Revell batholith, 3) hornblende tonalite to granodiorite rocks which occurs in two irregularly shaped zones surrounding the central core of the Revell batholith, 4) biotite tonalite to granodiorite rocks which occur along the southwestern and northeastern margins of the Revell batholith.

The 3D model has the batholith with a relatively flat base that extends to depths of nearly 4 km in some regions. The batholith is encapsulated within surrounding mafic metavolcanic rocks and felsic to intermediate metavolcanic rocks, referred to broadly as the greenstone unit. The biotite granite to granodiorite unit has a well-defined density (mean of 2.65 ± 0.05 g/cc), which is the lowest of the 4 rock units for the Revell batholith, and dominates the 3D model and the gravity signature of the batholith. This unit has been modelled with a nearly flat base at a depth around 2 km extending over most of the batholith. A model assigning the same density as that of the granite to granodiorite unit at 2.65 ± 0.05 g/cc to all of the batholith units in the model gave total thickness extending to 3km in most regions. This model was used to set a lower limit to the thickness of the entire batholith.

Incorporating the denser biotite tonalite to granodiorite and the hornblende tonalite to granodiorite units as distinctive units in the model has the effect of increasing the batholith overall thickness while raising the base of the biotite granite to granodiorite unit. It is anticipated that the model will be revised and refined as more field data is collected in the future.

TABLE OF CONTENTS

1. Introduction	1
1.1 Study Objective	1
1.2 Report Structure	1
2. Geological Setting	2
2.1 Structural and Metamorphic History	3
3. Data Extent and Processing	5
3.1 Model Extent	5
3.2 Aeromagnetic Data	5
3.3 Gravity Data	6
3.4 Topography Data	7
3.5 Rock Petrophysics Database	8
3.5.1 Density Measurements	9
3.5.2 Magnetic Susceptibility Measurements	10
3.6 Bedrock Geology	11
4. Pre-Modelling	13
4.1 2D Modeling	13
4.1.1 Introduction	13
4.1.2 2D Model Results	14
4.2 Two-Layer 3D Gravity Inversion Model	16
4.2.1 Introduction	16
4.2.2 Methodology	17
4.2.3 Model Results	17
5. GeoModeller® 3D Model	19
5.1 Modelling Approach	19
5.1.1 Geology Interpolation	19
5.1.2 Forward modelling	20
5.1.3 Optimization	20
5.1.4 Inversion modelling	21
5.2 Initial Geological Model	21
5.3 3D Forward Modelling	24
5.4 3D Inversion Modelling	26
5.4.1 Varying Levels of Constraint for Geological Controls	27
5.4.2 Inversion Results	28
5.4.3 Gravity-only Inversion	30
5.4.4 Magnetic-only Inversion	32
5.4.5 Joint Inversion	33
5.5 Model Comparisons	34
5.6 Model Discussion	35
6. Summary of Results	37
7. References	39
8. Figures Listing	43

LIST OF TABLES

Table 3.1 Model extents as X Eastings and Y Northings and Z depth in metres.....	5
Table 3.2 Densities of rock units represented in the 3D geophysical model	9
Table 3.3 Magnetic susceptibilities of rock units represented in the 3D geophysical model	11
Table 3.4 Average foliation dips and standard deviation in the greenstone belt units surrounding the Revell batholith (Figure 3.7). Foliation orientations are transferred to the boundaries between the greenstone belts and the batholith rock units.	12
Table 4.1: Coordinates of the start and end of 2D geophysical forward model profile lines and coordinates of the sections within the 3D geophysical model domain (UTM 15N, NAD83(CSRS)).	13
Table 5.1 Model chronological order and colours of units	22
Table 5.2 GeoModeller® suggested susceptibilities and ranges from property optimization of magnetic susceptibilities.....	26
Table 5.3 Settings of levels of inversion constraint for geological controls	28
Table 5.4 Inversion output file names and descriptions	29
Table 5.5 Summary statistics files for the voxets	30

Appendix

A. Figures

1. Introduction

This technical report documents the creation of 3-dimensional (3D) geophysical forward and inverse models of the Revell batholith, to assist in assessing the suitability of the Ignace area to safely host a deep geological repository (Golder, 2015).

1.1 Study Objective

The objective of this project is to produce a 3D geophysical model of the Revell batholith and the surrounding Raleigh Lake and Bending Lake greenstone belts within the Wabigoon Subprovince in Northwestern Ontario. The 3D geophysical model is created by forward and inverse modelling of airborne magnetic and gravity data constrained by known geological, geophysical and petrophysical information provided by NWMO in the form of maps and data sets. The steps employed to generate the 3D geophysical model are:

- Compile and integrate relevant peer-reviewed literature, government reports, company reports and publicly available data sets to constrain the development of the 3D geophysical model and its geological framework;
- Develop a 3D geophysical model by forward modelling and inversion of airborne geophysical data sets. The model will specify the 3D distribution of petrophysical bedrock properties, which will be used to infer and understand the subsurface distribution and volume of rock units within the Revell batholith study area. This process will include delineation of the surface boundaries between the Revell batholith and surrounding greenstone units and the rock units within the batholith itself. Due to the non-unique nature of forward and inverse geophysical modelling, sensitivity analysis is performed to estimate the degree of uncertainty in 3D geophysical models through statistical analysis of alternative model scenarios;
- Provide a technical report that outlines the modelling approach employed, the input data sets and data preparation procedures, the key model assumptions and constraints, the results of the modelling and describes the uncertainties of the model;
- Deliver a digital data set to NWMO of all modelled volumes, surfaces, grids, etc.

1.2 Report Structure

This interpretation report is broken down into eight sections and an appendix. Section 2 contains an overview of the geological setting of the Revell batholith. Section 3 describes the preparation of available magnetic, gravity, geological and petrophysical data. Section 4 presents 2D modelling and preliminary two-layer 3D gravity inversion results. Section 5 presents 3D forward modelling of the gravity and 3D inversion of gravity and magnetic data. Section 6 summarizes the results. References are listed in Section 7. All figures are listed in Section 8 and presented in Appendix A.

2. Geological Setting

The geological setting for the Revell batholith and surrounding area is described in detail in Parmenter et al (2020) and is summarized below.

The Revell Regional Area is situated in the northwestern part of the Superior Province of the Canadian Shield – a stable craton created from a collage of ancient plates and accreted juvenile arc terranes that were progressively amalgamated over a period of more than 2 billion years (Figure 2.1). The Canadian Shield forms the stable core of the North American continent. The Superior Province has historically been divided into various regionally extensive east-northeast-trending subprovinces based on rock type, age and metamorphism (Figure 2.1; Thurston, 1991). More recently, the Superior Province has been subdivided into lithotectonic terranes, defined as tectonically bounded regions with characteristics distinct from adjacent regions prior to their accretion into the Superior Province (Percival and Easton, 2007; Stott et al., 2010). The Revell Regional Area is situated in the south-central part of the Western Wabigoon terrane, adjacent to the boundary with the Marmion terrane (Figure 2.1).

A summary of the Archean and Proterozoic geological events that have shaped the bedrock in the Revell Regional Area is presented below and shown schematically in Figure 2.3. The western Wabigoon terrane, interpreted to represent a volcanic island arc, is predominantly composed of two main groups of rock. This includes ca. 2.745 to 2.711 Ga supracrustal rocks, comprising Archean mafic to intermediate to felsic metavolcanic rocks and subordinate sedimentary rocks distributed in greenstone belts, and, ca. 2.70 to 2.67 Ga rocks of granitoid affinity predominantly consisting of felsic plutonic rocks. These two major rock groups are a common characteristic of granite-greenstone belts, and granite-greenstone subprovinces, across the entire western Superior province.

The Archean supracrustal rocks in the Revell Regional Area wrap entirely around the northern margin of the Archean Revell batholith (Figure 2.1). The supracrustal rocks distributed to the southwest of the batholith belong to the Bending Lake greenstone belt and those distributed to the northeast of the batholith belong to the Raleigh Lake greenstone belt. Both of these greenstone belts, as well as the additional supracrustal rocks wrapping around the northern boundary of the batholith, represent contiguous parts of the Kakagi Lake-Savant Lake greenstone belt that underlies the entire western Wabigoon terrane. Five main rock units are identified in the supracrustal rock group: mafic metavolcanic rocks, intermediate to felsic metavolcanic rocks, metasedimentary rocks, iron formation, and mafic intrusive rocks (Figure 2.2). Sedimentation within the supracrustal rock assemblage was largely synvolcanic, although sediment deposition in the Bending Lake area may have continued past the volcanic period (Stone, 2009; Stone, 2010a; Stone, 2010b). All supracrustal rocks are affected, to varying degrees, by penetrative brittle-ductile to ductile deformation under greenschist- to amphibolite-facies metamorphic conditions (Blackburn and Hinz, 1996; Stone et al., 1998). In some locations, primary features, such as pillow basalt or bedding in sedimentary rocks are preserved, in other locations, primary relationships are completely masked by penetrative deformation. Uranium-lead (U-Pb) geochronological analysis of the supracrustal rocks produced ages that range between 2734.6 +/-1.1 Ma and 2725 +/-5 Ma (Stone et al., 2010).

The Revell batholith is roughly rectangular in shape, trends northwest, is approximately 40 km in length, and covers an area of approximately 455 km² (Figure 2.1). Three main suites of plutonic rock are recognized in the Revell batholith, including, from oldest to youngest: a Biotite Tonalite to Granodiorite suite, a Hornblende Tonalite to Granodiorite suite, and a Biotite Granite to Granodiorite suite (Figure 2.2). Plutonic rocks of the Biotite Tonalite to Granodiorite suite occur

along the southwestern and northeastern margins of the Revell batholith. The principal type of rock within this suite is a white to grey, medium-grained, variably massive to foliated or weakly gneissic, biotite tonalite to granodiorite. One sample of foliated and medium-grained biotite tonalite produced a U-Pb age of 2734.2 \pm 0.8 Ma (Stone et al., 2010). The Hornblende Tonalite to Granodiorite suite occurs in two irregularly shaped zones surrounding the central core of the Revell batholith. Rocks of the Hornblende Tonalite to Granodiorite suite range compositionally from tonalite through granodiorite to granite and also include significant proportions of quartz diorite and quartz monzodiorite. One sample of coarse-grained grey mesocratic hornblende tonalite produced a U-Pb age of 2732.3 \pm 0.8 Ma (Stone et al., 2010). Rocks of the Biotite Granite to Granodiorite suite underlie most of the northern, central and southern portions of the Revell batholith. Rocks of this suite are typically coarse-grained, massive to weakly foliated, and white to pink in colour. The Biotite Granite to Granodiorite suite ranges compositionally from granite through granodiorite to tonalite. A distinct potassium (K)-Feldspar Megacrystic Granite phase of the Biotite Granite to Granodiorite suite occurs as an oval-shaped body in the central portion of the Revell batholith (Figure 2.2). One sample of coarse-grained, pink, massive K-feldspar megacrystic biotite granite produced a U-Pb age of 2694.0 \pm 0.9 Ma (Stone et al., 2010). Szewczyk and West (1976) interpreted this batholith to be a sheet-like intrusion that is approximately 1.6 km thick. Recent 2.5D gravity modelling suggests that the batholith is on the order of 2 km to 3 km thick through the center of the northern part of the batholith (SGL, 2015).

West-northwest trending mafic dykes interpreted from aeromagnetic data extend across the northern portion of the Revell batholith and into the surrounding greenstone belts. One mafic dyke occurrence is approximately 15-20 m wide (Figure 2.2). All of these mafic dykes have a similar character and are interpreted to be part of the Wabigoon dyke swarm. One sample from the same Wabigoon swarm produced a U-Pb age of 1887 \pm 13 Ma (Stone et al., 2010), indicating that these mafic dykes are Proterozoic in age. It is assumed based on surface measurements that these mafic dykes are sub-vertical (Golder and PGW, 2017).

2.1 Structural and Metamorphic History

The structural and metamorphic history of the Revell Regional Area is summarized below and the documented sequence of deformation events is also shown in Figure 2.3. The information presented below is based on a synthesis of results from studies undertaken across the Wabigoon Subprovince (e.g., Percival et al., 2004; Bethune et al., 2006; Sanborn-Barrie and Skulski, 2006; Stone, 2010a). It is acknowledged that there is some uncertainty in applying the results from a regional synthesis to the Revell Regional Area.

In the earliest stage, the Marmion terrane underwent a complex history of magmatism, deformation and metamorphism ending with the collision of the Marmion and Winnipeg River terranes, between 2.93 and 2.87 Ga (Tomlinson et al., 2004). As a result of the collision, this part of the evolving Superior Province was amalgamated into the composite Winnipeg River-Marmion terrane (Tomlinson et al., 2004). The Western Wabigoon terrane is interpreted to have collided with this older terrane between 2.71 and 2.70 Ga (Sanborn-Barrie and Skulski, 2006). Subsequent plutonic activity took place throughout the Western Wabigoon terrane following this second collision event.

Pre-, syn-, and post-collisional tectonic events recorded in the Western Wabigoon terrane included five episodes of penetrative deformation (D1 to D5) and one prolonged episode of brittle deformation (D6). D1-D2 deformation occurred between 2.725 and 2.713 Ga. These two deformation events are recognized in gneissic rocks within the Western Wabigoon terrane. However, studies that were focused in the greenstone belts did not recognize any fabrics related to the D1-D2 event (e.g., Sanborn-Barrie and Skulski, 2006). Regional D3-D4 penetrative

deformation (D1-D2 of Sanborn-Barrie and Skulski, 2006) finished prior to 2.698 Ga and was characterised by the development of F3 northwest-trending folds and an associated S3 axial planar cleavage. D4 east- to northeast-striking structures locally overprint the northwest-striking S3 foliation. An S4 foliation occurs as a moderately- to strongly developed, steeply-dipping, schistosity (Percival et al., 2004).

D5 deformation included events occurring between 2.690 Ga (Davis, 1989) and 2.678 Ga (Brown, 2002). D5 is characterized by the development of regional-scale conjugate shear zones in plutonic and gneissic rocks (Percival et al., 2004; Sanborn-Barrie and Skulski, 2006). These shear zones are associated with significant sinistral strike-slip displacement along northeast-trending structures and dextral strike-slip motion along east- to east-southeast-trending structures (Bethune et al., 2006). The D5 event spanned the transition between ductile and brittle deformation into a poorly constrained and protracted series of episodic events that continued until approximately 2.4 Ga (Hanes and Archibald, 1998).

The D6 event is interpreted to have continued the episodic re-activation of pre-existing structures across the region (Kamineni et al., 1990). Evidence for D6 brittle deformation includes the presence of 1.947 Ga pseudotachylite, a product of friction melting, observed along the northern boundary of the Quetico Subprovince, to the south of the Western Wabigoon and Marmion terranes (Figure 2.1; Peterman and Day, 1989). Both the supracrustal rocks and the plutonic rocks of the Western Wabigoon terrane are transected by north-west trending Proterozoic mafic dykes of the Wabigoon Swarm. The emplacement age of these mafic dykes is 1.887 Ga, based on U-Pb geochronology (Stone et al., 2010), providing evidence of a younger Proterozoic brittle deformation event. Later rifting and intrusion associated with Midcontinent Rift magmatism, between 1.150 and 1.130 Ga (Heaman and Easton, 2006; Easton et al., 2007), may suggest a prolongation of the D6 event at a broader regional scale. It is unclear, however, to what extent this event contributed to the brittle deformation history in the Revell Regional Area.

The collision between terranes 2.7 Ga years ago is interpreted to have coincided with the peak of regional metamorphism of the Western Wabigoon terrane (Easton, 2000). A greenschist to amphibolite facies metamorphic overprint is widespread in the Raleigh Lake greenstone belt with the highest grade metamorphic overprint indicated by numerous amphibolite and garnetiferous layers and clasts in the metavolcanic rocks (Blackburn and Hinz, 1996). In the Bending Lake greenstone belt, mineral assemblages are generally indicative of low to medium grade greenschist metamorphism. Kresz (1987) identified a thermal metamorphic overprint that extends up to 1.5 km away from the western contact between the Revell batholith and the adjacent supracrustal rocks. This contact metamorphism, caused by the emplacement of the batholith, caused recrystallization that destroyed earlier fabrics in the bedrock. The metamorphosed rocks are now, typically, massive hornfels. Distal to the pluton, albite-epidote hornfels is characteristic, whereas closer to the pluton contact, lower hornblende hornfels facies is suggested by the presence of hornblende (Kresz, 1987). Similar contact metamorphism was documented by Satterly (1960) and Stone (2010a) from other locations proximal to the margin of the Revell batholith.

3. Data Extent and Processing

This section describes the model extent and how the available geophysical, petrophysical and geological data sets were prepared for the generation of 3D geophysical models.

3.1 Model Extent

A model extent of 31.4 km north-south by 30.7 km east-west was selected. This covers the central and northern portion of the Revell batholith. The areal limits of the model are represented by a dashed rectangular box (e.g. Figures 3.1 to 3.4) with the coordinates listed in (Table 3.1).

The extents were selected in order to incorporate most of the low gravity anomaly associated with the Revell batholith and to minimise effects of the model edge cutting across a large feature. The model limits were extended to the east to ensure that the peak of the gravity anomaly associated with the edge of the batholith falls well within the model extents. Extension of the model to the north and west was avoided as this would entail incorporating more gravity data from outside of the high-resolution airborne gravity data coverage, as discussed in the gravity data section below.

Based on preliminary modelling in the Phase 2 report (SGL 2015) and initial GM-SYS™ models performed here in Section 4, a modelled depth of four kilometres, was deemed appropriate. The depth extent of the model extends from 1 km above mean sea level to 4 km below mean sea level (Table 3.1).

Table 3.1 Model extents as X Eastings and Y Northings and Z depth in metres

Model Extents: NAD83 UTM zone 15N, (Z relative to Mean Sea Level, positive up)					
X minimum	542900	X maximum	574300	X extent	31400 m
Y minimum	5465600	Y maximum	5496300	Y extent	30700 m
Z minimum	-4000	Z maximum	1000	Z extent	5000 m

3.2 Aeromagnetic Data

The aeromagnetic data used for 3D geophysical modelling was generated by merging the southwest part of a larger magnetic airborne survey data acquired by Sander Geophysics (SGL) in 2014 with airborne survey data acquired by Fugro Airborne Surveys (Fugro) in 2000-2001 (Data Set 1107d-Revision 1, OGS, 2011). The Fugro data set was obtained as part of a combined GEOTEM and MEGATEM airborne electromagnetic survey with a line spacing of 200 m and a magnetic sensor height of approximately 73 m above the ground, and was gridded with a 50 m grid cell size. The SGL dataset was flown with a 100 m line spacing at an average height of 98 m above the ground, and gridded with a 25 m grid cell size. Due to differences in the processing applied to the two data sets, several post-processing steps, detailed below, were applied prior to merging.

Both data sets were previously reduced to a residual magnetic anomaly field by removal of the International Geomagnetic Reference Field (IGRF). IGRF removal from the Fugro magnetic data employed the year 2000 IGRF model that was extrapolated to a single day, the 24

December 2000. In contrast, IGRF removal from the SGL magnetic data employed the year 2010 IGRF model, and in addition the adjustment was extrapolated to match each individual day upon which data were acquired. Both of these IGRF adjustments were backed off to provide un-adjusted versions of the data. The most recent year 2015 IGRF model was then used to calculate and remove the IGRF extrapolated to match each individual day upon which data were acquired for both data sets, thus reconciling the IGRF adjustments.

In addition to IGRF reconciliation, the Fugro magnetic data was corrected to account for the height difference between the magnetic sensors in the two surveys. This was done by upward continuing the Fugro data set by the difference of the average flight heights of the two surveys. For the Fugro survey, the average sensor height is estimated to be 73 m above the ground while the SGL survey was flown at an average of 98 m above the ground. Therefore, the Fugro data was upward continued by 25 m. Note that downward continuation of the SGL data was also an option, however for our interpretation needs upward continuation of the Fugro data was preferred. This maintained the resolution of the SGL data and avoided the issue of instability of the downward continuation process and its tendency to amplify noise.

After post-processing, grids of each data set were generated using a minimum curvature algorithm suitable for potential field data (Briggs, 1974) with a 25 m grid cell size. The grids were then merged together; for efficiency the merged grid was then sub-sampled to a 50 m grid which was adequate for use in the 3D geophysical model where the smallest areal pixel size used was 100 m x 100 m. When merging the data, priority was given to the SGL data set over the Fugro data set where they overlap due to the higher spatial resolution of the SGL data. The grid merging process required application of a constant shift of 73 nT to the Fugro data in order to level it with the SGL data. The most likely reason for this offset is a difference in the estimated magnetic anomalies at the reference base stations used to monitor and correct for diurnal variations in the magnetic field for each survey. Once this constant shift was applied, the grids were stitched together. A taper was applied at the overlap between the two data sets that applies a weighted average to the data that scales linearly from one data set to the other over a distance of 1000 m. This mitigates edge effects from the stitching process. Horizontal derivatives were calculated as a quality control check for edge effects and the vertical derivative was calculated to check that the short wavelength signal was preserved. Low-pass filtered grids and difference grids between the original and merged data sets were calculated and were used to check the preservation of the regional signal. Figures 3.1 and 3.2 show magnetic anomaly data over the 3D model window prior to merging and after merging.

3.3 Gravity Data

The gravity data used for 3D geophysical modelling was generated by merging airborne gravity data acquired by SGL in 2014 with ground gravity measurements obtained by the Geological Survey of Canada (GSC) between 1944 and 2018 (Figures 3.3 (a) and (b)). The airborne gravity data was acquired with a line spacing of 100 m and flown at an average of 98 m above the ground. A sub-set of survey lines were extended by approximately 5 km beyond the survey boundary to acquire additional data at a 1km line spacing that provides lower resolution gravity data around the main area of interest. The thick solid black outline in Figure 3.3 (b) marks the limit of the 100 m line spacing data overlain on the 1 km line spacing data. Note that the magnetic data from the 1 km spaced lines were not used in the grids of magnetic data due to the large line spacing that under samples the shorter wavelength magnetic anomaly. The survey was flown at an average height of approximately 98 m above the ground surface. The GSC regional ground gravity stations are spaced approximately 12 km apart but are not acquired along straight lines and are unevenly distributed. In order to ensure that the data sets were compatible, the GSC gravity data were reprocessed using SGL gravity correction

standards (SGL, 2015). The observed ground gravity values were reprocessed by starting with the raw observed vertical gravity measurement and recalculating the normal (latitude), free-air and Bouguer corrections (Hinze et al. 2005). These corrections are applied to the raw ground observed data to obtain the Bouguer gravity anomaly that reflects local rock density contrasts within the sub-surface.

The Bouguer corrections incorporate adjustments for the effects of terrain. Shuttle Radar Terrain Mission (SRTM) digital elevation model (DEM) data were used to calculate the terrain corrections for the ground gravity data, consistent with how the airborne gravity data was corrected. The SRTM data contains information in a grid with a 1 arc second spacing, approximately equal to a 30 m cell size. The SRTM is higher resolution between the survey lines than the DEM derived from the SGL 2014 survey data, although the SGL survey data is higher resolution along the survey lines. Overall, the SRTM data provides a DEM at a similar resolution to the SGL survey data and at a much better resolution than from the scattered GSC data points. SRTM Coverage extending to 167 km from each gravity data point was utilized to ensure regional gravity terrain effects are corrected. Terrain corrections were applied to all ground gravity stations using a crustal average density of 2.67 g/cm³ to match the corrections applied to the SGL airborne gravity data.

Unlike the magnetic data which was merged in grid format, the gravity data was merged by combining the airborne line data with the ground point data to create a master database. The large resolution difference between the data sets makes it difficult to merge grids made independently, instead the data was gridded all together using a minimum curvature gridding algorithm (Briggs 1974) that does a good job of smoothing the boundary between the data sets. The grid was made with a 500 m grid cell size. Consistent with the processing applied to the SGL airborne gravity data, a low-pass cosine tapered filter with a 2 km full wavelength mid-point was applied to the grid. The filtering is equivalent to spatial averaging, and enhances the signal to noise ratio by cancelling out random noise on adjacent survey lines. A grid matching the magnetic data cell size was created by interpolating the grid to a 50 m cell size.

Once the data were merged and gridded, horizontal derivatives were calculated in the X and Y directions (not shown) in order to ensure there were no edge artefacts as a result of the boundary between the different data sources. A 15 km low-pass filter was also applied and compared to the original data to ensure that long-wavelength gravity signals were preserved and vertical derivatives were calculated to ensure the preservation of high frequency data. Finally, a difference grid was taken between the original SGL high-resolution airborne grid and the final merged grid to ensure that minimal gravity signal related to subsurface geology is lost in the merging process. The final merged Bouguer gravity and the first vertical derivative grids are shown in Figures 3.3 (c) and (d) limited to the extent of the 3D model.

3.4 Topography Data

The Digital Elevation Model (DEM) terrain grid used for gravity modelling was created by merging data from three sources with different resolutions (Figure 3.4). Most of the 3D geophysical model has 1 m spatial resolution LiDAR coverage acquired by ATLAS Geomatics. To extend the coverage this data set was combined with terrain survey data, acquired by SGL in 2014 from altimeter measurements and GPS data, gridded with a 25 m cell size. One arc-second resolution Shuttle Radar Topography Mission (SRTM) data (approximately 30 m cell size) were used to provide coverage to the outer extents of the model area. While the SRTM data has better resolution than the airborne survey DEM data between lines, and is preferred for use in correcting the gravity data, the airborne survey DEM data was used to make this DEM, where available, due to its much higher sampling interval along the lines. Both options are a

compromise, but the choice of SGL DEM data over SRTM for the purpose of modelling is not critical due to the lower resolution of the modelled gravity response compared to the effects expected to arise from the differences in resolution of the two optional DEM sources.

Merging of the three topographic data grids was carried out using a similar procedure to the airborne magnetic data. A 500 m wide taper between grid boundaries was applied during stitching. The final digital elevation model was gridded using a 25 m cell size (Figure 3.4 (c)). A grid matching the magnetic data cell size was created by sub-sampling the data at 50 m. Horizontal derivatives of the DEM were calculated to ensure there were no boundary effects left over from the stitching, while the first vertical derivative was calculated to check for preservation of high frequency information.

For the purpose of modelling it is necessary to define the level of observation of the data. For an airborne survey this is the altitude at which the survey is performed. Commonly in airborne gravity and magnetic surveys, the aircraft acquires data at specified heights above the ground by following a predetermined “drape” surface that ensures that the altitude flown varies smoothly over the survey area. Although vertical deviations from this surface naturally occur during survey flights, the deviations are generally small (within 10 m) and post survey data processing is designed to remove the impact of these deviations. Therefore, the drape surface is the natural choice for the level of observation. The drape surface is derived from the terrain, which is adjusted to remove any steep climbs and descents based on the performance capabilities of the aircraft. The entire surface is then low pass filtered to remove any sudden changes between climb and decent (a 2500 m Butterworth filter was used), and a constant nominal flying height is added to this smoothed terrain surface to get the drape surface that provides vertical guidance to the survey aircraft when on survey operations. This was the approach employed during the Sander 2014 survey. However, the Fugro 2000-2001 surveys were flown as a combined electromagnetic (EM) and aeromagnetic survey. A drape surface is not generally employed when flying EM surveys where low survey altitude is prioritized over the need for consistency of survey altitude above the ground. In order to define a consistent level of observation for the two merged aeromagnetic data sets, the following procedure was adopted. A hypothetical drape surface was created for the Fugro survey areas by adding the average survey height above ground of 98 m to the DEM. The hypothetical Fugro survey area drape was then merged to the actual SGL survey area drape. To smooth out sharp terrain features and the transition between the drapes, a Butterworth convolution filter was applied to this merged grid similar to the 2500 m Butterworth filter used to create the original SGL drape, resulting in a consistent drape surface for the entire model area (Figure 3.4 (d)). This surface is converted to altitude above mean sea level and is used in the forward and inverse modelling workflow.

3.5 Rock Petrophysics Database

The petrophysical data used to constrain the 3D geophysical models comprise magnetic susceptibility and density measurements from NWMO, Ontario Geological Survey (OGS), and Geological Survey of Canada (GSC). Figure 3.5 and 3.6 shows the regional geology map and the distribution of locations of the petrophysical samples for lithologies included in the 3D geophysical model. Where no petrophysical data were available within the model domain, petrophysical measurements from samples collected outside the 3D geophysical model area were used as proxies for the specific rock units.

3.5.1 Density Measurements

Density measurements from the three data sources were obtained using a wet/dry method to determine the specific gravity using procedures specified by the OGS Geoscience Laboratories (Rainsford, 2018).

The NWMO measurements are primarily focused in the Revell batholith region, with a significant number of measurements on samples collected from the biotite granite to granodiorite unit (Figure 3.6 (a)). These measurements were collected by NWMO as a part of the Phase 2 Geoscientific Preliminary Assessment and are used here as the primary source of data for calculating the mean, standard deviation, and statistical distribution of density for the biotite granite to granodiorite unit. Rock units missing from, or poorly represented in the NWMO petrophysical data set were supplemented by OGS data from samples collected from similar rock units within the neighbouring region. The OGS petrophysical data set is a catalogue of over 26,000 samples collected across Ontario between 1970 and 2014 (Rainsford et al., 2018). The GSC database (Enkin, 2018) was used to assess whether the density values for each rock unit from the NWMO and OGS data sets fall within Canada-wide averages.

A total of 82 density measurements from samples of biotite granite to granodiorite, hornblende tonalite to granodiorite and the feldspar megacrystic granite were used from the NWMO petrophysical dataset. Of these samples, 74 are from the biotite granite to granodiorite unit; three high density outliers are excluded that have high densities that are clearly anomalous and too high to generate the gravity low associated with this unit. Inclusion of these three outliers has minimal impact on the average density so their exclusion or inclusion is not significant to the modelling results. Only 5 samples are identified as hornblende tonalite to granodiorite, and 3 from the feldspar megacrystic granite. The sparsity of density data in the latter rock units is a potential source of error in the 3D geophysical model, which can be addressed by additional petrophysical sampling within these units. All the remaining rock units are included in the OGS density database with the exception of the metasedimentary unit. Additional measurements of the metasedimentary unit could provide better constraints on the models of gravity data. In order to determine a mean density for the metasedimentary rock unit, OGS density catalogue density measurements from samples of a similar rock unit to the north of the 3D geophysical model domain were used as a proxy (unit P7 in Figure 3.5). A summary of the final assigned rock unit densities and standard deviations is presented in Table 3.2. The density values for each unit are assumed to have a normal distribution for this study. Proxy data is denoted with the letter P for rock units where density data is not available within the 3D geophysical model domain (Figure 3.5).

Table 3.2 Densities of rock units represented in the 3D geophysical model

Unit	Density (g/cc)	Standard Deviation	Number of Samples	Notes
Biotite Granite to Granodiorite	2.65	0.05	74	Calculated from NWMO measurements. 3 high density outliers excluded.
Biotite Tonalite to Granodiorite	2.68	0.04	18	Calculated using a proxy to the west (P2) due to lack of NWMO measurements.
Hornblende Tonalite to Granodiorite	2.76	0.06	5	Calculated from NWMO measurements. Only 5 measurements.

Feldspar Megacrystic Granite	2.64	0.006	3	Calculated from NWMO measurements. Only 3 measurements.
Felsic to Intermediate Metavolcanic Rock	2.80	0.1	3	Calculated from OGS measurements from within the model area.
Mafic Metavolcanics	2.89	0.1	56	Calculated from OGS measurements from within the model area.
Metasedimentary Rock	2.77	0.1	10	Calculated from OGS measurements using proxy to the north (P7).
Metasedimentary to Metavolcanic Rock	2.89	0.1	N/A	Originally combined with metasedimentary rock unit then separated and derived during forward modelling.
Mafic Intrusive Rock	3.11	0.07	4	Calculated from OGS measurements from within the model area. Only 4 measurements.
Iron Formation	3.11	0.7	N/A	Assumed to be similar to the mafic intrusive rock. Larger error assigned.
NE Biotite Tonalite to Granodiorite	2.68	0.04	N/A	Density assumed to be equivalent to other Biotite Tonalite to Granodiorite unit.

3.5.2 Magnetic Susceptibility Measurements

Similar to the density data, field-based measurements used to assign magnetic susceptibilities to each rock unit came from data sets collected by NWMO and the OGS (Muir, 2013). These values were compared with the country-wide average values from the GSC database (Enkin, 2018).

The NWMO database contains 260 measurements from outcrops (stations) within the Revell batholith and 136 within the Basket Lake batholith. Of these measurements, 302 were within lithologies of interest and therefore used to assign magnetic susceptibility to rock units defined in the 3D geophysical model. Most measurement stations within the Revell batholith are located within the biotite granite to granodiorite unit with the remainder being from both tonalite to granodiorite units. The northeastern biotite tonalite to granodiorite unit within the Basket Lake batholith has been designated as a separate unit from the Revell batholith biotite tonalite to granodiorite unit due to its higher magnetic susceptibility. The petrophysical properties of this unit were assigned using values from the NWMO Basket Lake batholith database.

The OGS dataset was used to supplement susceptibility measurements for rock units not present in the NWMO dataset. The OGS dataset was collected between 2001 and 2012 in a similar manner to the NWMO measurements (Muir, 2013). Unfortunately, none of the OGS readings were collected from rock units defined in the 3D geophysical model. Therefore, nearby units with similar composition were used as proxies for rock units not present in the NWMO dataset (Figure 3.5). The felsic to intermediate metavolcanic rock unit and the mafic metavolcanics rock unit were assigned values using proxy measurements from the Zarn Lake area to the north east, while the mafic intrusive rock unit used a proxy measurement from the south east of the model domain. The magnetic susceptibilities assigned to each rock unit are given in Table 3.3. Susceptibility values for each rock unit are assumed to have a log-normal distribution based on the distribution patterns of the data.

Table 3.3 Magnetic susceptibilities of rock units represented in the 3D geophysical model

Unit	Magnetic Susceptibility (SI)	Standard Deviation	Number of Meas.	Notes
Biotite Granite to Granodiorite	0.0002	0.0003	228	Calculated from NWMO measurements.
Biotite Tonalite to Granodiorite	0.0006	0.0008	4	Calculated excluding the values from the northeast biotite tonalite unit due to higher magnetic signature. Only 4 measurements used.
Hornblende Tonalite to Granodiorite	0.0006	0.0008	35	Calculated from NWMO measurements.
Feldspar Megacrystic Granite	0.012	0.001	N/A	No magnetic susceptibility determined due to lack of measurements and viable proxy data. Value determined via 2-D profile modelling.
Felsic to Intermediate Metavolcanics	0.0007	0.003	39	Calculated from OGS measurements using proxy data from the Zarn Lake area to the northeast (P5).
Mafic Metavolcanics	0.0007	0.0006	35	Calculated from OGS measurements using proxy data from the Zarn Lake area to the northeast (P6).
Metasedimentary	0.0006	0.0003	N/A	No viable susceptibility proxy data. Value determined via 2-D profile modelling.
Metasedimentary to Metavolcanic Rock	0.0006	0.0003	N/A	No viable susceptibility proxy data. Value determined via 2-D profile modelling.
Iron Formation	1	0.001	N/A	Derived during forward modelling. Larger susceptibility assigned to address under sampling due to cells being larger than the unit.
Mafic Intrusives	0.0012	0.004	58	Calculated from OGS measurements using proxy data from the southeast (P8).
NE Biotite Tonalite to Granodiorite	0.0035	0.006	35	Calculated from NWMO measurements.

3.6 Bedrock Geology

Information on the bedrock geology was made available by NWMO in shape-file format in which polygons depict boundaries of rock units and poly-lines represent structural features and dykes (Parmenter et al., 2020). A database of structural information with foliation trends and, in some instances, foliation strikes and dips was also made available. Figure 3.7 plots foliation strikes and dips overlain on bedrock geology. The foliation in the greenstones surrounding the Revell batholith display systematic variations, which have been used to infer the average dips of the contacts between the greenstones and the batholith. Table 3.4 lists arithmetic means of the foliation dips for different areas adjacent to the batholith with more or less consistent strike of the foliation which provides a simplified approximation that was used when creating the 3D geological model and are marked on Figure 3.7.

Table 3.4 Average foliation dips and standard deviation in the greenstone belt units surrounding the Revell batholith (Figure 3.7). Foliation orientations are transferred to the boundaries between the greenstone belts and the batholith rock units.

Unit Label	Unit	Dip	Standard Deviation	Mean Dip Direction	Number of Meas.	Notes
1	Biotite Granite to Granodiorite	70	6.0	327	19	Northwest portion of the batholith.
2	Biotite Granite to Granodiorite	78	6.2	220	20	Northeast portion of the batholith.
3	Biotite Granite to Granodiorite	61	7.8	34	3	Eastern edge of the northern part of the batholith. Only 3 measurements.
4	Biotite Granite to Granodiorite	64	9.4	258	8	Western edge of the northern part of the batholith.
5	NE Biotite Tonalite to Granodiorite	56	8.5	223	27	Highly magnetic biotite tonalite to granodiorite unit in the northeast.
6	Biotite Granite to Granodiorite	70	10.6	46	48	Eastern edge of the Revell batholith.
7	Biotite Tonalite to Granodiorite	75	4.4	218	13	Small portion of biotite tonalite to granodiorite east of the main batholith.
8	Biotite Tonalite to Granodiorite	51	13.6	237	89	Western edge of the batholith.
9	Greenstone Belt Units	64	10.5	226	210	Western greenstone units.
10	Greenstone Belt Units	56	12.7	220	147	Shallower dipping greenstone units in the southwest.

4. Pre-Modelling

Prior to creating and running time consuming and elaborate 3D geophysical models it is prudent to construct relatively simple 2D and 3D geophysical models that can be refined at a later stage. This investigation into the likely 3D model geometry and suitable model extents prior to detailed 3D modelling is referred to here as the Pre-Modelling stage.

This section describes 2D forward modelling of gravity and magnetic data carried out using the GM-SYS™ Profile Software module within Seequent®'s Geosoft software package (Seequent®, 2020).

Three forward model profiles across the Revell batholith are presented in NWMO's Phase 2 Geoscientific Preliminary Assessment (SGL, 2015). These 3 profiles are modified to incorporate the additional petrophysical data and structural information available.

The section also presents a simple two-layer 3D gravity inversion model created using the GM-SYS™ 3D software module within Geosoft™, the results of which are incorporated into the revised 2D forward models.

4.1 2D Modeling

4.1.1 Introduction

Figure 4.1 shows the location of the 3 profile lines within the extents of the 3D model, overlain on the Bouguer gravity, the anomalous magnetic field, topography and on bedrock geology maps. The coordinates for the end points of each of the 2D lines, as defined in the Phase 2 project (SGL, 2015), are given in Table 4.1, as are the end coordinates of the section of each profile that falls within the 3D geophysical modelling domain.

Table 4.1: Coordinates of the start and end of 2D geophysical forward model profile lines and coordinates of the sections within the 3D geophysical model domain (UTM 15N, NAD83(CSRS)).

Profile Line	Model				Window over 3D model			
	Start		End		Start		End	
	UTM X	UTM Y	UTM X	UTM Y	UTM X	UTM Y	UTM X	UTM Y
1	548381	5474037	577603	5515917	542951.2	5466265.9	563913.0	5496296.9
2	556452	5464754	588713	5510990	557070.0	5465639.6	574287.4	5490315.4
3	586310	5463390	542857	5493709	574298.0	5471771.4	542901.0	5493678.3

Phase 2 versions of the 2D geophysical forward models (SGL, 2015) were built based on a single lithology for the Revell batholith and a single lithology representing the surrounding Raleigh Lake and Bending Lake greenstones. These Phase 2 models were used as the starting point for the new geophysical modelling effort, updated with the new information described in Sections 2 and 3 to create new “preliminary 2D forward models”. In these preliminary models, the geology was updated (Section 2) to include 4 different rock units within the batholith and, similarly, more rock units were delineated in the country rocks. In addition, the petrophysical properties of each rock unit (Section 3) were updated to accurately reflect new data collected in the region since the creation of Phase 2 forward models. The 2D model profiles were tied to the most recent geological mapping in the region at the surface. Foliation and other structural data were used to incorporate known or inferred dips for each rock unit at the surface. Results from

the unconstrained 2-layer 3D inversion (Section 4.3) were used as a guideline for the depth to the bottom of the batholith. The preliminary 2D models were forward modelled to fit the Phase 2 Free Air Gravity data only.

Finally, the observed gravity and magnetic data were updated again using the merged grids described in Section 3. These data were used for forward modelling to fit both gravity and magnetic anomalies to generate the “updated 2D forward models” presented below.

4.1.2 2D Model Results

This section discusses the results of the 2D forward modelling for each of the 3 profile lines. The modelling results for the preliminary and updated models are shown on Figures 4.2 to 4.7. All the figures show in panel (a) the 2D forward modelled gravity data (e.g. Figure 4.2(a)) including the observed gravity data along the profile line, the gravity response calculated from the model, and the RMS error (root mean square error). The RMS error is a measure of the difference between the observed gravity data and the calculated gravity response. Panel (b) (e.g. Figure 4.2 (b)) shows the 2D model and the assigned rock density values for each of the bedrock units in the model, as well as a profile of the simple two-layer 3D gravity inversion model described in section 4.2. The colour of the units is related to the density. Panels (c) and (d) in figures for the updated models (e.g. Figure 4.3 (c) and (d)) show a similar set of result as panels (a) and (b) but for magnetic data. The observed magnetic data and calculated magnetic response, as well as the RMS error between them are in panel (c) and the magnetic susceptibility values assigned to each of the bedrock units in the model are in panel (d). Panel (e) (e.g. Figure 4.2 (e)) provides the view of the model with the colours indicative of the rock units assigned to the models.

4.1.2.1 Results for Profile Line 1

Profile line 1 traverses the Revell batholith and the Raleigh Lake and Bending Lake greenstone belts from southwest to northeast. The orientation of the line is perpendicular to the overall orientation of the batholith and greenstone belts and their associated magnetic and gravity anomalies (Figure 4.1).

Within the limits of the 3D geophysical model domain, the section of the line over the Revell batholith profile mostly traverses the biotite granite to granodiorite unit and a small section of biotite tonalite to granodiorite at the southern edge of the batholith. The biotite tonalite to granodiorite unit and the greenstones are modelled as being continuous beneath the biotite granite to granodiorite unit. (Figure 4.2). This creates two counteracting and unconstrained boundaries in the model of the batholith. Model responses due to changes in position and physical property contrast at one boundary can be nullified by making changes in position and physical properties at the other boundary while changing the overall thickness of the batholith.

In the initial 2D models from Phase 2 (SGL, 2015) the contacts were modelled as near vertical with an alternative model where greenstones or gneissic units underlie the batholith, giving a simple fit to the data. In these initial and updated models, the biotite tonalite to granodiorite and hornblende tonalite to granodiorite units have been modelled as continuous and connecting beneath the biotite granite to granodiorite unit, and are underlain by greenstones following the recommendation of NWMO (NWMO personal comm., 2019). The assumption that only denser greenstones underlay the batholith is preferred because it sets a lower limit to the thickness of the batholith. A broad empirical relationship has been identified between the horizontal width of plutons or laccoliths and their vertical thicknesses (Cruden, 2008, Cruden et al., 2018). This empirical rule was used to provide a rough estimate of the depth of the biotite granite to

granodiorite unit. The thickness (T in metres) of a pluton is given by:

$$T = bL^a$$

where L is the horizontal width (in metres) defined as the approximate diameter of a circle with the same area as the body, and a and b are coefficients defined based on the type of the intrusive body. For a pluton, these coefficients are 0.6 ± 0.1 and 0.6 ± 0.15 for a and b respectively with the error limits describing variation at the 95th percentile level. The section of the biotite granite to granodiorite north of the feldspar megacrystic granite unit has an approximate horizontal width of 14 km, therefore the empirical geometric scaling yields an approximate thickness for this part of the rock unit of 2.9 km with an error range of 1.7 km to 5.4 km.

The preliminary gravity forward model was generated using the SGL Free Air Bouguer gravity data (Figure 4.2). After adjustments to this model, the base of the biotite granite to granodiorite unit is set to less than 2500 m below sea level and the underlying biotite tonalite to granodiorite unit extends to 3500 m depth below sea level. The overall shape of the original Phase 2 Revell batholith (SGL, 2015) is maintained with the batholith thinning out northward.

The updated forward model utilizes the merged gravity and magnetic data (Figure 4.3), which provides gravity data that extends to the limits of the 3D geophysical model domain. The merged data set did not include free air gravity, thus, the forward modelling used Bouguer gravity rather than free air gravity data as previously employed in Phase 2 (SGL, 2015). The updated forward model has a minor change to the base of the Revell batholith. Two mafic dykes that are traversed by the profile line were incorporated in the model. Dyke-like features within the greenstone belts were incorporated into the model to account for short wavelength high amplitude magnetic anomalies surrounding the batholith. Dips of the dyke-like features were inferred from the dips of mapped foliations and zero remanant magnetization was assumed.

4.1.2.2 Results for Profile Line 2

Profile Line 2 is parallel to profile line 1, located approximately 12 km to the east, and likewise traverses the Revell batholith, and the Raleigh Lake and Bending Lake greenstone belts in a southwest-northeast direction. The orientation of the line is perpendicular to the overall orientation of the batholiths and greenstone belts and their associated magnetic and gravity anomalies. Profile line 2 crosses the middle of the feldspar megacrystic granite unit in the centre of the Revell batholith, which is associated with a strong magnetic fabric and magnetic anomaly high (Figure 4.1 (b), Figure 4.5 (c)).

The incorporation of four rock units in the model of the batholith results in four unconstrained unit boundaries under any point near the centre of the batholith (Figure 4.4). The difference in the estimated mean density of the feldspar megacrystic granite unit and the surrounding biotite granite to granodiorite unit is only 0.01 g/cc (Table 3.2), therefore no associated gravity anomaly response is anticipated from the boundary between these rock units. The thickness of the feldspar megacrystic granite unit was estimated to be 2.1 km using the empirical relationship between the width of a pluton and its thickness with error limits of 1.3 km to 3.2 km based on a width of 8 km. This thickness estimate was used as a constraint in the forward model. The thickness of the biotite granite to granodiorite was estimated using the same empirical relationship as used for Profile Line 1 as described above and implemented as a second model constraint.

The continuity of the hornblende tonalite to granodiorite and biotite tonalite to granodiorite units extending beneath the biotite granite to granodiorite unit in the preliminary model is a significant modification from the Phase 2 model. The impact of this change is addressed in the discussion of the modelling results (Section 5.5). The Phase 2 model assumed that these units pinched out against the biotite granite to granodiorite at depth. The introduction of the underlying hornblende tonalite to granodiorite and biotite tonalite to granodiorite units, with densities that fall between the greenstones and the biotite granite to granodiorite (Table 3.2), resulted in a significant increase in the average thickness of the batholith from 2 km to around 3.4 km below sea level (Figure 4.4). Within the batholith, the base of the biotite granite to granodiorite unit roughly coincides with the base of the batholith in the Phase 2 models.

Updating the forward model to utilize the merged gravity and magnetic data (Figure 4.5) results in minor changes. Unlike profile line 1, profile line 2 falls completely in the section of the model covered by SGL airborne gravity (Figure 4.1 (a)). Thus, it can be modelled using the SGL free air gravity data. Without modification to the shape of the feldspar megacrystic granite unit defined from the preliminary model, a magnetic susceptibility of 0.012 SI was required to produce an acceptable fit for its associated magnetic anomaly. A dyke cut by the profile was also incorporated.

4.1.2.3 Results for Profile Line 3

Profile line 3 is oriented southeast-northwest so that it intersects perpendicular to profile lines 1 and 2. Profile line 3 traverses the northern half of the Revell batholith largely parallel to the flanking greenstone belts. The profile line also traverses the feldspar megacrystic granite unit.

Similar to profile line 2, profile line 3 incorporates hornblende tonalite to granodiorite and biotite tonalite to granodiorite units that are continuous beneath the biotite granite to granodiorite unit. The biotite granite to granodiorite unit is constrained at a depth of 2.9 km and the feldspar megacrystic granite unit is constrained at a thickness of 2.1 km based on thickness estimates as described for Profile Line 1 and 2 above. As in Profile Line 2, the introduction of the underlying hornblende tonalite to granodiorite and biotite tonalite to granodiorite units resulted in a significant increase in the average thickness of the batholith from between 2.0 km and 2.5 km in Phase 2 model versions to just under 4 km depth below sea level (Figure 4.6). Within the batholith, the base of the biotite granite to granodiorite unit in the preliminary model roughly coincides with the base of the batholith in the Phase 2 models.

The updated forward model utilises the merged gravity and magnetic data to provide full coverage of the 3D geophysical model domain (Figure 4.7). Updating the model results in minor changes to the overall shape of the batholith and some internal structural changes. The magnetic data results in changes in the shape of the feldspar megacrystic granite unit. A dyke crossed by the profile was incorporated in the model. Dyke-like features within the greenstone belts were also incorporated to model the short wavelength high amplitude magnetic anomalies surrounding the batholith.

4.2 Two-Layer 3D Gravity Inversion Model

4.2.1 Introduction

A simple two-layer 3D gravity inversion was created to determine a rough estimate of the overall shape of the Revell batholith, which is the main contributor to the observed gravity anomaly. The starting model has two rock units separated by a flat horizon with an elevation that is shifted

up and down during inversion. The model was based on a single density of 2.65 g/cc for the batholith and a single density of 2.89 g/cc for the surrounding and underlying greenstones. The gravity anomaly can be used as a proxy for the shape of the base of the batholith with gravity lows representing deeper depths. The simple model provides a rapid approximate quantification of the 3D geometry of the batholith. In this simple model, density variations within the batholith and the greenstones are not accounted for in the inversion and will inevitably manifest as variation in the base of the batholith, resulting in more structural relief of the base than is actually present.

4.2.2 Methodology

A GM-SYS™ 3D model consists of rock units at different depths with associated densities and or magnetic susceptibilities. The physical property of a unit can be defined as constant or with lateral or vertical variations. The calculated gravity grid is the forward-modelled response from the geological model and the difference between the calculated response and observed data grid is the provided by the error grid. Inversion computations are carried out in order to minimize the error grid by modifications to either the geometry of a rock unit or the physical properties of a rock unit. The inversion process is terminated after exceeding a set number of iterations or the standard deviation of the error grid becomes less than a set convergence limit.

This version of GM-SYS™ can only invert observed data located at a constant reference altitude, therefore the observed gravity data were upward-continued to a surface of constant observation altitude above the highest ground elevation within the survey area. An altitude of 575 m above mean sea level (MSL) was used. An inversion that only allowed variation in geometry, not physical properties, was run using a starting model that employed a flat surface as the boundary between the two rock units at 1 km below sea level. A second similar inversion was run that employed an initial surface that mimics the topography at 50 m below ground level, and gave a similar result.

4.2.3 Model Results

Figure 4.8 shows the results of a two-layer 3D inversion. Grids of the calculated gravity response and error (observed minus calculated) are presented in Figures 4.8 (a) and (b) respectively. The dominant misfit occurs at the northwestern end of the model, suggesting that the underlying greenstones must be denser than 2.89 g/cc in this locality. This interpretation would only be valid if the observed gravity field in the northwestern corner is predominantly due to the underlying greenstones. A more likely scenario is that there is a source in the northwest that is in close proximity to, but outside the model extents, producing an anomaly that falls within the model area.

Figures 4.8 (c) and (d) show the depth to base of the batholith above MSL and thickness of the batholith (depth below surface) respectively. The relief at the modelled base of the batholith has been extracted along the 2D profile lines and incorporated into the 2D forward models (displayed as the red curve, e.g. Figure 4.2b).

Although this is a simplistic 3D model that assumes a batholith with a constant density of 2.65 g/cc surrounded by greenstones with a constant density of 2.89 g/cc and does a poor job of modelling the finer detailed geometry of the batholith, it can still be used to address some geological and geophysical questions. The large number of peaks and troughs modelled at the base of the batholith are artifacts of the inversion process which can be interpreted to suggest significant density variations must occur within or below the batholith. But the lateral extent of

the peaks and troughs also suggest near-surface density variation, and therefore density variation is more likely to be within the batholith rather than in the underlying greenstones. Overall, the model gives maximum depth to the base of the batholith of just under 4 km. Larger depths would be obtained if the density contrast between the batholith and the greenstones was reduced while increasing the density contrast would result in shallower depths. The simple model obtained allows an assessment of where contrast changes occur.

5. GeoModeller[®] 3D Model

This section describes the creation of combined 3D gravity and magnetic data inversion models carried out using GeoModeller[®] software (Intrepid Geophysics[®]). A summary of the complete process to create the 3D models is provided in Section 5.1, with full details available in the GeoModeller[®] manuals (Intrepid Geophysics[®], 2020). The creation of the 3D geology model based only on the interpolation of surface bedrock geology data is provided in Section 5.2. A description of how this initial 3D geology model is improved based on 3D forward modelling of the gravity data and the results from the 2D profile forward modelling described in Section 4.1 is given in Section 5.3. This improved model is then used as the starting model for the 3D inversion models. The results from gravity only inversion, magnetic only inversion, and joint gravity and magnetic inversion are presented in Section 5.4. A comparison of the various models is documented in Section 5.5 and a discussion of the model results is presented in Section 5.6.

5.1 Modelling Approach

Figure 5.1 shows a summary workflow of the steps for creating a 3D model using GeoModeller[®]. The process can be separated into 4 broad stages: 1) geology interpolation stage, 2) forward modelling stage, 3) optimisation stage and 4) inversion stage. In the geology interpolation stage, GeoModeller[®] uses bedrock units and foliation orientation information to calculate a 3D geology model defined by a set of mathematical equations. In the forward modelling stage, rock properties are assigned to the model rock units allowing for the calculation of the model fields. Mismatch between observed and calculated fields are addressed through modifications in the geology interpolation stage using additional geological structural information inferred or derived from geophysical interpretation. A set of software tools are available in the optimization stage for addressing either rock property optimization or inversion settings optimization. The final stage is running the 3D inversions.

5.1.1 Geology Interpolation

In the geology interpolation stage, the location and orientation of known features from geological mapping are imported as observed data. The geology outlines from the surface geology map are imported as shape files and projected on to the model ground surface defined by topography data. The geology outlines define the boundaries between model units at ground level. A boundary or section of a boundary can be assigned a dip where it is known or inferred. Additional structural information like dip and strike and the chronological order of rock units are assigned to different units and boundaries within the model and are incorporated as model controls during model interpolation. These are commonly referred to as “rules”. GeoModeller[®] refers to this calculated model as the Geology-only model since it can be created based on the available geological information without any reference to geophysical observations. Geological information from geophysical interpretations can be incorporated as inferred or interpreted geological data to update the Geology-only model. The updated model was created by incorporating the results of 2D forward modelling as described in Section 5.3.

This rule-based model creation allows for simple updating of the model as additional geological data becomes available. When new data is added or old data is modified, the model is simply re-interpolated to incorporate the new geological information.

5.1.2 Forward modelling

With a satisfactory 3D model based on geological observations in place, the model is tested and modified depending on how well it can predict the observed gravity and/or magnetic fields in the forward modelling stage. The process entails assigning rock properties to the different rock units within the model. The forward model is calculated using only the mean densities or mean susceptibilities of the different units. However, it is normal to assign standard deviations and type of distribution i.e. normal or log normal, bi-modal or mono-modal at this stage for use later in the inversion stage. Model modification involves gradually introducing inferred geological structural information into the model, normally as strike and dip of contacts between the units. The model modification is an iterative process of model geometry modification and assessment of misfit between predicted and observed fields, until a satisfactory fit is achieved. The validity of a model is based on the feasibility of the geology from a visual inspection of the units and the misfit of the calculated field to observed field. The feasibility of the geology is assessed using known structural information and inferred/anticipated subsurface geometry, while the misfit grid is assessed in terms of the amplitude and spatial distribution of the errors. In GeoModeller[®], carrying out the forward model field calculation requires converting the model into voxel format, initially at a low resolution using large voxel sizes. The use of a lower resolution for initial calculations speeds up the process and allows for a rapid fit of large-scale features. Once these features are defined, the voxel size is decreased to obtain the desired final resolution.

5.1.3 Optimization

Prior to running inversions, there are a number of processes and tests, listed in the Optimization Toolbox in Figure 5.1 that may be utilized depending on the results of the forward modelling and inversion processes.

A Rock Property Optimization can be implemented if there is confidence in the model geometry, but it does not produce the desired fit to the observed data. This optimization process identifies more suitable rock property values and distributions, in order to reduce the misfit between calculated and observed fields. It is run using coarse cells and a larger scatter in the property distribution to give new recommended rock properties with associated errors for all model units. This optimization was implemented for magnetic susceptibilities only and not for densities since an acceptable fit was obtained with gravity data.

During the inversion, GeoModeller[®] utilizes geological constraints in order to limit model fragmentation and help create geologically coherent models. For example, the geological constraints comprise a set of evaluations that the geological association of a specific voxel must pass prior to being accepted and implemented. Available constraining parameters in GeoModeller[®] include preserving vertical relationships, commonality, shape ratio and volume ratio tests. Preserving vertical relationships refers to locking the chronological order of the units within a column. Commonality tests look at the degree to which the evolving inversion model is allowed to change from the initial reference model by limiting the deviation of spatial coincidence of the start and end models. Shape ratio looks at changes in a dimensionless shape parameter defined as the square root of the surface area divided by the cubed root of the volume. Volume ratio looks at volume changes in model units. Thus, a process of setting the appropriate geological constraints at suitable levels and then activating them is carried out prior to running an inversion.

With the geological constraints specified, a suite of “prior only” tests can be used to assess the effects of the geological constraints selected on the distribution of permitted model changes.

The prior only tests are implemented to analyze the probability that each voxel will change during the modelling process to assess the effectiveness of the constraints. The process is carried out without reference to the gravity or magnetic data and the rock properties remain unchanged. It addresses how the geological constraints set will influence the statistical selection process of voxels or properties in GeoModeller®. This test was implemented to help determine the final degree to which constraints were implemented in the inversions by inspecting a voxel of the number of times each voxel has changed. If the change values are overall close to zero, the constraints are high.

During the inversion process, small random changes are made to either the lithological model boundaries or the physical properties on a voxel-by-voxel basis. If the probability of property change is set to 100% a Property-only Case inversion is run (Figure 5.1) that keeps unit boundaries fixed. The inversion will try to match the observed fields and the assigned rock properties while not changing unit boundaries. When lithology, model geometry and bulk properties have been determined with some confidence, this inversion process can be used to identify property sub-classes if the properties within a rock unit display a multi-modal distribution. This will enhance the estimates of the rock properties within the specified model rock unit geometries. On the contrary, setting the probability of property change value to 0% will keep properties constant during the inversion and only change geological boundaries in order to produce a fit to the geophysical data. This inversion is referred to as the Geology-only Case (Figure 5.1). Both Property only and Geology only case inversions have the potential of improving the model as more rock properties become available. At this point these inversions were deemed of limited utility and therefore not employed.

5.1.4 Inversion modelling

During the final step, GeoModeller® has options to run inversions using gravity data only or magnetic data only. Once the model has been optimized for the gravity and magnetic data separately, an inversion is run that incorporates both types of potential-field data.















In a typical inversion, the misfit between the calculated and observed fields initially decreases rapidly with each iteration before slowing down and plateauing after a specific number of iterations referred to as the “burn-in point”. The inversion is allowed to run long past the burn-in point so GeoModeller® can store many well-fitting models to allow for a statistical mapping of the distribution of these acceptable models. Analyzing the summary statistics of the permitted models allows for a statistical evaluation of the inversion results, such as uncertainties associated with individual voxels. If the results are deemed to be unacceptable this means that some initial settings or inversion controls need to be adjusted.

5.2 Initial Geological Model

Incorporating known geology is carried out in the early stages of model building. This entailed identifying the dominant rock units in the mapped geology and their associated chronological relationships and then importing them into the model. The detailed bedrock geology was simplified mainly by removing small geological features or by smoothing out geological boundaries (Figure 5.2 (a) to (b)). This was a manual process applied using judgment to ensure that the small features being removed do not have prominent associated gravity or magnetic anomalies in the observed data. The geology was made available as shape-file polygons which are imported directly into GeoModeller® and draped onto topography. Table 5.1 shows the units that were selected for incorporation into the model and their chronological order. The basis for the model units selection is detailed below. In building the model GeoModeller® provides the

choice of either defining only the tops of the unit boundaries or only the bottoms of unit boundaries. With no added advantage for either selection in our case, the bottom of units was selected as the mapped contact in the models.

Table 5.1 Model chronological order and colours of units

Rock Unit name (Chronologic order)	Rock Unit Colour
Dyke 2	
Dyke 1	
Iron Formation	
Mafic Metavolcanic lens	
Feldspar Megacrystic Granite Unit	
Biotite Granite to Granodiorite Unit	
Hornblende Tonalite to Granodiorite Unit	
Northeast Biotite Tonalite to Granodiorite Unit	
Biotite Tonalite to Granodiorite Unit	
Mafic Intrusives	
Metasedimentary Unit	
Metasedimentary to Metavolcanic Unit	
Felsic to Intermediate Metavolcanic Unit	
Mafic Metavolcanic Unit	

The feldspar megacrystic granite unit is defined in the model by its associated prominent anomalous magnetic high. Though not noticeable from the gravity anomaly map, the average densities of 3 rock samples from the unit are slightly lower than those of the surrounding biotite granite to granodiorite unit (Table 3.2). The dominant biotite granite to granodiorite unit has a clear gravity low and smooth magnetic low signature. The biotite tonalite to granodiorite and hornblende tonalite to granodiorite units within the batholith do not have clear distinctive gravity or magnetic signatures, but the measured densities (Table 3.2) show both units as somewhat denser than the biotite granite to granodiorite unit, with the biotite tonalite slightly less dense than the hornblende tonalite.

The biotite tonalite to granodiorite unit at the northeastern corner of the model is associated with distinctive gravity low and magnetic high signatures; however, its response is slightly obscured by the close proximity of the Basket Lake batholith further north, just outside of the model limits. Therefore, it was assigned as a separate unit "northeast biotite tonalite to granodiorite" with rock properties that were modified to fit the regional fields associated with sources outside of the model limits. Thus, its inverted geometry and rock properties are biased.

Mafic metavolcanics and felsic to intermediate metavolcanics are mapped as the units surrounding the Revell batholith. Both the measured gravity and magnetic signatures suggest significantly more lithological variation within these units than is indicated from the geological map. However, the measured mean rock densities show only a very small amount of variation (Table 3.2). No magnetic susceptibility measurements are available from within the model limits for either of these units. The mafic metavolcanics, particularly to the north and northeast of the

batholith, show banding in the magnetic signature, which in part is also apparent in the gravity data as can be seen in the first vertical derivative of the Bouguer gravity data (Figure 5.3 (b)). Despite this apparent heterogeneity, no attempt was made to incorporate the banding in the geology interpolation model. As such, all variability in the magnetic and gravity data were accommodated in the inversion as rock property variations within the units. Mapped metasedimentary units and metasedimentary to metavolcanic units were also incorporated in the model. Though they are not the primary targets of the modelling and inversion, they are used primarily to help model the geophysical data in the area surrounding the batholith.

Two diabase dykes, some large mafic intrusives and an iron formation unit were incorporated into the model. The visualization and contribution of small features to the forward modelling and inversion processes are dependent on the choice of resolution during the conversion process from geological model to voxel representation. Although the iron formation is responsible for the largest amplitude magnetic anomaly within the model, it is mapped with a thickness of less than 30 m, less than the voxel sizes employed. Thus, when visualizing and during forward modelling and inversion calculations, which entail model simplification processes at the voxel level, its presence and relative contribution is obscured. GeoModeller® allows for variable dyke thickness but extrapolates any mapped dyke to the limits of the whole model. Dykes with limited extents are accommodated by reducing their thickness to significantly below the model voxel size where they are extrapolated so that their impact on the model is limited to where they actually occur.

The rock units in the model have been set in chronological order (Table 5.1) honouring the broader scale geological domains. The greenstones are the oldest, followed by the four units that make up the Revell batholith and the diabase dykes are the youngest. The younger units are allowed to truncate the boundaries of the older units during the interpolation process when calculating the geology only model. To incorporate a lens of the older metavolcanic rocks within the batholith, the lens was assigned a younger age (Table 5.1).

The geology polygon files were converted into lines representing contacts and segmented to allow for varying dips to be assigned per segment (Figure 3.7). The mapped foliation dips within the greenstone belt units have been taken to represent the contact orientations of the batholith. Subtle asymmetry in linear magnetic anomalies within the greenstones, in part, support the dip directions of their causative bodies being in agreement with the measured foliation dips. At the ground surface, the batholith is inferred to dip underneath the surrounding greenstone units in its western and northwestern parts, and in the central section close to the mapped feldspar megacrystic granite unit. The batholith lies on top of the greenstone unit at the northeastern end. The south and southeastern portions of the batholith are not surrounded by units with systematic orientation of foliation dips needed to infer a dip for the batholith contact. In these regions, a vertical contact between the batholith and the greenstones is assumed for the initial model (Figure 3.7). However, the contact geometry may vary as a result of the inversion to best fit the model response to the gravity and magnetic data.

The 3D GeoModeller® model based on the interpolation of the bedrock geology information is presented in Figures 5.4 and 5.5. Mismatches with mapped geology, or poor fit from forward modelling (Section 5.4) were used to guide the interpolation by adding inferred dip information to different units in the model.

Figure 5.5 presents 3D views of the modified interpolated geology only model, with successive panels showing intrusive phases of the Revell batholith being removed. The holes in the 3D view represent units extending to the base of the model. The batholith edges generally dip outwards thus the interpolated batholith model extends outwards down to the base of the model.

Note that the initial interpolated model has the batholith extending to the flat base of the model at 4 km, which is inconsistent with the 2D modelling in Section 4.1 above.

5.3 3D Forward Modelling

Prior to running inversions, a starting model that fits the dominant observed gravity and/or magnetic signature must be in place. This starting model is created and tested in the forward modelling stage. The process of forward modelling entails calculating the field predicted by a model, comparing it with the observed field and then iteratively modifying the model geometry and/or physical properties to improve the fit with the observed field. In order to calculate the predicted model fields, rock properties determined in Section 3.4 are assigned to the different model units. A reference density of 2.67 g/cc used in the Bouguer correction of the gravity data was assigned to the model. A Geomagnetic Reference Field with an intensity of 56525 nT, declination of -1.9° and inclination of 74.5° calculated for October 2019 at 49.4° N, -91.7° W (the approximate location of Ignace Airport) was also assigned to the model.

Figure 5.6 shows the gravity field from the interpolated bedrock geology model with the observed (Figure 5.6(a)) and the calculated (Figure 5.6(b)) gravity anomalies and their difference, the latter given by the observed minus the calculated field (Figure 5.6(c)). Bedrock geology is also included in panel (d) to allow for characterization of the mismatch (Figure 5.6(d)). The forward calculation for the gravity field is undertaken at progressively higher resolution (i.e. smaller voxel size) with the results in Figure 5.6 calculated using a $100\text{ m} \times 100\text{ m} \times 100\text{ m}$ voxel size, producing a voxel with $314 \times 307 \times 50$ cells in the easting (x), northing (y), and depth (z) directions, respectively.

It is interesting to note that this model, based primarily on interpolation of the known surface mapping with all units clipped at a depth of 4 km, broadly fits the observed gravity anomaly. This supports the assertion that the gravity anomaly is dominated by the density contrast between the units of the batholith and the greenstones, and for the most part the observed gravity field occurring within the model extents can be modelled by density variations that are shallower than 4 km depth. The northern end of the batholith, covering a section north of the mapped biotite tonalite to granodiorite unit, stands out with a prominent positive mismatch (observed minus calculated gravity) that falls within the polygon defining the limits of the LiDAR data coverage (feature GMA in Figure 5.6 (c)). The low-density batholith has been mapped with an edge that dips outwards to the northwest and to the west, suggesting that the batholith extends at depth in these directions. However, the gravity model response in this area has to be raised in order to reduce the gravity misfit. This can be achieved by a local increase of the density of the batholith or the greenstones in this area only. However, the misfit can be resolved if we consider that the dip of the boundary as indicated by the foliation is only at shallow levels in this location, and that the greenstones extend below the batholith at deeper levels. Therefore, to resolve the misfit, the base of the batholith where it extends beyond the surface outcrop can be made shallower in this region, bringing underlying denser greenstones closer to the surface. Since this is consistent with the shape of the batholith determined from 2D modelling, this interpretation is preferred to a local variation in density.

Another strong mismatch between the observed data and the calculated data is in the northwestern corner of the model (feature GMB in Figure 5.6 (c)). This occurs within the mapped greenstones and is part of a larger positive gravity anomaly centred outside of the model limits. The high also falls within the area only covered by lower resolution ground gravity data (Section 3.2), thus no attempt was made to introduce a unit to model the anomaly in the observed field, but rather it was incorporated as a density variation within the greenstones.

Based on the geological interpretation from 2D forward modelling along 3 profile lines (Section 4), the 3D model was updated, and as a result the bottom of the batholith does not extend to the maximum model depth. Raising the base of the batholith was also supported by preliminary GeoModeller® 3D inversions that used the interpolated surface geology only model as the initial model for the inversion. An interpolated geology model that incorporated the results of 2D forward models and some improvements based on alterations from 3D forward modelling is presented in Figure 5.7. In the 3D views, the curved bases to the model units imply that they are all shallower than the 4 km base of the model. If the units extended to the 4 km base of the model, they would have flat bottoms. Figure 5.8 shows the gravity field from the model with the observed and calculated anomalies and their difference and bedrock geology for characterization of the mismatch. The results in Figure 5.8 are also calculated using a 100 m x 100 m x 100 m voxel size. This model resolved the issue of the mismatch at the northern end of the batholith (GMA) with the remaining major mismatch being the high at the northwestern corner (GMB), addressed above. This model was used as the starting model for the final 3D inversions.

The calculated magnetic field for the starting model gave the results presented in Figure 5.9. The magnetic signature of the units of the batholith can be considered smooth enough to be adequately represented at the sample resolution of the model. The rest of the units responsible for the dominant magnetic anomalies within the model are mostly under sampled. The feldspar megacrystic granite unit has an associated magnetic high anomaly and was assigned a magnetic susceptibility of 0.012 SI based on the 2D modelling (Section 4). The biotite granite to granodiorite unit has a well-determined mean susceptibility of 0.0002 SI (Table 3.3) and the hornblende tonalite to granodiorite was determined to have a mean of 0.0006 SI which was also assigned to the biotite tonalite to granodiorite. The tonalitic unit in the northeastern corner was assigned a susceptibility of 0.0035 SI. The size and magnetic signature of these units lead to adequate sampling and representation in the model at most scales of model calculation and presentation.

The mafic metavolcanic unit and the felsic to intermediate metavolcanic unit which surround the batholith have mean susceptibilities of 0.0007 SI based on measurement on neighbouring greenstone belts (Table 3.3). From their magnetic signature, it is clear that assigning a single mean susceptibility value to these rock units is not appropriate. A bimodal distribution would be more suitable. The 2D forward modelling (Section 4) indicates that linear anomalies within the greenstone generally require associated magnetic sources with at least an order of magnitude higher magnetic susceptibilities than the assigned mean values. The narrow linear nature of the anomalies requires similar shaped causative source bodies that are subject to under sampling and under representation in a voxel model. Much higher mean susceptibility values were assigned to the smaller intrusives and iron formation to make up for the diminishing effect that averaging has on rock property when converting the model into voxel format.

As a result of the limited amount of magnetic susceptibility measurements in the area, multiple rock property optimizations were carried out with sample results presented in Table 3.3. The results of the optimization further highlight the issue of the under sampling of the small or thin, yet strongly magnetic, features in the model. Voxel representation of the small features using large voxel sizes can result in parts of these features being made much larger than they actually are, or on the other hand can result in their elimination from the model. The optimization results in magnetic susceptibilities for the smaller features that are at the lower bounds of the permitted range set prior to optimization based on the measured data. These include the dykes, the iron formation, the mafic intrusives and the mafic metavolcanic lens. The optimization also recommended lowering the magnetic susceptibilities of the units of the batholith which were already quite low. The optimization almost maintained the susceptibility of the mafic

metavolcanics, and lowered the susceptibilities of felsic to intermediate metavolcanics. Since these are sub-units that surround the batholith, the recommended property changes were considered to be alterations which the inversion process could accommodate using the measured or proxy model properties (Table 5.2), so the optimized values were not employed during inversion.

Since the forward modelling process produced an acceptable fit with the observed gravity data, a property optimization was not deemed a requirement for the densities.

Table 5.2 GeoModeller® suggested susceptibilities and ranges from property optimization of magnetic susceptibilities

Unit	Susceptibilities in SI units				
	Recommended	Input mean	Standard deviation	Lower bound	Upper bound
Dyke 2	0.0280	0.0300	0.0010	0.0280	0.0320
Dyke 2	0.0280	0.0300	0.0010	0.0280	0.0320
Iron Formation	0.9800	1.0000	0.0100	0.9800	1.0200
Mafic Metavolcanics lens	0.0001	0.0007	0.0003	0.0001	0.0013
Feldspar Megacrystic Granite	0.0080	0.0120	0.0020	0.0080	0.0160
Biotite Granite to Granodiorite	0.0000	0.0002	0.0003	-0.0004	0.0008
Hornblende Tonalite to Granodiorite	0.0000	0.0006	0.0008	-0.0010	0.0022
Northeast Biotite Tonalite to Granodiorite	0.0051	0.0035	0.0008	0.0019	0.0051
Biotite Tonalite to Granodiorite	0.0000	0.0006	0.0008	-0.0010	0.0022
Mafic Intrusives	0.0014	0.0012	0.0001	0.0010	0.0014
Metasedimentary	0.0018	0.0006	0.0006	-0.0006	0.0018
Metasedimentary to Metavolcanics	0.0000	0.0006	0.0006	-0.0006	0.0018
Felsic to Intermediate Metavolcanics	0.0000	0.0010	0.0060	-0.0110	0.0130
Mafic Metavolcanics	0.0010	0.0008	0.0006	-0.0004	0.0020

Levenberg-Marquardt returned after 200000 out of 200000 iterations. Reason: Maximum number of iterations reached. Initial misfit:269.90441. Final misfit: 196.491279. Misfit Threshold 0.100000.

5.4 3D Inversion Modelling

Inversion tends to be an iterative process in a manner similar to forward modelling in which initial conditions and constraints are put in place. Depending on an evaluation of how close the predicted results are to the measured results, the inversion algorithm adjusts the initial conditions, recalculates the response and re-evaluates the predicted results. This adjustment, prediction and re-evaluation is repeated if the predicted results are not sufficiently close to the measured results. As a time saving strategy preliminary inversion runs are normally carried out with large voxel sizes which are progressively reduced down to a level of resolution appropriate to the resolution of the observed data or computational capabilities of the computer. Only final results deemed essential in defining the final model are presented here.

With an acceptable starting model in place, the following steps are applied to run an inversion in GeoModeller®.

1. Identify the data set or joint data sets being modelled. The options available in GeoModeller® are the gravity and magnetic data, their associated tensors or derivatives and components. A trend in the observed data can be defined and removed at different

stages of an inversion to reduce the effect of geology outside the project space. The option of implementing a constant shift to the data at the start of an inversion run was employed in all the inversions presented. This has the effect of centring the misfit errors around zero.

2. The observation/modelling surface is assigned, which is where the geophysical responses are calculated by GeoModeller®. This was selected as the final drape surface (Section 3).
3. Setting the voxel properties. This will determine model resolution. Determining the voxel size is a trade-off between desired model resolution and processing time.
4. A review of the selected geophysical properties set for the model rock units. An option of mirroring the geology of the model along all edges to reduce model edge effects is available and was activated for all the inversion runs.
5. Shared geological settings are selected and the decision on whether to activate them or not is made just prior to starting the inversion. Shared geological settings are global settings affecting all rock units in the model. An example is setting the probability of rock property changes versus lithological change on a boundary cell in a given inversion iteration. For all inversion runs, the default setting of equal probability was chosen. The lithology of all cells that intersected the surface were fixed based on geological surface mapping, however their physical properties were allowed to change.
6. Lithology-specific geological settings are set with the decision on whether to activate them or not being made later in the process, just prior to starting the inversion. These apply to each lithology separately. Chronologic ordering can be activated by setting which lithologies are always below a given lithology. For all final inversion runs presented no chronologic ordering was implemented. This allows for on-lapping of older geological units over younger units, which effectively allows intrusions into older units. Geological constraints which reduce model fragmentation and maintain geological consistency are set. Commonality and shape ratio (discussed in Section 5.1) were set for all final runs presented. However, the volume ratio constraint was not utilized. This is the preferred option if acceptable inversion results are obtained without activating this additional constraint.
7. Run settings. The number of iterations is set. Tests using the settings assigned above can be activated or deactivated for a given inversion run. The selection is made here. For all the final runs presented here, the geophysical misfit test, allowing for fitting the observed data, in addition to the commonality and shape ratio tests for the geological constraints were activated.
8. The inversions are run either in an iterative mode or in batch mode which is recommended for large number of iterations.

5.4.1 Varying Levels of Constraint for Geological Controls

The inversion results selected for final presentation are from 3 gravity only inversion runs, 3 magnetic only inversion runs and 3 joint inversion runs. After trial and error, three inversions were selected to represent three levels of tightness in constraints (Table 5.3). These were assigned to the four main units within the Revell batholith and the surrounding mafic

metavolcanics and felsic to intermediate metavolcanics.

Table 5.3 Settings of levels of inversion constraint for geological controls

	Commonality		Shape Ratio	
	Scale	Shape	Mean	Standard deviation
Very tight constraint	0.1	1	1	0.07
Moderate constraint	0.5	1	1	0.1
Loose constraint	0.5	1	1	0.5

Inversion in GeoModeller[®] utilizes stochastic processes that respect statistical models. The models that govern allowable changes are constrained to follow selectable probability distribution functions. For commonality, GeoModeller[®] recommends using a Weibull distribution for the commonality misfit function used in calculating the acceptance probability of a proposed change to the state of a current model during an inversion run. A shape parameter of 1 for all levels was chosen, making the Weibull distribution an exponential distribution which implies that the reference model is considered the best estimate of the geology. A shape parameter value greater than 1 would imply the reference model is wrong but the models to be evaluated are similar to the reference model. The scale factor is a measure of uncertainty, with larger values indicating greater uncertainty in the reference model. A value of 0.1 was used for the very tight constraint setting (Table 5.3), indicating an overlap with the reference field between 80% and 90%, while 0.5 for both moderate and loose constraints represents a 70% overlap.

The recommended law to use for controlling a shape ratio constraint is log-normal while defining a mean and a standard deviation as input parameters. The mean is defined as the shape of the revised unit divided by its previous shape and the standard deviation is defined as the variability/spread of the mean from the starting model. A mean of 1 centres around no overall change in shape ratio. A value of 1.1 would mean 10% rougher while 0.9 would mean 10% smoother. A value of 1 was assigned to all the levels of constraint (Table 5.3). The standard deviation was set at 0.07 for a very tight constraint, 0.1 for moderate constraint, and 0.5 for loose constraint.

The settings were determined using the GeoModeller[®] suggested values for tight, moderate and loose shape ratio constraints and adjusting them based on the results. The final settings were based on creating a moderate constraint level that gave all the final accepted models presented below. Tight and loose constraints were created to allow assessing model sensitivity to the constraints.

5.4.2 Inversion Results

After an inversion run, the results are evaluated visually by comparing the observed and calculated fields of the final model and the associated misfits and displaying the model in 3D. This allows for a quick detection of areas where the model is failing to produce an acceptable fit. Acceptable fits should have low amplitude misfits with near random spatial distribution of the errors.

A tool in GeoModeller[®], the Results Explorer, allows for the visualization of the data. The tool incorporates options for removal of regional trends and displaying the de-trended field. Visualization of the full 3D data requires running a tool that generates summary voxets from the inversion detailing model changes on a voxel by voxel basis. The tool displays a misfit-variation

curve which allows for setting an appropriate burn-in level recorded as the number of iterations from the start of the inversion (e.g. Figure 5.10). The models created after the burn-in iteration are incorporated in the calculation of a statistically averaged “most probable model”. The threshold level setting in the tool allows for the creation of a most probable model with lithologies identified above a selected level of confidence. Setting both the burn-in level and threshold level is a post inversion procedure used in visualization of the results. Levels can be adjusted iteratively for different levels of confidence in visualizing the final result.

Table 5.4 lists GeoModeller® inversion output file names of 2D grids and 3D voxets with description provided. Details of the contents of the summary statistics files for the changes made to the voxets throughout the inversions are presented in Table 5.5. Visualizing in 2D and 3D the MostProbable (Table 5.5) file, which represents the most often assigned lithology for each voxel is a good starting point for the 3D assessment of the inversion results. Meanwhile, an indication of the model stability can be assessed by visualization of the MostProbableThresholded field, where a lithology assigned to a given voxel is only displayed if it is assigned that lithology more frequently than a specified display threshold percentage. An indication of the evolution of a model during inversion can be obtained by inspecting the voxel change count and entropy. The change count is simply the number of times a particular voxel has changed. A less intuitive parameter is the entropy. It is a record of the volatility of a particular voxel ranging from 0 for low volatility and 1 for high based on, among other parameters, how often the voxel changed from one rock type to another and how many rock types it changed to during an inversion. It refers to boundary or frontier changes and is viewed as some measure of geology boundary uncertainty rather than property uncertainty. Rock properties, their associated standard deviations, and the probability of finding a given lithology for each voxel are available for visualization. The output files allow for a full evaluation of an inversion with only a limited view possible in print form. An additional visualization tool is the creation of inversion movies that show the progression of the model modifications as the inversion iterates and evolves. These videos show progressive displays of either rock unit, density or magnetic susceptibility of the voxels along selected cross-sections. Videos of the progression of the models during inversion are supplied as part of the final deliverable files.

Table 5.4 Inversion output file names and descriptions

Inversion output files	
Files(s)	Description
misfit.csv	Numeric record of the misfit evolution (misfit value for gravity and magnetic data as a function of iteration number where misfit is the least squares differences between the observed and the current computed geophysics grid, [dist = sqrt(dist / count);].
Summary.txt	A summary of proposal acceptances and rejections for each geological and geophysical constraint for the full inversion.
compute_Surface_1.grd	2d grid of the surface on which to compute the Gravimetry response
observed_Gravimetry_1.grd	2d grid of the measured gravity.
initial_Gravimetry_1.grd	2d grid of the computed gravity response from the initial iteration of the inversion.
final_Gravimetry_1.grd	2d grid of the computed gravity response from the final iteration of the inversion.
compute_Surface_2.grd	2d grid of surface on which to compute the magnetic anomaly response
observed_TMI_2.grd	2d grid of the measured magnetic field.
initial_TMI_2.grd	2d grid of the computed magnetic response from the initial iteration of the inversion.
final_TMI_2.grd	2d grid of the computed magnetic response from the final iteration of the inversion.

initial.vo	Initial voxel (3D grid) for the state of the model at the initial iteration - 4 attributes: initial lithologies; fixed cells; initial densities; initial susceptibilities.
final.vo	Voxel (3D grid) for the state of the model at the final iteration - 4 attributes: final lithologies; fixed cells; final densities; final susceptibilities.
Stats_"x"_"y"_T90.vo	A summary statistics mesh grid (voxet) for inversion iterations "x" to "y" (post burn-in). For further details see Table 5.5 below.

Table 5.5 Summary statistics files for the voxets

Summary statistics mesh grid (Stats_"x"_"y"_T"P".vo)	
Files(s)	Description
Entropy	Records the volatility of the particular voxel during inversion. Computed as a number from 0 (low volatility) to 1 (high volatility).
ChangeCount	The number of times this particular voxel has changed.
MeanDensity	The mean density as derived from the accumulated accepted inversion proposals/models which occurred during the chosen range of iterations.
StdDevDensity	Related to the above mean and derived from initial property distribution function (PDF).
MeanSusceptibility	The mean magnetic susceptibility as derived from the accumulated accepted inversion proposals/models which occurred during the chosen range of iterations.
StdDevSusceptibility	Related to the above mean and derived from initial PDF.
MostProbable	For each voxel location, this field records the lithology index most often assigned to that voxel over the iteration range selected. The lithology index is an integer starting at 1 and incrementing by 1 from the base of the chronologic pile up. The AboveTopo unit is assigned the number 0.
MostProbableThresholded	As above, but the most often assigned lithology for a voxel location must have been accepted as that lithology for "≥ the threshold (e.g. 90%) of the number of proposals" over the iteration range selected, otherwise a "Null" is recorded instead of a lithology index. Areas of uncertainty will appear as Null gaps around geological boundaries.
Prob_ xxxx	Within the whole model space, the probability of finding "xxxx" varies between 0 and 100%. Display values in a black/grey/white colour scale.
(Stats_"x"_"y"_T90.vo)	Default name of summary voxel with inversion results from iteration "x" to "y" at a threshold level of "P" %

5.4.3 Gravity-only Inversion

Results from the three final gravity only inversion models are presented in Figures 5.11 to 5.19. These are for tight, moderate and loose geological inversion constraint settings (Table 5.3). The results presented here focus on the inversions with moderate constraint setting determined to produce the most geologically realistic models with a good fit to observed data. The models were run for 30 million iterations. For visualization, a burn-in point at 20 million iterations for acceptable models was chosen, based on the flattening in the misfit curves (Figure 5.10 (c)). A display threshold setting of 90% was chosen to limit the most probable rock type. All final results displayed are from inversions using a 157 m x 153.5 m x 125 m voxel size producing a voxel with 200 x 200 x 40 cells in the x, y, and z directions, respectively.

Visualizing the misfit between observed and calculated gravity of the last iteration allows for an initial comparative assessment of the performance of the different geological constraint settings (Figure 5.11 and 5.12). With the starting model having been created using 3D forward modelling of gravity data, it is not surprising that all the inversion constraint settings produced

acceptably low final misfits (Figure 5.10 (c)). The more the model is allowed to change during inversion the lower the final misfit, though the more varied, and potentially geologically unrealistic the model becomes. The models have two small misfits where the observed gravity field is higher than the calculated to gravity data that are associated with the feldspar megacrystic granite unit (labelled as GMC and GMD in Figure 5.11), that can be traced back to local high anomalies in the observed data. Likely origins of the models failing to fit the anomalies are discussed below.

Cross-section displays along the three 2D model lines (Section 4) were created in order to visualize the inversion model results in 2D. Figure 5.13 shows the most probable model units of the batholith overlain with the starting model image in the background. The model boundaries are drawn as dotted, solid and faint black lines for tight, moderate and loose inversion constraints, respectively. Visualizing the modelled unit boundaries from inversions at different constraint levels allows for an assessment of the consistency of the inversions in defining the boundaries. The inversion statistics defined in Table 5.5 give additional information about the model evolution and variability during the inversion for each set of constraint parameters. Figure 5.14 shows an example of some of these inversion statistics along Profile Line 3 at a moderate constraint level. The 90% thresholding, entropy, and change count statistics reveal model changes mostly at unit boundaries with fewer, fairly uniformly distributed, changes occurring within units. Along Line 1 all the models are fairly consistent (i.e. almost coinciding) and suggest a deepening of the batholith by about 1 km at its southwestern end. Along Line 2 the outside edges of the batholith are generally consistently unchanged at all geological constraint levels, with some suggestion of an increase in depth to bottom in parts. Variations in the internal boundaries of the batholith are mainly associated with the feldspar megacrystic granite unit and are associated with the two small misfits to the gravity data mentioned above (GMC and GMD). Line 3 has fairly consistent boundary definition at all levels of constraint with some variations related to the misfit under the feldspar megacrystic granite unit.

Figure 5.15 shows the mean density distribution along the cross-sections and Figure 5.16 shows the mean density distribution on a number of horizons for inversion results, both from the moderately constrained inversion. The modelled density distributions for each unit are presented in Figures 5.17 and 5.18 with associated statistics. Depth slices of the density distribution from the moderately constrained inversion (Figure 5.16) show that a lot of the short wavelength signal in the observed gravity is modelled as near-surface density variations which almost disappears at 1 km below MSL. This is as to be expected because of the signal wavelength. It should be noted that there may be equal variation at depth, however this is not captured in the data due to signal attenuation with depth to source. It is also apparent in the figures that the modelled density variation within the feldspar megacrystic granite unit is much less than in the rest of the units within the batholith. This fits the initial setting of the density of the unit (Table 3.2). Due to the small sample size of observed densities with very similar values, the feldspar megacrystic granite is set to have a standard deviation roughly an order of magnitude smaller than the other rock units in the batholith. By limiting the permitted density variation, short wavelength gravity variations under the feldspar megacrystic granite unit had to be modelled as variations in depth to the bottom of the unit, or density variations in underlying deeper unit. The tight constraint of the density for this unit is considered the likely reason behind the two gravity high misfits (GMC and GMD) within the feldspar megacrystic granite. It is likely that with additional density measurements within the unit, a larger associated error will be determined, allowing for a better fit to the anomalies. However, there might also be a dense phase within the feldspar megacrystic granite that does not outcrop.

An additional gravity only inversion was run with all of the batholith units in the model assigned the same density as that of the granite to granodiorite unit at 2.65 ± 0.05 g/cc. Moderate

geological constraint settings were employed for this inversion. This model was used in setting a lower limit to the thickness of the batholith. Figure 5.19 shows the results of the inversion with the single density batholith model in black overlain on the multi-density model results. As expected, the larger average density contrast between the batholith and host rocks associated with the single density batholith results in a slightly shallower batholith, however the thickness remains more than 3 km in most regions.

5.4.4 Magnetic-only Inversion

Results from the three final magnetic only inversion models are presented in Figures 5.20 to 5.27. These are for tight, moderate and loose geological inversion constraint settings (Table 5.3). The results presented here focus on the inversions with moderate constraint setting determined to produce the most geologically realistic models with a good fit to the observed data. The models were run for 30 million iterations. For visualization, a burn-in point at 25 million iterations was chosen for acceptable models, based on a degree of flattening in the misfit curves (Figure 5.10 (d)). The inability of the model to fit the short wavelength anomalies associated with narrow geological features resulted in high misfit values (Figure 5.10 (d)). Clipping the sharp short wavelength anomalies in the observed magnetic data reduces the misfit values without any effect on the inversion results, but the option of working with unclipped data was preferred.

Visualizing the misfit between the observed and calculated magnetic anomalies of the last iteration allows for an initial comparative assessment of the performance of the different constraint settings (Figure 5.20 and 5.21). Unlike the case for gravity data, the observed magnetic anomaly data over the model is dominated by high amplitude short wavelength anomalies which are poorly represented in the model and thus dominate the misfit. This makes the visualization of the field from larger, less magnetic units problematic. It is apparent in Figure 5.21 that in some cases the misfit is reduced with reduction of the amount of constraint applied to the models, but it requires very close scrutiny of the images (e.g. the misfit around the periphery of the feldspar megacrystic granite unit).

Cross-section displays along the three 2D model lines were created in order to visualize the models in 2D along these sections. Figure 5.22 shows the most probable model rock units of the batholith overlain on the starting model image in the background. The model boundaries are drawn as dotted, solid and faint blue lines for tight, moderate and loose inversion constraints respectively. Figure 5.23 shows an example of some inversion statistics along Profile Line 3 for the moderately constrained inversion. The 90% thresholding, entropy, and change count statistics show changes mostly within model units with fewer boundary changes. This is likely the result of the large standard deviations associated with the magnetic susceptibilities assigned to each unit.

Along Line 1 all the models are fairly consistent and all suggest a slight deepening of the batholith at the tapered end to the northeast. This change can be viewed as an increase in the size of the biotite granite to granodiorite unit of the batholith only. This unit expands into the biotite tonalite to granodiorite at the southern end and into greenstones at the northern end of the line.

Along Line 2, the outside edges of the batholith are generally maintained by all models. Variations in the internal boundaries are associated with the feldspar megacrystic granite unit with a lot more complex geometry being modelled along the bottom boundary when using the loose geological constraint settings. Generally, the models suggest a slightly shallower depth to bottom for the feldspar megacrystic granite unit. They also suggest a slight increase in the size

of the biotite granite to granodiorite unit immediately below the feldspar megacrystic granite.

Similar to Line 1, on Line 3 the models suggest a slight deepening of the batholith at the northern end. As with Line 2, this can be viewed as an increase in size of the biotite granite to granodiorite unit of the batholith only. A slightly shallower feldspar megacrystic granite unit extending and deepening to the southeastern end is modelled.

Figure 5.24 shows the mean magnetic susceptibility distribution along the cross-sections and Figure 5.25 shows the mean magnetic susceptibility distribution on a number of horizons for inversion results with moderate constraint. The modelled magnetic susceptibility distributions are presented in Figures 5.26 and 5.27 with associated statistics. Depth slices of the magnetic susceptibility distribution from the moderately constrained inversion (Figure 5.25) show, as for the gravity data, that a lot of the short wavelength signal in the observed magnetic data are modelled as near surface magnetic susceptibility variations which almost disappears at 1 km below MSL. It is possible that similar short wavelength susceptibility variations are present at depth however this is not captured in the data due to signal attenuation with depth to source.

It is also apparent from Figures 5.26 and 5.27 that the modelled magnetic susceptibility variations are bi-modal for the greenstone formations such as the mafic metavolcanics and the metasedimentary to metavolcanics. This is most likely because the magnetic signature in these greenstone units is predominantly generated by relatively thin layers of variable magnetic susceptibility. By comparison, the batholith units are mostly magnetically homogeneous.

It is apparent from the Table 3.2 and 3.3 that the magnetic susceptibilities of the different units in the model have much higher associated errors compared to the errors associated with the densities. This is expected to limit the utility of magnetic inversions in resolving the depth to the bottom of the batholith. Reducing the errors would be expected to force more changes in the shape of the model while reducing magnetic susceptibility variations. This poses the problem of whether the large measured errors are a representation of limited or poor sampling of the geology for magnetic susceptibility measurements or a valid representation of the variability in magnetic susceptibility for the different units. Additional field measurements are needed to help resolve the issue.

5.4.5 Joint Inversion

Results from the three final equal weight joint gravity and magnetic inversion models are presented in Figures 5.28 to 5.41. These are for tight, moderate and loose geological inversion constraint settings (Table 5.3). The results presented here focus on the inversions with moderate constraint setting determined to produce the most geologically realistic models with a good fit to observed data. The models were run for 50 million iterations. For visualization, a burn-in point at 40 million iterations for acceptable models was chosen, based on the flattening in the misfit curves (Figure 5.10 (a) and (b)). The same starting model as for gravity only and magnetic only inversions was used. Though improvements from both gravity only and magnetic only inversions were considered valid, they were not large enough to warrant modification to the starting model for joint inversions.

Figures 5.28 to 5.31 show the misfit between observed and calculated gravity and magnetic fields of the final iteration of an inversion run for an initial comparative assessment of the performance of the different constraint settings. The final misfits for the gravity data (Figure 5.29), though at acceptable levels, are slightly higher than for gravity only inversions for the equivalent inversion constraint level. Aside from the two misfit within the feldspar megacrystic granite which are addressed above (GMC and GMD in Figures 5.11), another misfit

where the observed gravity data is higher than the calculated gravity runs along the inside edge of the batholith, suggesting some type of geological differences that has resulted in a local density increase.

The misfits to the magnetic data (Figure 5.31) are dominated by high amplitude, short wavelength anomalies which are poorly represented in the model, creating problems of visualization of the larger, less magnetic units. The resulting misfits to the magnetic data are comparable to those from the magnetic only inversion.

Cross-section displays along the three 2D forward modelled lines were created in order to visualize the models in 2D along these sections. Figure 5.32 shows the most probable model geometry of the batholith overlain on the starting model image in the background. The model boundaries are drawn as dotted, solid and faint brown lines for tight, moderate and loose inversion constraints respectively. Figure 5.33 shows an example of some inversion statistics along Profile Line 3. The 90% thresholding, entropy, and change count show changes both at unit boundaries and within the units.

Along profile line 1, all of the models are fairly consistent and all suggest an overall slight deepening of the batholith. Internally an increase in the size of the biotite granite to granodiorite unit into the biotite tonalite to granodiorite is suggested. In addition, the expansion of this biotite granite to granodiorite unit into underlying greenstones in the north end of the batholith is modelled.

Along profile line 2, the outside edges of the batholith remain fixed on all model constraint levels, however the loose constraint version has boundaries that are quite irregular. Generally, the models suggest a slightly shallower depth to bottom for the feldspar megacrystic granite unit.

Along profile line 3, the depth to bottom on the batholith only increases significantly at the northwestern end of the batholith. An increase in size of the biotite granite to granodiorite unit is also suggested at the base, except at the extreme southeast of the batholith where the biotite granite to granodiorite has been changed to feldspar megacrystic granite unit. This was not seen in the gravity only inversion (Figure 5.13), so it suggests that this change is driven by the magnetic contrast of the feldspar megacrystic granite unit. Note that these are near-surface changes, suggesting magnetics has the strongest impact at shallow depth. Note however that the joint inversion does not result in a significant change of the depth to the bottom of the batholith.

The density distributions (Figure 5.34 to Figure 5.37) and magnetic susceptibility distributions (Figure 5.38 to 5.41) show the same characteristics and features as the distributions from gravity only and magnetic only inversions. This suggests that the magnetic data does not make a significant contribution to the joint inversion except for extending the feldspar megacrystic granite to the southeast on line 3 close to the surface.

5.5 Model Comparisons

While the joint gravity and magnetic inversion runs give equal weighting to the two data sets, the starting model for all of the inversions was established using the gravity data forward modelling only. From the gravity controlled starting model, the model modifications from gravity only inversion were primarily a slight increase in depth to bottom and internal variability, primarily associated with the feldspar megacrystic granite unit. The changes can be noted at all levels of geological constraint applied to the inversions, thus allowing for the selection of the moderate

geological constraint level setting as a representative level (Figure 5.13).

For magnetic only inversion runs (Figure 5.22) consistent model changes can be seen at tight and moderate geological constraint level while the loose constraint levels incorporates extreme model variability in some regions. Overall, while consistently maintaining the outside boundary of the batholith, the magnetic only inversions suggest an increase in the size of the biotite granite to granodiorite unit into underlying biotite tonalite to granodiorite and hornblende tonalite to granodiorite units or greenstones. Changes in the shape of the feldspar megacrystic granite unit is also modelled. The moderate geological constraint setting was also considered a representative level.

Joint inversion results (Figure 5.32) incorporate the change from gravity only and magnetic only inversion changes. A slight increase in depth to bottom of the overall batholith is modelled, similar to the gravity-only inversions. An increase in size of the biotite granite to granodiorite into underlying units is modelled and changes to the shape of the feldspar magacrystic granite unit occur. Consistent results are obtained with tight and moderate geological constraint settings while loose settings result in irregular boundaries.

The results from a joint inversion with the moderate geological constraint settings were selected as the final representative model (Figure 5.42), shown as a colour image, with the boundaries of the starting model shown as colour lines, where the colour corresponds to the overlying unit. In order to allow for an assessment of changes in boundary definition as a result of the joint inversion, the results from gravity only and magnetic only inversions, both with moderate geological constraints applied, are overlain on the final representative model in Figure 5.43. These are in black for gravity and blue for magnetic data. This allows for identification of boundaries defined well by both data sets. When they differ, it is possible to assess which data set had a bigger influence on the joint inversion. Figure 5.44 is a similar figure to Figure 5.43, however it presents the results for the loosely constrained inversions thus ensuring that no consistent model changes have been limited or blocked as a result of the level of the geological constraint.

A 3D visualization of the changes in the shape of the units within the batholith from the joint inversion, with moderate geological constraint settings is presented in Figures 5.45 and 5.46. This allows for an extension of the model visualization to that presented along the three cross-sections.

5.6 Model Discussion

The purpose of this study is to determine the depth of the batholith for the purposes of having confidence that it is a good location for a deep geological repository. The 3D geophysical model of the batholith was created from inverting the observed gravity and magnetic data. Modelling was constrained by near surface bedrock geological mapping and rock densities and magnetic susceptibility measurements. Even in an idealistic setting of detailed coverage of the physical rock properties and the observed fields, the model building would rely on some geological assumptions when extending the known surface geology to depth. As an example, the biotite tonalite to granodiorite and hornblende tonalite to granodiorite units have been modelled as continuous and connecting beneath the biotite granite to granodiorite units with a net effect of significantly increasing the depth of the batholith compared to a situation where these units are pinched out at depth. In addition, an empirical rule relating the surficial width of a pluton to its thickness (Cruden, 2008) was used to limit the biotite granite to granodiorite to an approximate thickness of 2.9 km representing the mean of the estimate, while the error estimation in this empirical relationship allows for the thickness to go as low as 1.7 km and as high as 5.4 km.

The geophysical data can be used to verify and refine the accepted geological model, but the choice of geological model itself will have a significant impact on the result that is difficult to quantify. In other words, the geological model selected will have a significant impact on the predicted depth of the batholith that has no quantifiable error associated with it.

Simplified models of the geology can be used to evaluate the implications of varying the geological assumption made. The biotite granite to granodiorite unit has the best defined density in the model of 2.65 ± 0.05 g/cc based on a large number of sample measurements. Densities of the biotite tonalite to granodiorite and hornblende tonalite to granodiorite units of the batholith are less well defined but are clearly significantly more dense than the biotite granite to granodiorite unit with densities of 2.68 ± 0.04 g/cc and 2.76 ± 0.06 g/cc, respectively. The densities of the surrounding greenstones (a geological assumption addressed below) are not as well defined with 2.80 ± 0.1 g/cc and $2.89 \pm$ g/cc for felsic to intermediate metavolcanic units and mafic metavolcanic units, respectively. No matter the geological assumptions made for the internal geometry of the batholith, it is safe to assume that the average density of the batholith is higher than that of the biotite granite to granodiorite unit since the underlying units of the batholith are comprised of denser material. Thus, a model that uses the measured density of the biotite granite to granodiorite unit of 2.65 ± 0.05 g/cc to represent the whole batholith would have a density contrast with the greenstones greater than or equal to the true contrast. That model (Figure 5.19) could be considered a lower limit to true depth. The larger the density contrast the shallower the modelled depth to the bottom of the batholith.

If we adopt the model where the units of intermediate density that are to the east and west of the biotite granite to granodiorite connect at depth so they lie between the biotite granite to granodiorite unit and the greenstones, the base of the biotite granite to granodiorite will become shallower while the overall batholith will increase in thickness. As a result, irrespective of the geological assumptions made, the resultant modelled thickness of the biotite granite to granodiorite unit based on this geological assumption can be viewed as representing a well defined upper limit to the base of the batholith. Setting a limit to the maximum depth of the batholith still remains problematic as it is more dependent on the geological assumptions made. The dense greenstones have been assumed to be continuous beneath the batholith, however in a geological scenario where this is not the case, this would imply one or more less dense units underlying the batholith. This would result in a reduction in the density contrast between the batholith units and the underlying rock which would increase the depths of units that make up the batholith.

6. Summary of Results

Airborne magnetic data acquired by Sander Geophysics (SGL) in 2014 was merged with airborne data acquired by Fugro Airborne Ltd. in 2000-2001. This process required the reversal of previously applied versions of the IGRF corrections and updating these corrections with the most recent IGRF version. Airborne gravity data acquired by SGL in 2014 was merged with ground data collected by the Geological Survey of Canada (GSC) in a process which required reprocessing of the ground data starting with the observed station value of gravity referred to the IGSN71 network using the same standards as the airborne data. LiDAR digital elevation data (ATLIS Geomatics) was augmented in part with terrain data obtained during the SGL survey in 2014 and with data from the Shuttle Radar Topography Mission (SRTM). Rock unit mean densities and mean susceptibilities as well as associated errors and distributions were calculated based on measurements from NWMO, Ontario Geological Survey (OGS), and GSC datasets. Averaged foliation dips based on bedrock geology (NWMO) were used to calculate approximate dips in the greenstones surrounding the Revel batholith, and to infer the dip of the batholith to greenstone contact near the surface.

A 3D model of the batholith created in GeoModeller[®] based only on surface data vertically extrapolating mapped bedrock units and foliation orientation information extends the batholith beyond the depth limit of 4 km. However, forward modelling of the observed gravity field suggested a shallower depth to the bottom of the batholith. Incorporation of the 2D gravity models created in GM-SYS[™] into the 3D forward modelling carried out in GeoModeller[®] resulted in a model with batholith base that is never deeper than 4km, and this was used as the starting model for 3D inversion. Gravity only inversions and magnetic only inversions, in addition to joint inversions, were run at three levels of constraint: tightly constrained, moderately constrained and loosely constrained. The statistical approach of the GeoModeller[®] inversion process allows for an assessment of the variability of the model boundaries by presenting a whole range of acceptable models from an inversion for analysis. Additionally, multiple inversions run using different combinations of data sets with different constraint levels allow for further analysis.

The main results of the forward modelling and inversion of the batholith are as follows:

3D models of the Revell batholith that incorporate the 4 mapped units have been created giving a shape with a relatively flat base that extends to depths of nearly 4 km in some regions. The batholith is encapsulated within surrounding mafic and felsic to intermediate metavolcanics, referred to broadly as the greenstone unit. The biotite granite to granodiorite unit with a well-defined low density (mean of 2.65 ± 0.05 g/cc) dominates the 3D model and the gravity signature of the batholith. This unit has been modelled with a nearly flat base at a depth around 2 km and extending over most of the batholith. Its base mimics previous models of the base of the batholith (NWMO Phase 2), built with a single unit batholith model.

The feldspar megacrystic granite unit has a clear low amplitude, short wavelength, high magnetic signature associated with it, causing it to stand out over the smooth, near-zero magnetic fabric of the biotite granite to granodiorite unit. The feldspar megacrystic granite unit has been tentatively assigned a mean density slightly less than that of the biotite granite to granodiorite unit, however this is poorly defined due to low sampling of the unit. The feldspar megacrystic granite has been modelled with a geometry generally under a kilometre in thickness which is encapsulated within the surrounding biotite granite to granodiorite unit. This unit has little or no impact on the overall shape of the extremity of the batholith.

Incorporating the biotite tonalite to granodiorite and the hornblende tonalite to granodiorite units as distinctive units in the model has significant impact on the overall geometry of the batholith. With a smooth near-zero magnetic fabric for both units, their incorporation was based on their gravity response. Mean densities are tentatively assigned as 2.68 ± 0.04 g/cc for the biotite tonalite to granodiorite and 2.76 ± 0.06 g/cc for hornblende tonalite to granodiorite unit, between the 2.65 ± 0.05 g/cc biotite granite to granodiorite unit and surrounding mafic and felsic to intermediate metavolcanics that are assigned densities of 2.89 ± 0.1 g/cc and 2.80 ± 0.1 g/cc respectively. However, similar to the feldspar megacrystic granite unit, the mean densities of these could be vastly improved with additional sampling.

Models have been created with the biotite tonalite to granodiorite and hornblende tonalite to granodiorite units connecting beneath the overlying biotite granite to granodiorite unit, extending the overall depth to bottom of the batholith to almost 4 km. Treating the biotite tonalite to granodiorite and hornblende tonalite to granodiorite units as separate or combined units does not have a significant impact on the overall shape and depth of the batholith. The modelled thickness of the biotite granite to granodiorite unit based on the connection of the biotite tonalite to granodiorite and hornblende tonalite to granodiorite units beneath it provides an upper limit boundary to the base of the batholith. It is difficult to determine a limit to the maximum depth of the batholith since is more dependent on the geological assumptions.

It is anticipated that models will be revised and refined if more field data is collected in the future. Density measurements of the biotite tonalite to granodiorite and hornblende tonalite to granodiorite units would improve model definition and also provide data to help decide if separating the units is warranted. The assignment of a density value to the feldspar megacrystic granite unit with a comparatively small standard deviation has noticeable implications to the inversion, and requires validation. Additional magnetic susceptibility measurements for almost all units, specifically, the surrounding greenstones and the feldspar megacrystic granite are needed with the exception of the biotite granite to granodiorite unit. These would contribute to an improved definition of near-surface model geometry.

7. References

- Bethune, K.M., Helmstaedt, H.H. and McNicoll, V.J. 2006. Structural analysis of the Miniss River and related faults, western Superior Province: post-collisional displacement initiated at terrane boundaries; *Can. J. Earth Sci.*, v. 43, p. 1031–1054.
- Blackburn, C.E., Hinz, P. 1996. Gold and base metal potential of the northwest part of the Raleigh Lake greenstone belt, northwestern Ontario-Kenora Resident Geologist's District; in *Summary of Field Work and Other Activities 1996*, Ontario Geological Survey, Miscellaneous Paper 166, p.113-115.
- Briggs, I.C., 1974. Machine Contouring using Minimum Curvature. *Geophysics*, Vol. 39, No. 1., P.39-48.
- Brown, J.L., 2002. Neoproterozoic evolution of the western—central Wabigoon boundary zone, Brightsand Forest area, Ontario. Unpublished M.Sc. thesis, University of Ottawa, Ottawa.
- Cruden, A. R., 2008. Emplacement mechanisms and structural influences of a younger granite intrusion into older wall rocks – a principal study with application to the Götemar and Uthamar granites Site-descriptive modelling. Svensk Kärnbränslehantering AB Swedish Nuclear Fuel and Waste Management Co., ISSN 1402-3091, SKB Rapport R-08-138.
- Cruden, A. R., McCaffrey, K. J. W., & Bungler, A., 2018. Geometric Scaling of Tabular Igneous Intrusions: Implications for Emplacement and Growth. In C. Breiterkreuz, & S. Rocchi (Eds.), *Physical Geology of Shallow Magmatic Systems: Dykes, Sills and Laccoliths* (1 ed., pp. 11-38). (Advances in Volcanology: An Official Book Series of the International Association of Volcanology and Chemistry of the Earth's Interior). Switzerland: Springer.
- Davis, D.W., 1989. Final report for the Ontario Geological Survey on precise U–Pb age constraints on the tectonic evolution of the western Wabigoon subprovince, Superior Province, Ontario. Earth Science Department, Royal Ontario Museum, 30 p.
- Easton, R.M. 2000. Metamorphism of the Canadian Shield, Ontario, Canada. Volume I, The Superior Province. *The Canadian Mineralogist*, v. 38, p. 287-317.
- Easton, R.M., Hart, T.R., Hollings, P., Heaman, L.M., MacDonald, C.A. and Smyk, M. 2007. Further refinement of the timing of Mesoproterozoic magmatism, Lake Nipigon region, Ontario; *Canadian Journal of Earth Sciences*, v.44, p.1055-186.
- Enkin, R.J., 2018. Canadian rock physical property database: first public release; Geological Survey of Canada, Open File 8460, 1 .zip file. <https://doi.org/10.4095/313389>

- Golder (Golder Associates Ltd.), 2015. Phase 2 Geoscientific Preliminary Assessment, Initial Phase 2 Geoscience Field Studies Findings, Township of Ignace, Ontario. Prepared for the Nuclear Waste Management Organization (NWMO), NWMO Report Number: APM-REP-06145-0001.
- Hanes, J.A. and Archibald, D.A. 1998. Post-orogenic tectonothermal history of the Archean western Superior Province of the Canadian Shield by conventional and laser Ar-Ar dating. Abstracts with programs - Geological Society of America, v. 30(7), p.110-110.
- Hinze, W.J., Aiken, C., Brozena, J., Coakley, B., Flanagan, G., Kucks, R., Forsberg, R., Li, X., Hildenbrand, T., Mainville, A., Dater, D., Keller, G.R., Morin, R., Pilkington, M., Plouff, D., Ravat, D., Roman, D., Kellogg, J., Urrutia-Fucugauchi, J., Veronneau, M., Webring, M. and Winester, D. 2005. New standards for reducing gravity data: The North American gravity database. *Geophysics*, Vol. 70, No. 4 (July-August 2005); P. J25–J32.
- Heaman, L.M. and Easton, R.M. 2006. Preliminary U-Pb geochronology results from the Lake Nipigon Region Geoscience Initiative; Ontario Geological Survey, Miscellaneous Release—Data 191.
- Intrepid Geophysics®, 2020, GeoModeller®, Version 4.0.7, Intrepid Geophysics®, BRGM. <https://docs.intrepid-geophysics.com/geomodeller/>
- Kamineni, D.C., Stone, D. and Peterman, Z. E. 1990. Early Proterozoic deformation in the western Superior province, Canadian Shield, *Geological Society of America Bulletin*, v. 102, p. 1623-1634.
- Kresz, D.U., 1987. Geology of the Kawashegamuk Lake area, District of Kenora; Ontario Geological Survey, Open File Report 5659, 201p.
- Muir, T.L. 2013. Ontario Precambrian bedrock magnetic susceptibility geodatabase for 2001 to 2012; Ontario Geological Survey, Miscellaneous Release—Data 273 – Revised.
- OGS (Ontario Geological Survey), 2011. 1:250 000 scale bedrock geology of Ontario, Ontario Geological Survey, Miscellaneous Release Data 126 - Revision 1.
- OGS (Ontario Geological Survey), 2011. Ontario airborne geophysical surveys, magnetic and electromagnetic data, profile data (Geosoft™ format), Stormy Lake area; Ontario Geological Survey, Geophysical Data Set 1107d - Revision 1.
- Parmenter, A., Waffle, L., DesRoches, A. 2020. An updated bedrock geology map and geological database for the northern portion of the Revell batholith. Nuclear Waste Management Organization, NWMO-TR-2020-01.

- Percival, J.A., McNicoll, V.J., Brown, J.L. and Whalen, J.B. 2004. Convergent margin tectonic, central Wabigoon subprovince, Superior Province, Canada. *Precambrian Research*, v. 132, p. 213-244.
- Percival, J.A. and R.M. Easton, 2007. Geology of the Canadian Shield in Ontario: an update. Ontario Power Generation, Report No. 06819-REP-01200-10158-R00 and Ontario Geological Survey, Open File Report 6196, 65p.
- Peterman, Z.E. and Day, W. 1989. Early Proterozoic activity on Archean faults in the western Superior Province: Evidence from pseudotachylite. *Geology*, v. 17, p. 1089-1092.
- Rainsford, D.R.B., Carter-McAuslan, A. and Ashick-Stinson, L.C. 2018. Ontario specific gravity data for bedrock samples acquired from 1970 to 2014, Ontario Geological Survey, Miscellaneous Release—Data 371.
- Sanborn-Barrie, M., and Skulski, T. 2006. Sedimentary and structural evidence for 2.7 Ga continental arc-oceanic-arc collision in the Savant-Sturgeon greenstone belt, western Superior Province, Canada. *Canadian Journal of Earth Sciences*, v. 43, p. 995-1030.
- Satterly, J. 1960. Geology of the Dymont area, Ontario Department of Mines, Annual Report Vol. 69, pt. 6, 32p.
- Seequent®, 2020, Geosoft™, Oasis montaj geophysical processing system, v 9.7.1, <https://www.seequent.com/products-solutions/geosoft-software/>
- SGL (Sander Geophysics), 2015. Phase 2 Geoscientific Preliminary Assessment: Acquisition, Processing and Interpretation of High-Resolution Airborne Geophysical Data, Township of Ignace, Ontario. Prepared for the Nuclear Waste Management Organization (NWMO), NWMO Report Number: APM-REP-06145-0002.
- SRK (SRK Consulting, Inc)., Golder (Golder Associates Ltd)., 2015. Phase 2 Geoscientific Preliminary Assessment, Observation of General Geological Features, Township of Ignace, Ontario. Prepared for Nuclear Waste Management Organization. NWMO Report Number: APM-REP-06145-0004.
- Stone, D., 2009. Geology of the Bending Lake Area, Northwestern Ontario (); in Summary of Field Work and Other Activities 2009. Ontario Geological Survey. Open File Report 6240.
- Stone, D., 2010a. Geology of the Stormy Lake Area, Northwestern Ontario(); in Summary of Field Work and Other Activities 2010. Ontario Geological Survey, Open File Report 6260.

Stone, D., 2010b. Precambrian geology of the central Wabigoon Subprovince area, northwestern Ontario. Ontario Geological Survey, Open File Report 5422.

Stone, D., Halle, J., Chaloux, E., 1998. Geology of the Ignace and Pekagoning Lake Areas, Central Wabigoon Subprovince; in Summary of Field Work and Other Activities 1998, Ontario Geological Survey, Misc. Paper 169.

Stone, D., Davis, D.W., Hamilton, M.A., Falcon, A., 2010. Interpretation of 2009 Geochronology in the Central Wabigoon Subprovince and Bending Lake Areas, Northwestern Ontario, in Summary of Field Work and Other Activities 2010, Ontario Geological Survey, Open File Report 6260.

Stott, G.M., Corkery, M. T., Percival, J.A., Simard, M. and Goutier, J. 2010. A revised terrane subdivision of the Superior Province; in Summary of Field Work and Other Activities 2010, Ontario Geological Survey, Open File Report 6260, p.20-1 to 20-10.

Szewczyk, Z.J. and West, G.F. 1976. Gravity study of an Archean granitic area northwest of Ignace, Ontario Canadian Journal of Earth Sciences, v. 13, p. 1119-1130.

Thurston, P. 1991. Geology of Ontario: Introduction; in Geology of Ontario, Ontario Geological Survey, Special Volume 4, Part 1, p. 3-25.

Tomlinson, K.Y., Stott, G.M., Percival, J.A. and Stone, D. 2004. Basement terrane correlations and crustal recycling in the western Superior Province: Nd isotopic character of granitoid and felsic volcanic rocks in the Wabigoon Subprovince, N. Ontario, Canada; Precambrian Research, v. 132, p. 245-274.

8. Figures Listing

Figure 2.1 Geological setting of the Superior Province in Northwestern Ontario (after Thurston, 1991) around the Revell Regional Area (red outline on main map) and showing the outline of the Revell batholith (RB). Inset at top right shows the 1:250,000 scale outline of the Revell batholith and surrounding greenstone belts. The Winnipeg River, Marmion and Western Wabigoon terranes are part of the Wabigoon subprovince.

Figure 2.2 Summary of Archean and Proterozoic geological events for the Revell Regional Area.

Figure 2.3 Bedrock geology map of the Revell batholith and surrounding greenstone belt area.

Figure 3.1 Magnetic anomaly data grids over the 3D model window prior to merging. (a) SGL magnetic anomaly with a 25 m grid cell size (b) Fugro magnetic anomaly data with a 50 m grid cell size (c) first vertical derivative of SGL data (d) first vertical derivative of Fugro data. The dashed blue line marks the LiDAR coverage.

Figure 3.2 Magnetic anomaly data grids over the 3D model window after merging. (a) magnetic anomaly with a 50 m grid cell size (b) first vertical derivative. The dashed white line marks the location of the merge and the dashed blue line is the LiDAR coverage.

Figure 3.3 Gravity data coverage around 3D model area. (a) a window of the GSC regional ground gravity with station locations marked (b) SGL airborne gravity with GSC ground station locations (c) merged Bouguer gravity (d) first vertical derivative of the merged Bouguer gravity. The dashed white line marks the location of the merge and the dashed blue line is the LiDAR coverage.

Figure 3.4 DEM data over the 3D model area. (a) LiDAR 1 m cells size (b) SGL survey data 25 m cell size (c) merged DEM data 25 m cell size (d) pseudo-drape approximating the flying height. The dashed white line marks the location of the merge and the dashed blue line is the LiDAR coverage.

Figure 3.5 The location of model units, numbered 1 to 9, used for petrophysical properties and the location of units used for proxy petrophysical properties labelled with a prefix "P". The model area is represented by the small rectangular black box.

Figure 3.6 Distribution of the location of petrophysical measurements. (a) sample locations for NWMO and OGS density measurements (b) sample locations for NWMO and OGS magnetic susceptibility measurements. The model area is represented by the small rectangular black box.

Figure 3.7 Foliation strike and dip in black, overlain on surface geology. Units within the model area marked by the black box are simplified for modelling purposes. Dip values in degrees shown in blue are assigned to local contacts between units. Units are numbered in orange corresponding to Table 3.4.

Figure 4.1 Location of 2D models overlain on (a) Bouguer gravity (b) anomalous magnetic field (c) topography above MSL (d) simplified bedrock geology. The 3D model extents (dashed rectangle in black) and LiDAR data limits (dashed polygon in blue) are overlain on all figures and the limits of SGL airborne gravity coverage (white line) overlain in (a).

Figure 4.2 Line 1 forward modelling results for the preliminary model. (a) gravity profile showing observed and calculated gravity field and misfit (b) model view showing model densities (c) blank (d) blank (e) model view showing model units. Intersections with the other profiles and the start and end of section within 3D model extents are marked by a circle and vertical line and labelled. Blank Subset (c) and (d) are inserted to maintain the same figure layout for the 2D models.

Figure 4.3 Line 1 forward modelling results for the updated model. (a) gravity profile showing observed and calculated gravity field and misfit (b) model view showing model densities (c) magnetic profile showing observed and calculated anomalous magnetic field (d) model view showing model magnetic susceptibilities (e) model view with model units. Intersections with the other profiles and the start and end of section within 3D model extents are marked by a circle and vertical line and labelled.

Figure 4.4 Line 2 forward modelling results for the preliminary model. (a) gravity profile showing observed and calculated gravity field and misfit (b) model view showing model densities (c) blank (d) blank (e) model view showing model units. Intersections with the other profiles and the start and end of section within 3D model extents are marked by a circle and vertical line and labelled. Blank Subset (c) and (d) are inserted to maintain the same figure layout for the 2D models.

Figure 4.5 Line 2 forward modelling results for the updated model. (a) gravity profile showing observed and calculated gravity field and misfit (b) model view showing model densities (c) magnetic profile showing observed and calculated anomalous magnetic field (d) model view showing model magnetic susceptibilities (e) model view with model units. Intersections with the other profiles and the start and end of section within 3D model extents are marked by a circle and vertical line and labelled.

Figure 4.6 Line 3 forward modelling results for the preliminary model. (a) gravity profile showing observed and calculated gravity field and misfit (b) model view showing model densities (c) blank (d) blank (e) model view showing model units. Intersections with the other profiles and the start and end of section within 3D model extents are marked by a circle and vertical line and labelled. Blank Subset (c) and (d) are inserted to maintain the same figure layout for the 2D models.

Figure 4.7 Line 3 forward modelling results for the updated model. (a) gravity profile showing observed and calculated gravity field and misfit (b) model view showing model densities (c) magnetic profile showing observed and calculated anomalous magnetic field (d) model view showing model magnetic susceptibilities (e) model view with model units. Intersections with the other profiles and the start and end of section within 3D model extents are marked by a circle and vertical line and labelled.

Figure 4.8 Two layer 3D inversion results from Geosoft. (a) calculated gravity field (b) observed minus calculated gravity field (c) base of batholith/top of greenstones (d) thickness of batholith/depth to greenstones. The dashed blue line marks the LiDAR coverage.

Figure 5.1 3D geophysical model creation workflow.

Figure 5.2 Model extents (dashed rectangle in black) and LiDAR data limits (dashed polygon in blue) overlain on (a) bedrock geology (b) simplified bedrock geology (c) topography above MSL.

Figure 5.3 Model extents (dashed rectangle) and LiDAR data limits (dashed polygon) overlain on (a) observed Bouguer gravity (b) first vertical derivative of observed Bouguer gravity (c) observed anomalous magnetic field (d) first vertical derivative of the anomalous magnetic field.

Figure 5.4 Interpolated bedrock geology at ground level from GeoModeller. Profile lines are shown in yellow, two dykes cross-cut the region in a NW-SE direction in navy blue and the saw-tooth pattern at the edges of units depict dip direction. The colour scheme for the rock units matches that of the bedrock geology figures in Section 2.

Figure 5.5 Multiple 3D views of the same interpolated geology model based solely on surface geology with no subsurface constraints. Batholith units are progressively removed from the displays with (a) the full model and (b) feldspar megacrystic granite unit removed (c) biotite granite to granodiorite removed (d) hornblende tonalite to granodiorite removed (e) and (f) biotite tonalite to granodiorite removed.

Figure 5.6 Comparison of observed gravity anomaly with predicted anomaly from the interpolated geology model based solely on surface geology. (a) observed Bouguer gravity (b) calculated Bouguer gravity (c) observed minus calculated gravity (d) simplified bedrock geology. In panel (c), features labelled GMA and GMB are prominent misfits discussed in Section 6.4. The dashed blue line marks the LiDAR coverage.

Figure 5.7 Interpolated geology model based on results from 2D modelling and surface geology. (a) full model (b) all units within the batholith (c) batholith without the biotite tonalite to granodiorite unit (d) batholith without the biotite tonalite to granodiorite and the hornblende tonalite to granodiorite units (e) feldspar megacrystic granite unit (f) displays of the 2D models used in creating the 3D model.

Figure 5.8 Comparison of observed gravity anomaly with predicted anomaly from the model based on results from 2D modelling and surface geology. (a) observed Bouguer gravity (b) calculated Bouguer gravity (c) observed minus calculated gravity (d) simplified bedrock geology. The dashed blue line marks the LiDAR coverage.

Figure 5.9 Comparison of observed magnetic anomaly with predicted anomaly from the model based on results from 2D modelling and surface geology. (a) observed anomalous magnetic field (b) calculated anomalous magnetic field (c) observed minus calculated anomalous magnetic field (d) simplified bedrock geology. The dashed blue line marks the LiDAR coverage.

Figure 5.10 Graph examples showing misfit variation with iteration number for (a) joint inversion gravity misfit (b) joint inversion magnetic misfit (c) gravity only inversion gravity misfit (d) magnetic only inversion magnetic misfit. The black, blue and red curves are for tight, moderate and loose inversion constraint respectively. Vertical red lines show selected burn-in points.

Figure 5.11 Comparison of observed gravity anomaly with predicted anomaly from the gravity only inversion with moderate constraint. (a) observed Bouguer gravity (b) calculated Bouguer gravity (c) observed minus calculated gravity (d) simplified bedrock geology. Features GMC and GMD labelled in (a) and (c) are prominent misfits within the feldspar megacrystic granite unit. The dashed blue line marks the LiDAR coverage.

Figure 5.12 Gravity only inversion residuals for (a) tightly constrained (b) moderately constrained (c) loosely constrained inversions with (d) simplified bedrock geology. The dashed blue line marks the LiDAR coverage.

Figure 5.13 Gravity only inversion results along (a) Line 1 (b) Line 2 (c) Line 3. The coloured image in the background is the starting model. Dotted black lines are for inversion with very tight constraint, solid lines are for moderate constraint and faint lines for loose constraint.

Figure 5.14 Gravity only moderate constraint inversion results statistics along Profile Line 3. (a) 90% thresholded model units. Pixels below 90% threshold level are grayed out. (b) entropy (c) change count. Interpolated starting model boundaries appear as faint black lines.

Figure 5.15 Gravity only moderate constraint inversion density distribution results along (a) Line 1 (b) Line 2 (c) Line 3. Interpolated starting model boundaries and features appear as faint black lines on all images.

Figure 5.16 Gravity only moderate constraint inversion density distribution results on depth slices at (a) 300 m above MSL (b) 1 km below MSL (c) 2 km below MSL (d) 3 km below MSL. All densities are in g/cc. The dashed blue line marks the LiDAR coverage.

Figure 5.17 Histograms of mean model densities of the Revell batholith units from gravity only moderate constraint inversion.

Figure 5.18 Histograms of mean model densities of greenstone and other units surrounding the Revell batholith from gravity only moderate constraint inversion.

Figure 5.19 Boundary of batholith from a single density (2.65 g/cc) gravity only moderate constraint inversion overlain in black on gravity only moderate constraint inversion. (a) Line 1 (b) Line 2 (c) Line 3.

Figure 5.20 Comparison of observed magnetic anomaly with predicted anomaly from magnetic only inversion results with moderate constraint. (a) observed magnetic anomaly (b) calculated magnetic anomaly (c) observed minus calculated magnetic anomaly (d) simplified bedrock geology. The dashed blue line marks the LiDAR coverage.

Figure 5.21 Magnetic only inversion residuals. (a) tight constraint (b) moderate constraint (c) loose constraint (d) simplified bedrock geology. The dashed blue line marks the LiDAR coverage.

Figure 5.22 Magnetic only inversion results along (a) Line 1 (b) Line 2 (c) Line 3. The coloured image in the background is the starting model. Dotted blue lines are for inversion with very tight constraint, solid lines with moderate constraint and faint lines for loose constraints.

Figure 5.23 Magnetic only moderate constraint inversion results statistics along Line 3. (a) 90% thresholded model units. Pixels below 90% threshold level are grayed out. (b) entropy (c) change count. Interpolated starting model boundaries appear as faint black lines.

Figure 5.24 Magnetic only moderate constraint inversion susceptibility variations along (a) Line 1 (b) Line 2 (c) Line 3. Interpolated starting model boundaries and features appear as faint black lines on all images.

Figure 5.25 Magnetic only moderate constraint inversion magnetic susceptibility distribution results on depth slices at (a) 300 m above MSL (b) 1 km below MSL (c) 2 km below MSL (d) 3 km below MSL. Magnetic susceptibilities are in SI units. The dashed blue line marks the LiDAR coverage.

Figure 5.26 Histograms of mean model magnetic susceptibilities of the Revell batholith units from magnetic only moderate constraint inversion.

Figure 5.27 Histograms of mean model magnetic susceptibilities of greenstone and other units surrounding the Revell batholith from magnetic only moderate constraint inversion.

Figure 5.28 Comparison of observed gravity anomaly with predicted anomaly from joint gravity and magnetic inversion with moderate constraint. (a) observed Bouguer gravity (b) calculated Bouguer gravity (c) observed minus calculated gravity (d) simplified bedrock geology. The dashed blue line marks the LiDAR coverage.

Figure 5.29 Joint gravity and magnetic inversion gravity residuals. (a) tight constraint (b) moderate constraint (c) loose constraint (d) simplified bedrock geology. The dashed blue line marks the LiDAR coverage.

Figure 5.30 Comparison of observed magnetic anomaly with predicted anomaly from joint gravity and magnetic inversion results with moderate constraint. (a) observed magnetic anomaly (b) calculated magnetic anomaly (c) observed minus calculated magnetic anomaly (d) simplified bedrock geology. The dashed blue line marks the LiDAR coverage.

Figure 5.31 Joint gravity and magnetic inversion magnetic misfits, observed minus calculated fields. (a) tight constraint (b) moderate constraint (c) loose constraint (d) simplified bedrock geology. The dashed blue line marks the LiDAR coverage.

Figure 5.32 Joint gravity and magnetic inversion results along (a) Line 1 (b) Line 2 (c) Line 3. The coloured image in the background is the starting model. Dotted brown lines are for inversion with very tight constraint, solid lines with moderate constraint and faint lines for loose constraints.

Figure 5.33 Joint moderate constraint inversion results statistics along Line 3. (a) 90% thresholded model units. Pixels below 90% threshold level are grayed out. (b) entropy (c) change count. Interpolated starting model boundaries appear as faint black lines.

Figure 5.34 Joint gravity and magnetic inversion density variation along (a) Line 1 (b) Line 2 (c) Line 3. Interpolated starting model boundaries and features appear as faint black lines on all images.

Figure 5.35 Joint gravity and magnetic inversion density distribution results along depth slices at (a) 300 m above MSL (b) 1 km below MSL (c) 2 km below MSL (d) 3 km below MSL. Density units are in g/cc. The dashed blue line marks the LiDAR coverage.

Figure 5.36 Histograms of mean densities of the Revell batholith units from joint inversion with moderate constraint.

Figure 5.37 Histograms of mean densities of greenstone and other units surrounding the Revell batholith from joint inversion with moderate constraint.

Figure 5.38 Joint gravity and magnetic inversion magnetic susceptibility variation along (a) Line 1 (b) Line 2 (c) Line 3. Magnetic susceptibilities are in SI units. Interpolated starting model boundaries and features appear as faint black lines on all images.

Figure 5.39 Joint gravity and magnetic inversion magnetic susceptibility distribution results along depth slices at (a) 300 m above MSL (b) 1 km below MSL (c) 2 km below MSL (d) 3 km below MSL. Magnetic susceptibilities are in SI units. The dashed blue line marks the LiDAR coverage.

Figure 5.40 Joint inversion model magnetic susceptibility distributions for the Revell batholith units with associated statistics for each rock unit.

Figure 5.41 Joint inversion model magnetic susceptibility distributions for greenstone and other units surrounding the Revell batholith with associated statistics for each rock unit.

Figure 5.42 Joint gravity and magnetic moderate constraint inversion results in colour in the background along (a) Line 1 (b) Line 2 (c) Line 3. Interpolated starting model boundaries and features appear as faint lines on all images.

Figure 5.43 Joint gravity and magnetic moderate constraint inversion results in colour in the background along (a) Line 1 (b) Line 2 (c) Line 3. Solid black lines and blue lines are from gravity only inversion and magnetic only inversions respectively with moderate constraint.

Figure 5.44 Joint gravity and magnetic loose constraint inversion results in colour in the background along (a) Line 1 (b) Line 2 (c) Line 3. Solid black lines and blue lines are from gravity only inversion and magnetic only inversions respectively with loose constraint.

Figure 5.45 Different 3D views of units within the Revell batholith after joint inversion with moderate constraint. The arrows point from starting models to final models. The starting model for the feldspar megacrystic granite unit is shown in (a) and (b), and the final model in (c) and (d). The starting model for the Biotite granite to granodiorite unit is shown in panes (e) and (f), and the final model in (f) and (g).

Figure 5.46 Different 3D views of units within the Revell batholith after joint inversion with moderate constraint. The arrows point from starting models to final models. The starting model for the hornblende tonalite to granodiorite unit is shown in panes (a) and (b), and the final model in (c) and (d). The starting model for the biotite tonalite to granodiorite unit is shown in panes (e) and (f), and the final model in (g) and (h).



Appendix A



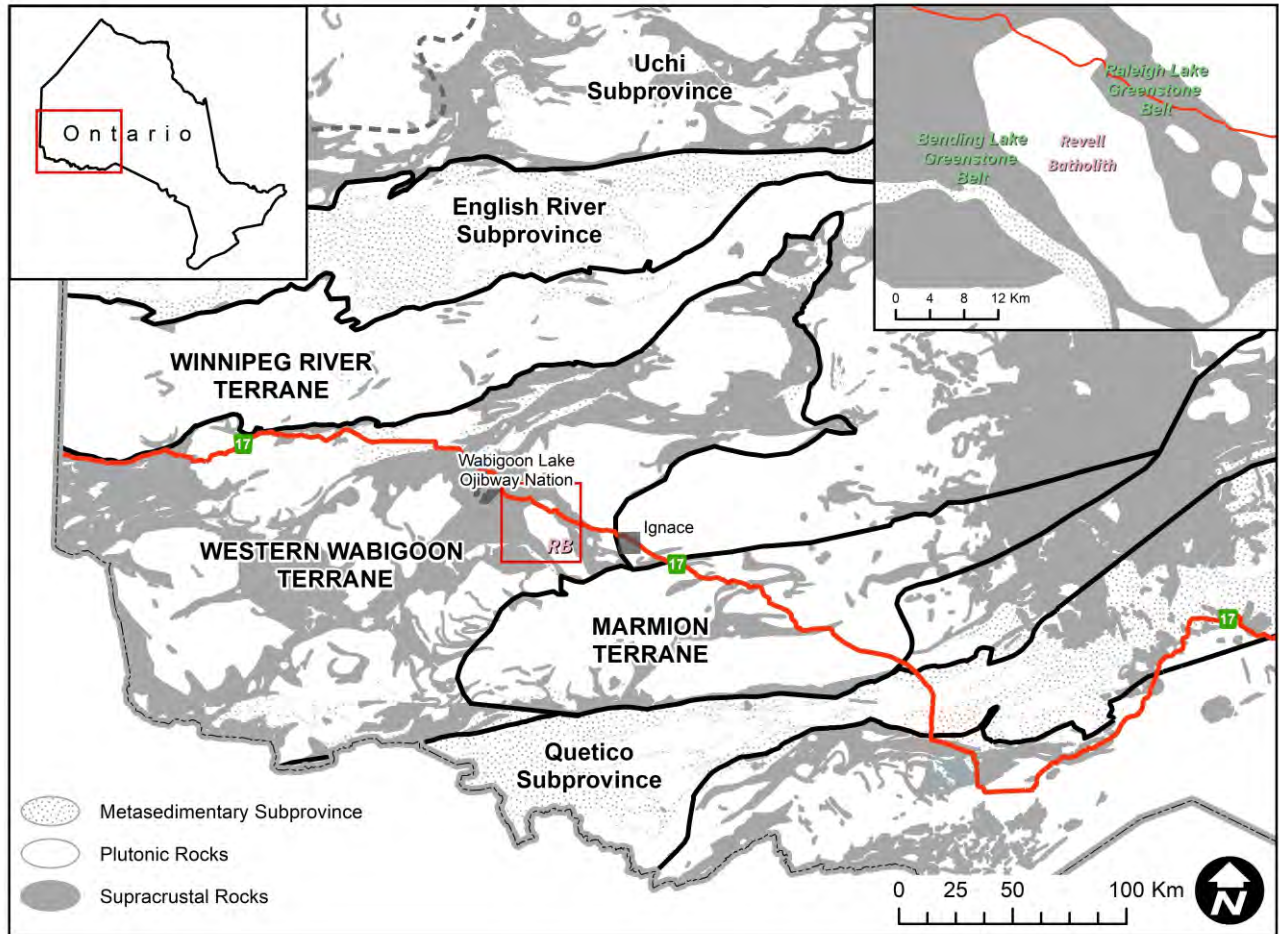


Figure 2.1 Geological setting of the Superior Province in Northwestern Ontario (after Thurston, 1991) around the Revell Regional Area (red outline on main map) and showing the outline of the Revell batholith (RB). Inset at top right shows the 1:250,000 scale outline of the Revell batholith and surrounding greenstone belts. The Winnipeg River, Marmion and Western Wabigoon terranes are part of the Wabigoon subprovince.

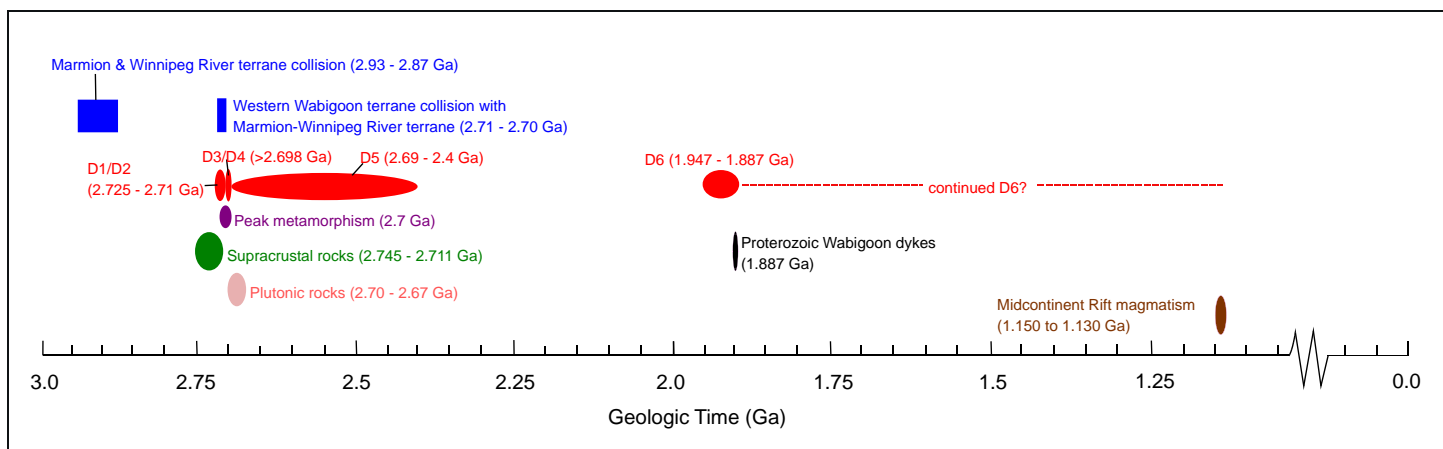


Figure 2.2 Summary of Archean and Proterozoic geological events for the Revell Regional Area.

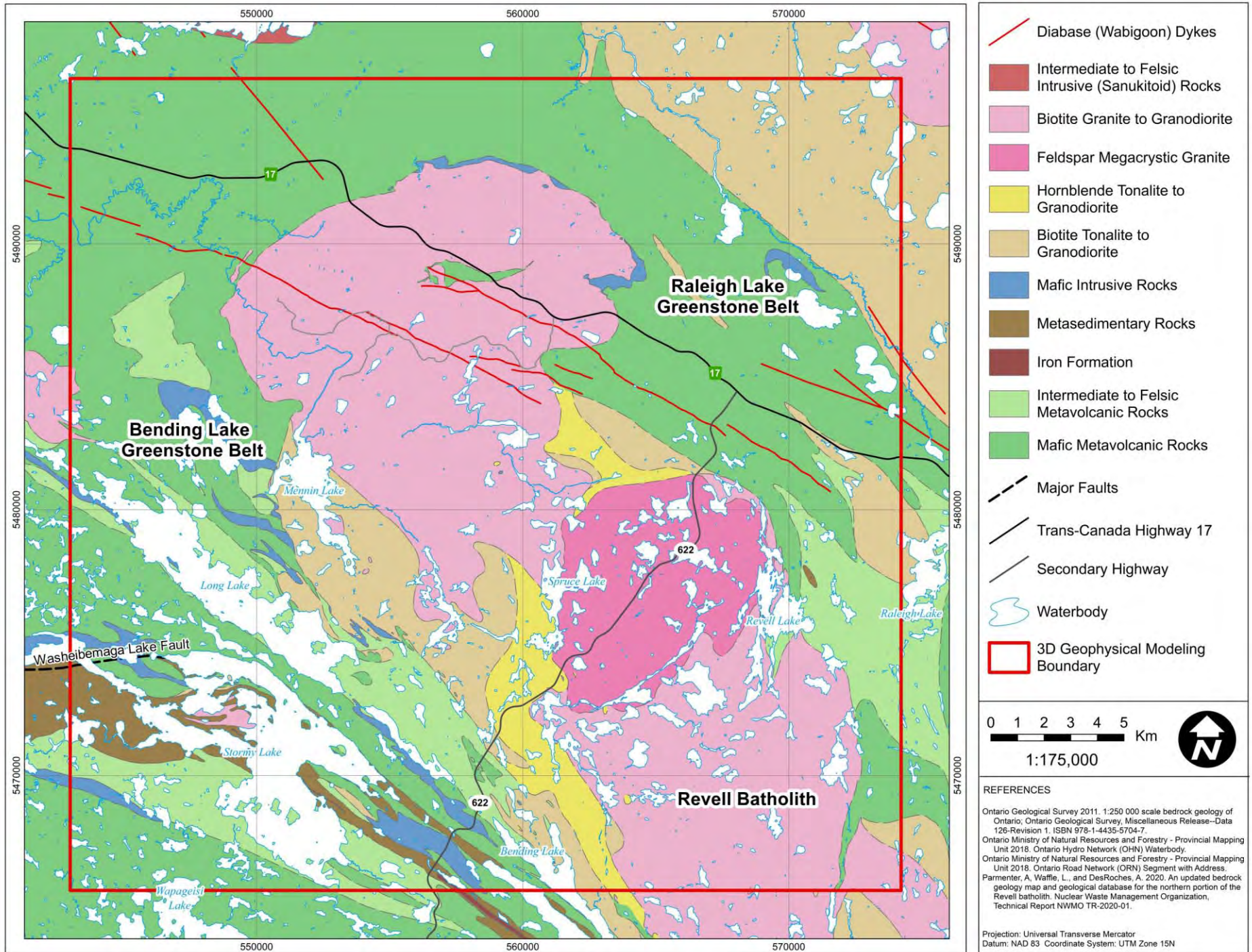
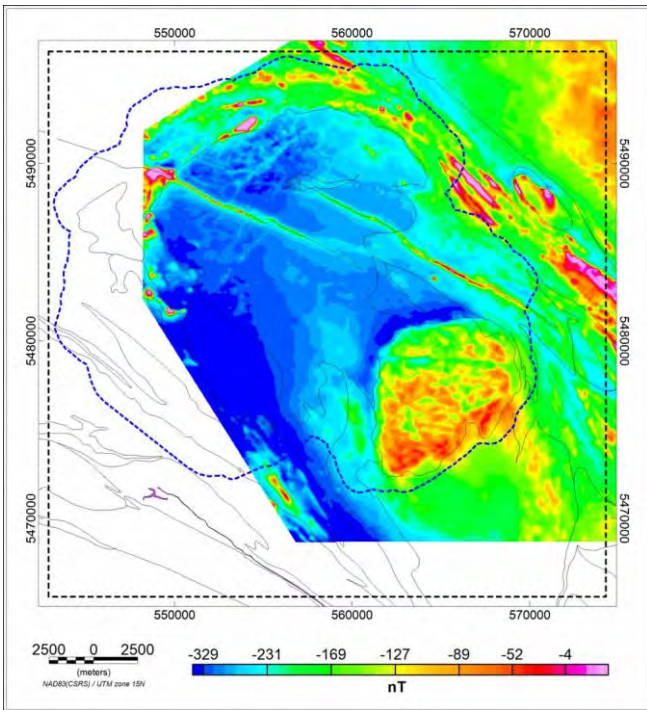
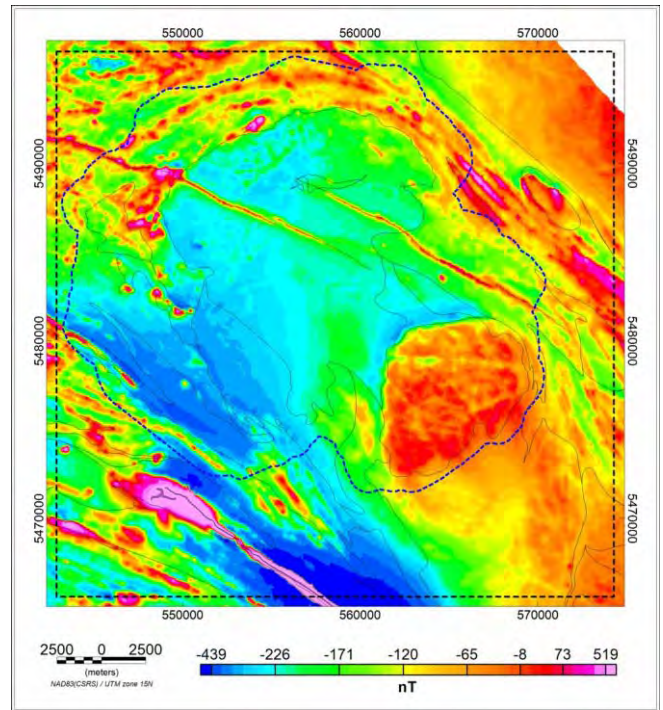


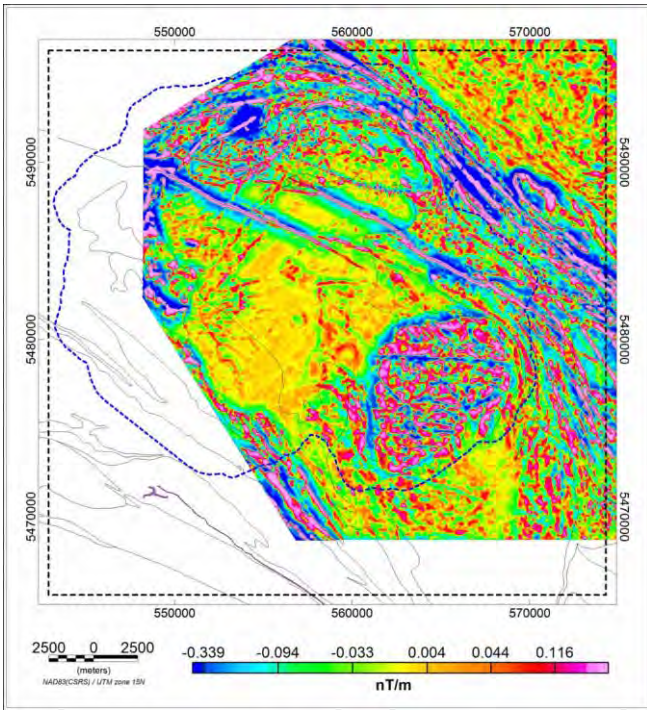
Figure 2.3 Bedrock geology map of the Revell batholith and surrounding greenstone belt area.



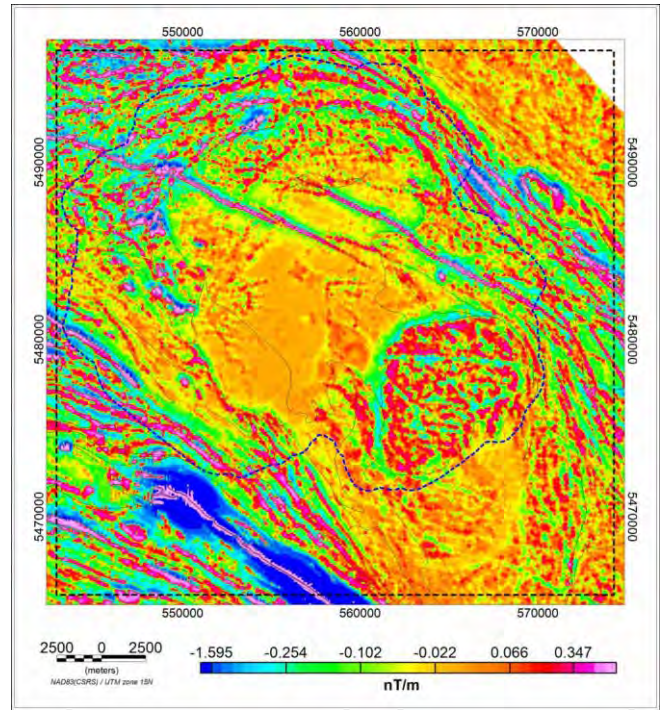
(a)



(b)

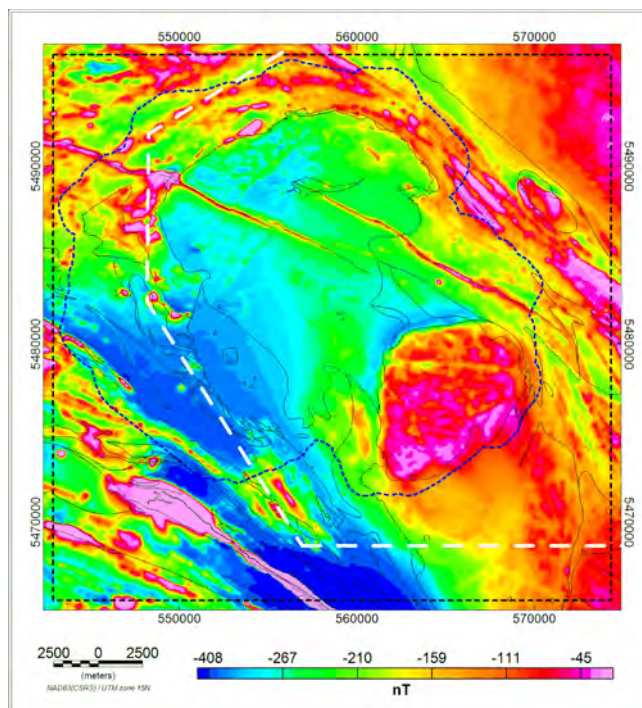


(c)

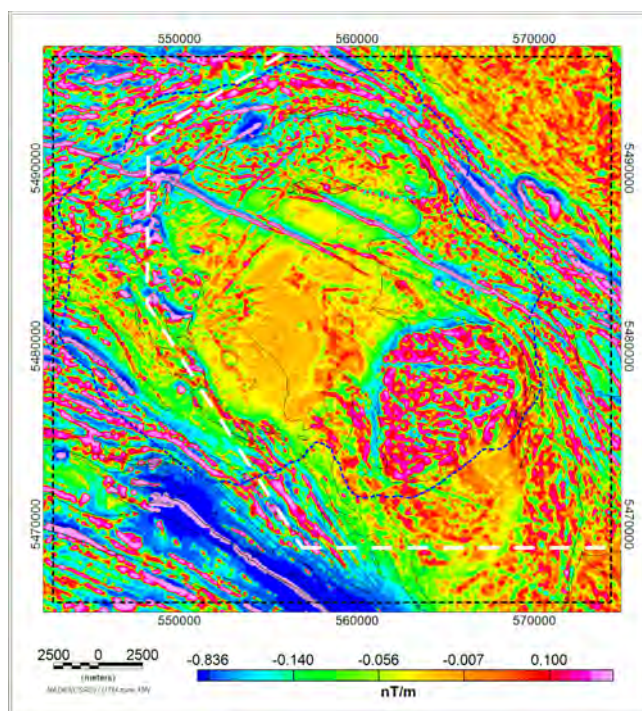


(d)

Figure 3.1 Magnetic anomaly data grids over the 3D model window prior to merging. (a) SGL magnetic anomaly with a 25 m grid cell size. (b) Fugro magnetic anomaly data with a 50 m grid cell size (c) first vertical derivative of SGL data (d) first vertical derivative of Fugro data. The dashed blue line marks the LiDAR coverage.

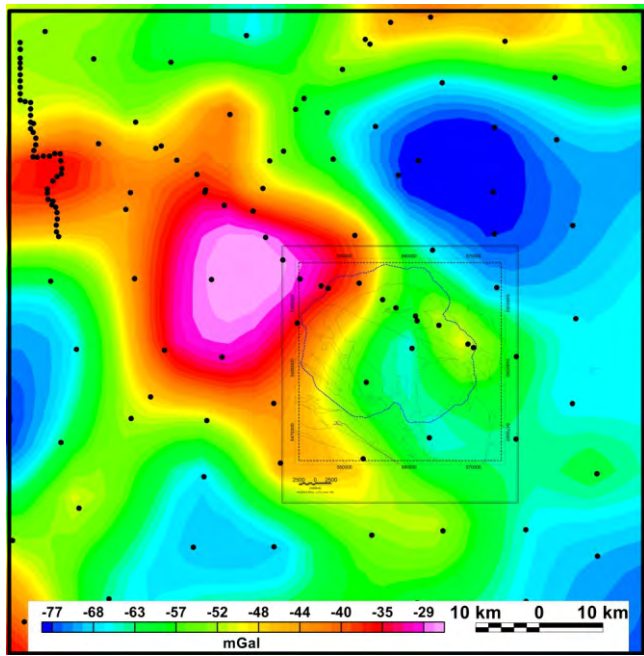


(a)

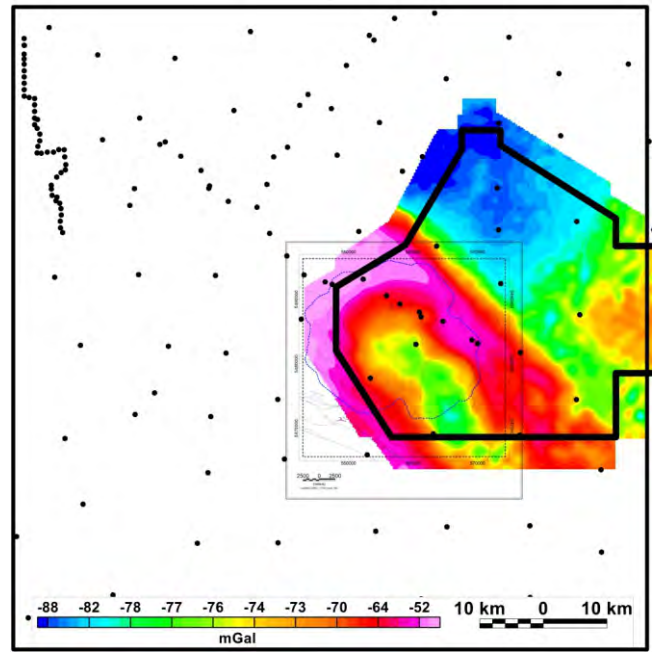


(b)

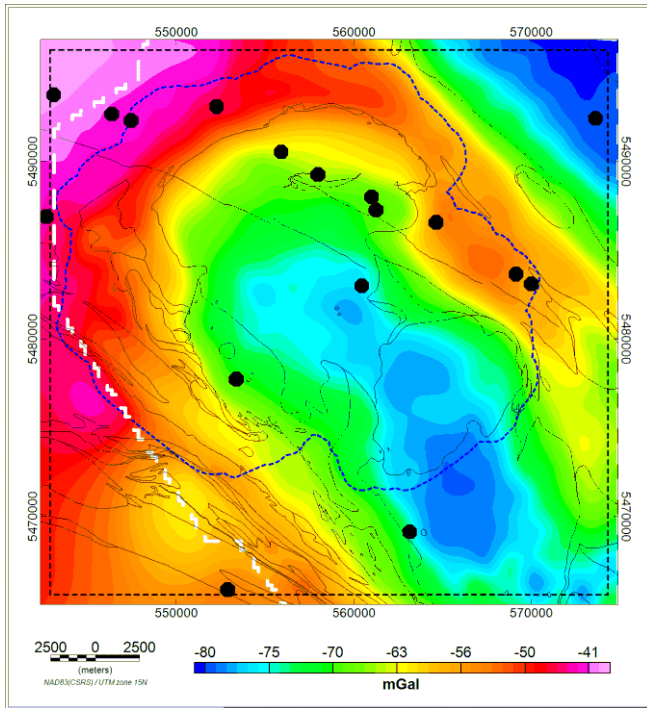
Figure 3.2 Magnetic anomaly data grids over the 3D model window after merging. (a) magnetic anomaly with a 50 m grid cell size. (b) first vertical derivative. The dashed white line marks the location of the merge and the dashed blue line is the LiDAR coverage.



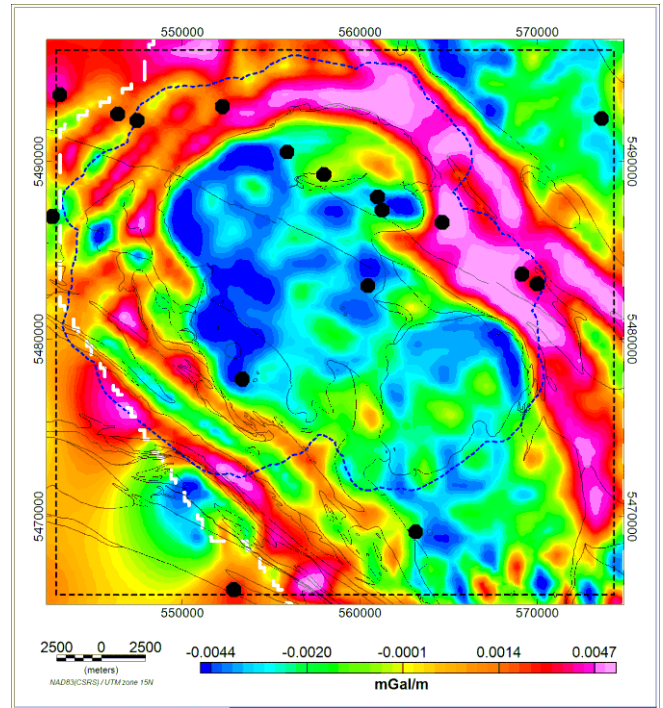
(a)



(b)

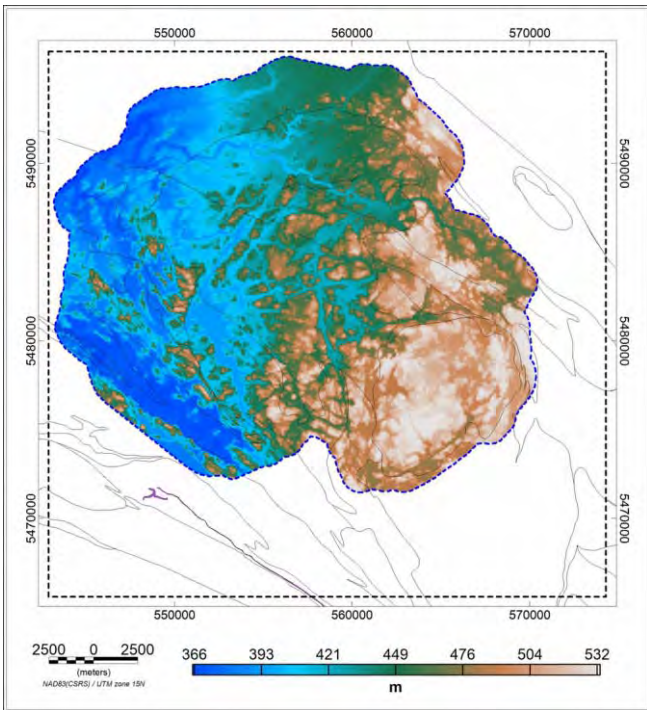


(c)

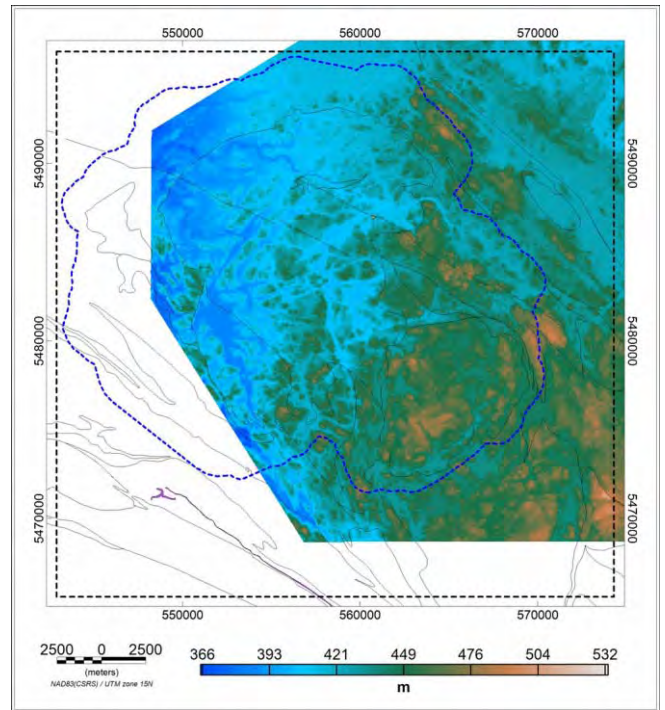


(d)

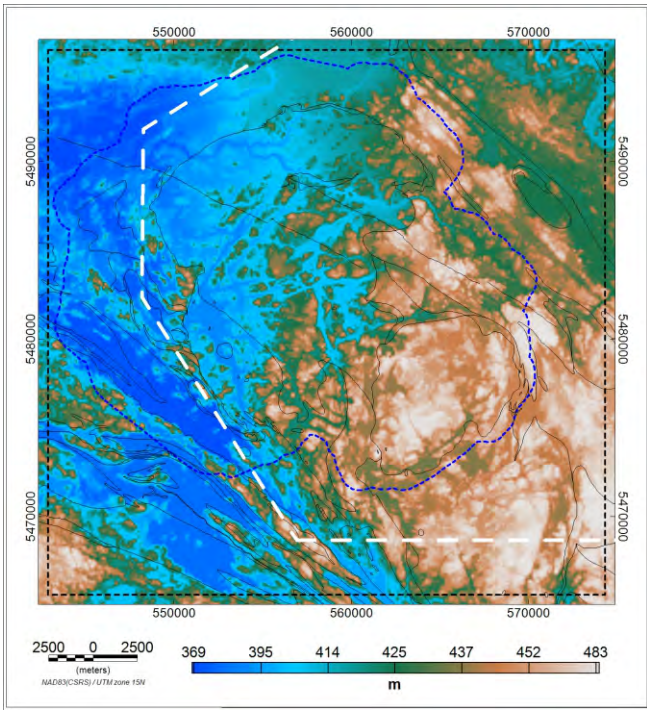
Figure 3.3 Gravity data coverage around 3D model area. (a) a window of the GSC regional ground gravity with station locations marked (b) SGL airborne gravity with GSC ground station locations (c) merged Bouguer gravity (d) first vertical derivative of the merged Bouguer gravity. The dashed white line marks the location of the merge and the dashed blue line is the LiDAR coverage.



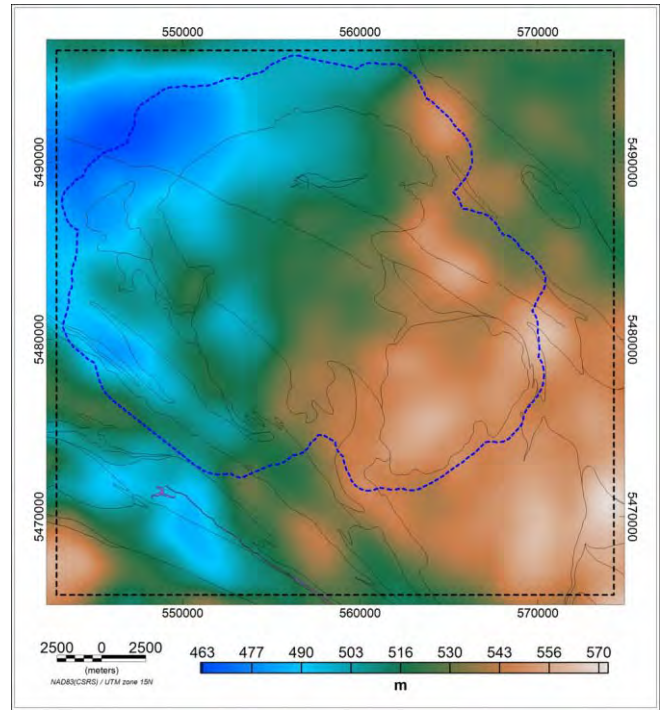
(a)



(b)



(c)



(d)

Figure 3.4 DEM data over the 3D model area (a) LiDAR 1 m cells size (b) SGL survey data 25 m cell size (c) merged DEM data 25 m cell size (d) pseudo-drape approximating the flying height. The dashed white line marks the location of the merge and the dashed blue line is the LiDAR coverage.

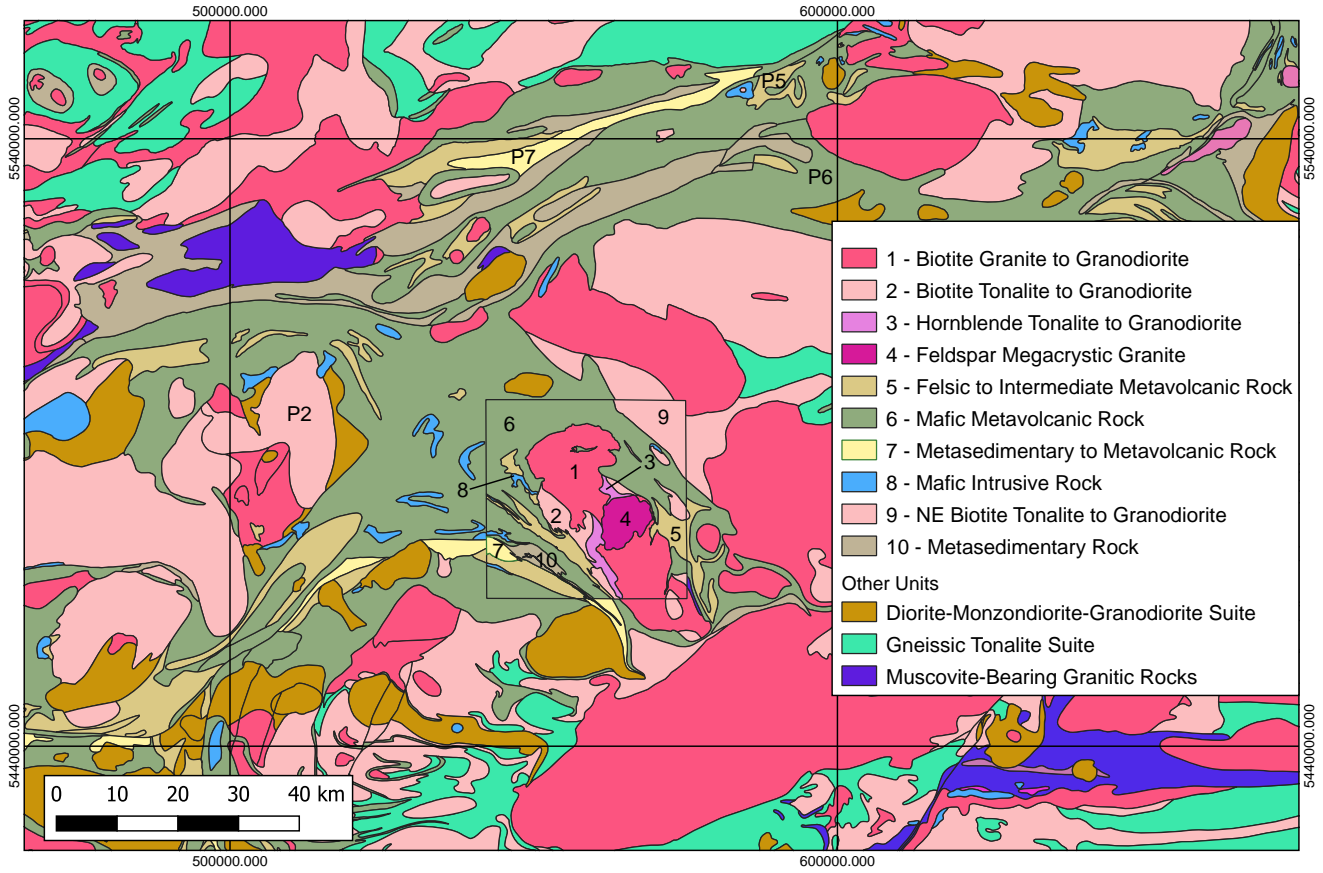
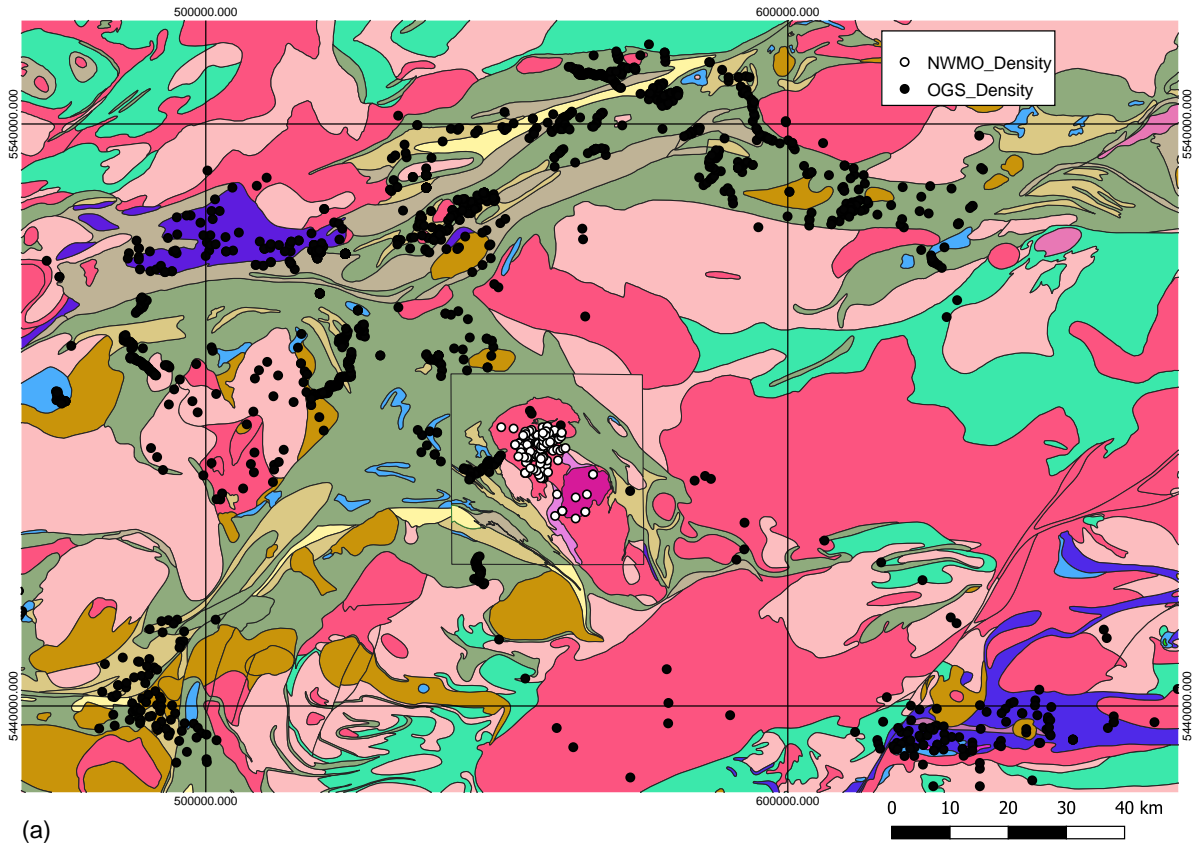
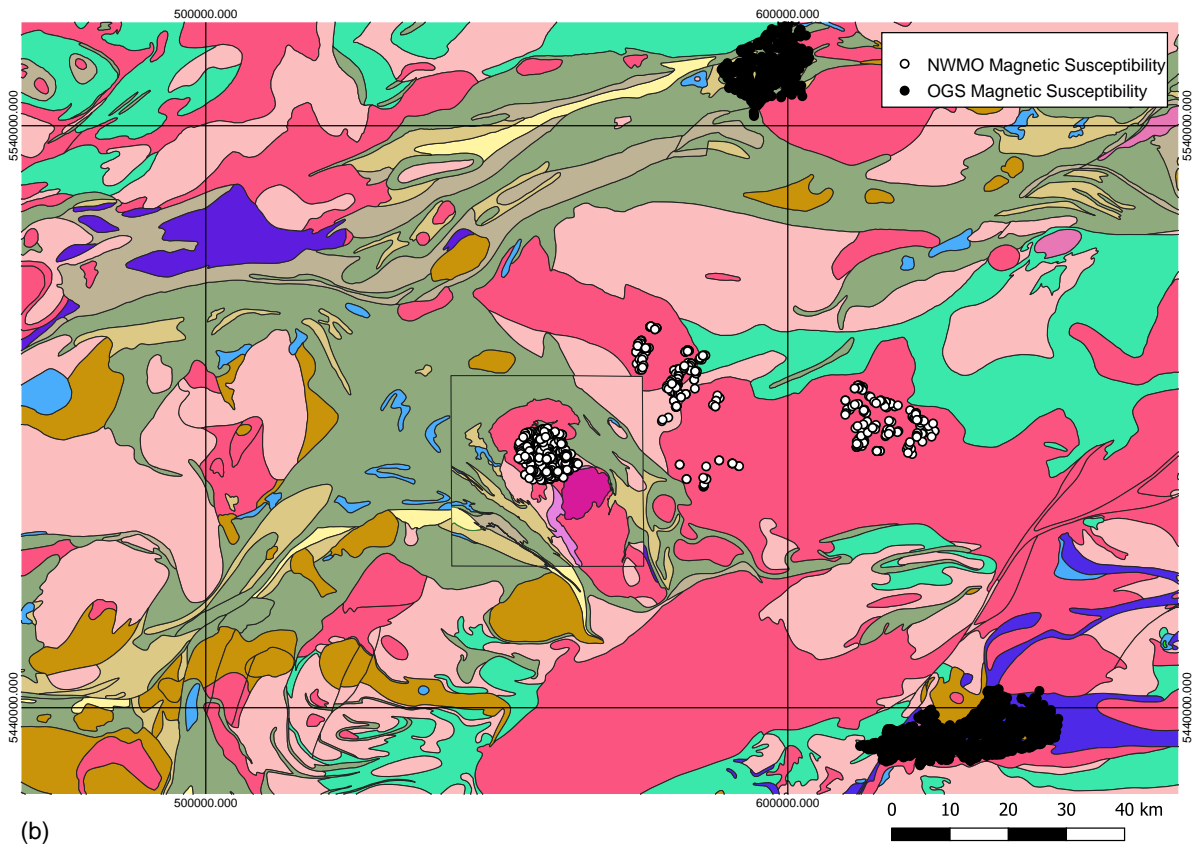


Figure 3.5 The location of model units, numbered 1 to 9, used for petrophysical properties and the location of units used for proxy petrophysical properties labelled with a prefix "P". The model area is represented by the small rectangular black box.



(a)



(b)

Figure 3.6 Distribution of the location of petrophysical measurements. (a) sample locations for NWMO and OGS density measurements (b) sample locations for NWMO and OGS magnetic susceptibility measurements. The model area is represented by the small rectangular black box.

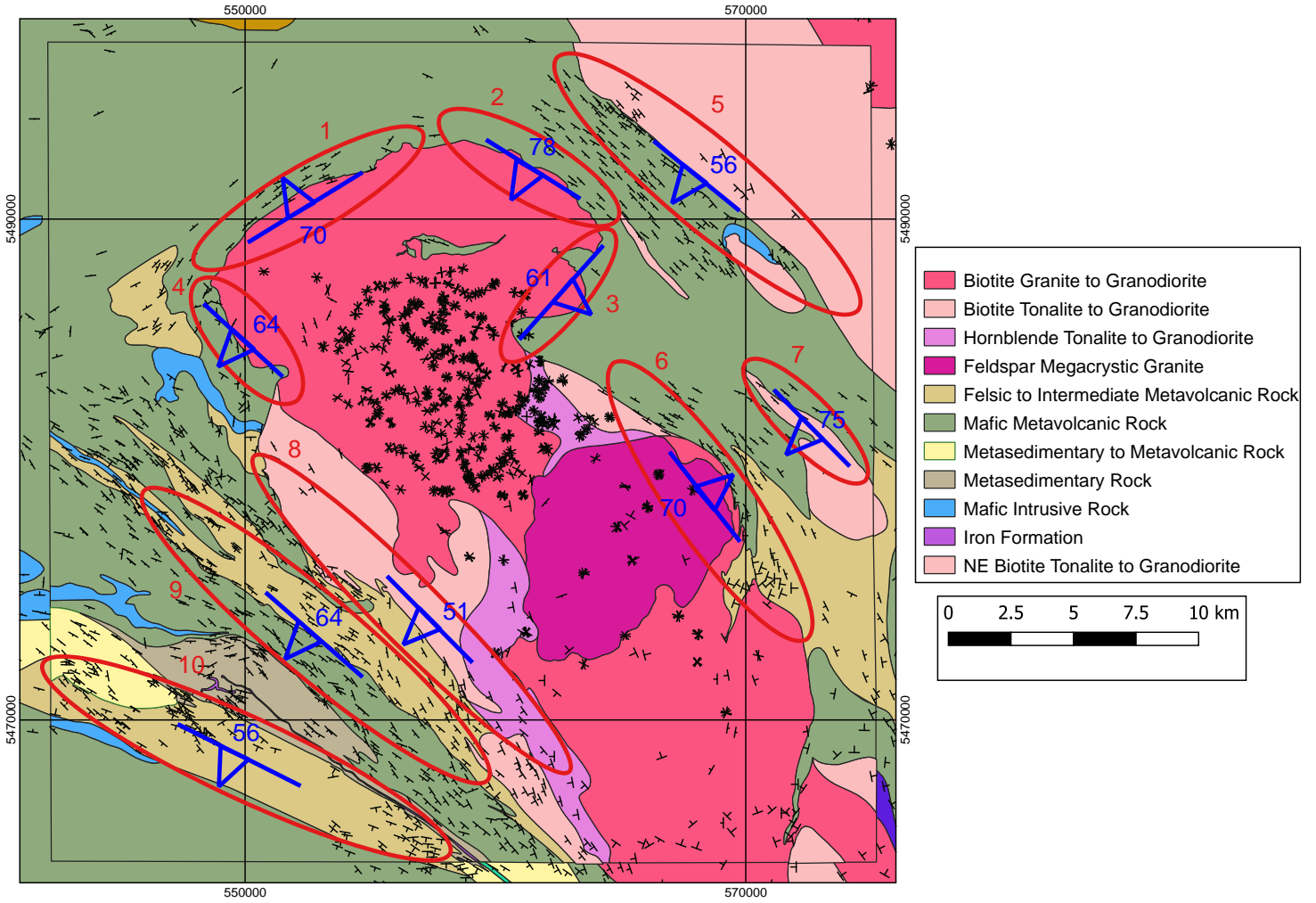
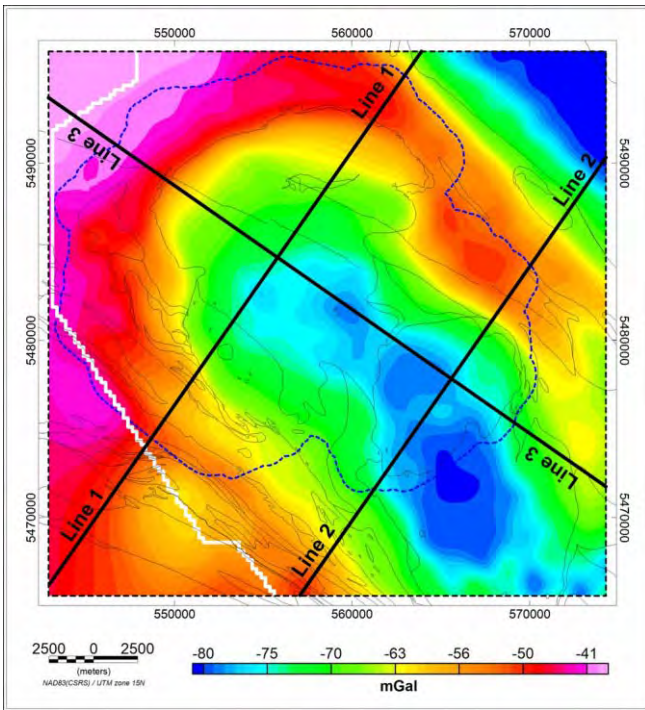
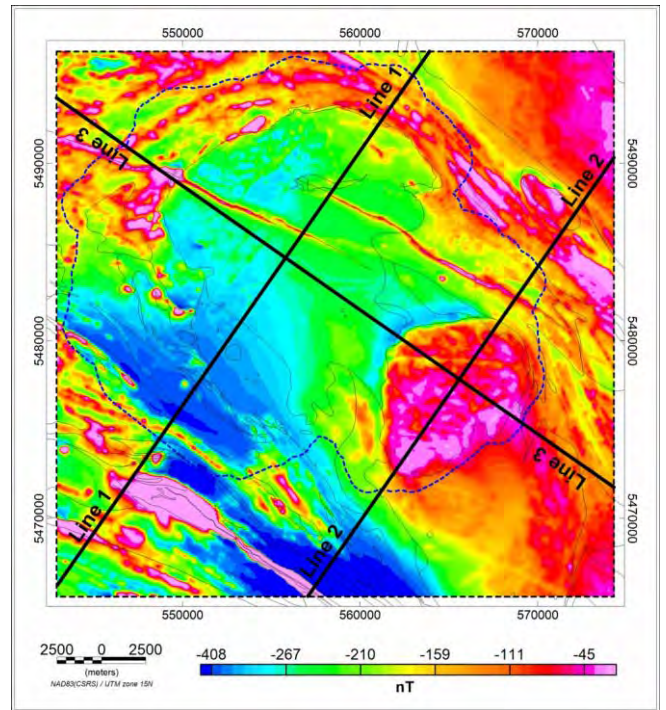


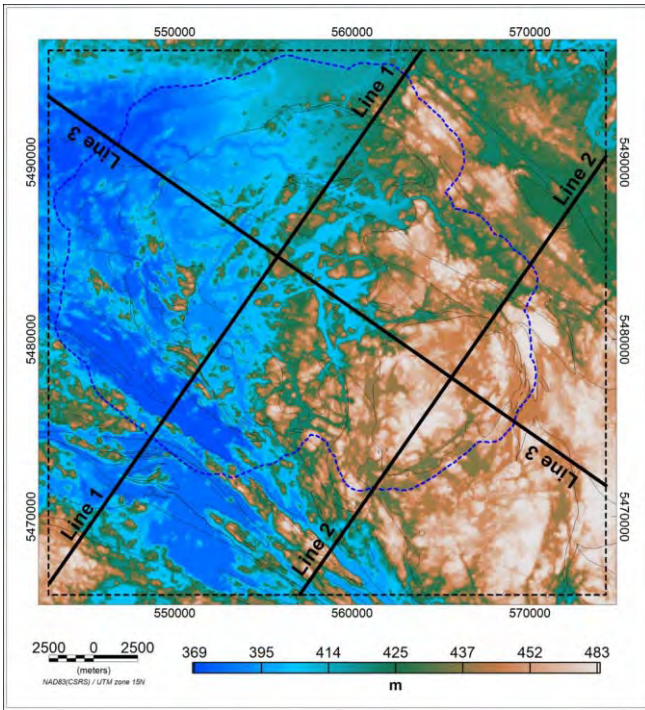
Figure 3.7 Foliation strike and dip in black, overlain on surface geology. Units within the model area marked by the black box are simplified for modelling purposes. Dip values in degrees shown in blue are assigned to local contacts between units. Units are numbered in orange corresponding to Table 3.3



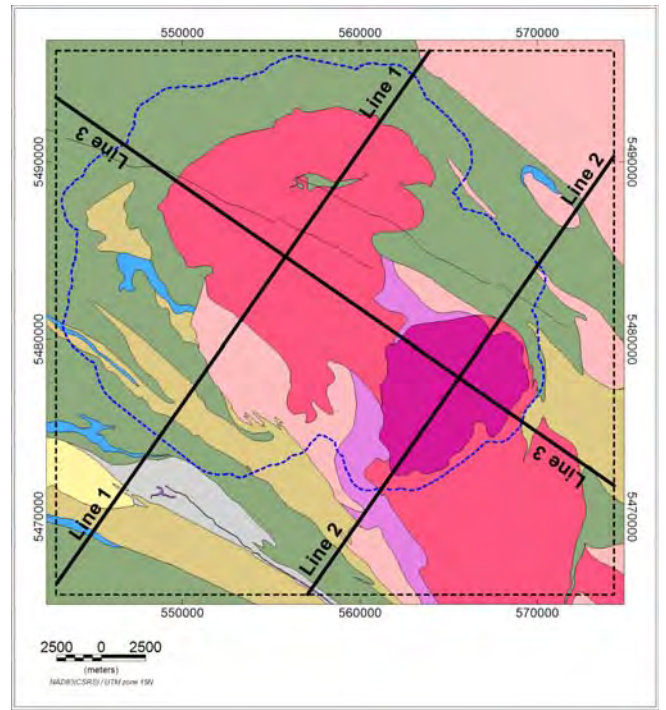
(a)



(b)

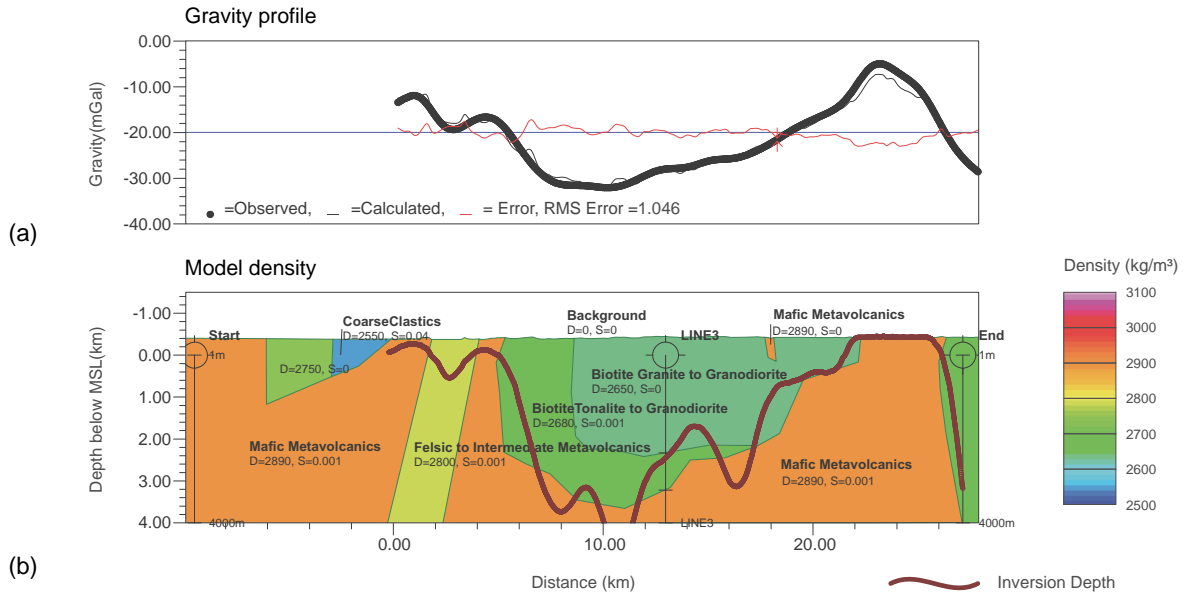


(c)



(d)

Figure 4.1: Location of 2D models overlain on (a) Bouguer gravity (b) anomalous magnetic field (c) topography above MSL (d) simplified bedrock geology. The 3D model extents (dashed rectangle in black) and LIDAR data limits (dashed polygon in blue) are overlain on all figures and the limits of SGL airborne gravity coverage (white line) overlain in (a).



(c)

(d)

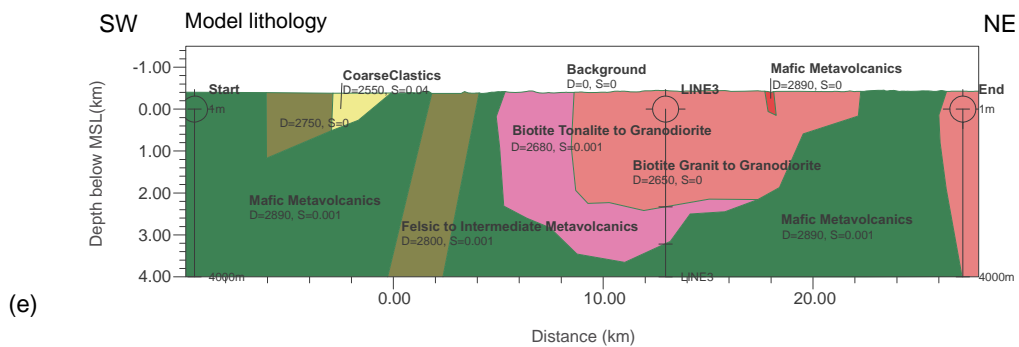


Figure 4.2: Line 1 forward modelling results for the preliminary model. (a) gravity profile showing observed and calculated gravity field and misfit (b) model view showing model densities (c) blank (d) blank (e) model view showing model units. Intersections with the other profiles and the start and end of section within 3D model extents are marked by a circle and vertical line and labelled. Blank subset (c) and (d) are inserted to maintain the same figure layout for the 2D models.

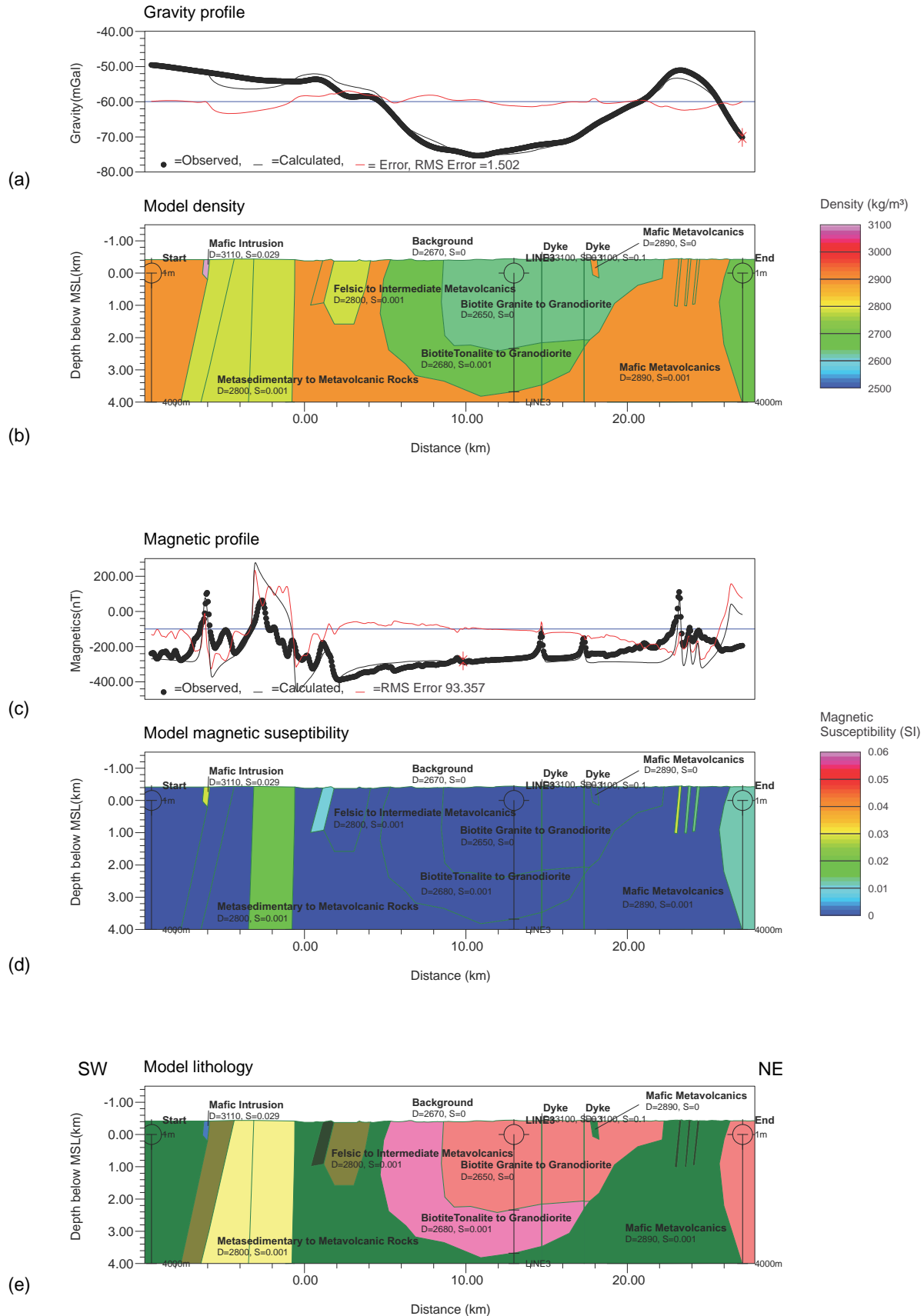


Figure 4.3 Line 1 forward modelling results for the updated model. (a) gravity profile showing observed and calculated gravity field and misfit (b) model view showing model densities (c) magnetic profile showing observed and calculated anomalous magnetic field (d) model view showing model magnetic susceptibilities (e) model view with model units. Intersections with the other profiles and the start and end of section within 3D model extents are marked by a circle and vertical line and labelled.

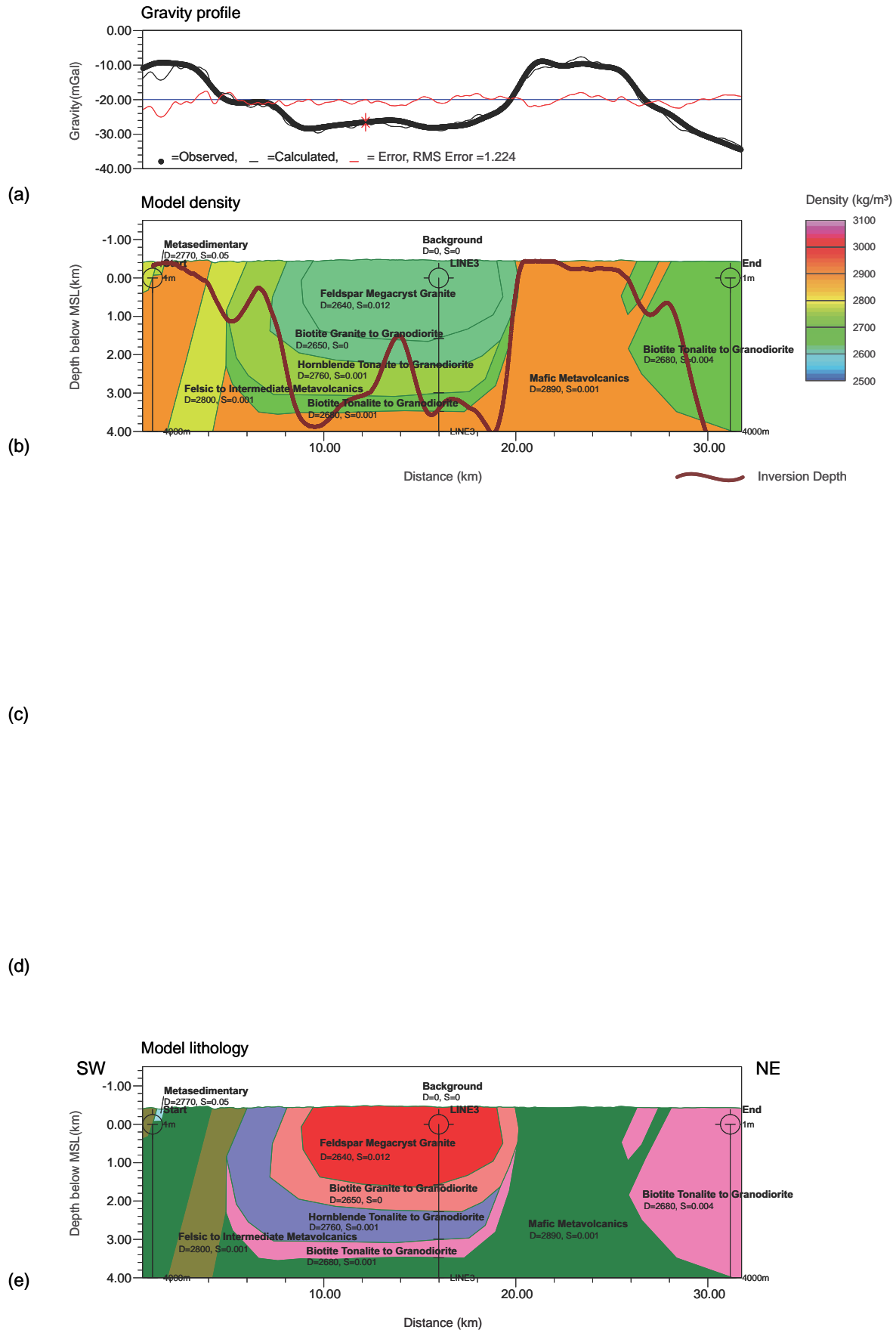


Figure 4.4: Line 2 forward modelling results for the preliminary model. (a) gravity profile showing observed and calculated gravity field and misfit (b) model view showing model densities (c) blank (d) blank (e) model view showing model units. Intersections with the other profiles and the start and end of section within 3D model extents are marked by a circle and vertical line and labelled. Blank Subset (c) and (d) are inserted to maintain the same figure layout for the 2D models.

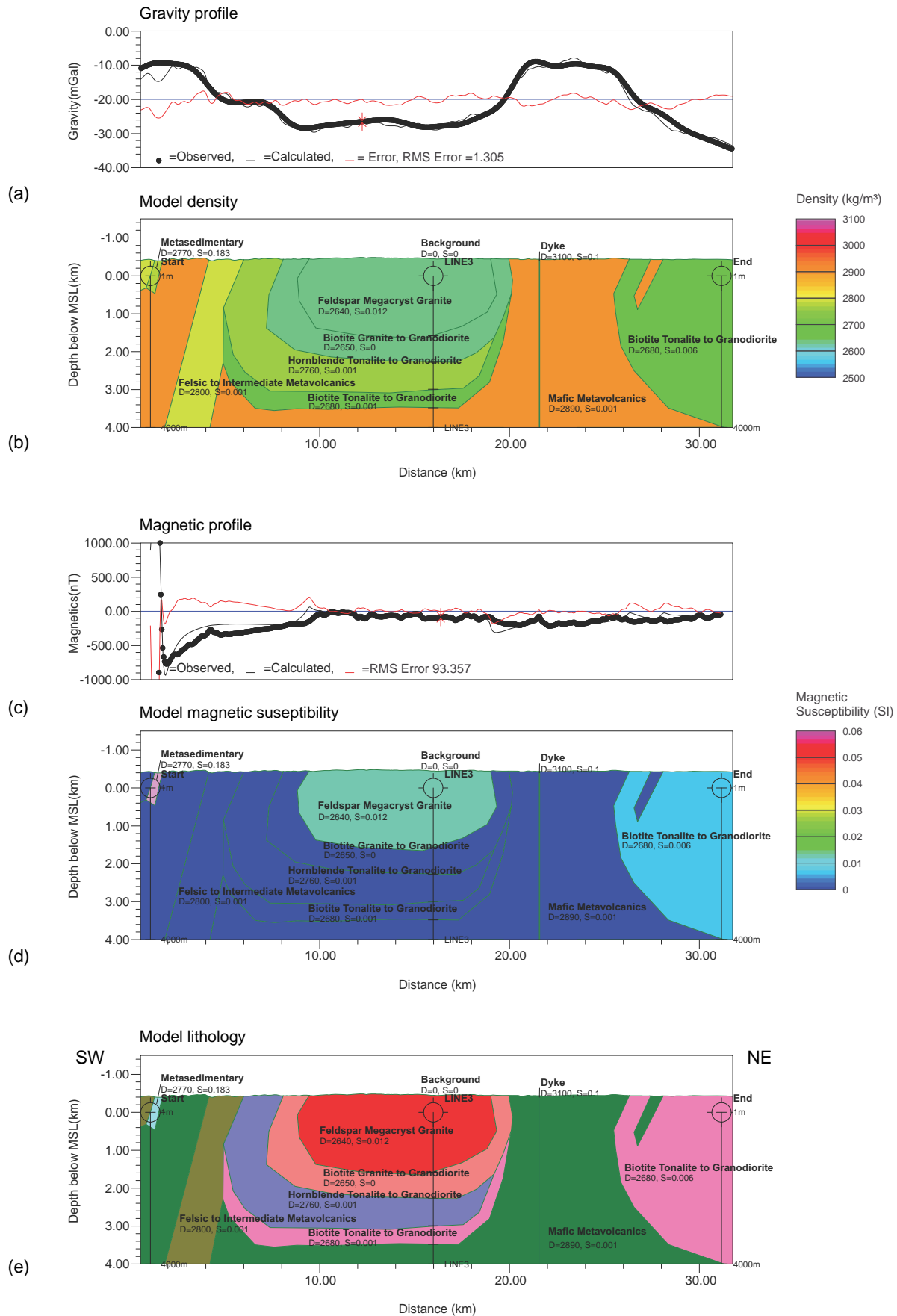


Figure 4.5 Line 2 forward modelling results for the updated model. (a) gravity profile showing observed and calculated gravity field and misfit (b) model view showing model densities (c) magnetic profile showing observed and calculated anomalous magnetic field. (d) model view showing model magnetic susceptibilities (e) model view with model units. Intersections with the other profiles and the start and end of section within 3D model extents are marked by a circle and vertical line and labelled.

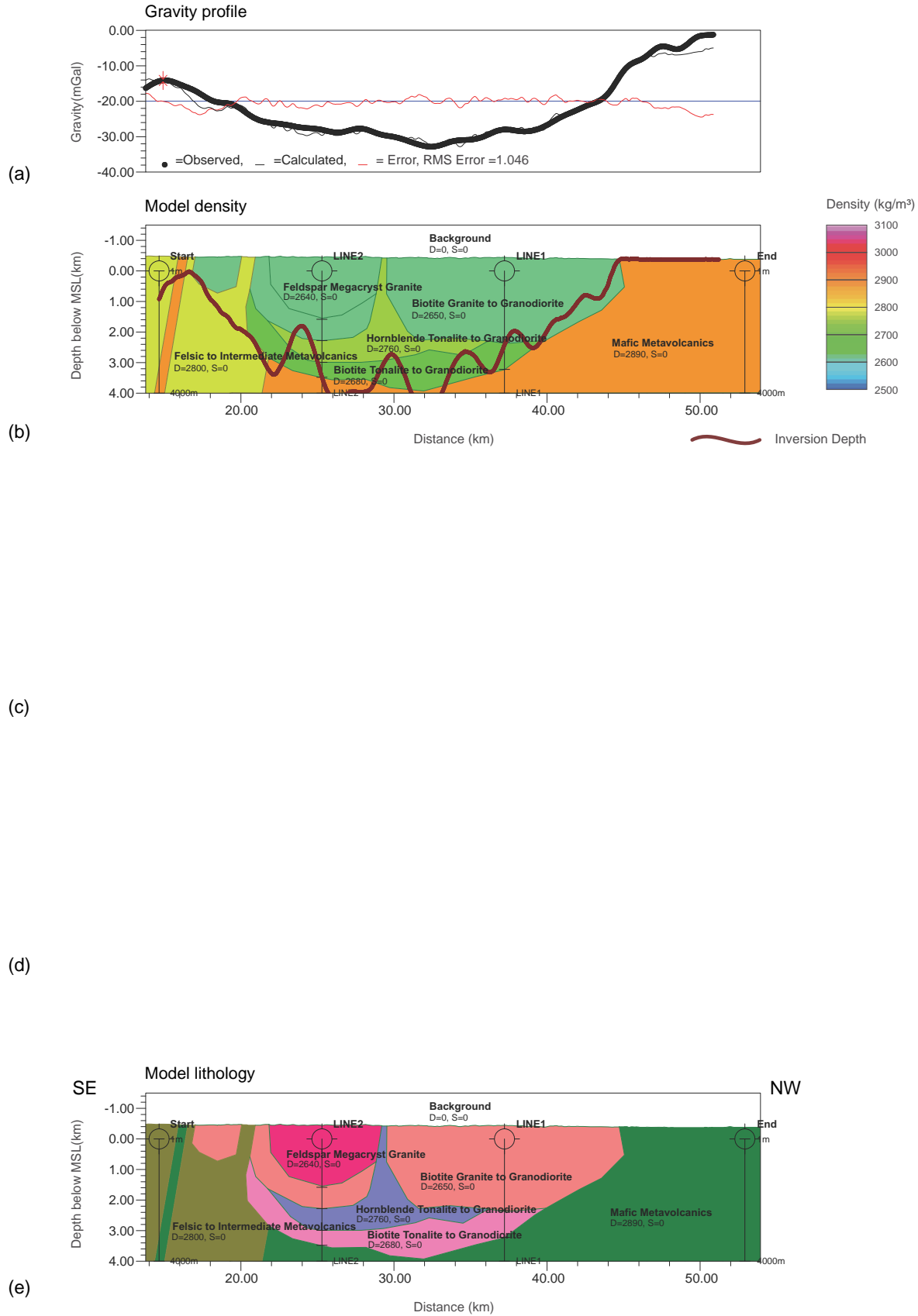


Figure 4.6: Line 3 forward modelling results for the preliminary model. (a) gravity profile showing observed and calculated gravity field and misfit (b) model view showing model densities (c) blank (d) blank (e) model view showing model units. Intersections with the other profiles and the start and end of section within 3D model extents are marked by a circle and vertical line and labelled. Blank Subset (c) and (d) are inserted to maintain the same figure layout for the 2D models.

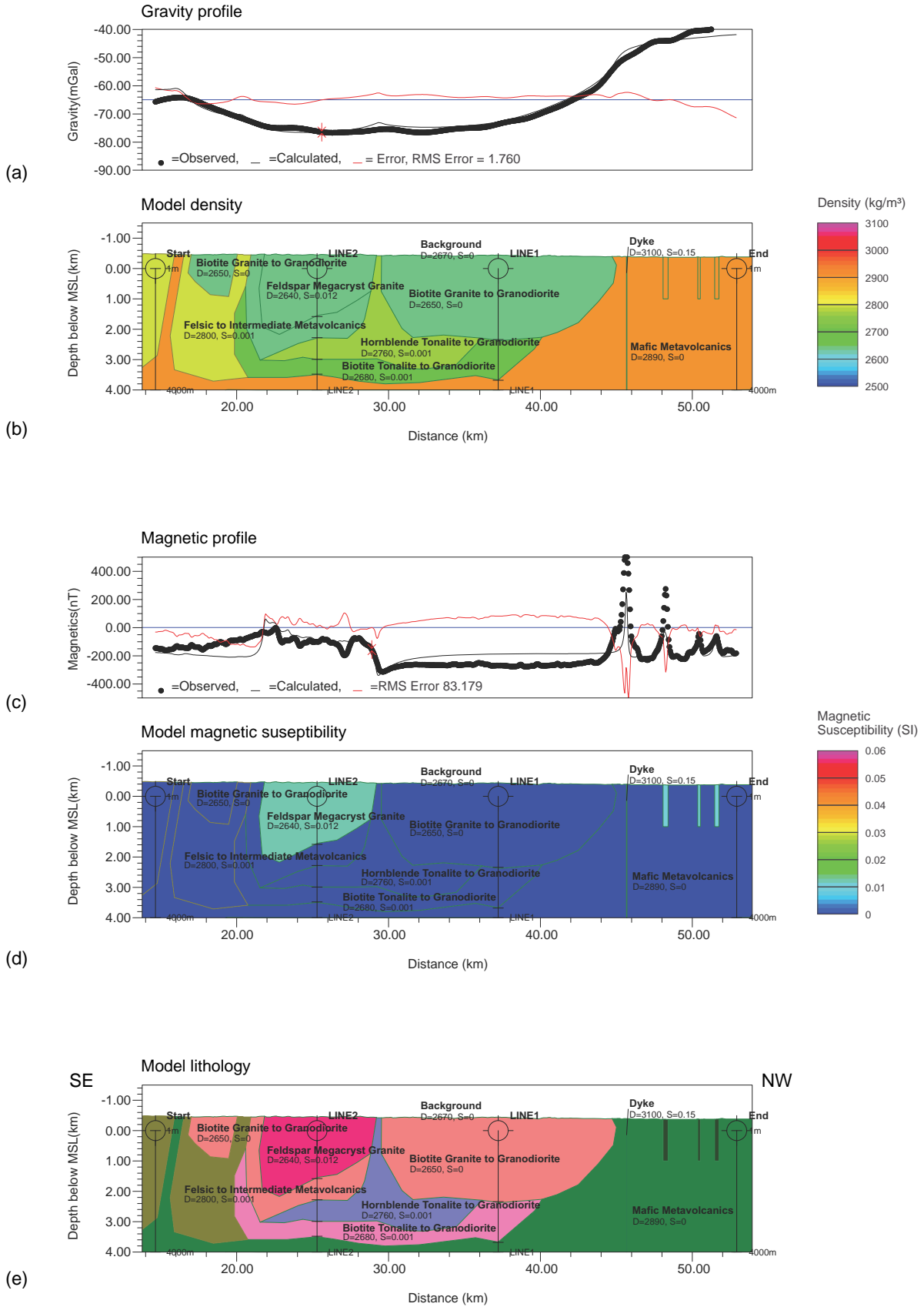
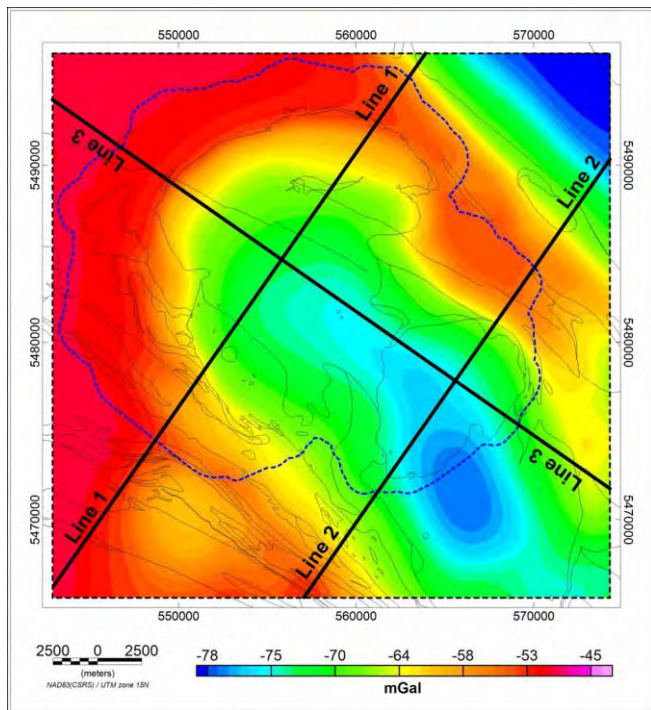
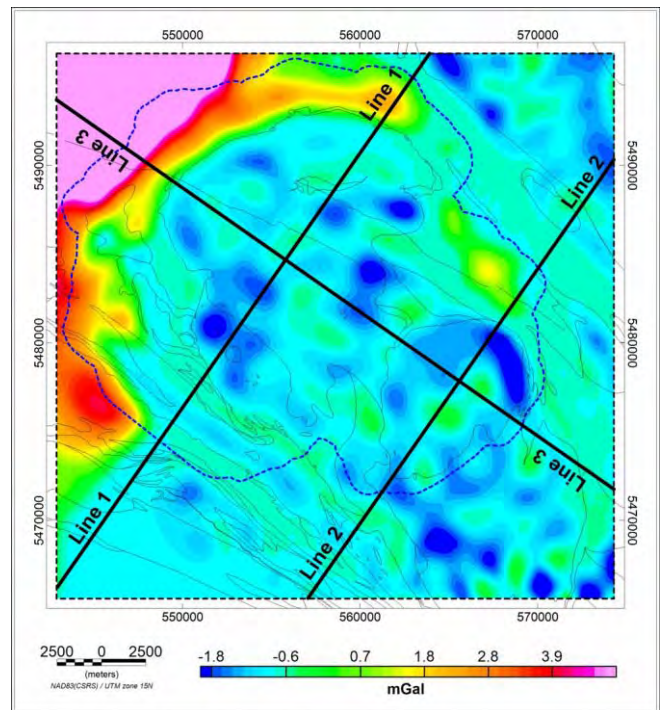


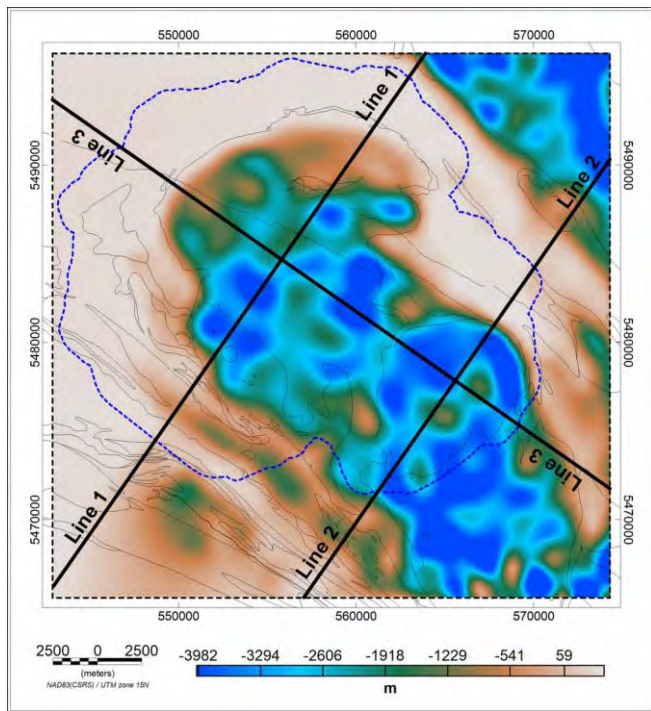
Figure 4.7 Line 3 forward modelling results for the updated model. (a) gravity profile showing observed and calculated gravity field and misfit (b) model view showing model densities (c) magnetic profile showing observed and calculated anomalous magnetic field. (d) model view showing model magnetic susceptibilities (e) model view with model units. Intersections with the other profiles and the start and end of section within 3D model extents are marked by a circle and vertical line and labelled.



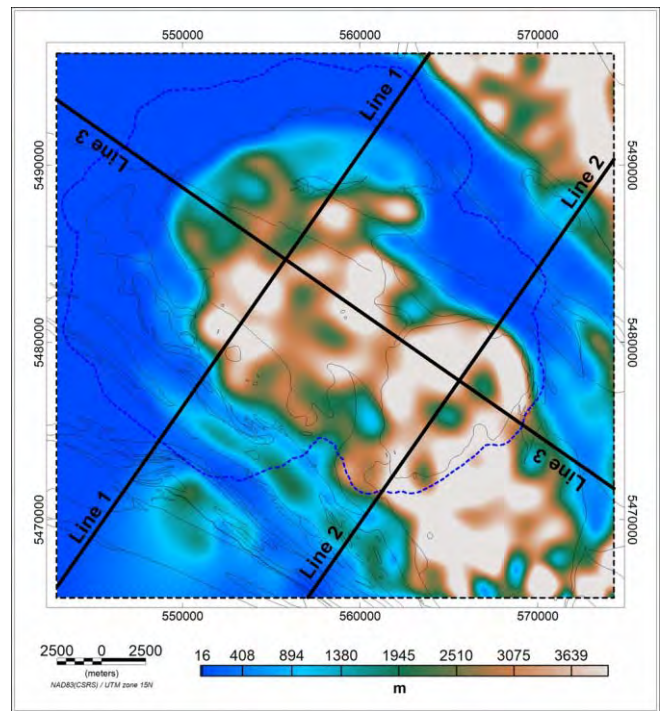
(a)



(b)



(c)



(d)

Figure 4.8 Two layer 3D inversion results from Geosoft. (a) calculated gravity field (b) observed minus calculated gravity field (c) base of batholith/top of greenstones (d) thickness of batholith/depth to greenstones. The dashed blue line marks the LiDAR coverage.

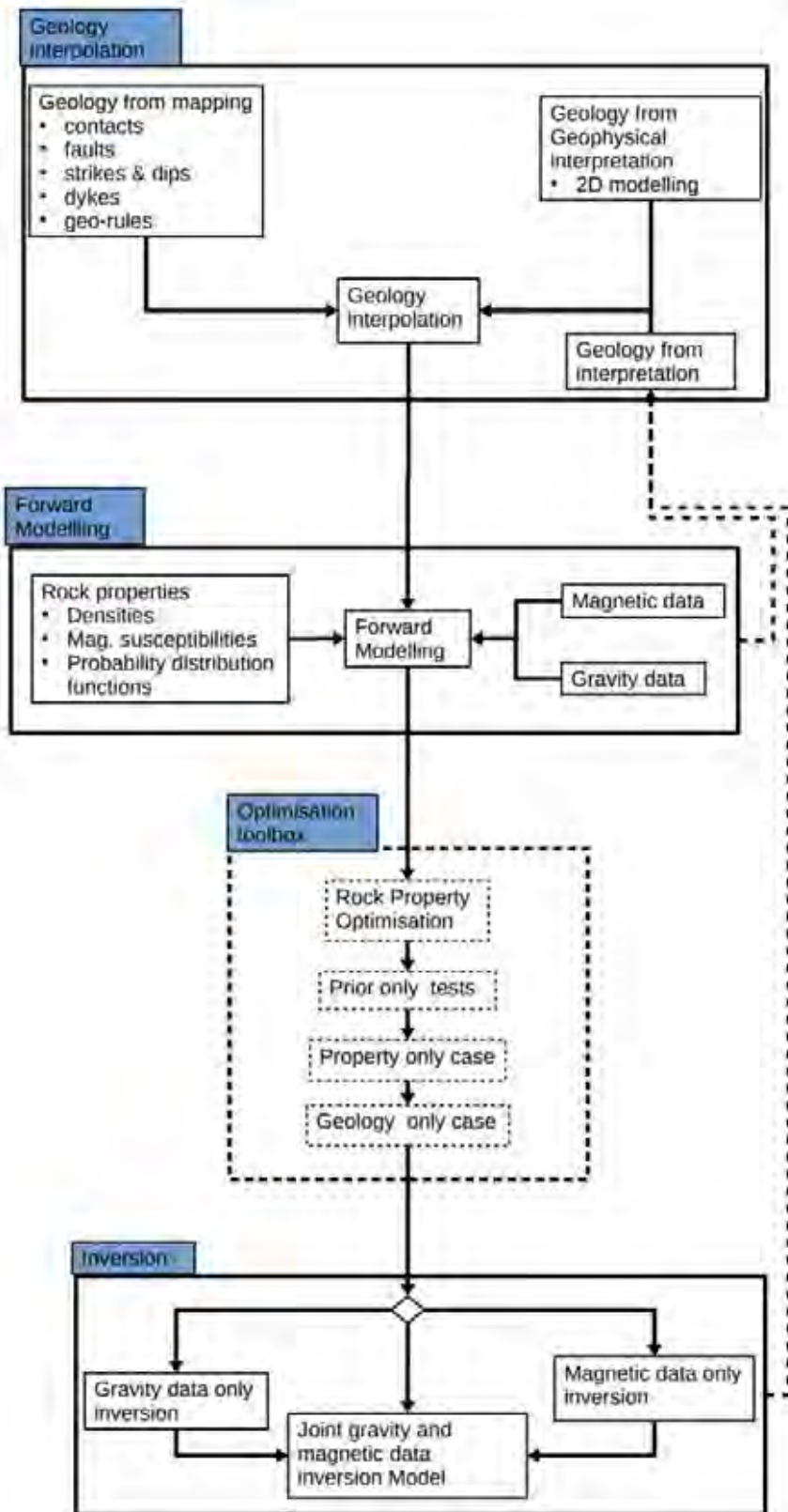
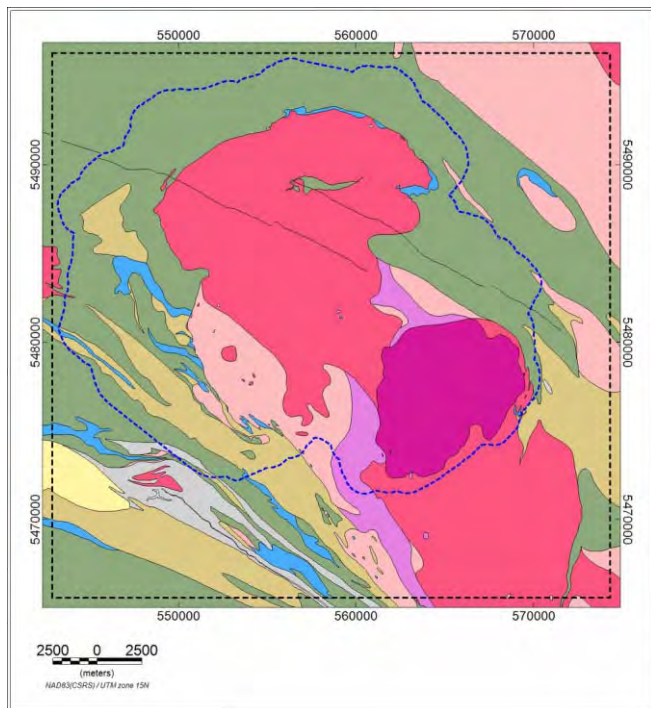
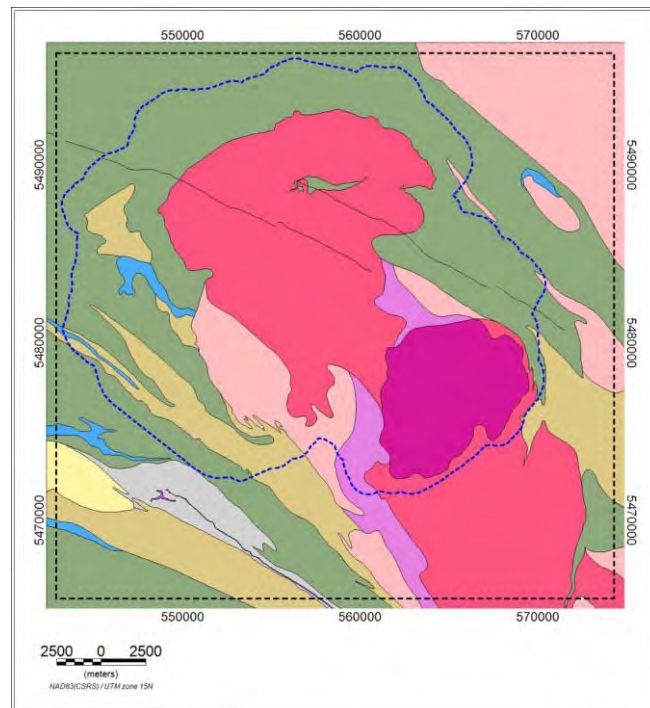


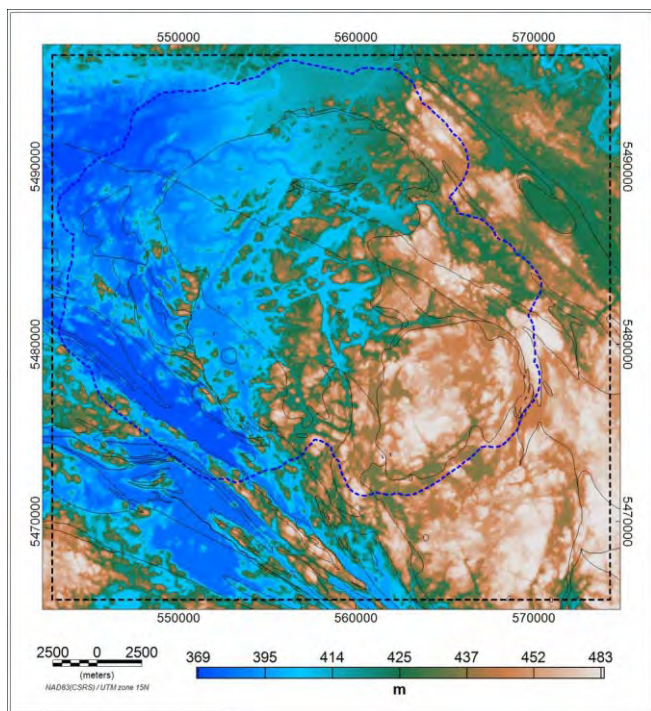
Figure 5.1 3D geophysical model creation work flow.



(a)

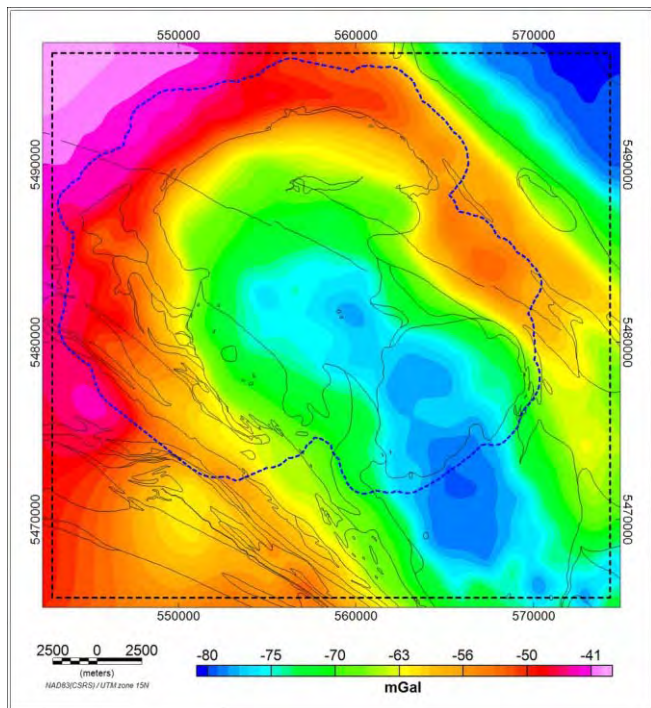


(b)

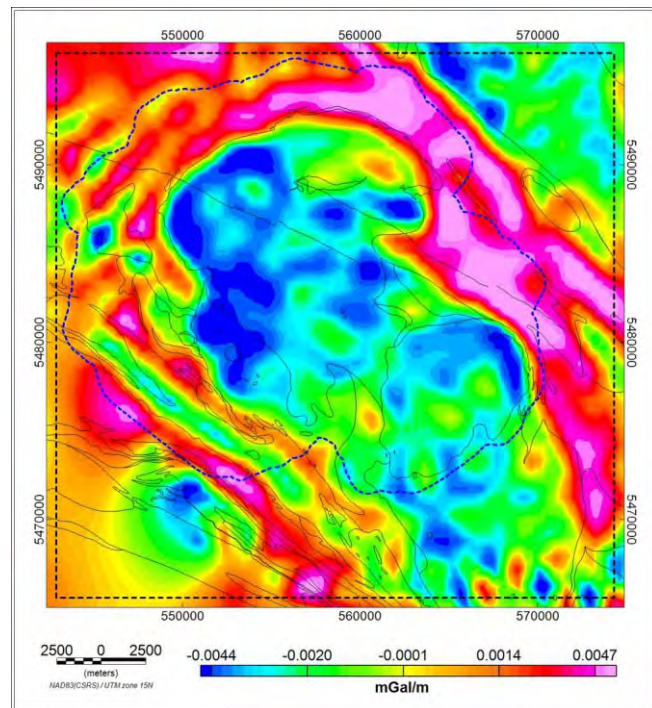


(c)

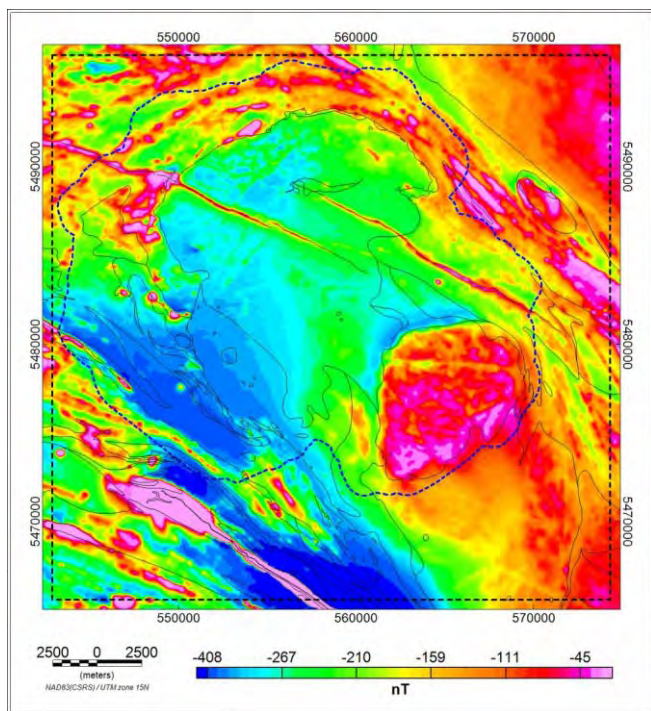
Figure 5.2 Model extents (dashed rectangle in black) and LiDAR data limits (dashed polygon in blue) overlain on (a) bedrock geology (b) simplified bedrock geology (c) topography above MSL.



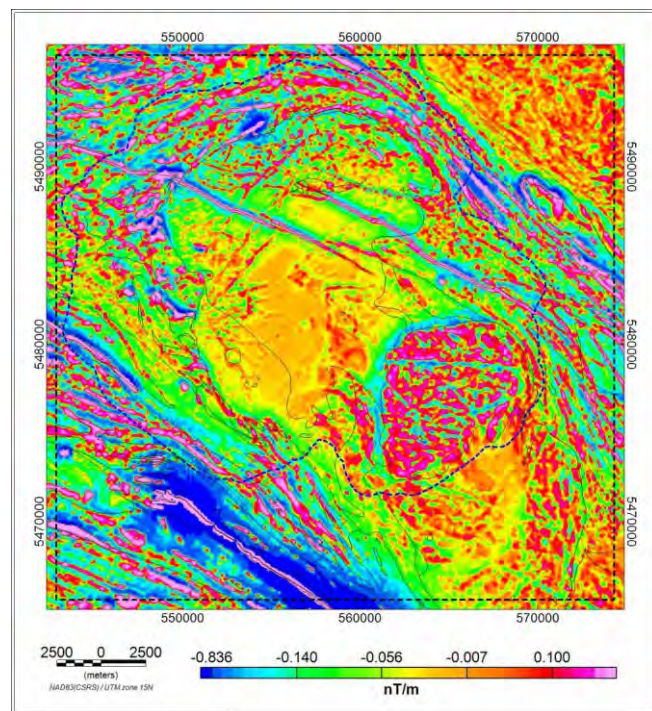
(a)



(b)



(c)



(d)

Figure 5.3 Model extents (dashed rectangle) and LiDAR data limits (dashed polygon) overlain on (a) observed Bouguer gravity (b) first vertical derivative of observed Bouguer gravity (c) observed anomalous magnetic field (d) first vertical derivative of the anomalous magnetic field.

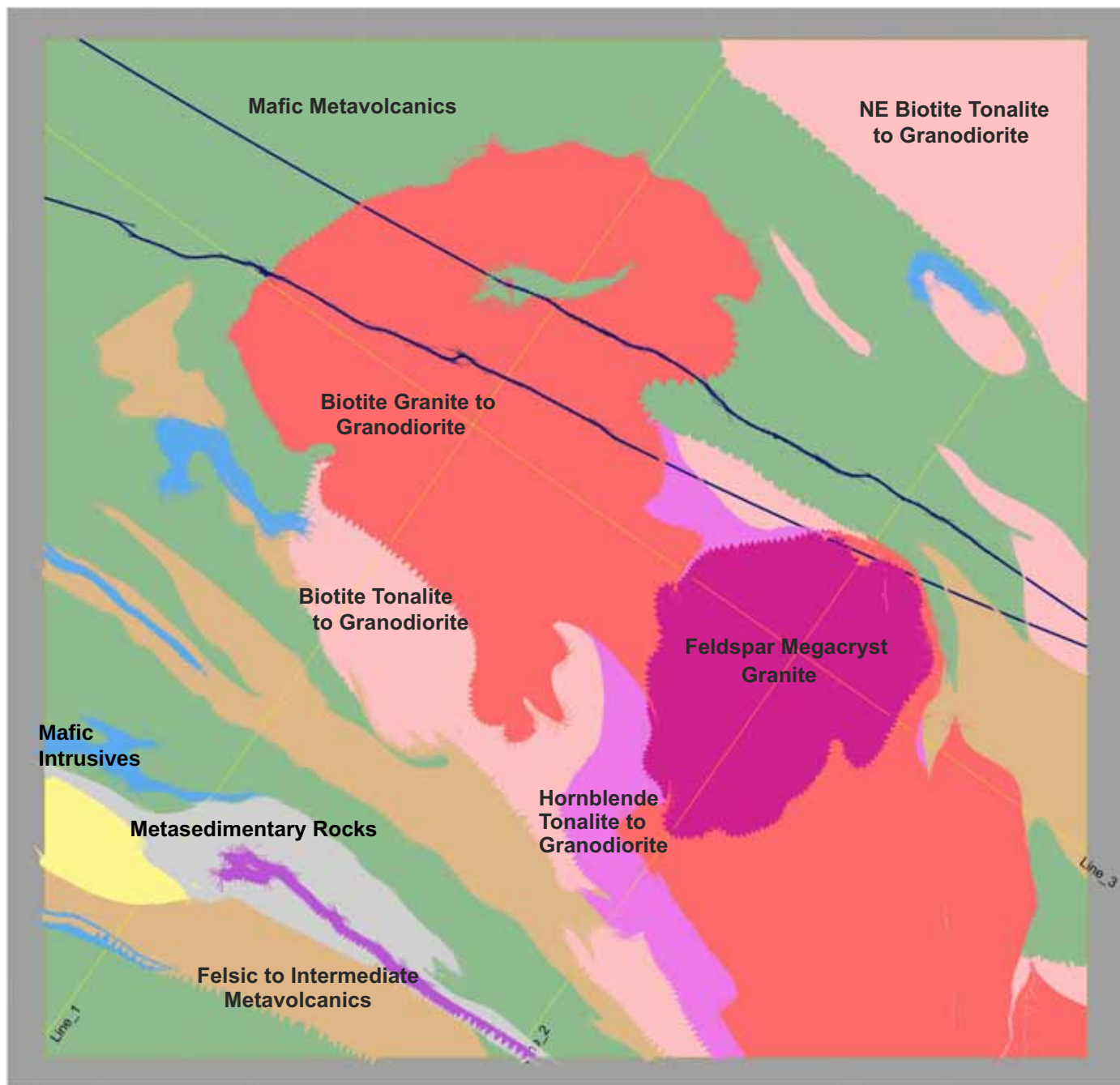


Figure 5.4: Interpolated bedrock geology at ground level from GeoModeller. Profile lines are shown in yellow, two dykes cross-cut the region in a NW-SE direction in navy blue and the saw-tooth pattern at the edges of units depict dip direction. The colour scheme for the rock units matches that of the bedrock geology figures in Section 2.

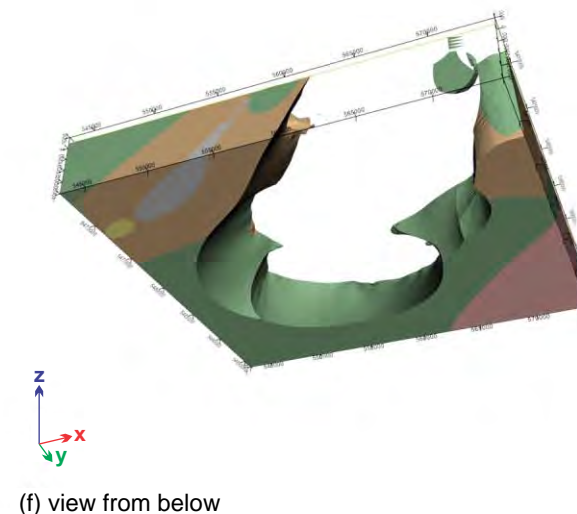
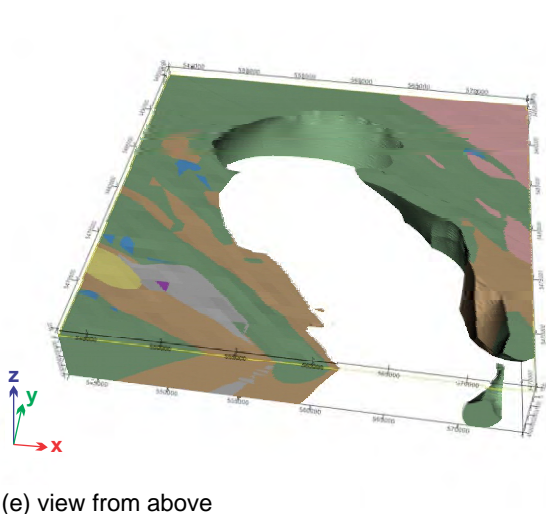
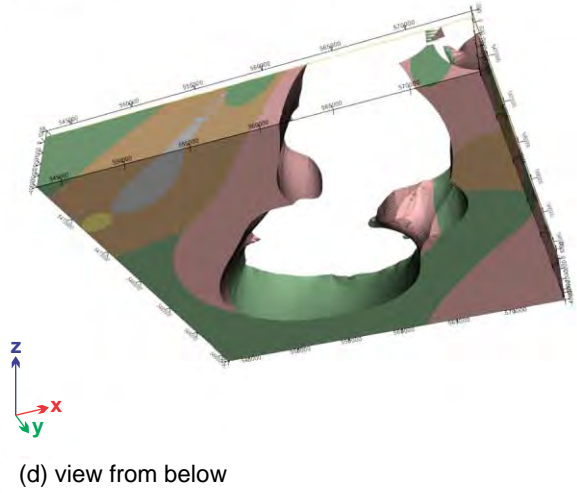
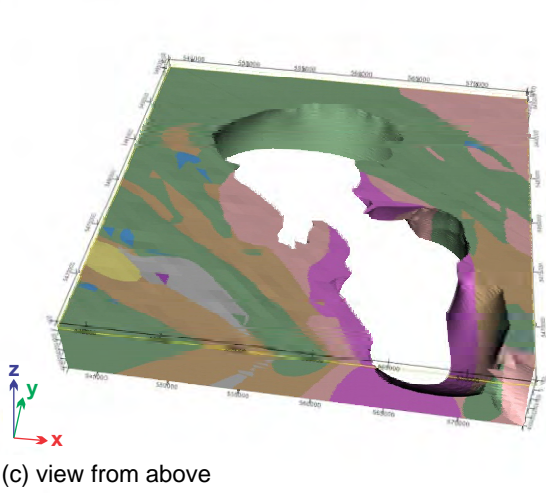
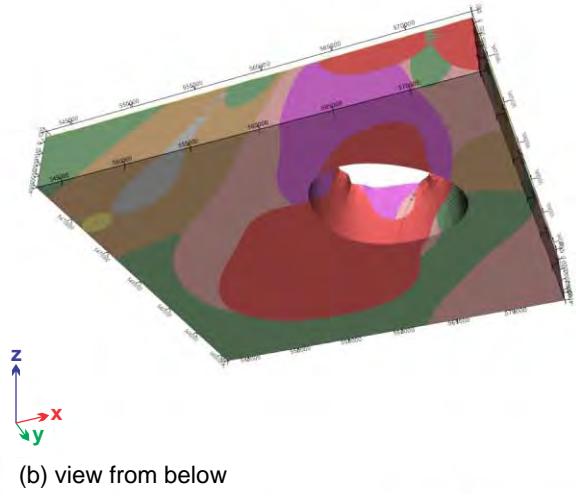
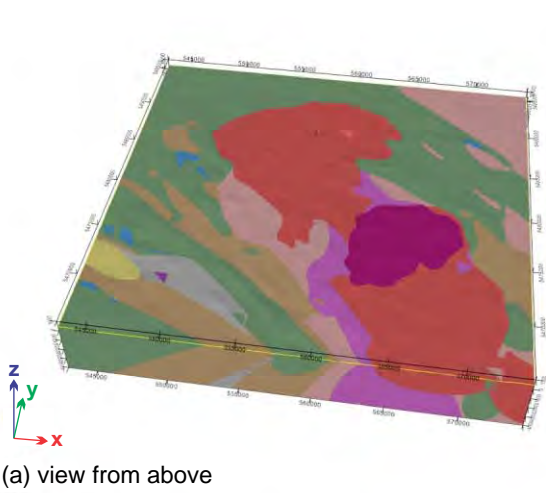
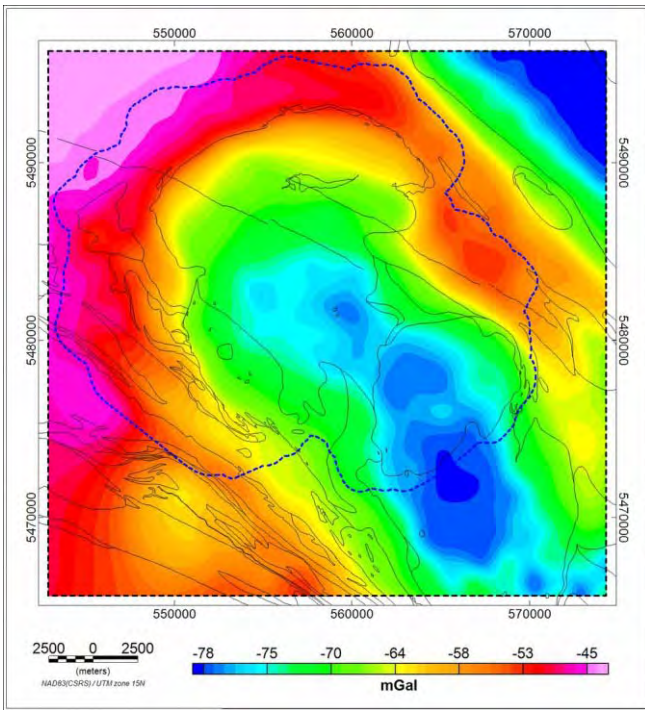
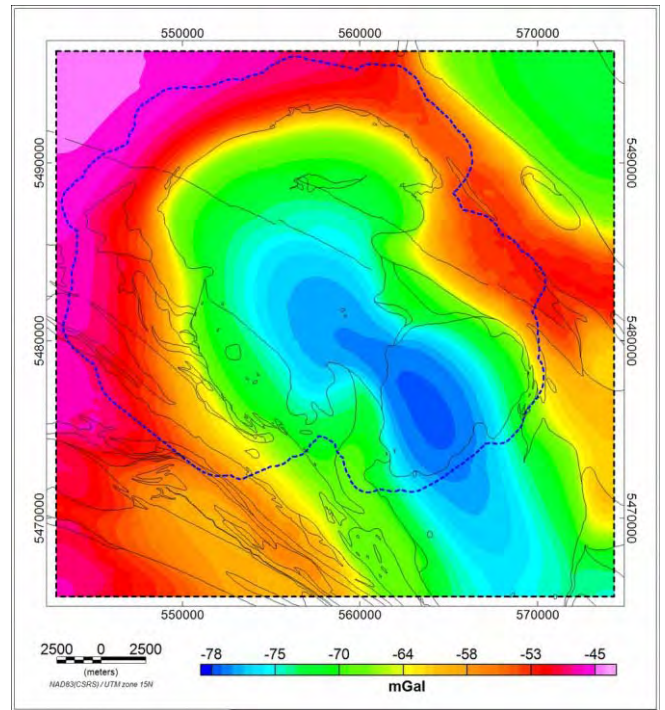


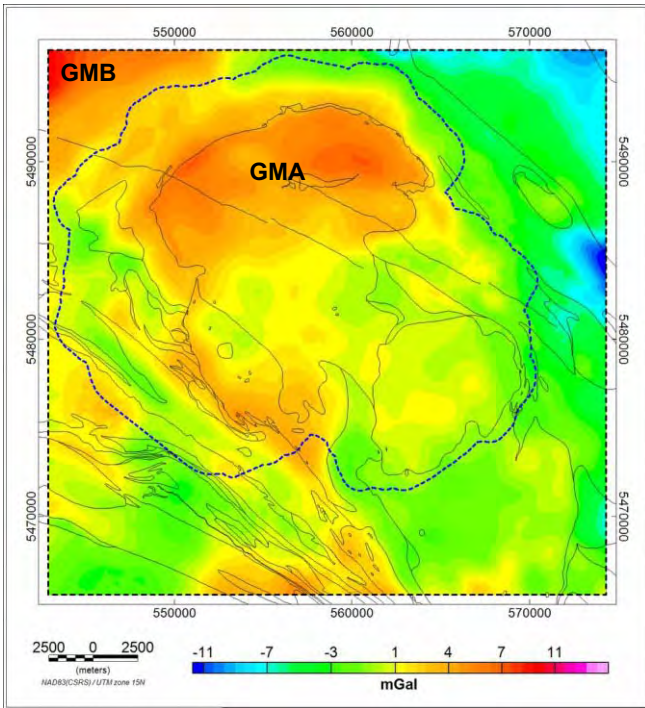
Figure 5.5: Multiple 3D views of the same interpolated geology model based solely on surface geology with no subsurface constraints. Batholith units are progressively removed from the displays with (a) the full model and (b) feldspar megacrystic granite unit removed (c) biotite granite to granodiorite removed (d) hornblende tonalite to granodiorite removed (e) and (f) biotite tonalite to granodiorite removed.



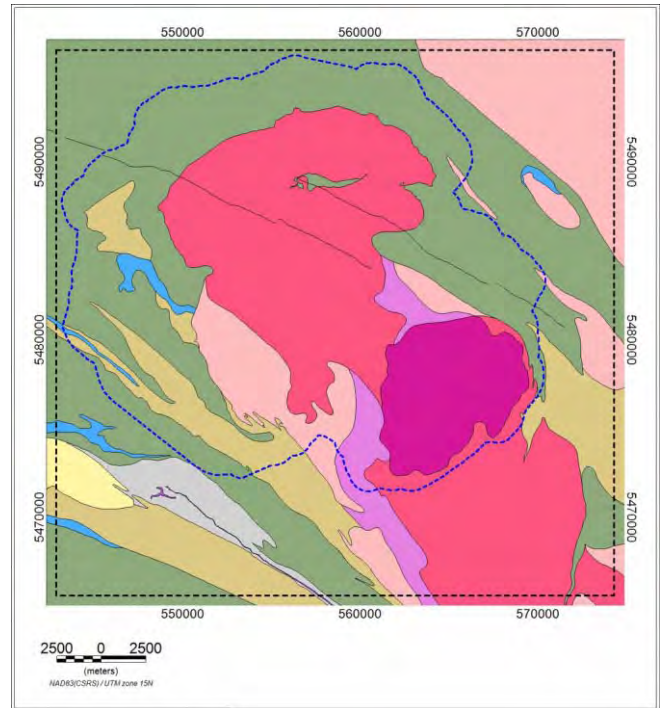
(a)



(b)

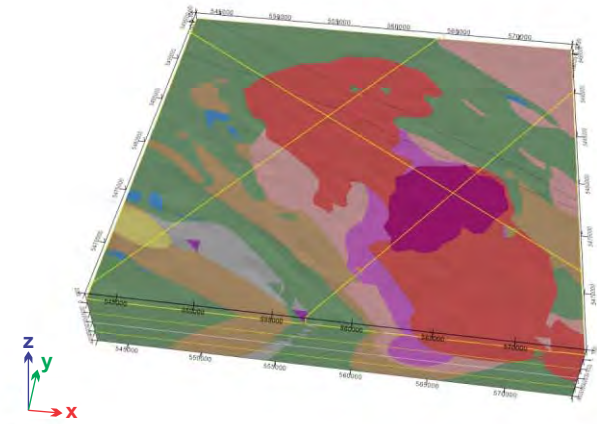


(c)

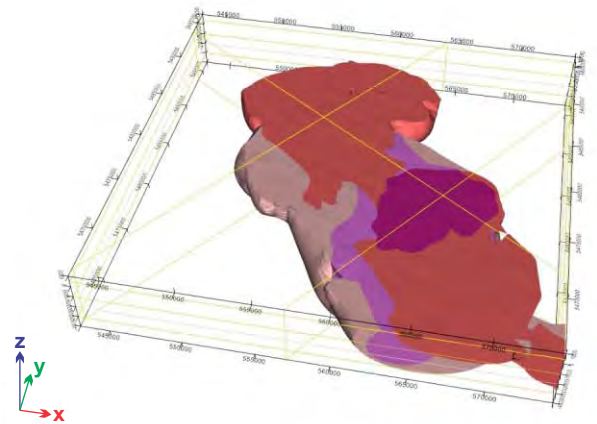


(d)

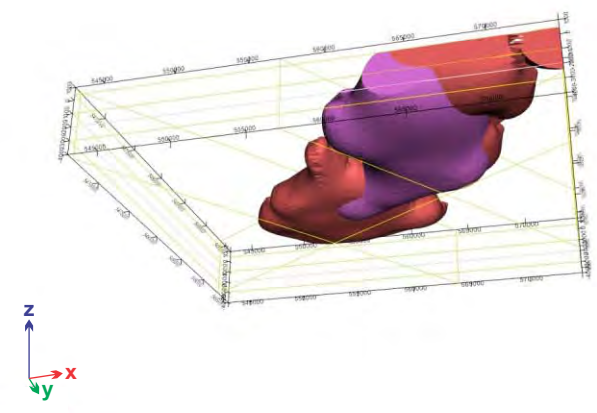
Figure 5.6: Comparison of observed gravity anomaly with predicted anomaly from the interpolated geology model based solely on surface geology. (a) observed Bouguer gravity (b) calculated Bouguer gravity (c) observed minus calculated gravity (d) simplified bedrock geology. In panel (c), features labelled GMA and GMB are prominent misfits discussed in Section 6.4. The dashed blue line marks the LiDAR coverage.



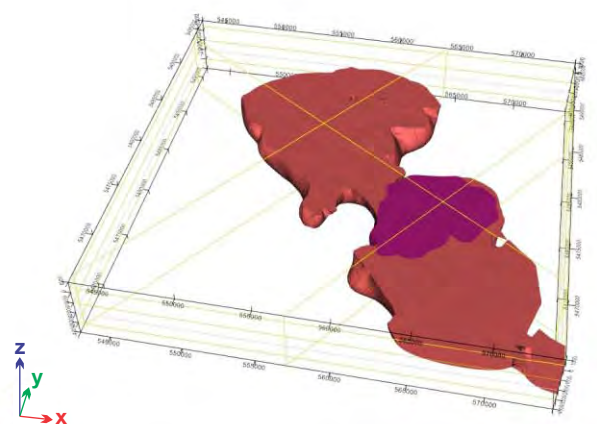
(a) view from above



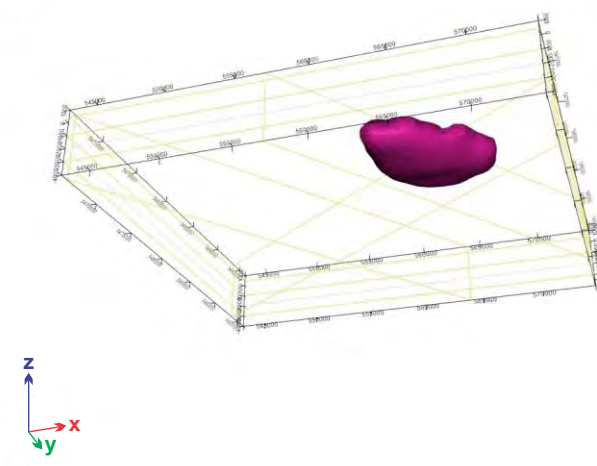
(b) view from above



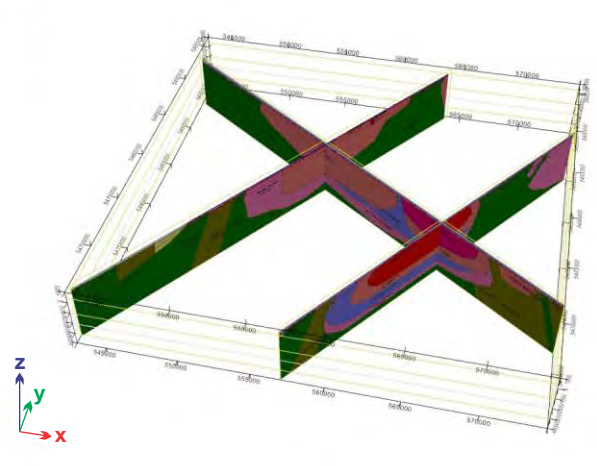
(c) view from below



(d) view from above

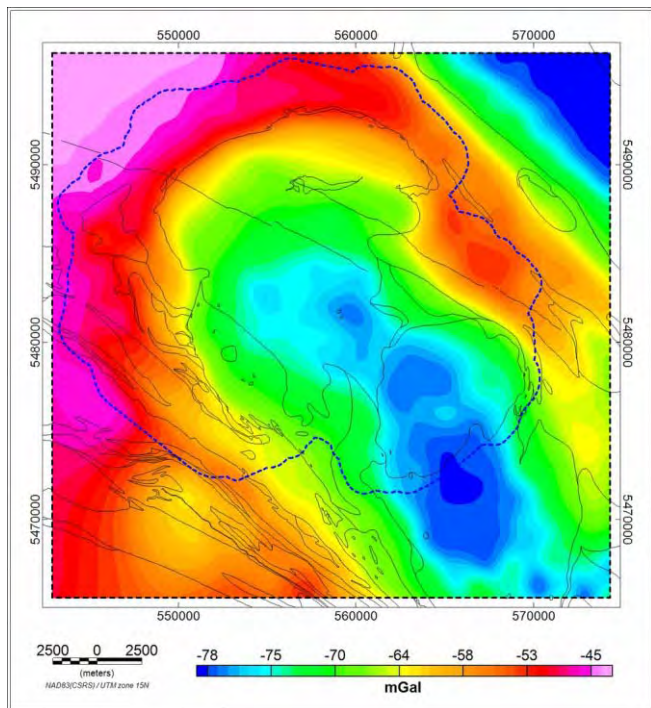


(e) view from below

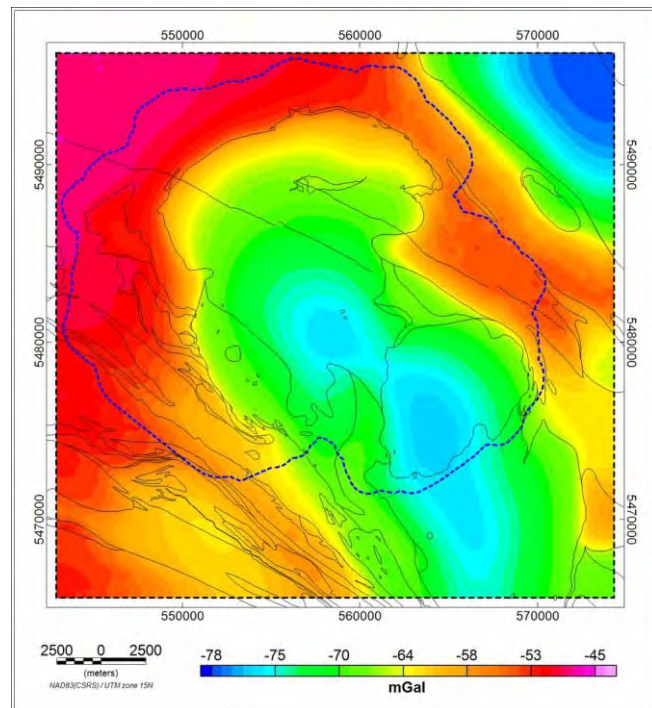


(f) view from above

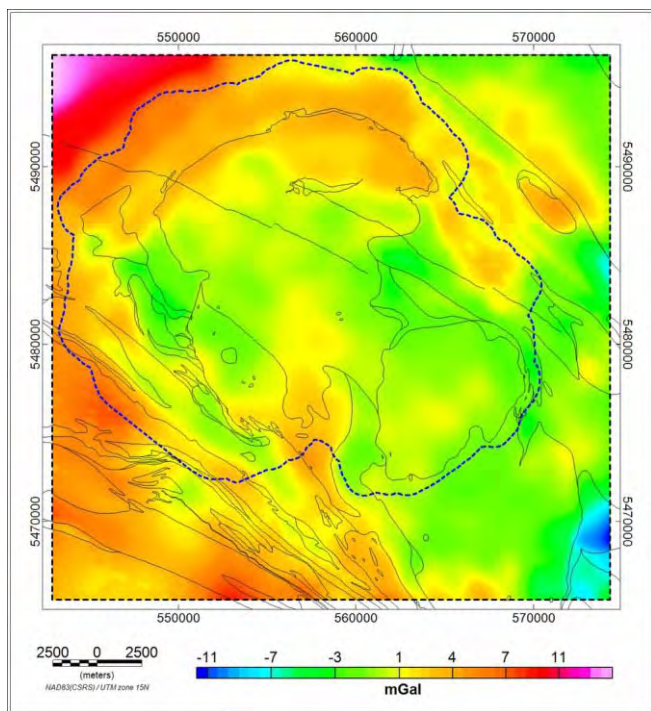
Figure 5.7 Interpolated geology model based on results from 2D modelling and surface geology. (a) full model (b) all units within the batholith (c) batholith without the biotite tonalite to granodiorite unit (d) batholith without the biotite tonalite to granodiorite and the hornblende tonalite to granodiorite units (e) feldspar megacrystic granite unit (f) displays of the 2D models used in creating the 3D model



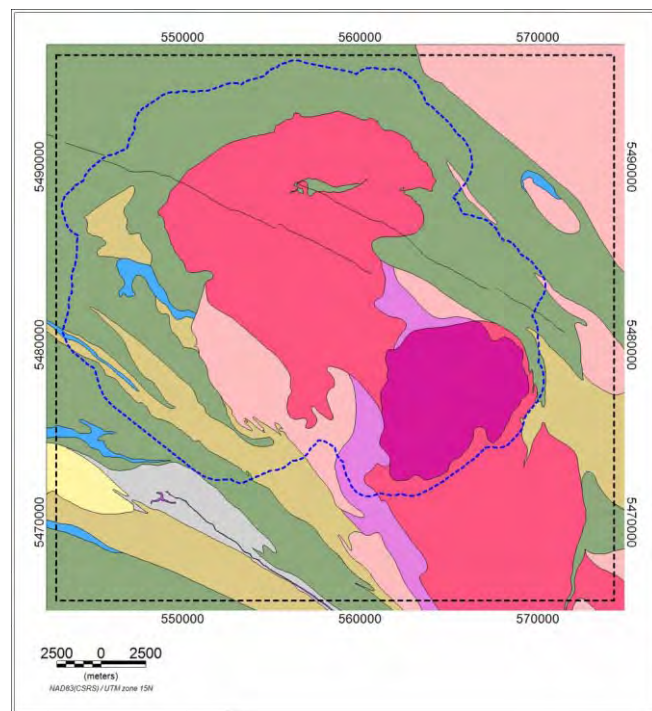
(a)



(b)

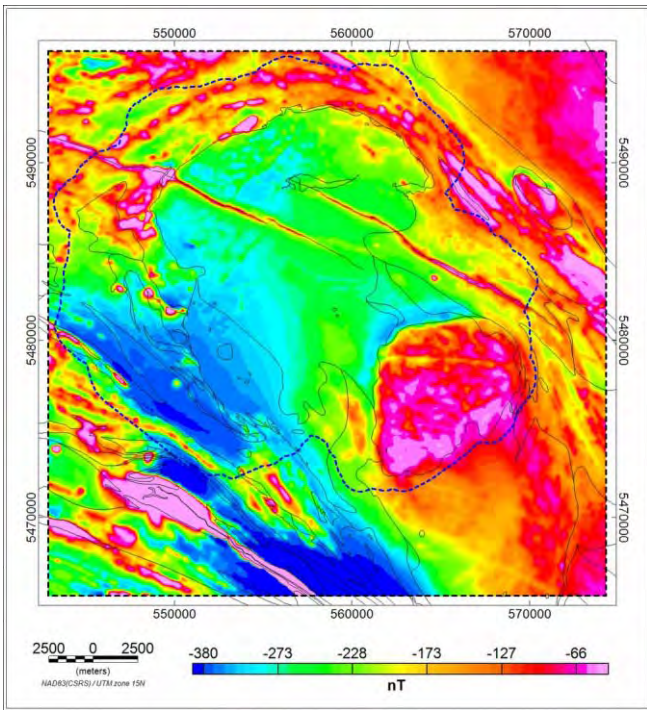


(c)

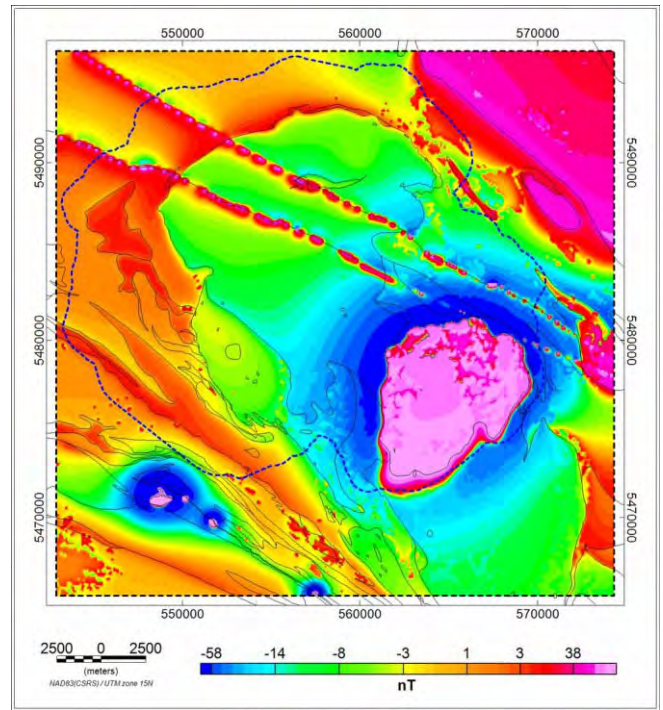


(d)

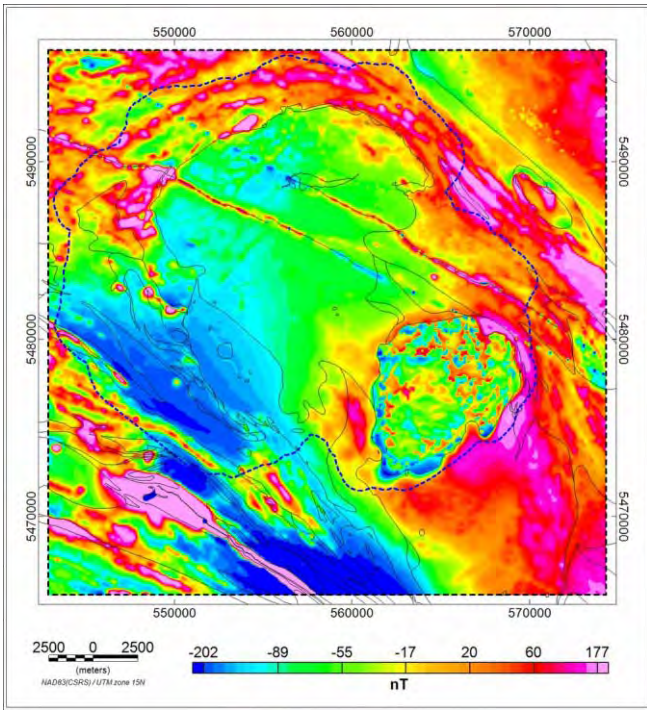
Figure 5.8 Comparison of observed gravity anomaly with predicted anomaly from the model based on results from 2D modelling and surface geology. (a) observed Bouguer gravity (b) calculated Bouguer gravity (c) observed minus calculated gravity (d) simplified bedrock geology.



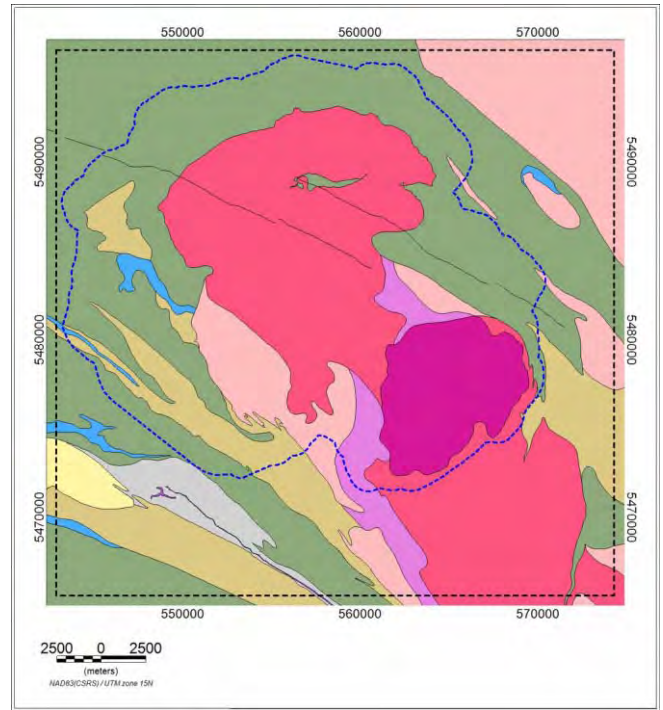
(a)



(b)

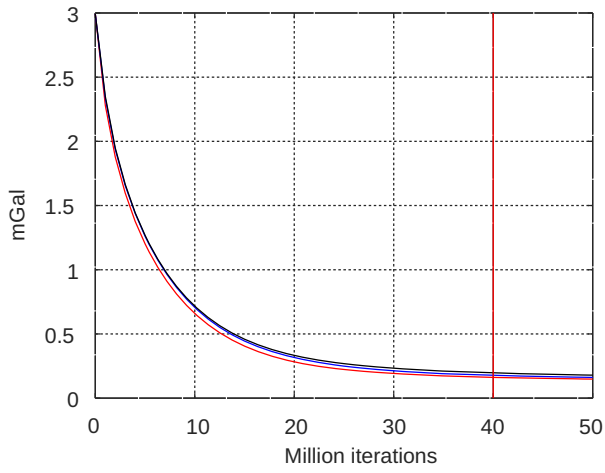


(c)

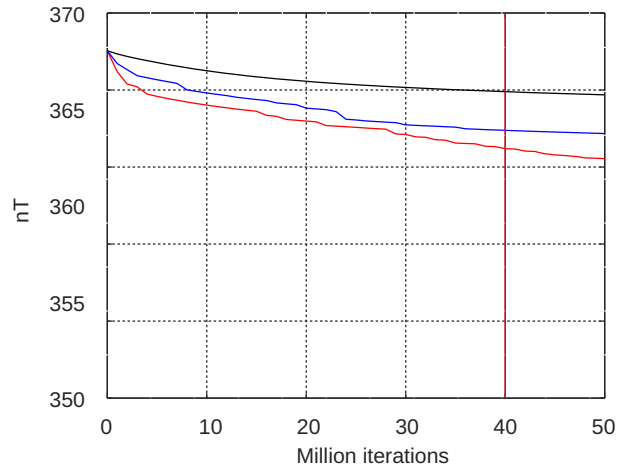


(d)

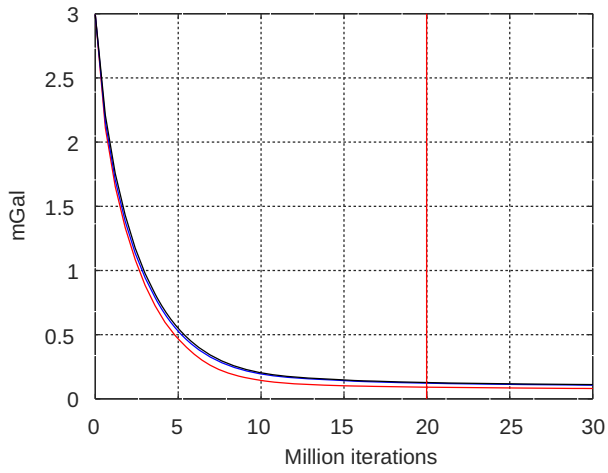
Figure 5.9 Comparison of observed magnetic anomaly with predicted anomaly from the model based on results from 2D modelling and surface geology. (a) observed anomalous magnetic field (b) calculated anomalous magnetic field (c) observed minus calculated anomalous magnetic field (d) simplified bedrock geology. The dashed blue line marks the LiDAR coverage.



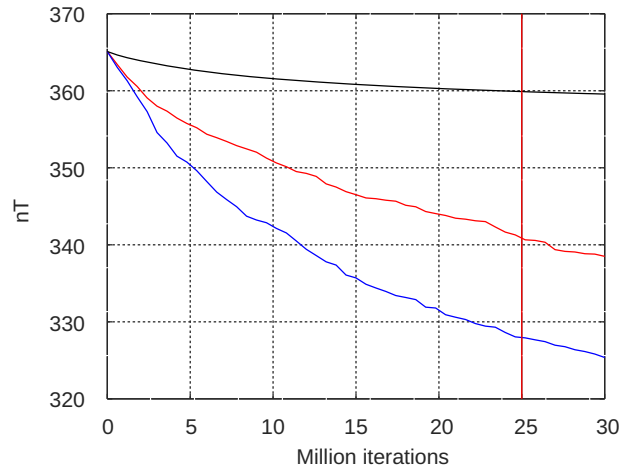
(a)



(b)

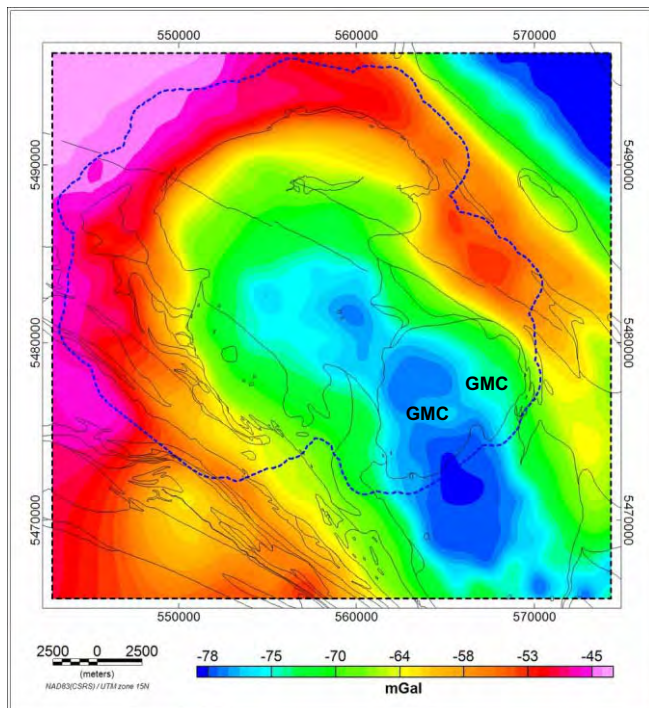


(c)

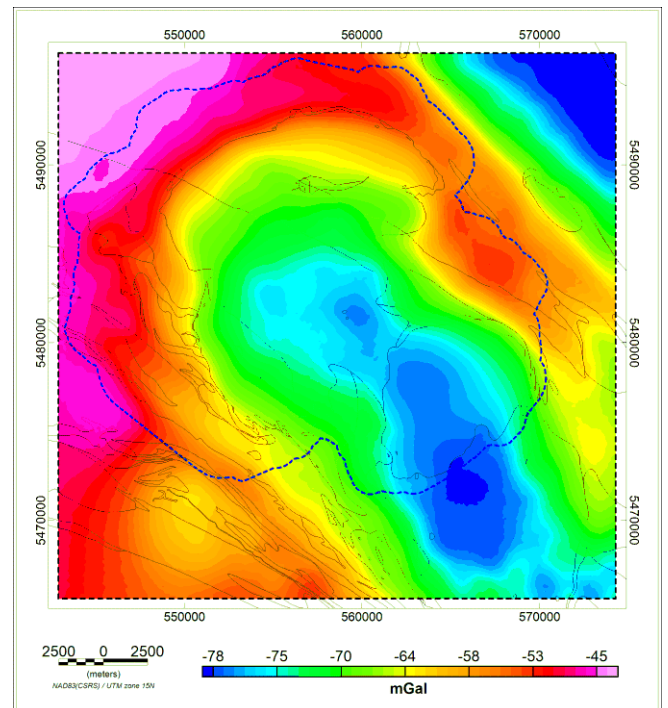


(d)

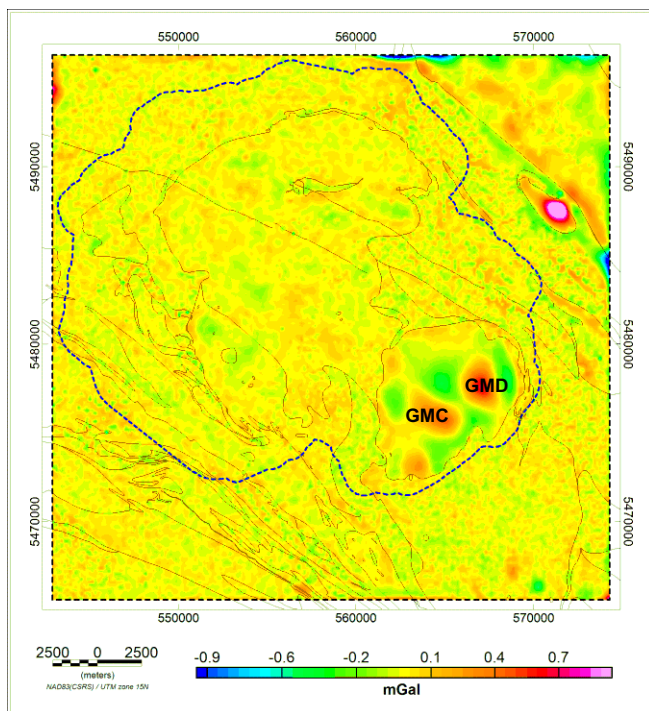
Figure 5.10: Graph examples showing misfit variation with iteration number for (a) joint inversion gravity misfit (b) joint inversion magnetic misfit (c) gravity only inversion gravity misfit (d) magnetic only inversion magnetic misfit. The black, blue and red curves are for tight, moderate and loose inversion constraint respectively. Vertical red lines show selected burn-in points.



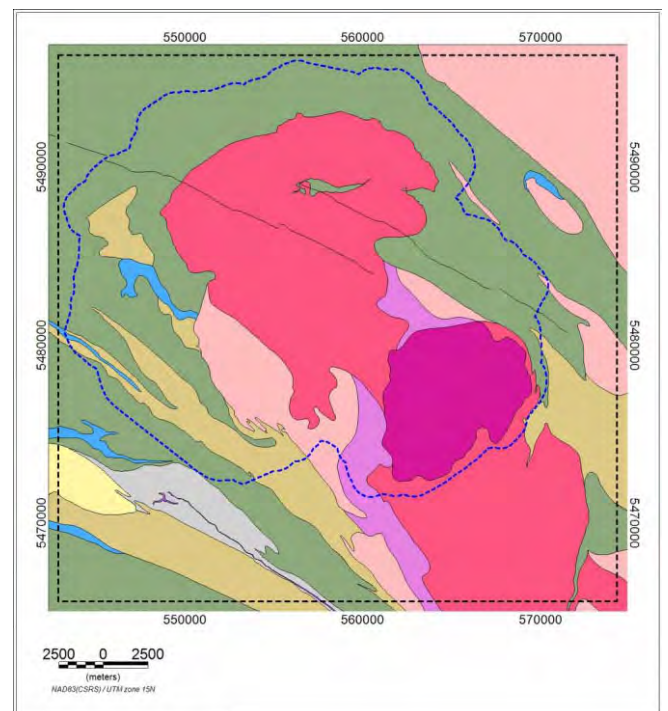
(a)



(b)

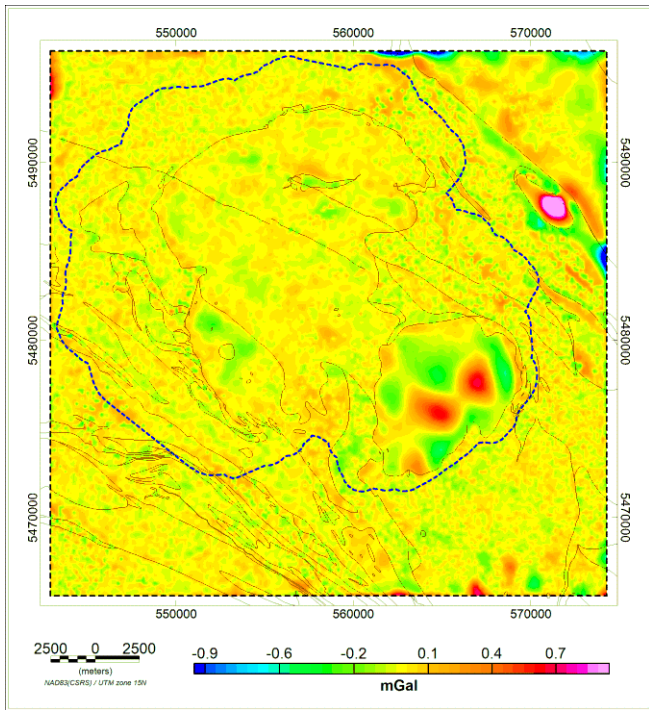


(c)

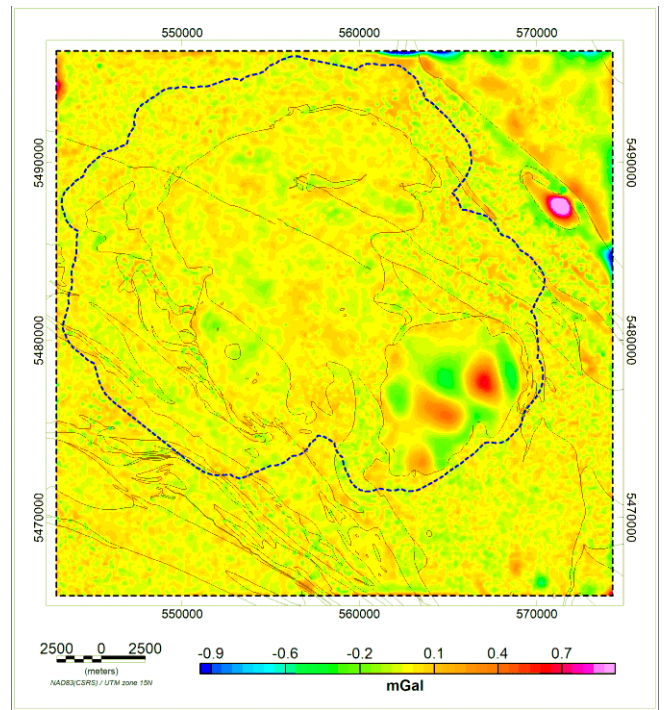


(d)

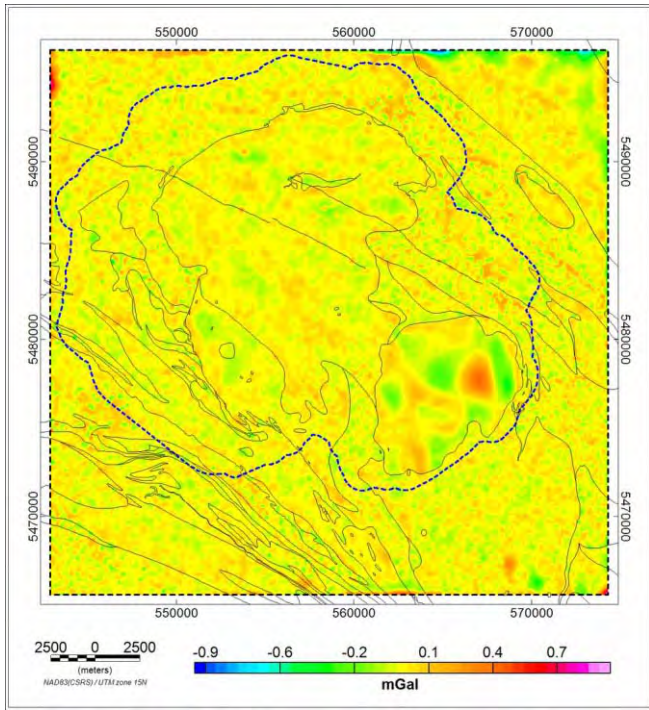
Figure 5.11 Comparison of observed gravity anomaly with predicted anomaly from the gravity only inversion with moderate constraint. (a) observed Bouguer gravity (b) calculated Bouguer gravity (c) observed minus calculated gravity (d) simplified bedrock geology. Features GMC and GMD labelled in (a) and (c) are prominent misfits within the feldspar megacryst unit. The dashed blue line marks the LiDAR coverage.



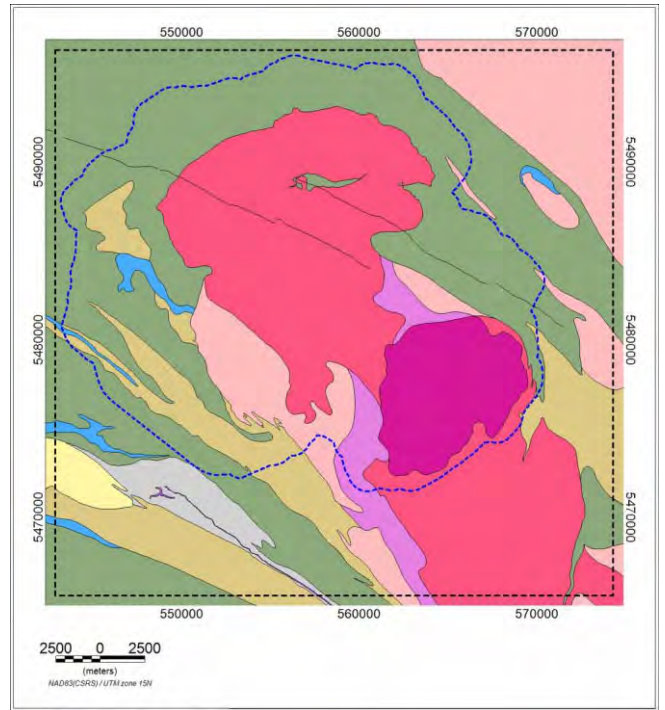
(a)



(b)

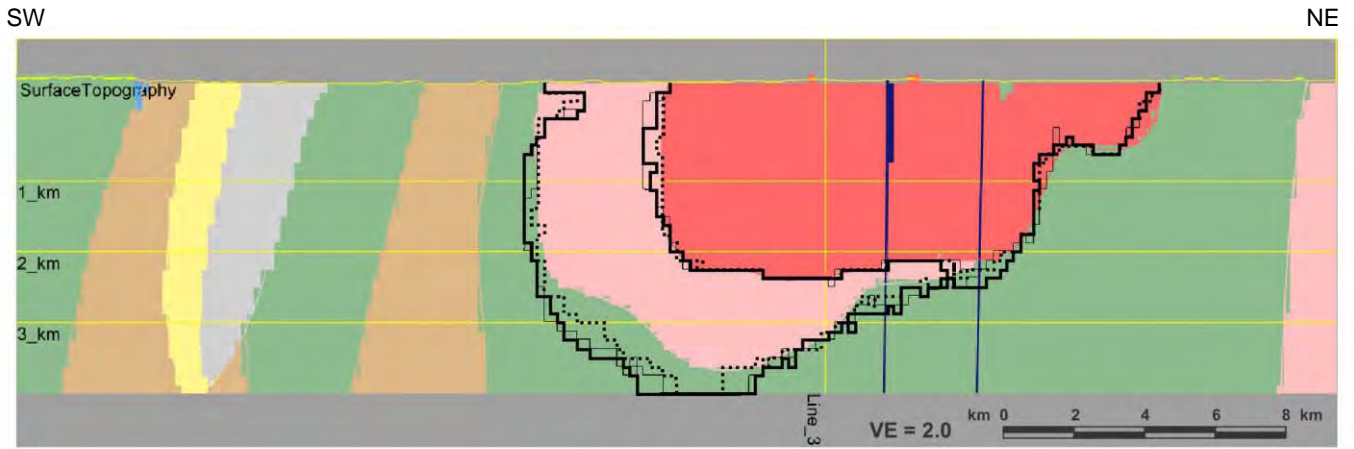


(c)

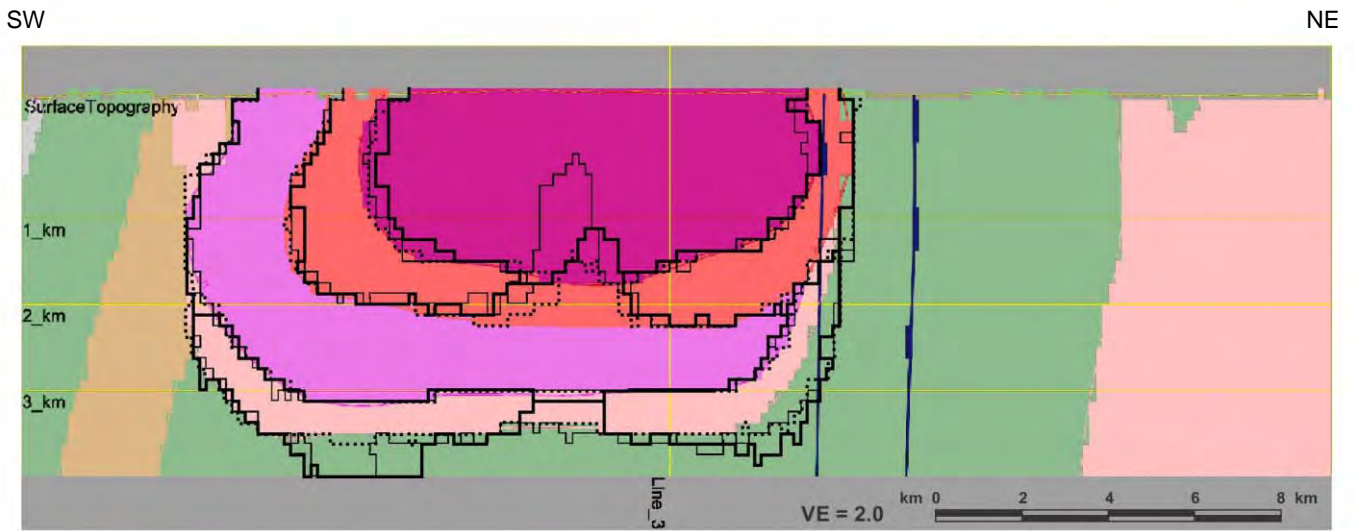


(d)

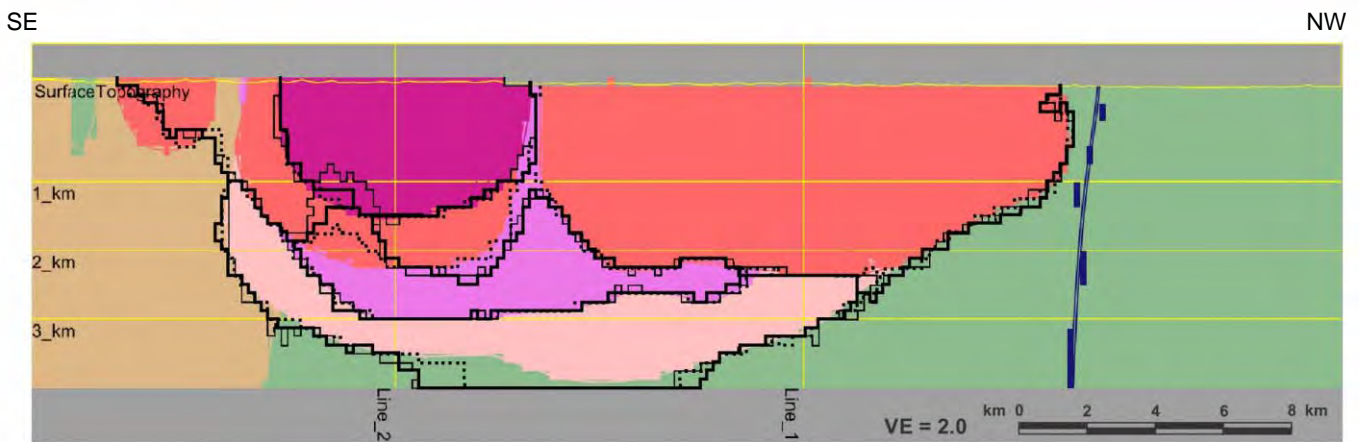
Figure 5.12 Gravity only inversion residuals for (a) tightly constrained (b) moderately constrained (c) loosely constrained inversions with (d) simplified bedrock geology. The dashed blue line marks the LiDAR coverage.



(a)

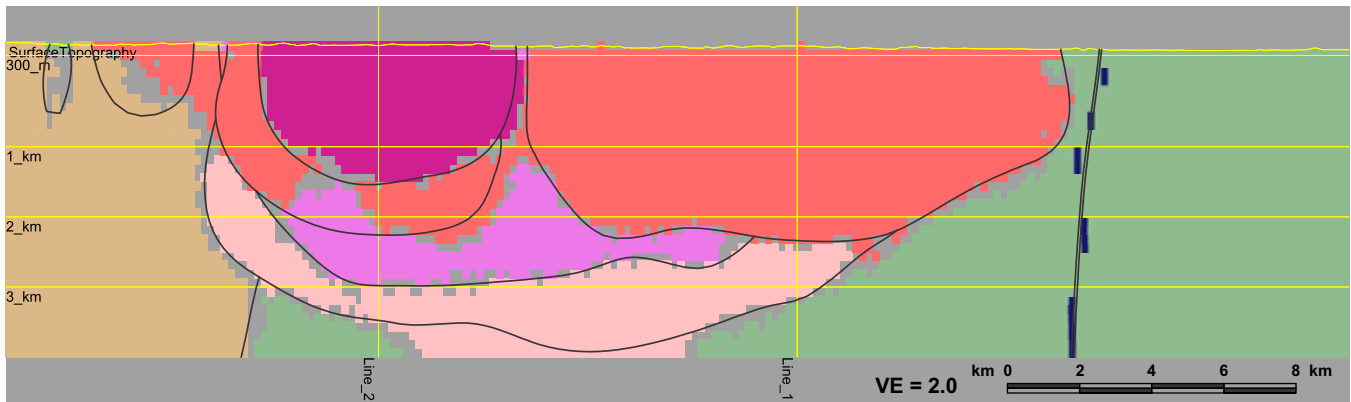


(b)

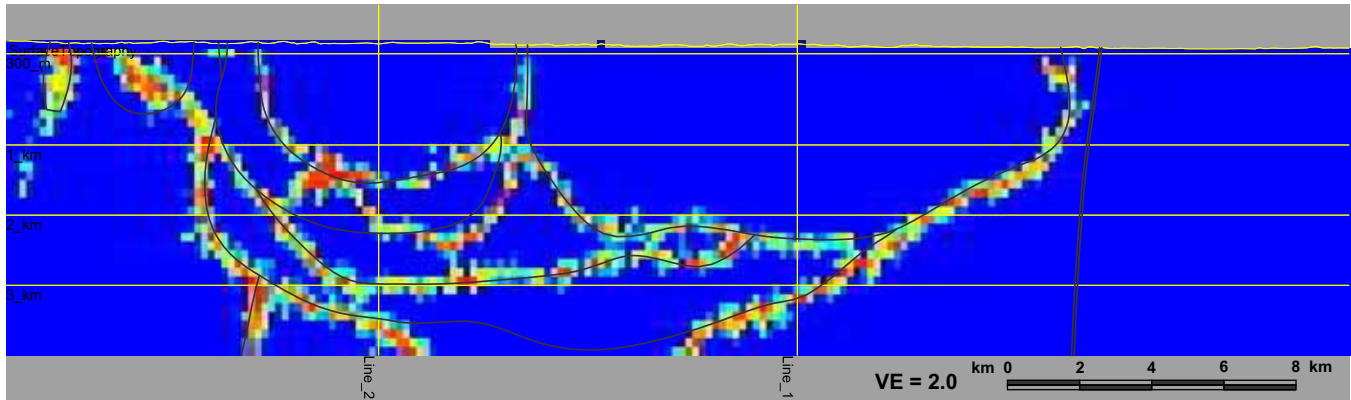


(c)

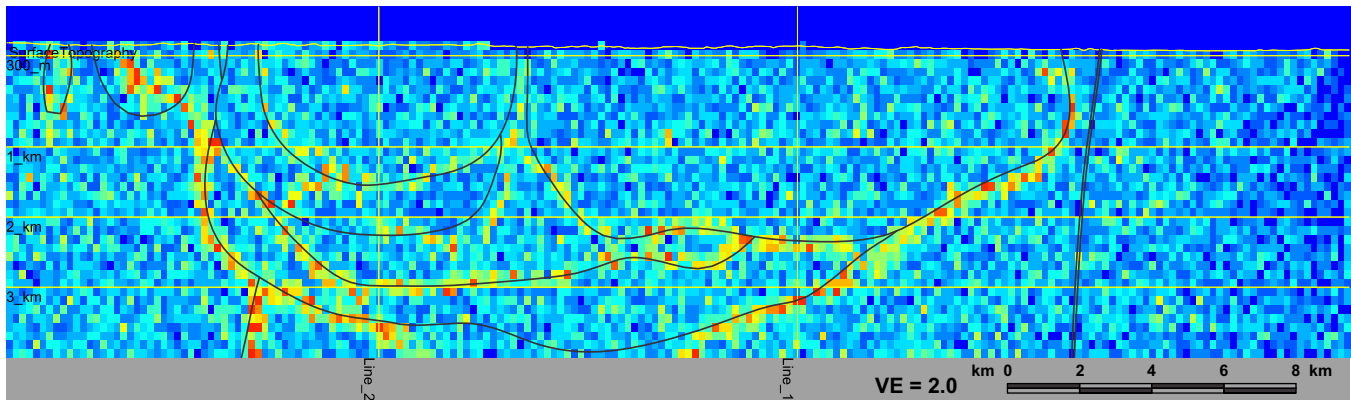
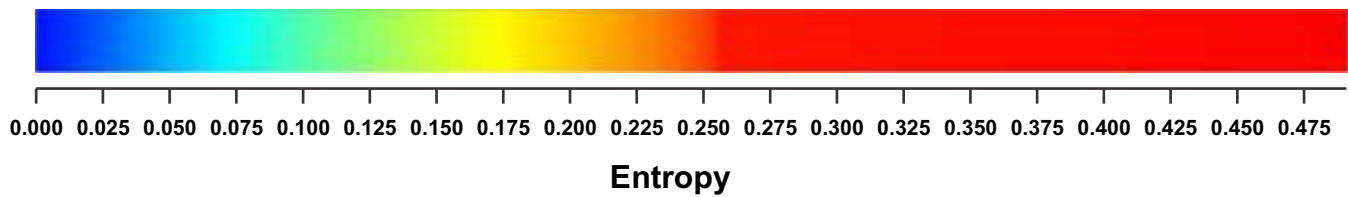
Figure 5.13 Gravity only inversion results along (a) Line 1 (b) Line 2 (c) Line 3. The coloured image in the background is the starting model. Dotted black lines are for inversion with very tight constraint, solid lines are for moderate constraint and faint lines for loose constraint.



(a)



(b)



(c)

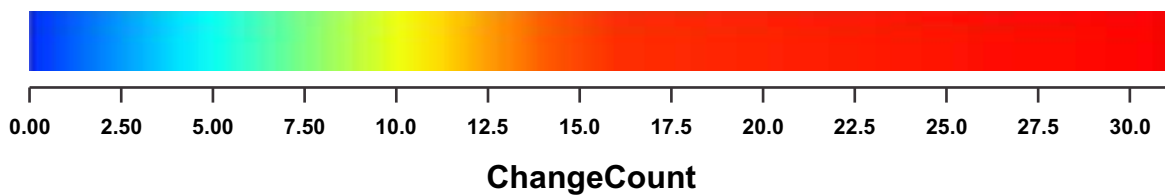
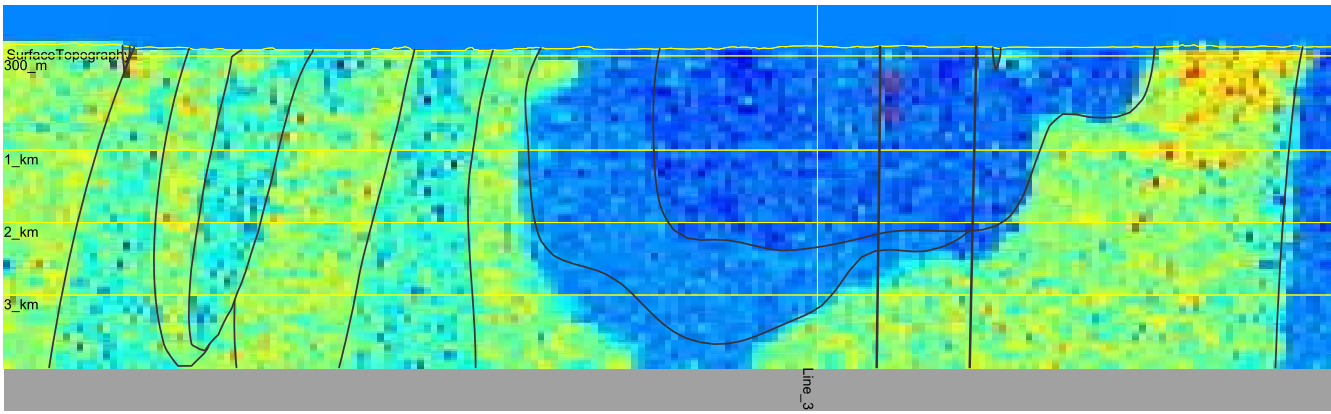


Figure 5.14 Gravity only moderate constraint inversion results statistics along Profile Line 3. (a) 90 % thresholded model units. Pixels below 90% threshold level are grayed out. (b) Entropy. (c) Change count. Interpolated starting model boundaries appear as faint black lines.

SW

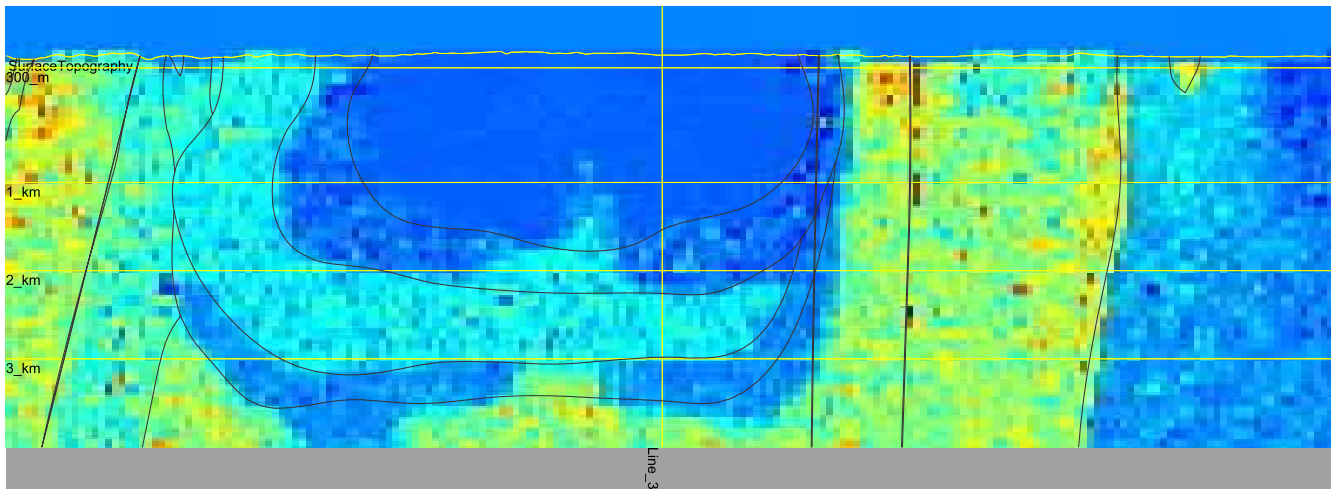
NE



(a)

SW

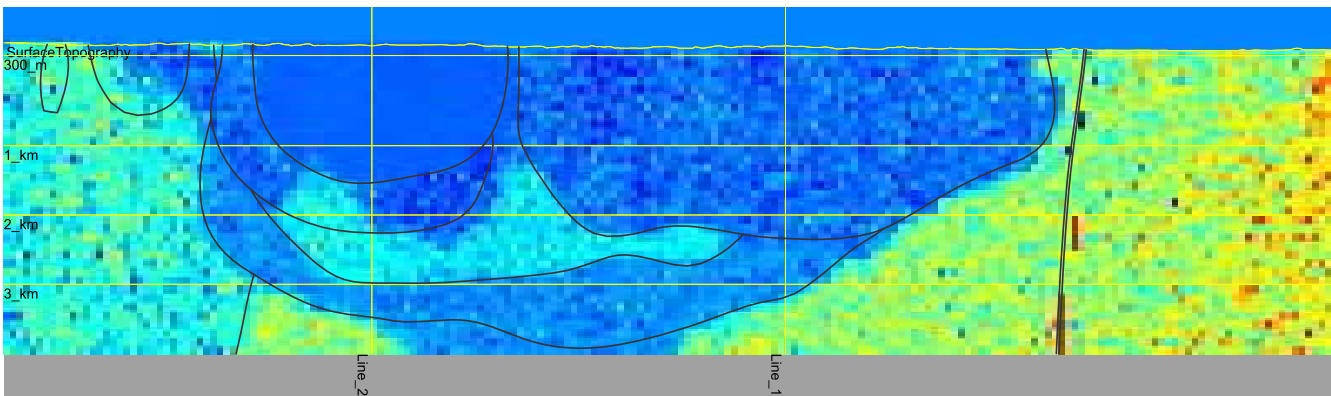
NE



(b)

SE

NW



(c)

(g/cc)

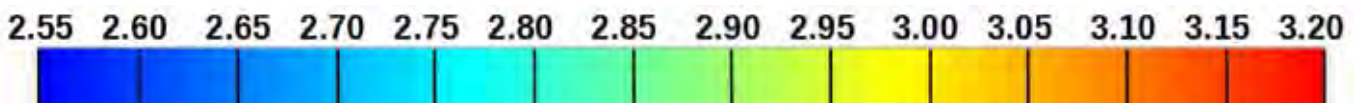
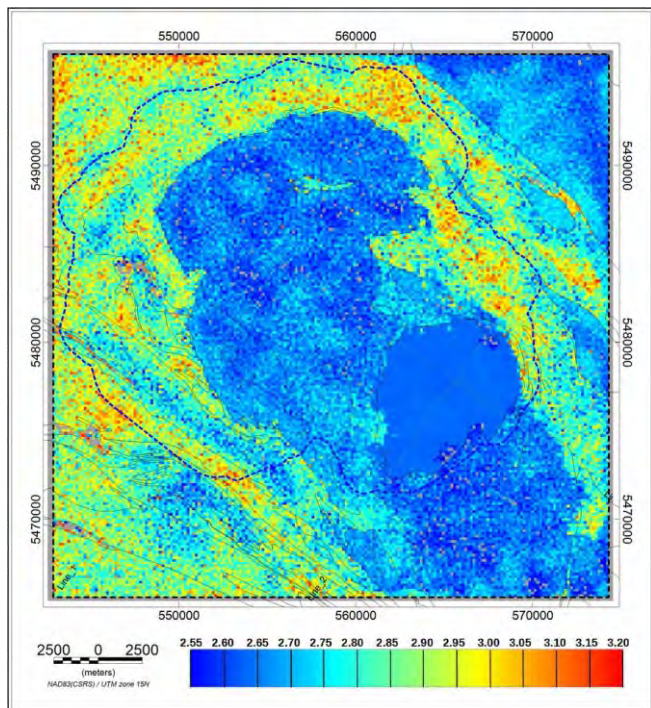
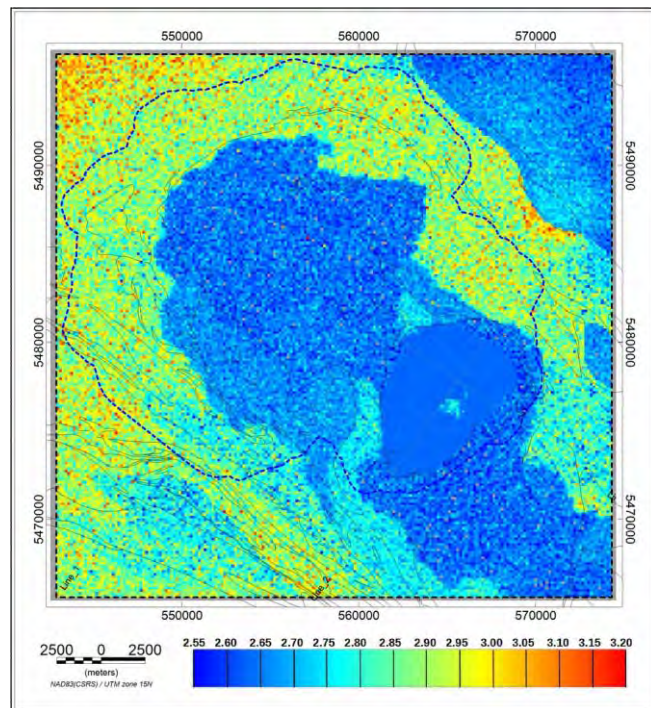


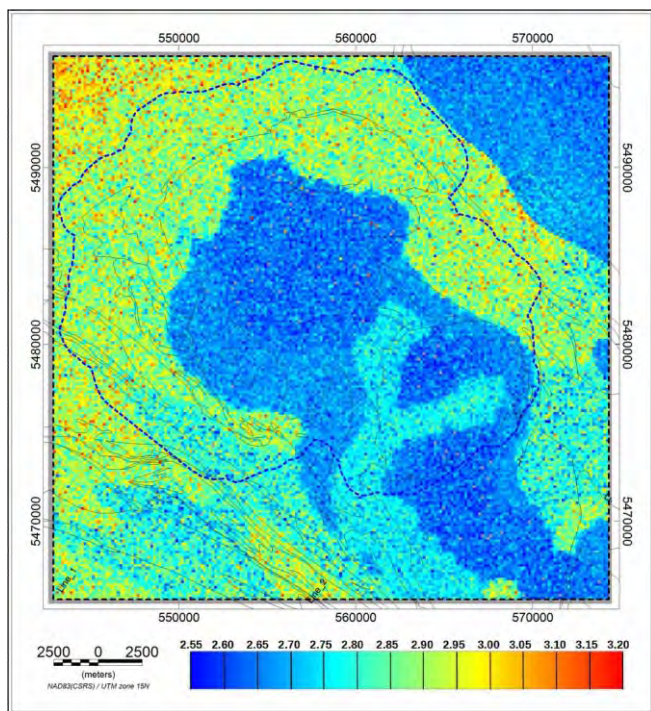
Figure 5.15 Gravity only moderate constraint inversion density distribution results along (a) Line 1 (b) Line 2 (c) Line 3. Interpolated starting model boundaries and features appear as faint black lines on all images.



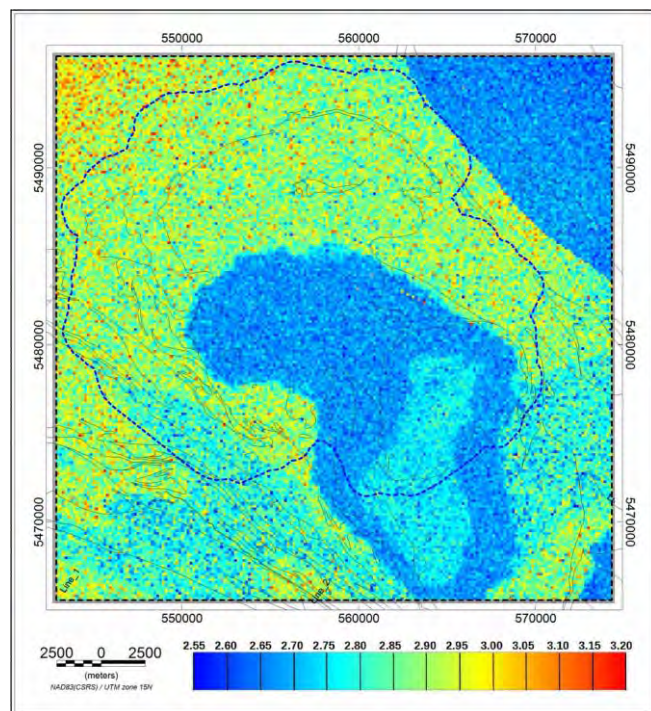
(a)



(b)



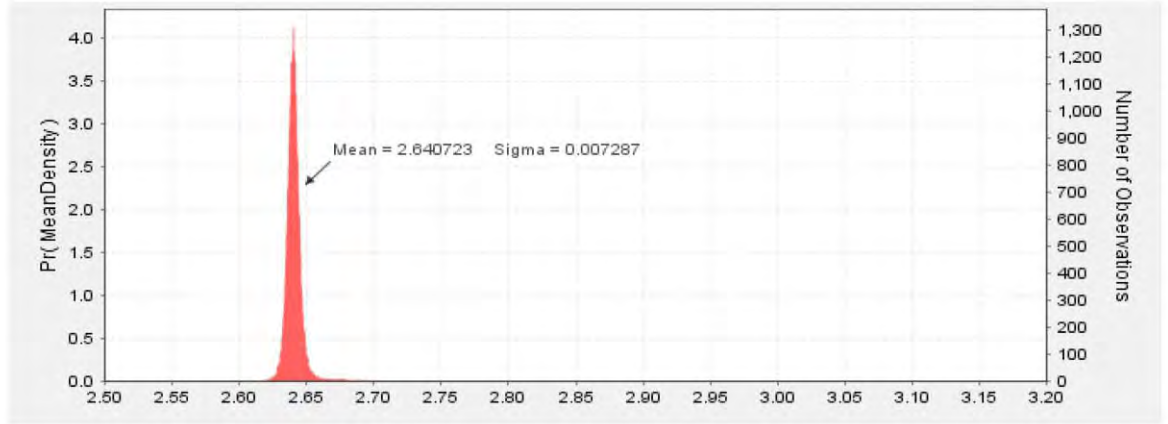
(c)



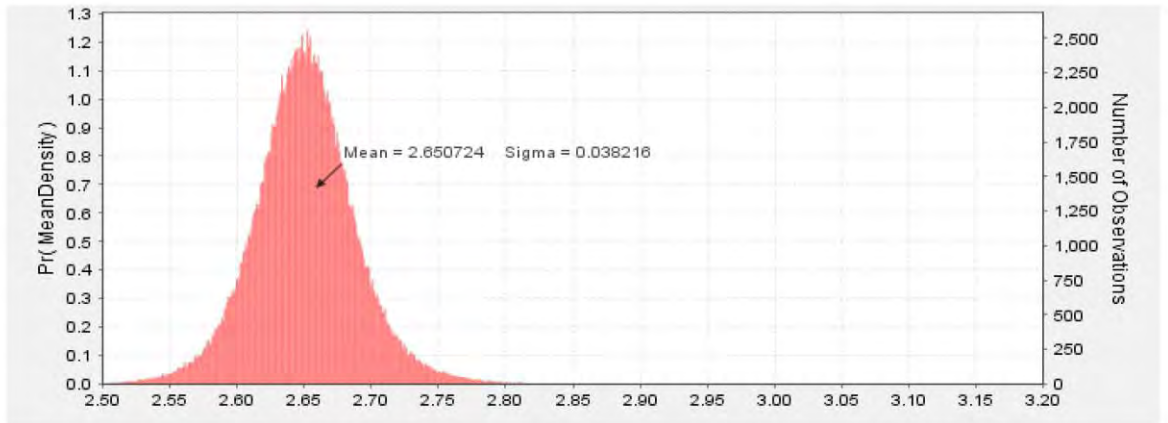
(d)

Figure 5.16 Gravity only moderate constraint inversion density distribution results on depth slices at (a) 300 m above MSL (b) 1 km below MSL (c) 2 km below MSL (d) 3 km below MSL. All densities are in g/cc. The dashed blue line marks the LiDAR coverage.

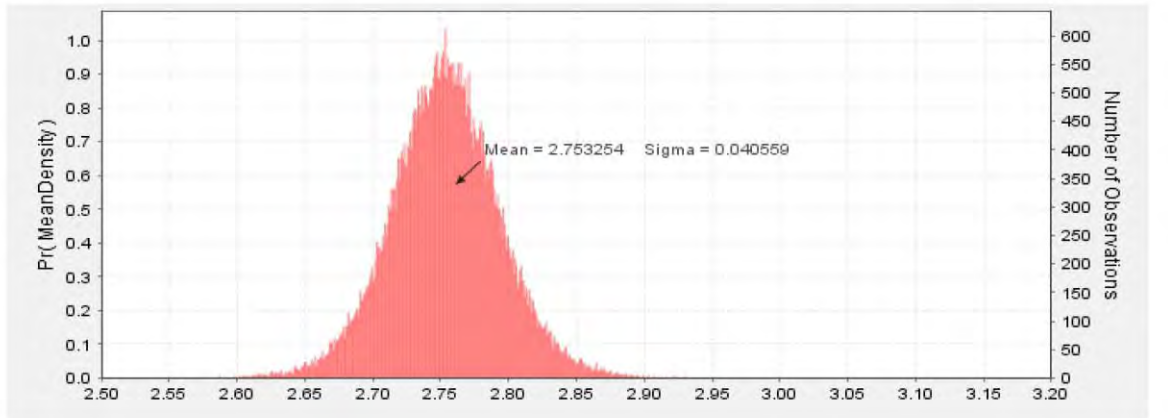
(a) Feldspar Megacryst
Granite
Mean = 2.640723
Std deviation = 0.007287
Minimum = 2.58746
Maximum = 2.78213



(b) Biotite granite to
granodiorite
Mean = 2.650724
Std deviation = 0.038216
Minimum = 2.414987
Maximum = 2.911117



(c) Hornblende tonalite to
granodiorite
Mean = 2.753254
Std deviation = 0.040559
Minimum = 2.533708
Maximum = 2.9702



(d) Biotite tonalite to
granodiorite
Mean = 2.684975
Std deviation = 0.031159
Minimum = 2.511703
Maximum = 2.895023

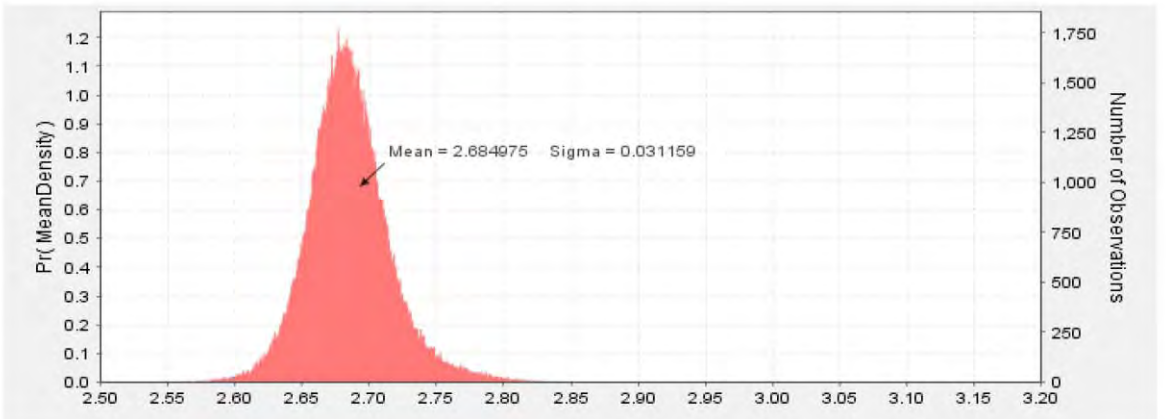
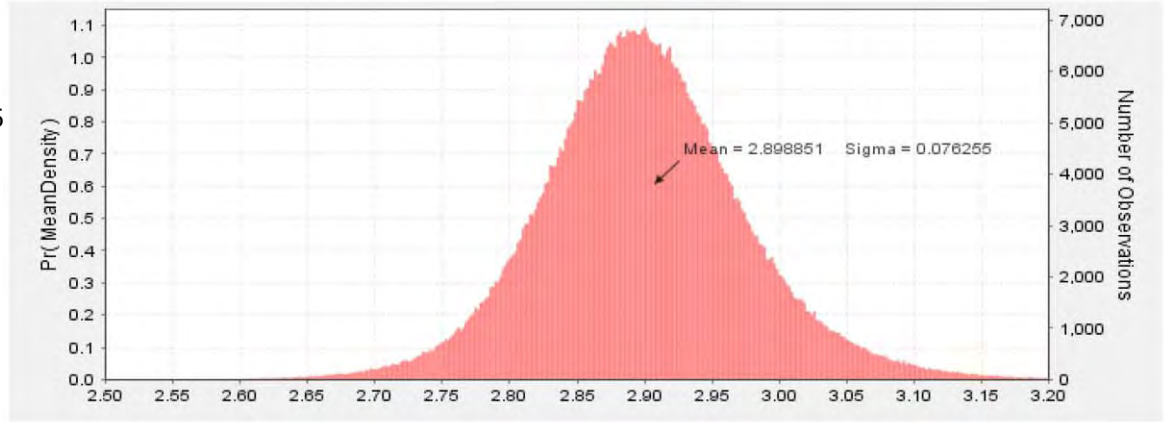


Figure 5.17 Histograms of mean model densities of the Revell batholith units from gravity only moderate constraint inversion.

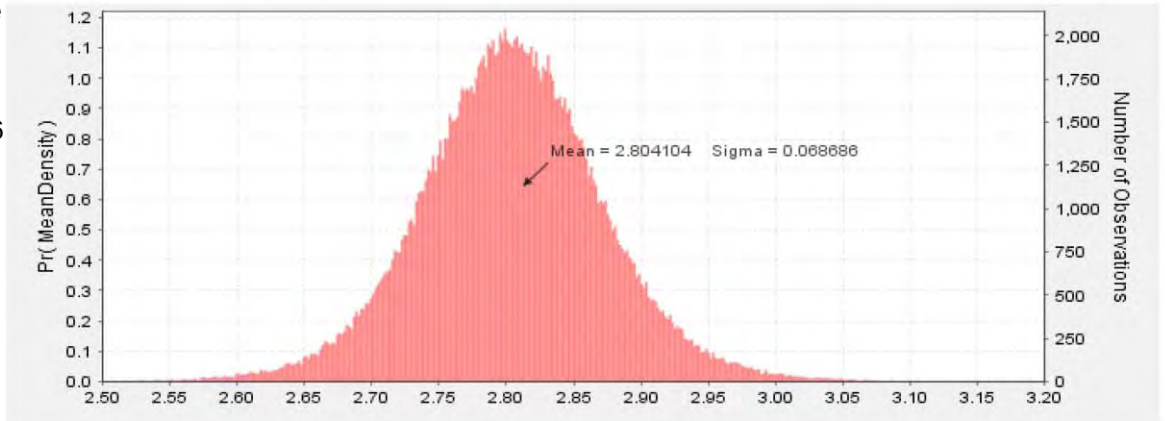
(a) Mafic metavolcanics

Mean = 2.898851
 Std deviation = 0.076255
 Minimum = 2.429798
 Maximum = 3.350546



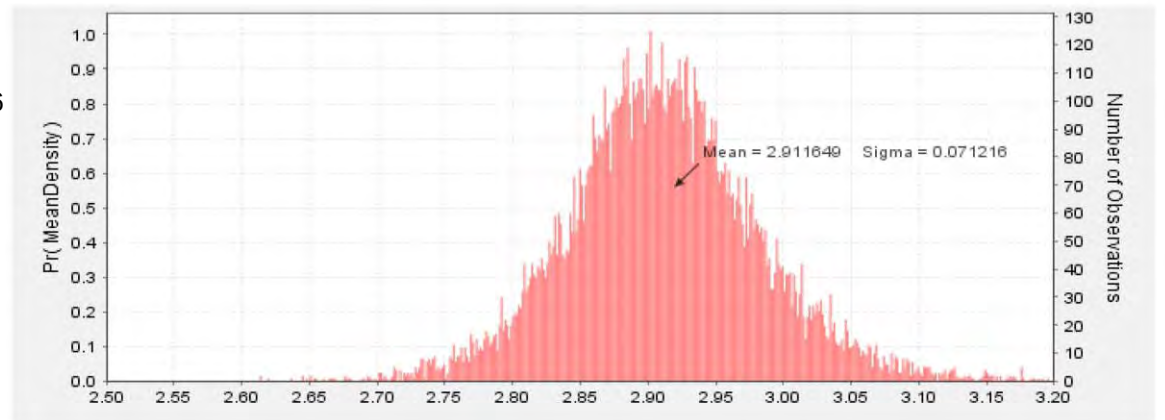
(b) Felsic to intermediate metavolcanics

Mean = 2.804104
 Std deviation = 0.068686
 Minimum = 2.363693
 Maximum = 3.25063



(c) Metasedimentary to Metavolcanics

Mean = 2.911649
 Std deviation = 0.071216
 Minimum = 2.614004
 Maximum = 3.318454



(d) Metasedimentary

Mean = 2.782759
 Std deviation = 0.074107
 Minimum = 2.409491
 Maximum = 3.177759

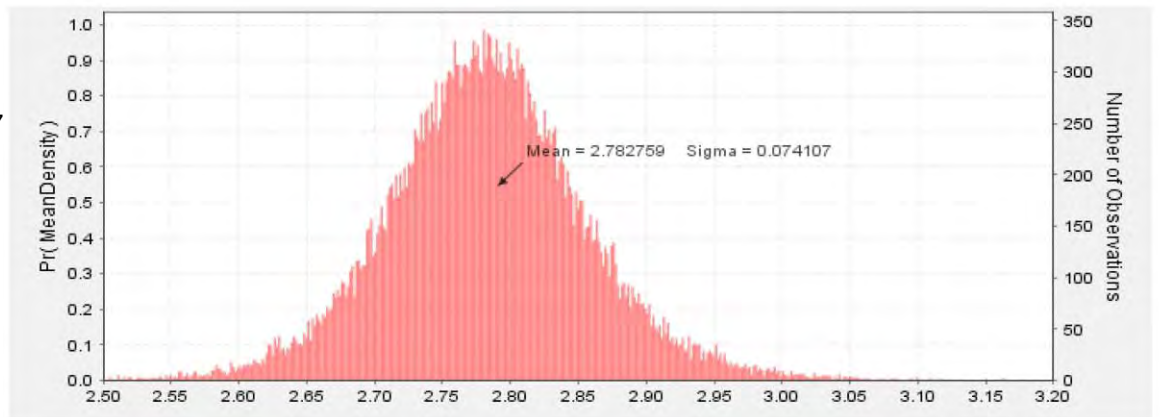
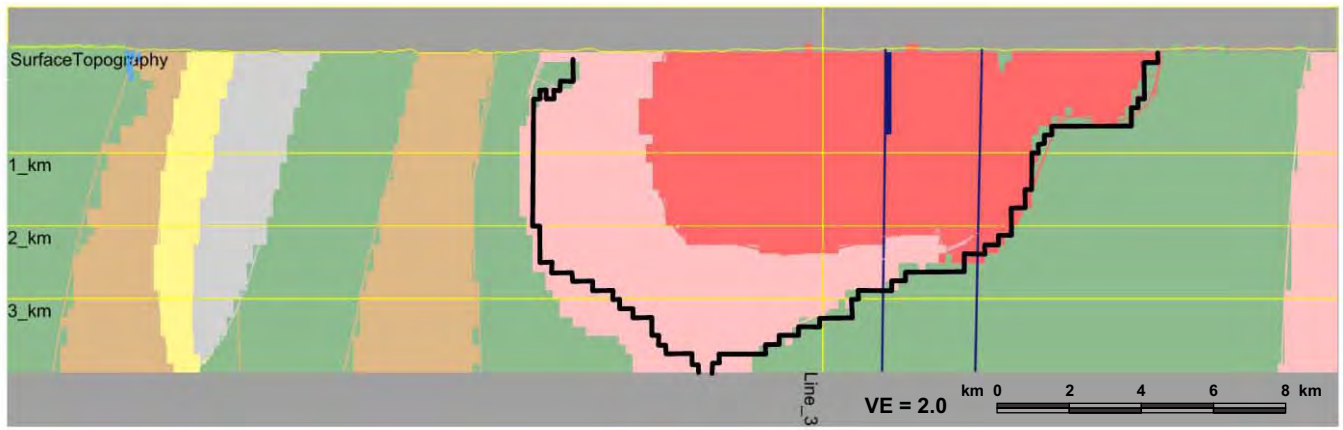
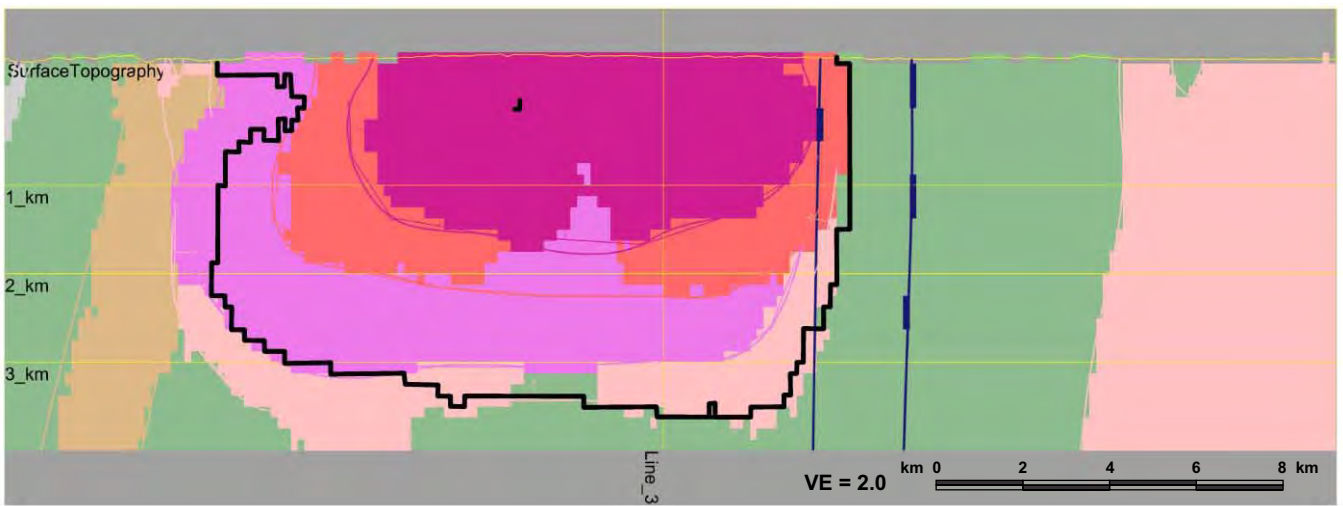


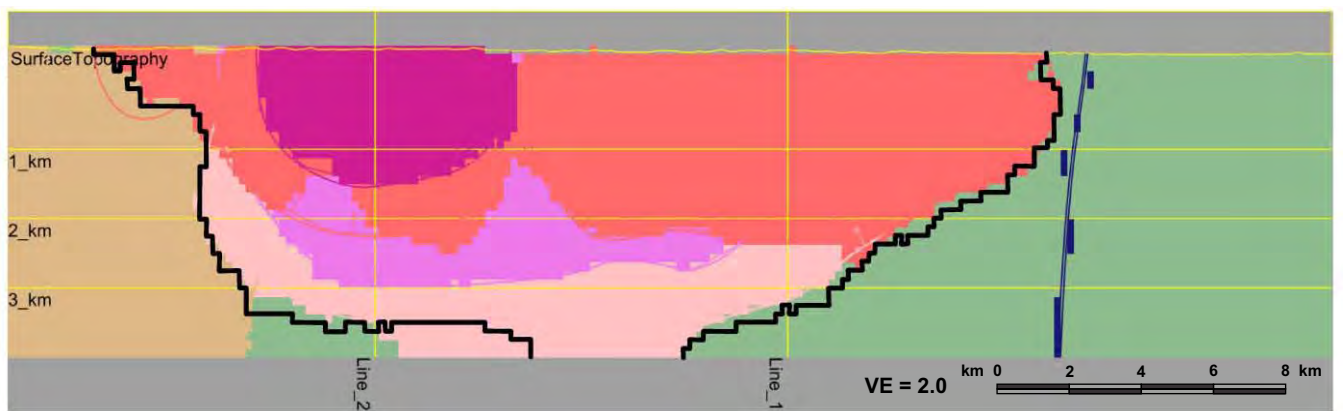
Figure 5.18 Histograms of mean model densities of greenstone and other units surrounding the Revell batholith from gravity only moderate constraint inversion.



(a)

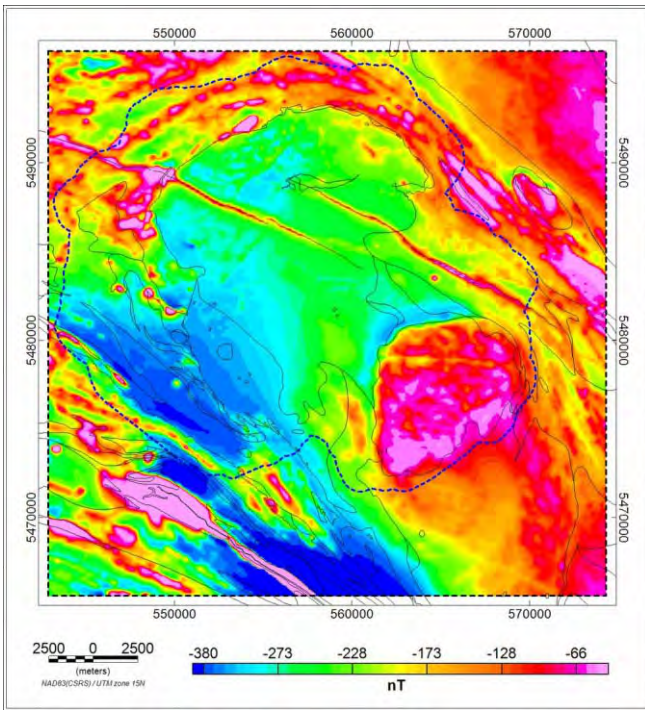


(b)

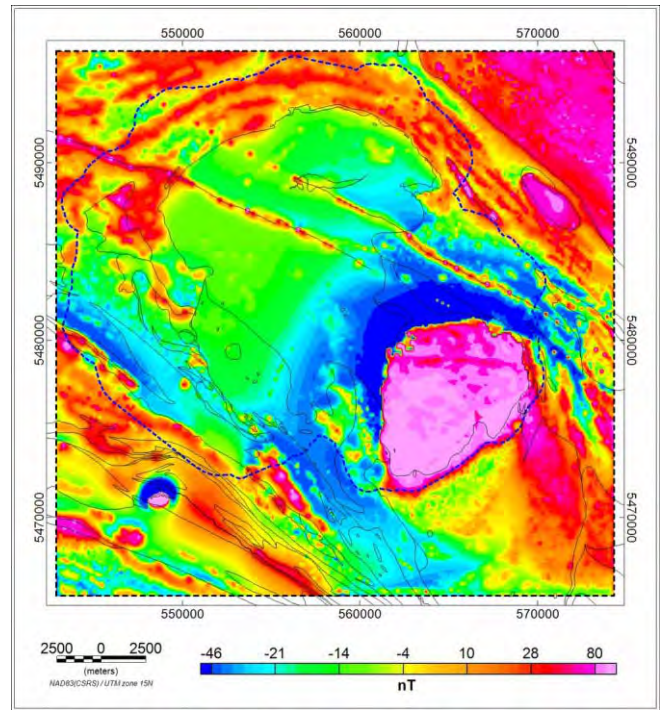


(c)

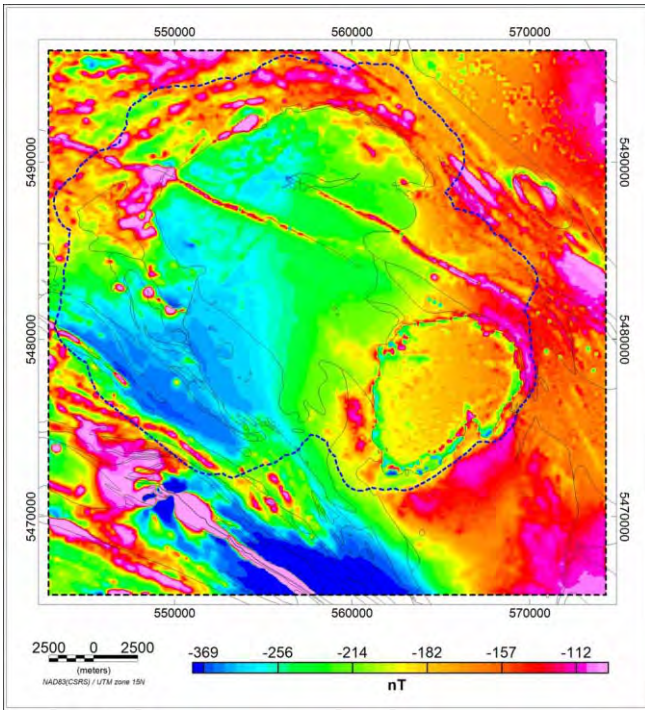
Figure 5.19 Boundary of batholith from a single density (2.65 g/cc) gravity only moderate constraint inversion overlain in black on gravity only moderate constraint inversion. (a) Line 1 (b) Line 2 (c) Line 3



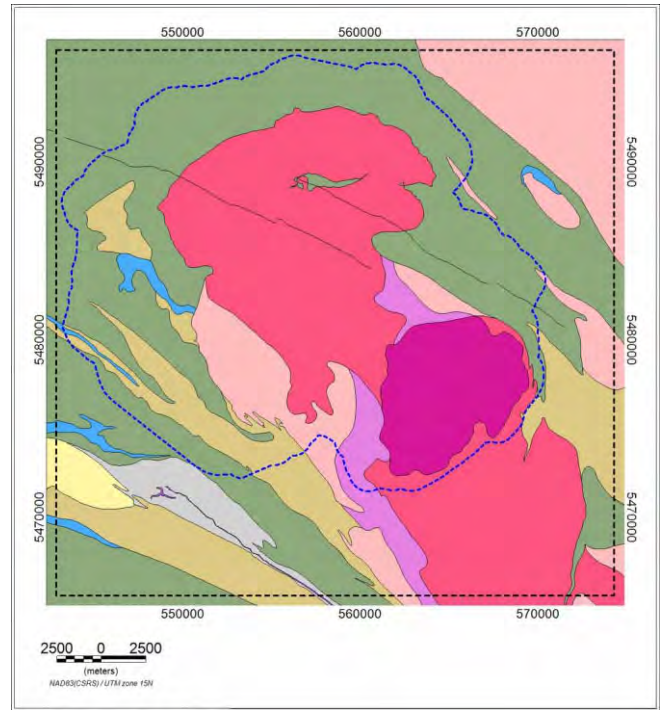
(a)



(b)

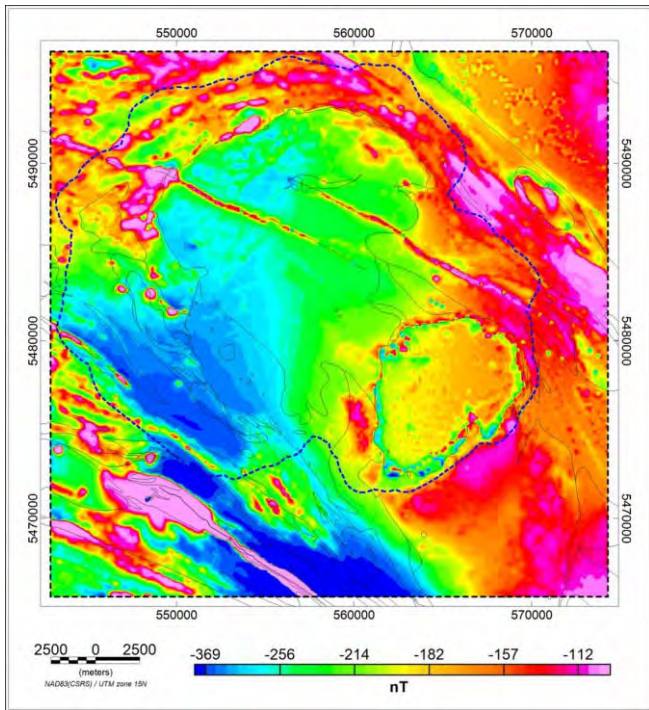


(c)

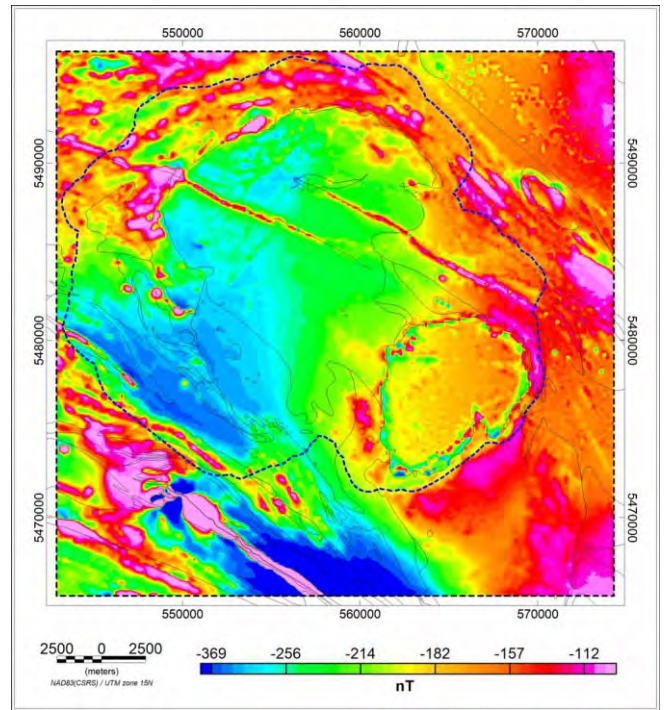


(d)

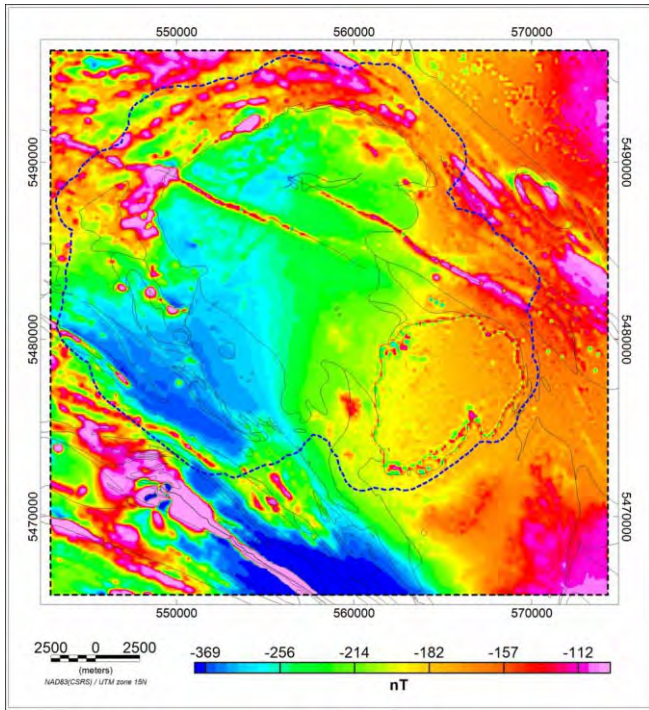
Figure 5.20 Comparison of observed magnetic anomaly with predicted anomaly from magnetic only inversion results with moderate constraint. (a) observed magnetic anomaly (b) calculated magnetic anomaly (c) observed minus calculated magnetic anomaly (d) simplified bedrock geology. The dashed blue line marks the LiDAR coverage.



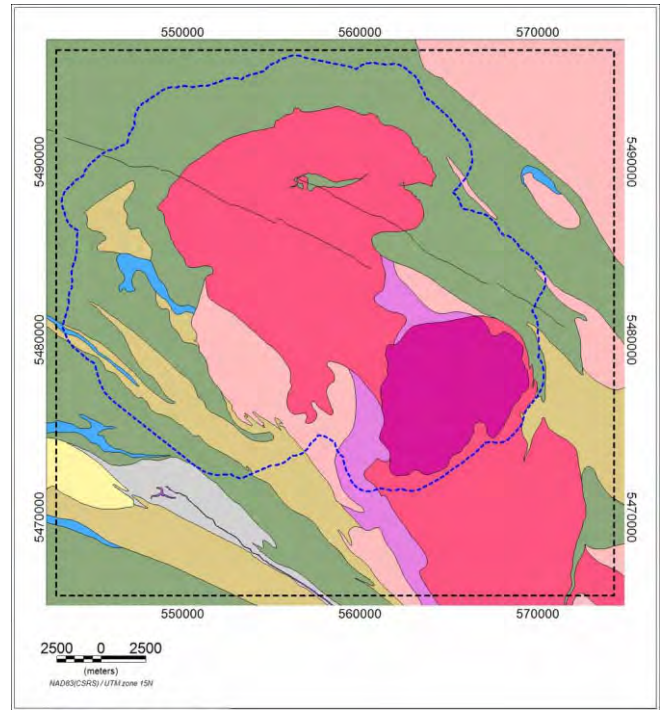
(a)



(b)

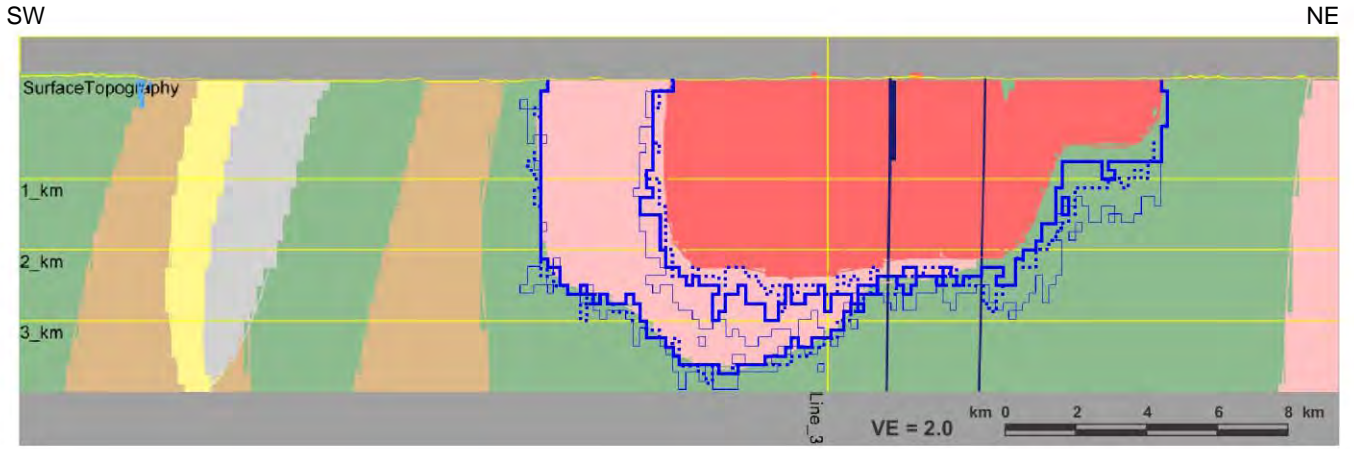


(c)

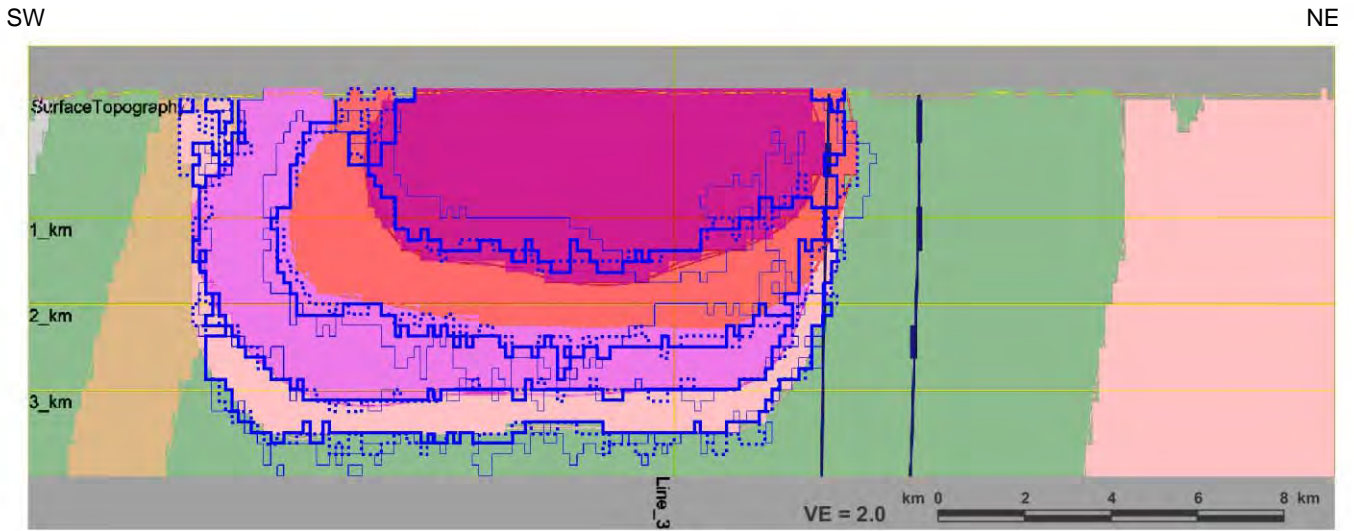


(d)

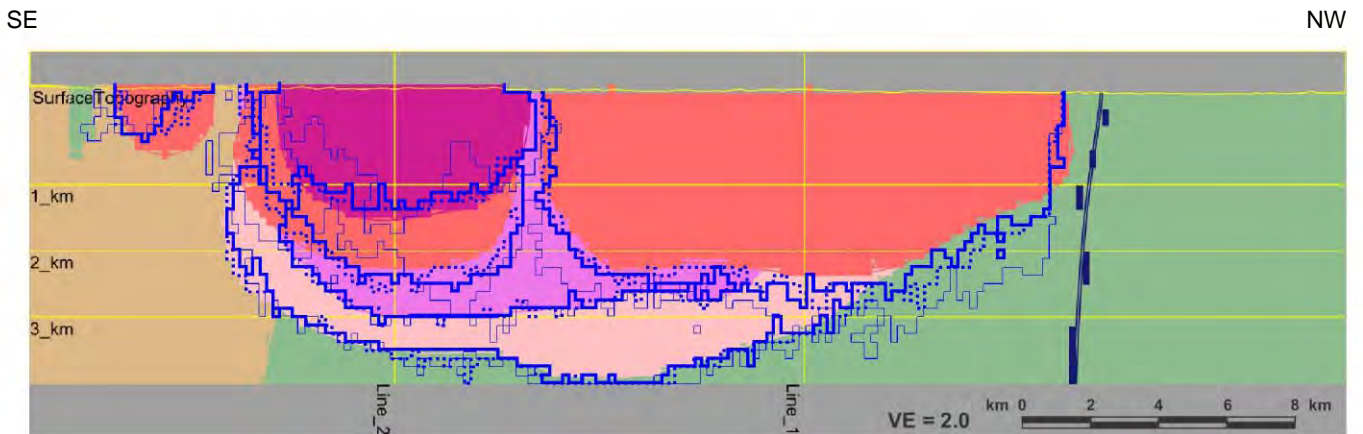
Figure 5.21 Magnetic only inversion residuals. (a) tight constraint (b) moderate constraint (c) loose constraint (d) simplified bedrock geology. The dashed blue line marks the LiDAR coverage.



(a)

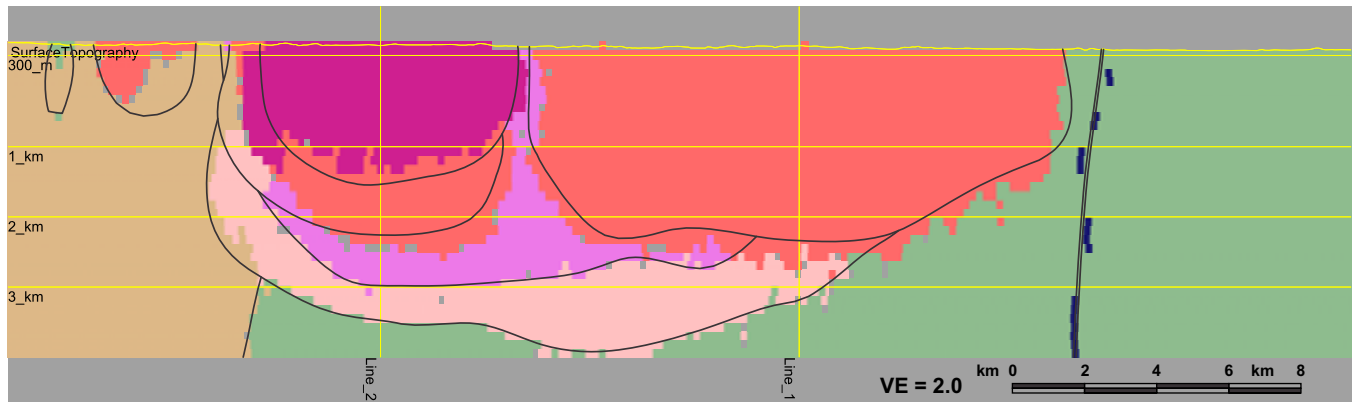


(b)

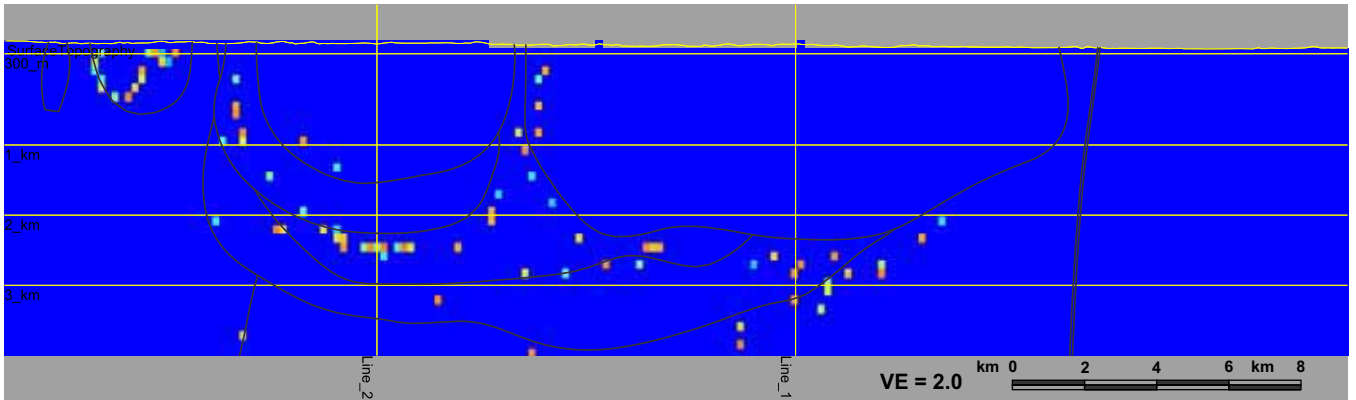


(c)

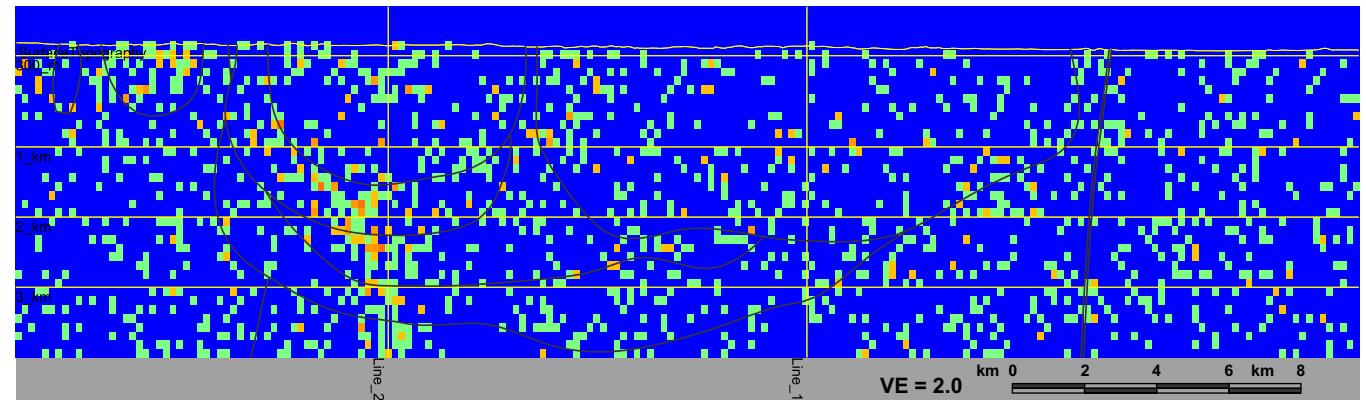
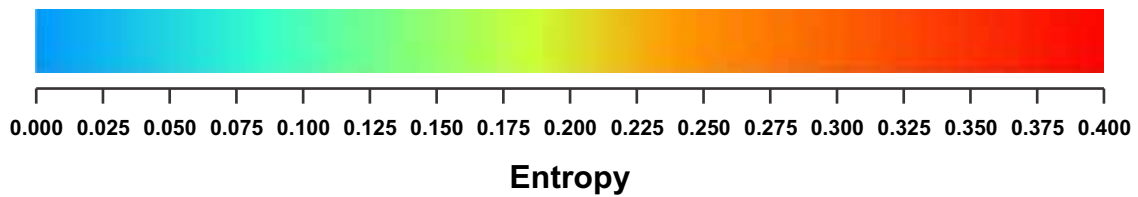
Figure 5.22 Magnetic only inversion results along (a) Line 1 (b) Line 2 (c) Line 3. The coloured image in the background is the starting model. Dotted blue lines are for inversion with very tight constraint, solid lines with moderate constraint and faint lines for loose constraints.



(a)



(b)



(c)

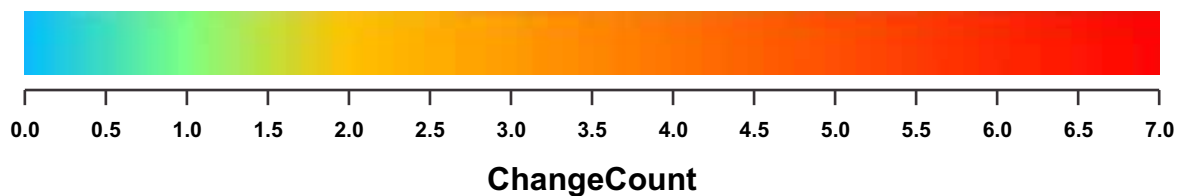
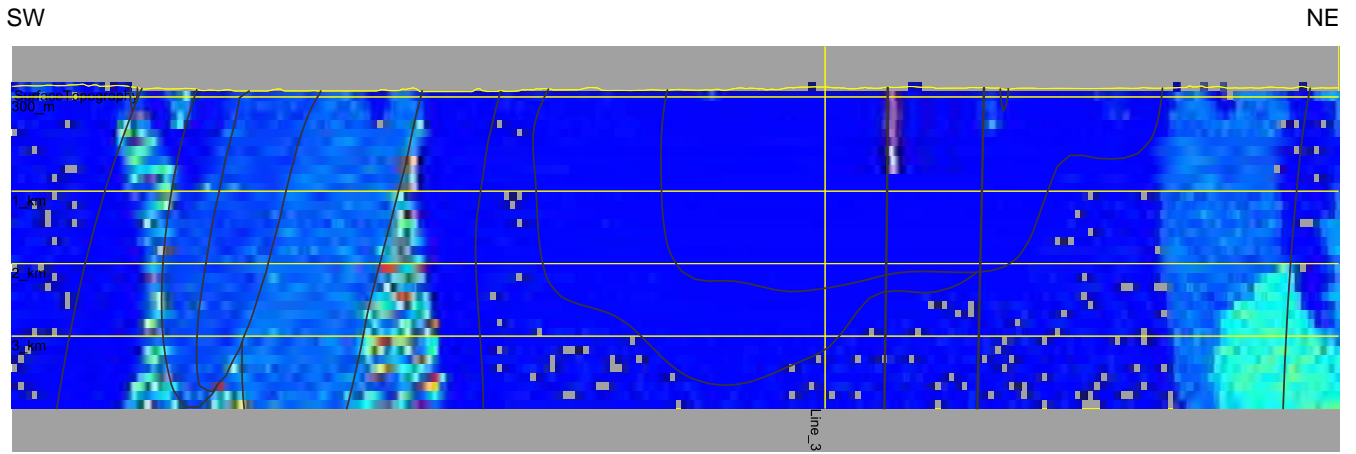
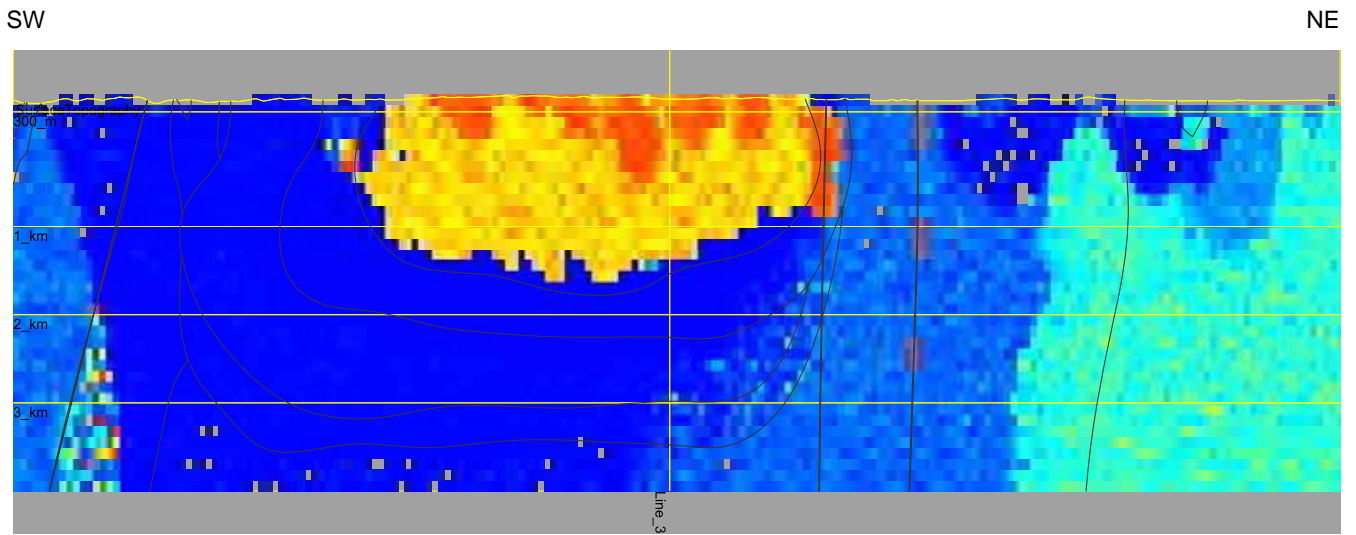


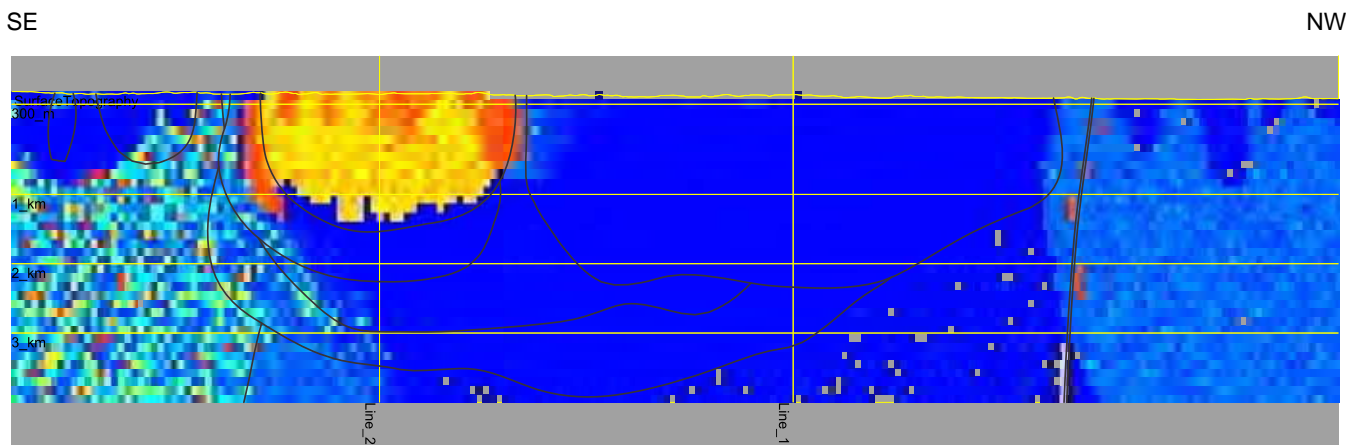
Figure 5.23 Magnetic only moderate constraint inversion results statistics along Line 3. (a) 90% thresholded model units. Pixels below 90% threshold level are grayed out. (b) entropy (c) change count. Interpolated starting model boundaries appear as faint black lines.



(a)



(b)



(c)

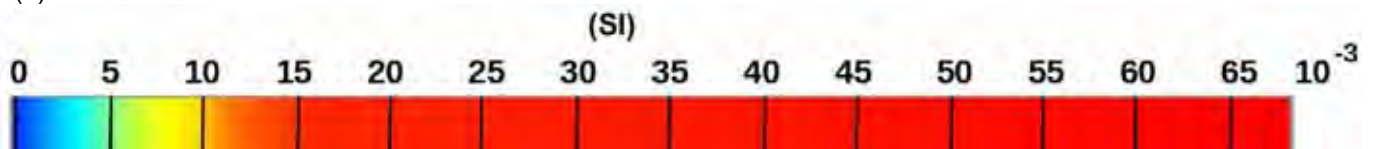
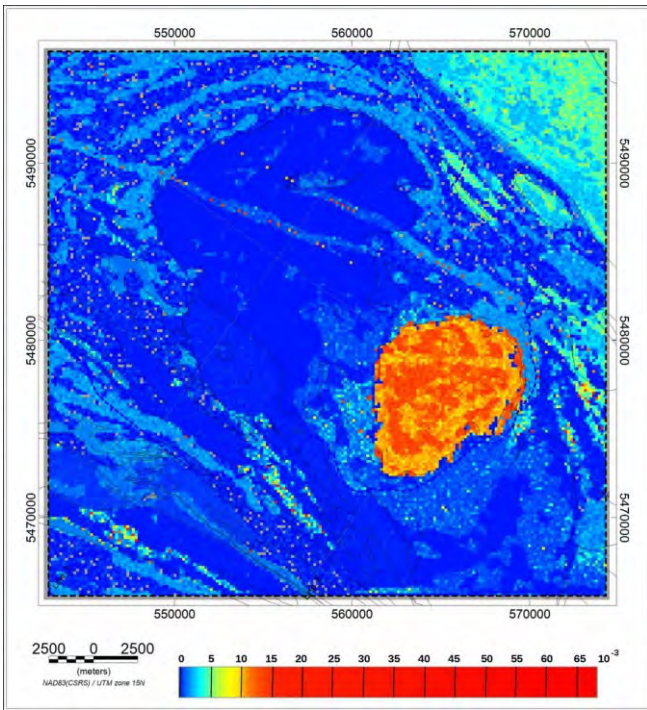
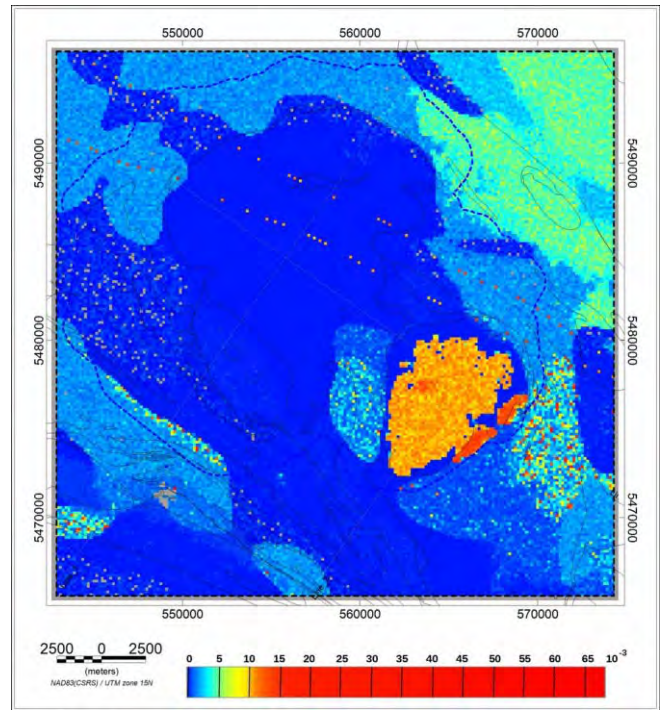


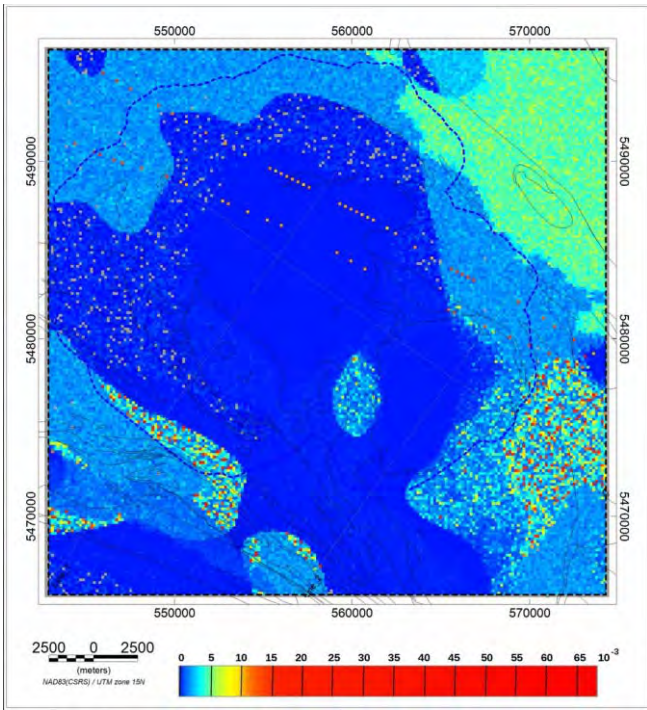
Figure 5.24 Magnetic only moderate constraint inversion susceptibility variations along (a) Line 1 (b) Line 2 (c) Line 3. Interpolated starting model boundaries and features appear as faint black lines on all images.



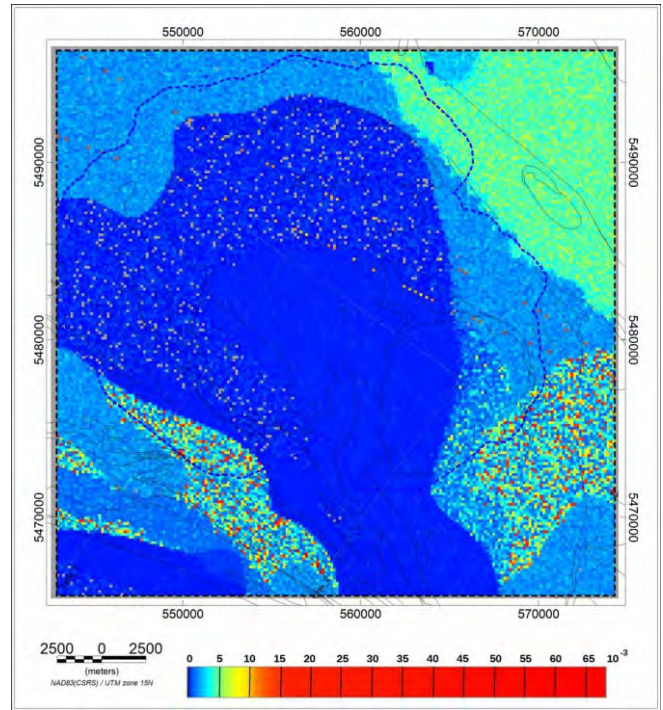
(a)



(b)



(c)

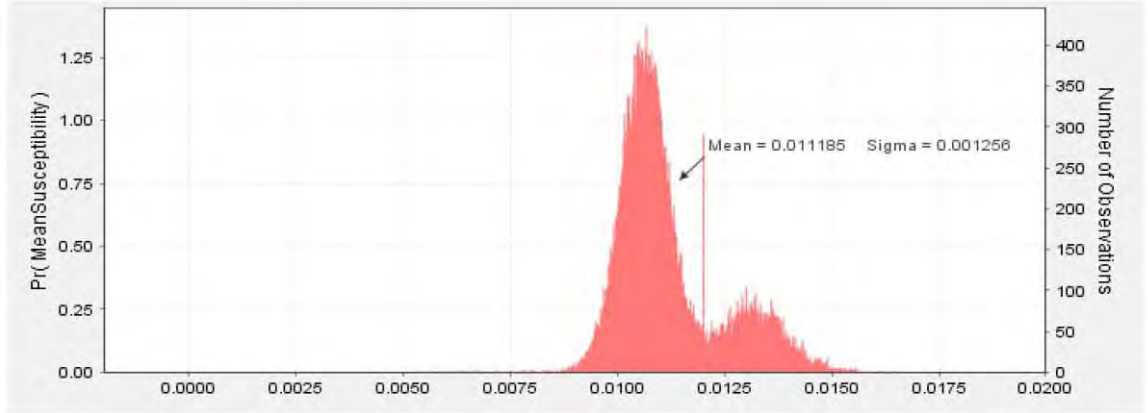


(d)

Figure 5.25 Magnetic only moderate constraint inversion magnetic susceptibility distribution results on depth slices at (a) 300 m above MSL (b) 1 km below MSL (c) 2 km below MSL (d) 3 km below MSL. Magnetic susceptibilities are in SI units. The dashed blue line marks the LiDAR coverage.

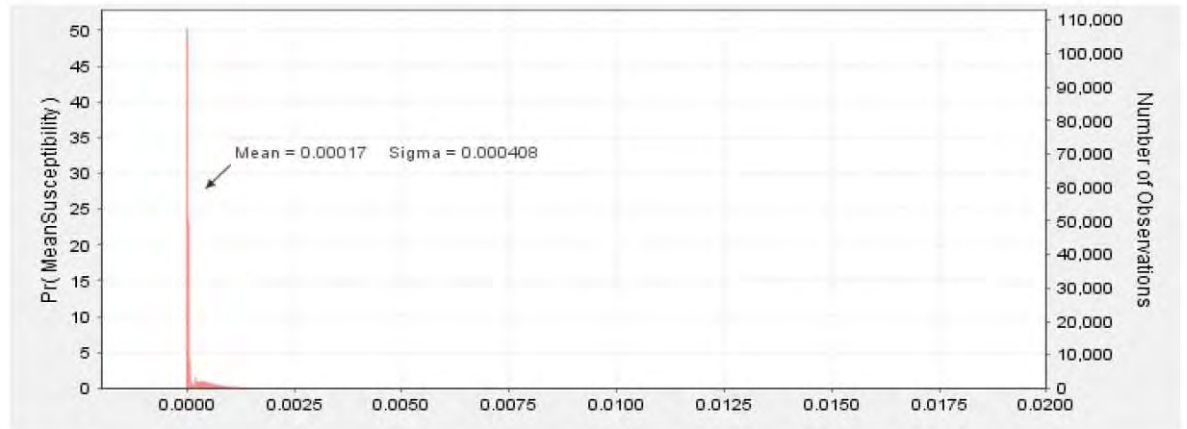
(a) Feldspar Megacryst Granite

Mean = 0.011185
 Stddeviation = 0.001256
 Minimum = 0.00509
 Maximum = 0.016735



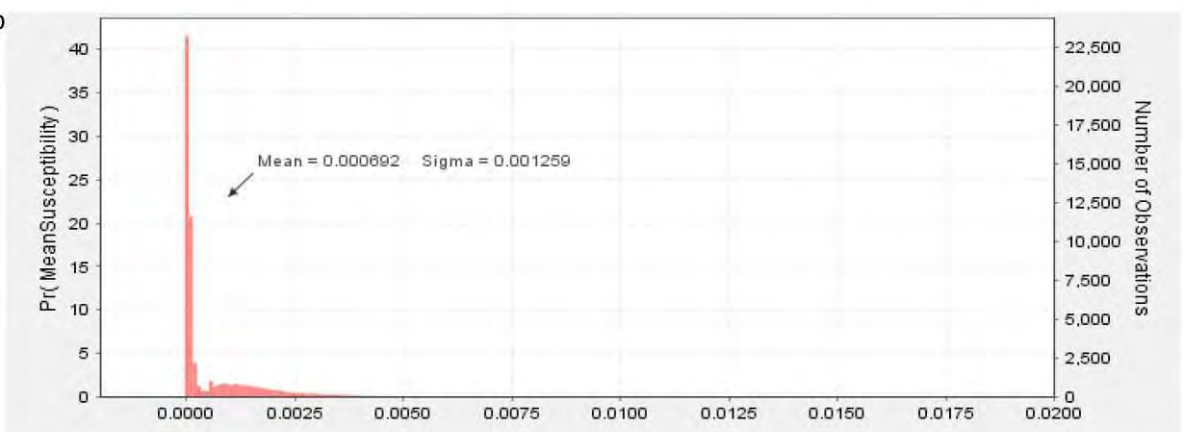
(b) Biotite granite to granodiorite

Mean = 0.00017
 Stddeviation = 0.000408
 Minimum = -0.000233
 Maximum = 0.016185



(c) Hornblende tonalite to granodiorite

Mean = 0.000692
 Stddeviation = 0.001259
 Minimum = 0.000002
 Maximum = 0.04604



(d) Biotite tonalite to granodiorite

Mean = 0.000479
 Stddeviation = 0.001053
 Minimum = -0.000087
 Maximum = 0.024768

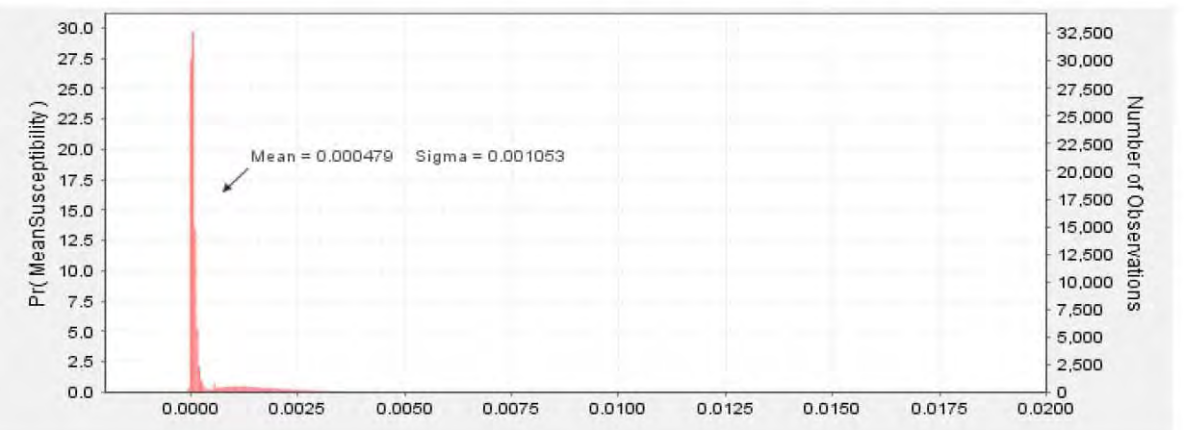
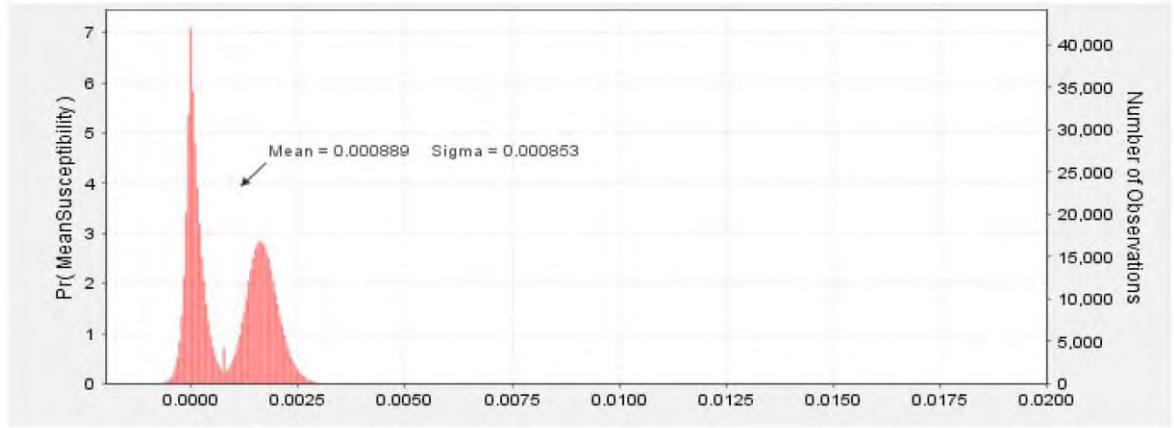


Figure 5.26: Histograms of mean model magnetic susceptibilities of the Revell batholith units from magnetic only moderate constraint inversion.

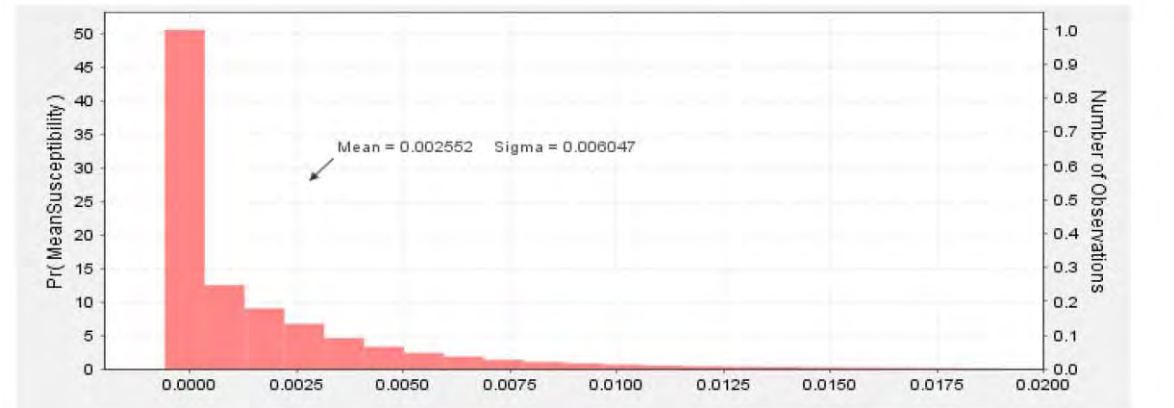
(a) Mafic metavolcanics

Mean= 0.000889
 Stddeviation=0.000853
 Minimum=-0.002145
 Maximum =0.023851



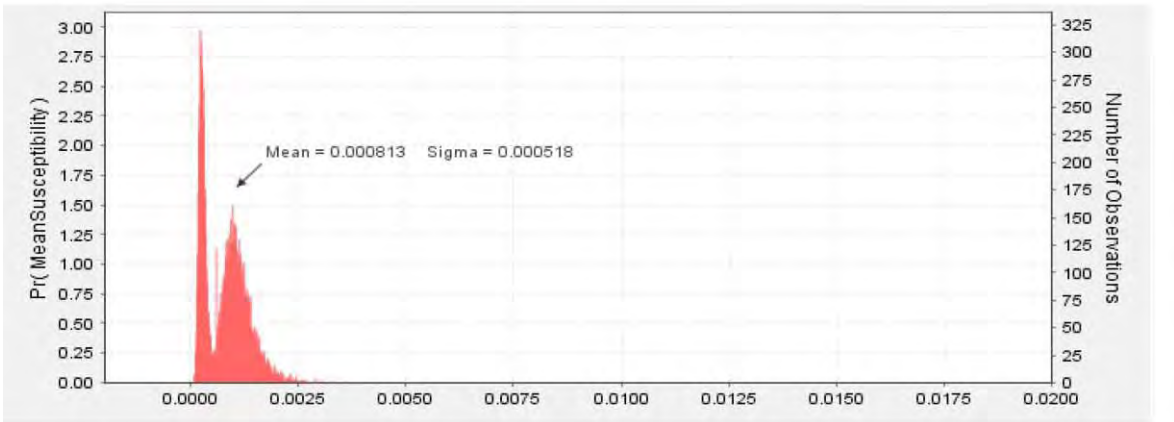
(b) Felsic to intermediate metavolcanics

Mean= 0.002552
 Stddeviation =0.006047
 Minimum=-0.000112
 Maximum =0.465454



(c) Metasedimentary to Metavolcanics

Mean =0.000813
 Stddeviation=0.000518
 Minimum=0.000078
 Maximum=0.007642



(d) Metasedimentary

Mean =0.001188
 Stddeviation=0.006732
 Minimum =0.000057
 Maximum= 0.247026

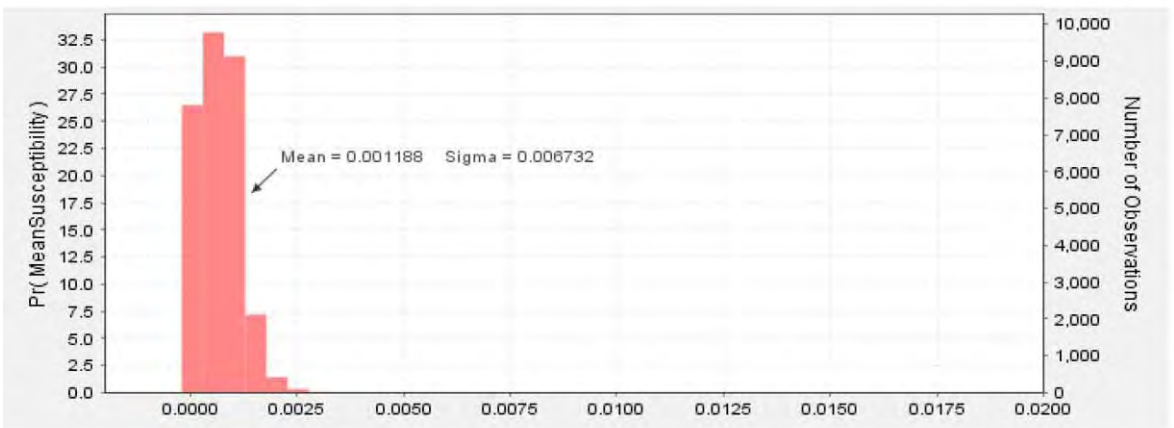
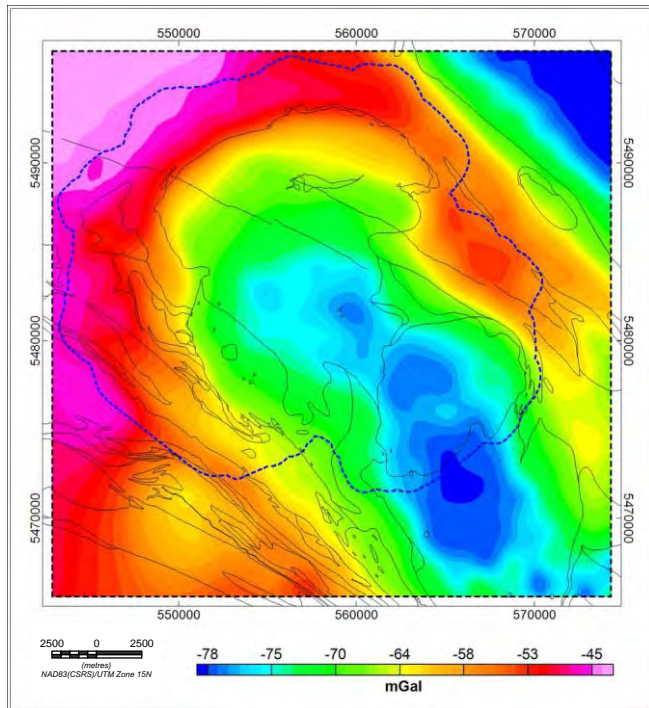
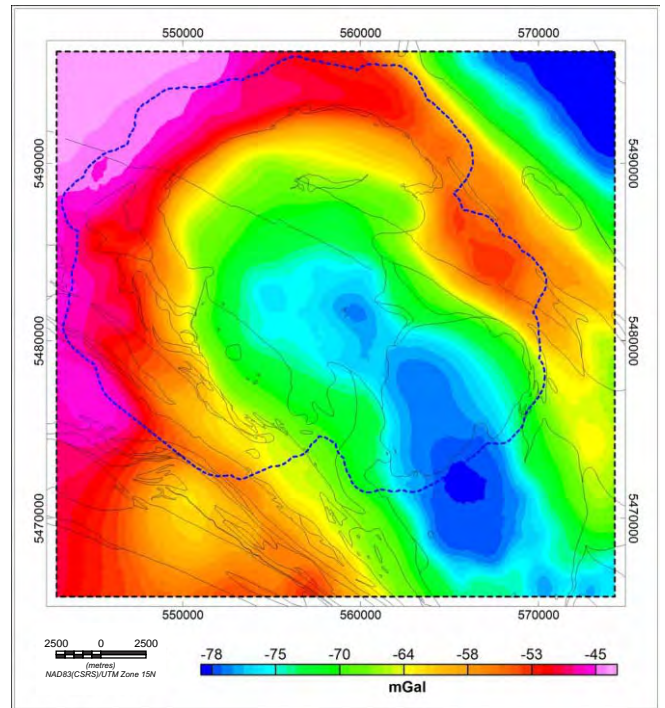


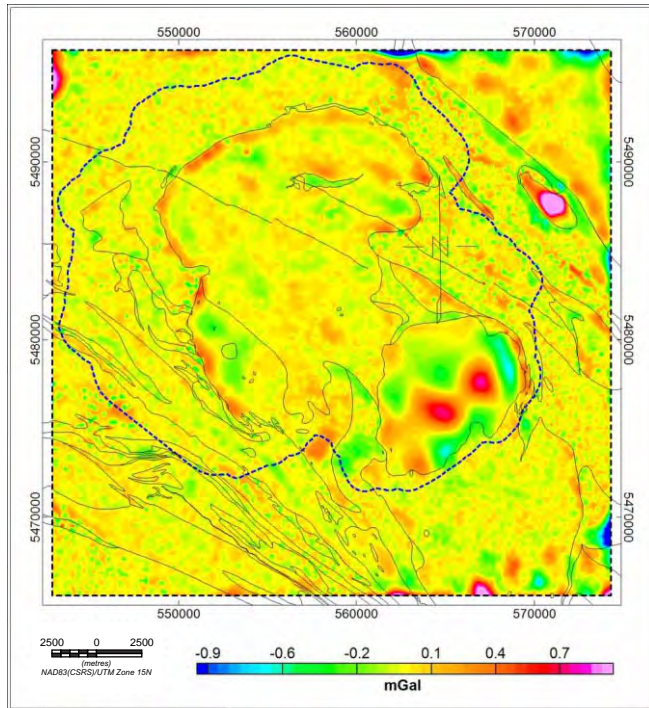
Figure 5.27: Histograms of mean model magnetic susceptibilities of greenstone and other units surrounding the Revell batholith from magnetic only moderate constraint inversion.



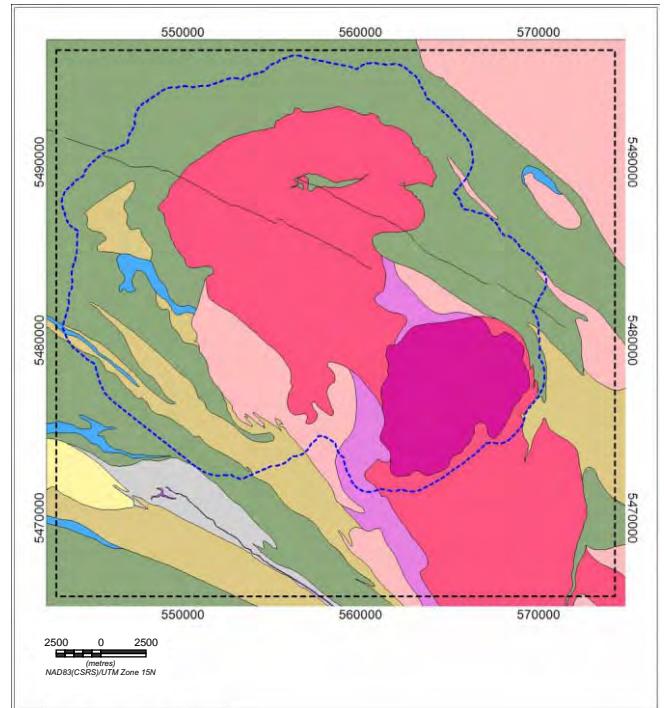
(a)



(b)

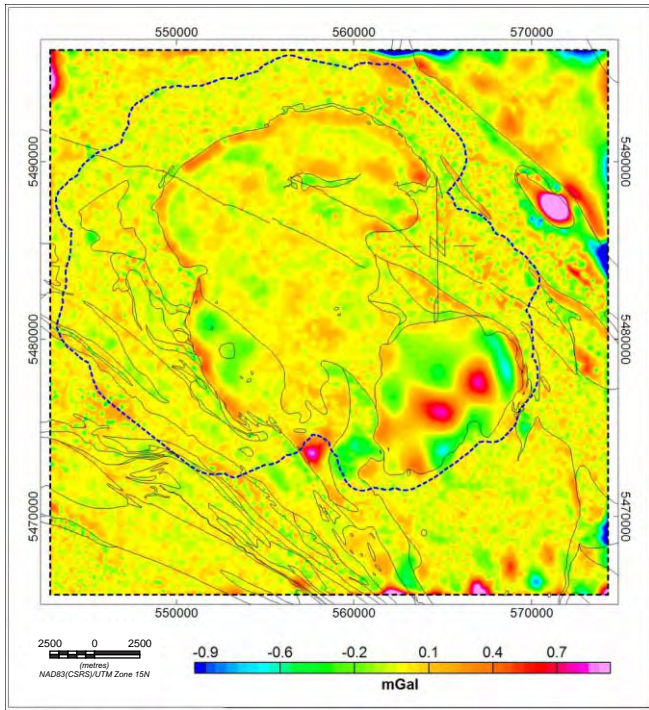


(c)

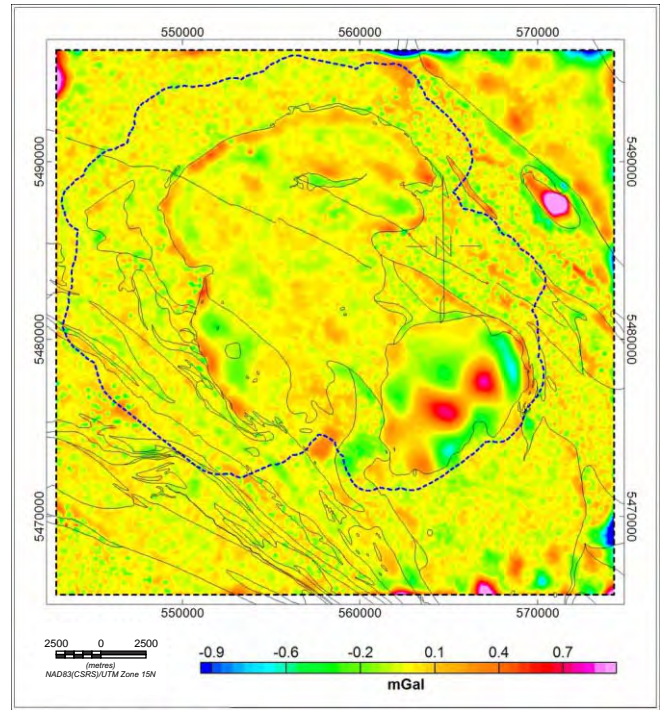


(d)

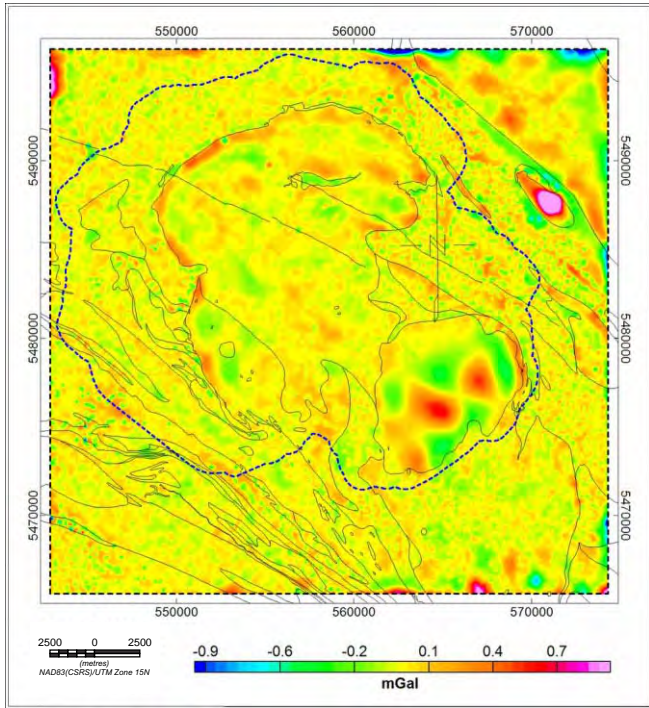
Figure 5.28 Comparison of observed gravity anomaly with predicted anomaly from joint gravity and magnetic inversion with moderate constraint. (a) observed Bouguer gravity (b) calculated Bouguer gravity (c) observed minus calculated gravity (d) simplified bedrock geology. The dashed blue line marks the LiDAR coverage.



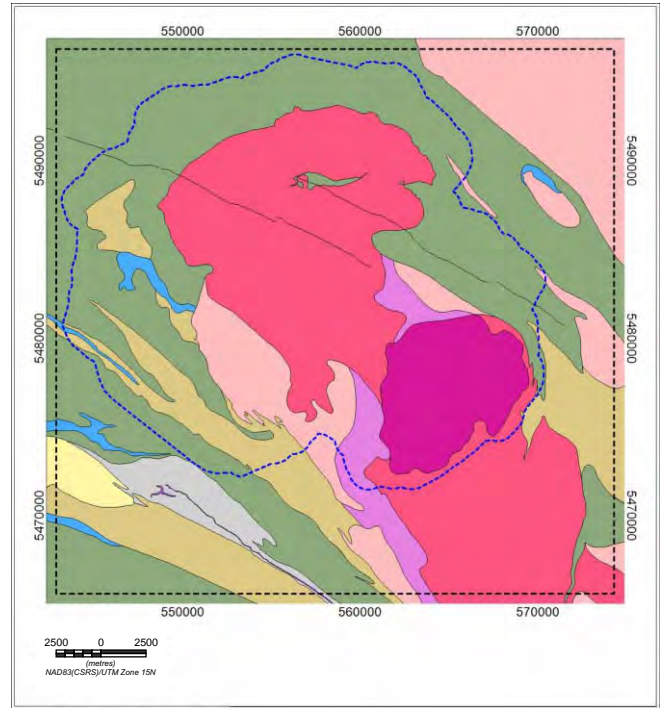
(a)



(b)

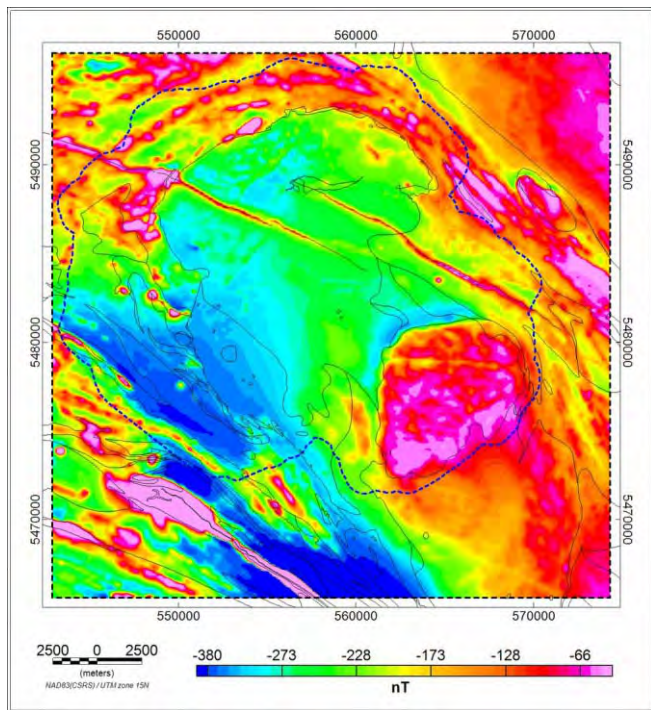


(c)

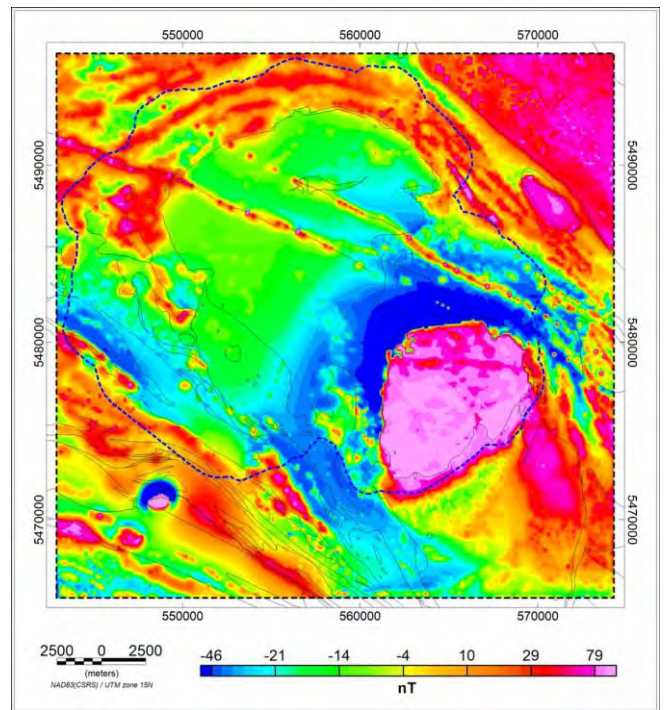


(d)

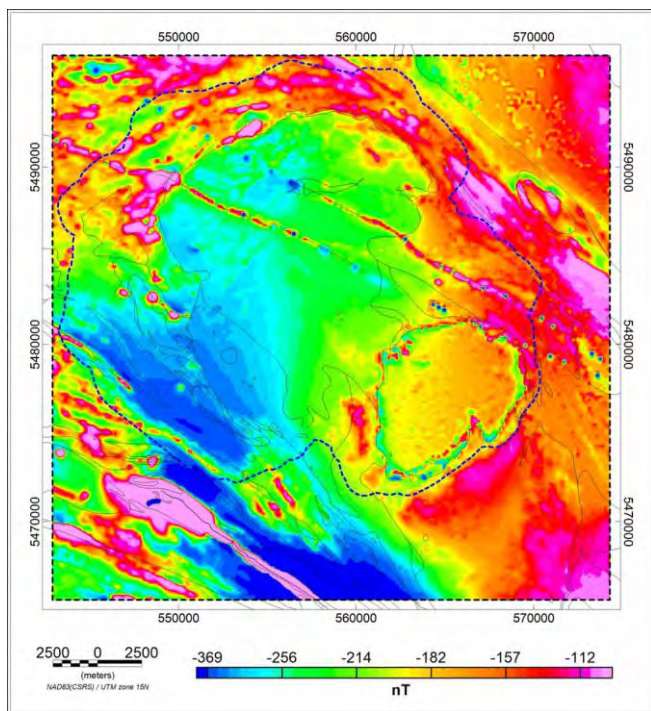
Figure 5.29 Joint gravity and magnetic inversion gravity residuals. (a) tight constraint (b) moderate constraint (c) loose constraint (d) simplified bedrock geology. The dashed blue line marks the LiDAR coverage.



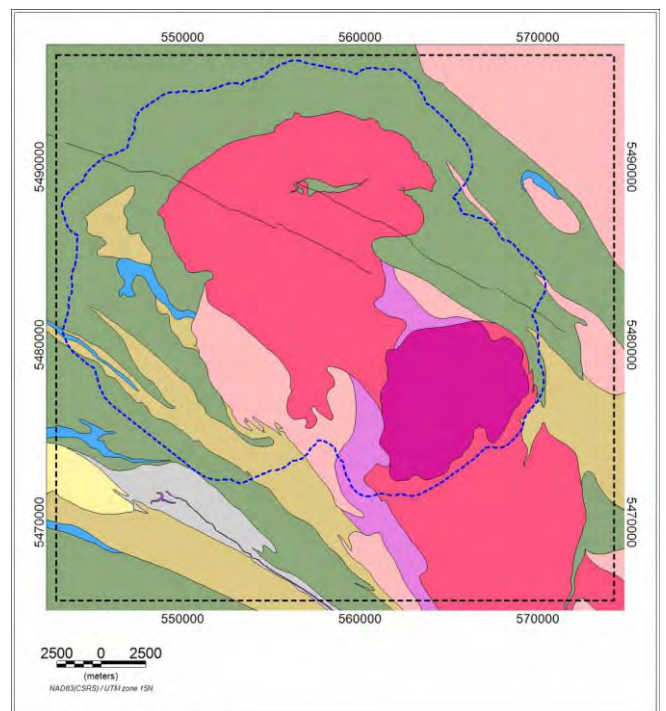
(a)



(b)

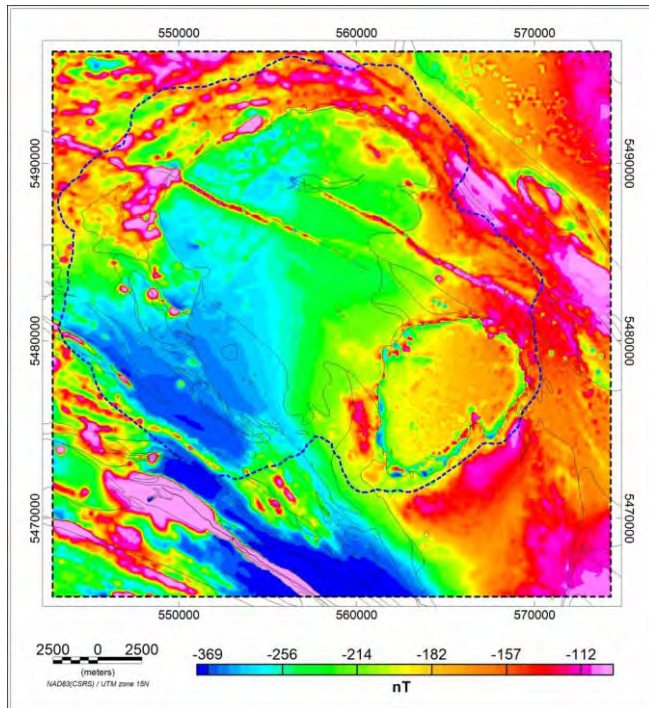


(c)

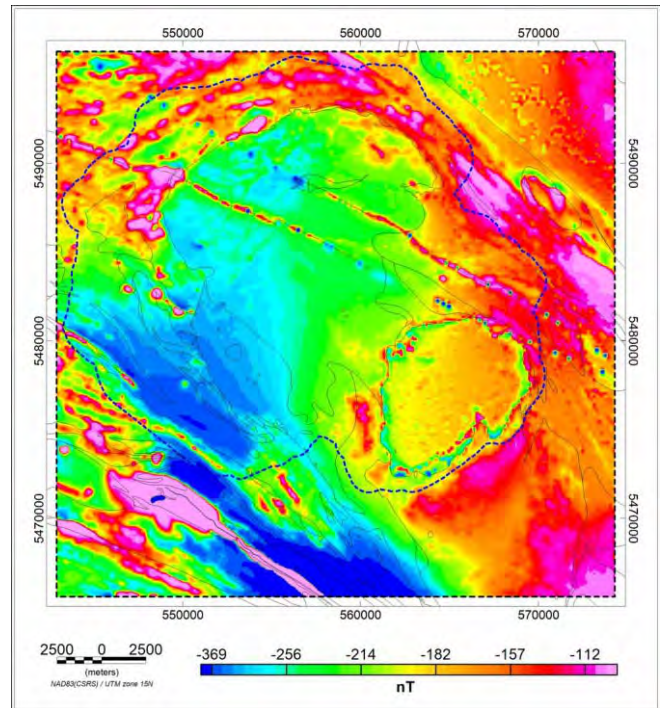


(d)

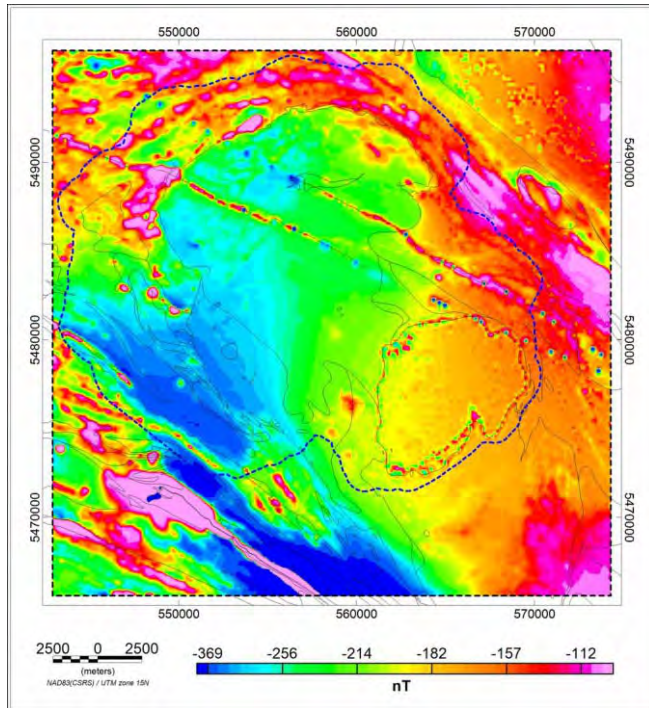
Figure 5.30 Comparison of observed magnetic anomaly with predicted anomaly from joint gravity and magnetic inversion results with moderate constraint. (a) observed magnetic anomaly (b) calculated magnetic anomaly (c) observed minus calculated magnetic anomaly (d) simplified bedrock geology. The dashed blue line marks the LiDAR coverage.



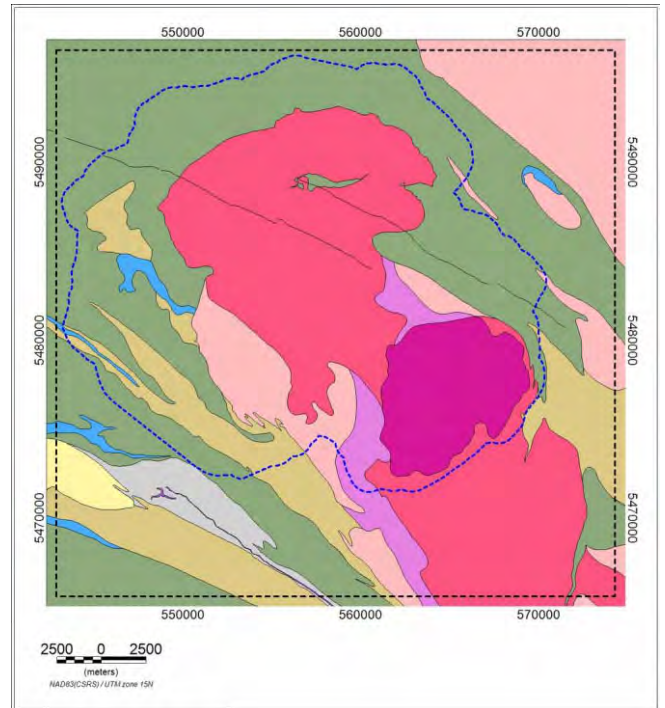
(a)



(b)

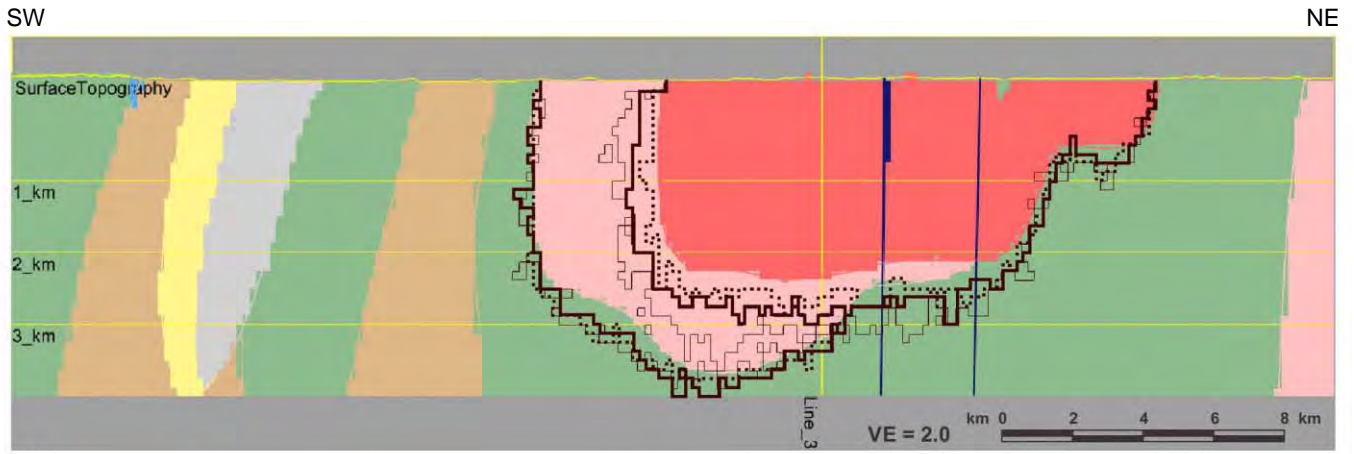


(c)

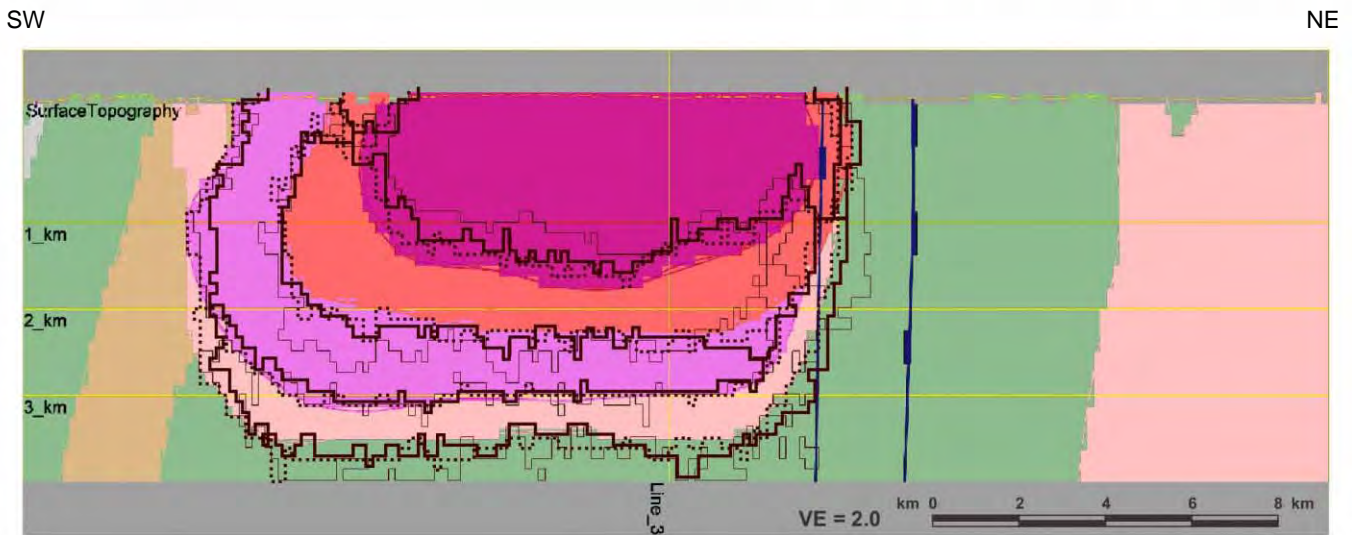


(d)

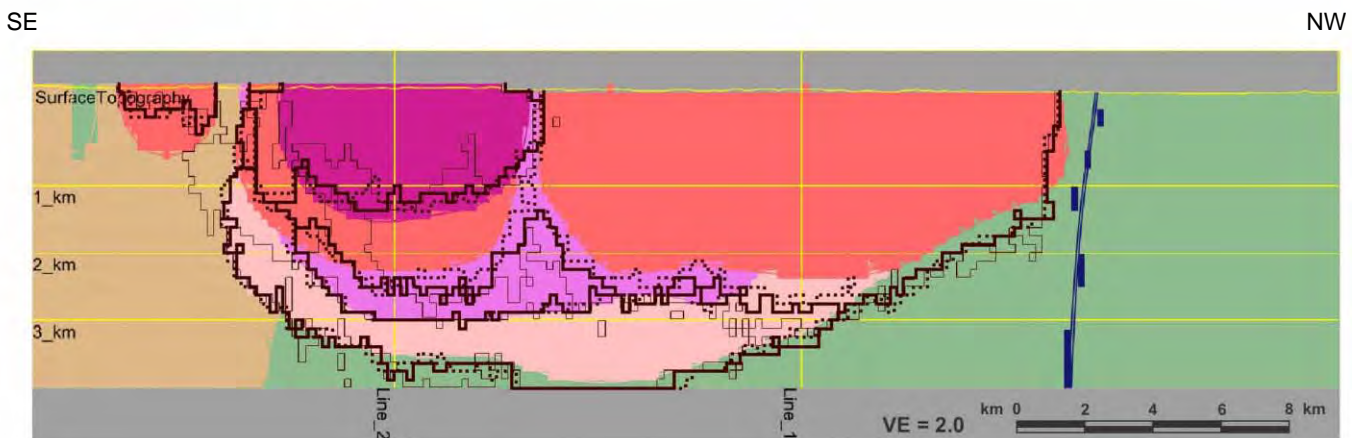
Figure 5.31 Joint gravity and magnetic inversion magnetic misfits, observed minus calculated fields. (a) tight constraint (b) moderate constraint (c) loose constraint (d) simplified bedrock geology. The dashed blue line marks the LiDAR coverage.



(a)

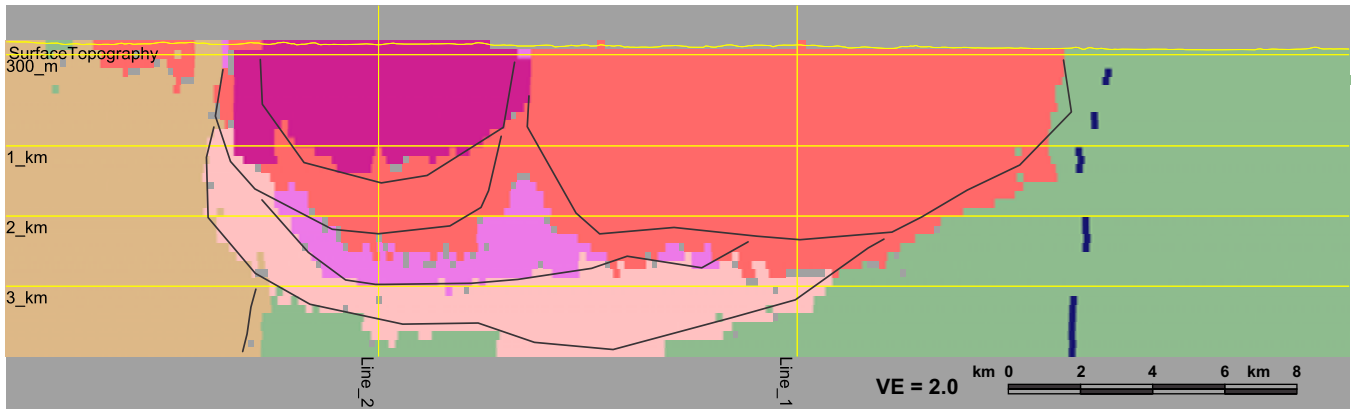


(b)

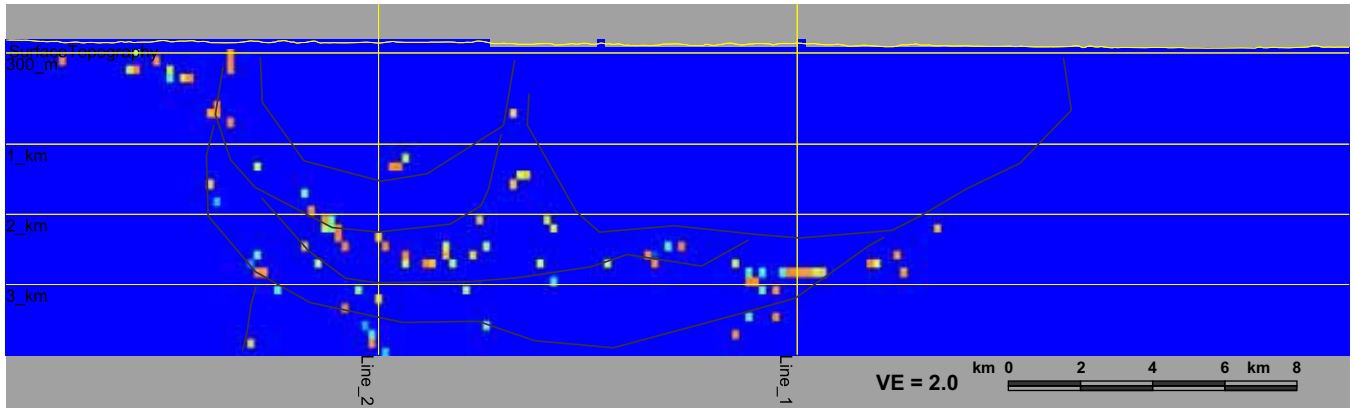


(c)

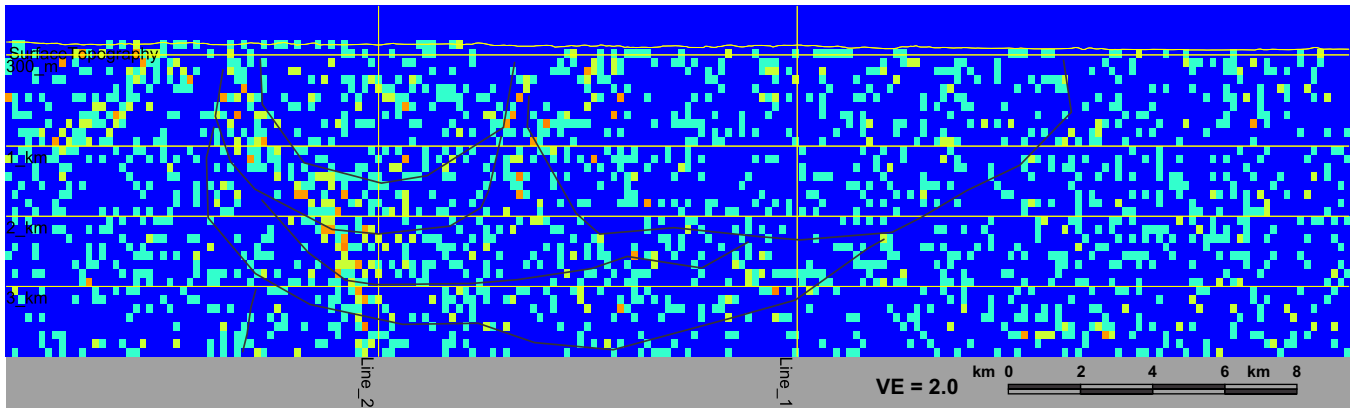
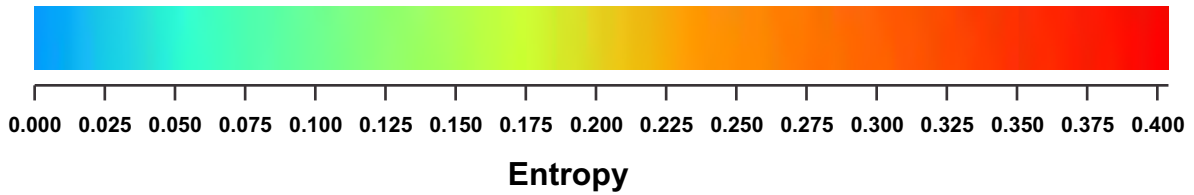
Figure 5.32 Joint gravity and magnetic inversion results along (a) Line 1 (b) Line 2 (c) Line 3. The coloured image in the background is the starting model. Dotted brown lines are for inversion with very tight constraint, solid lines with moderate constraint and faint lines for loose constraints.



(a)



(b)



(c)

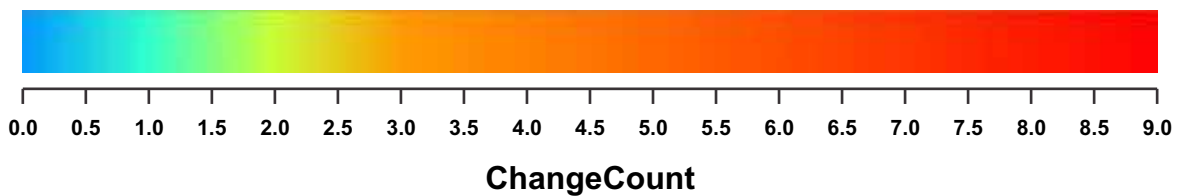
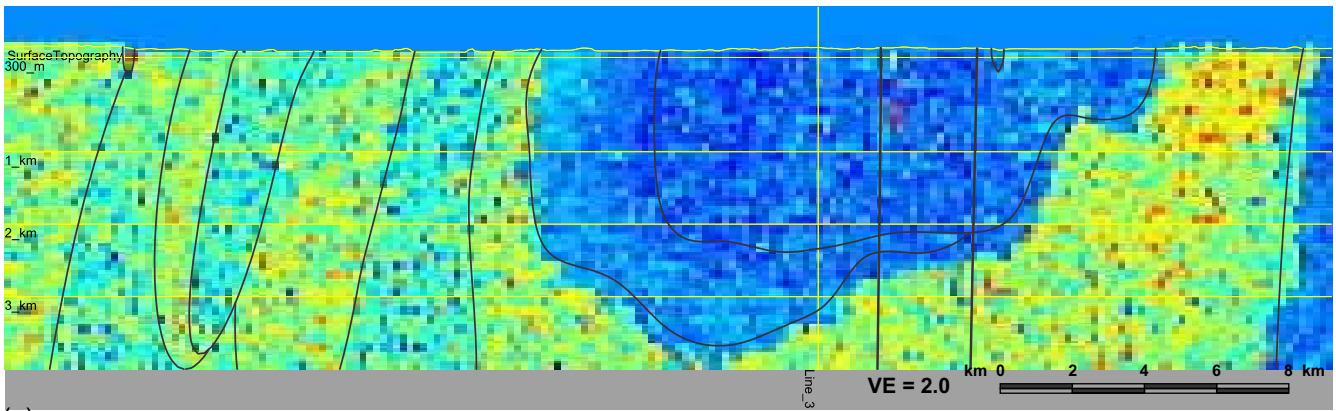


Figure 5.33 Joint moderate constraint inversion results statistics along Line 3. (a) 90 % thresholded model units. Pixels below 90% threshold level are grayed out. (b) entropy (c) change count. Interpolated starting model boundaries appear as faint black lines.

SW

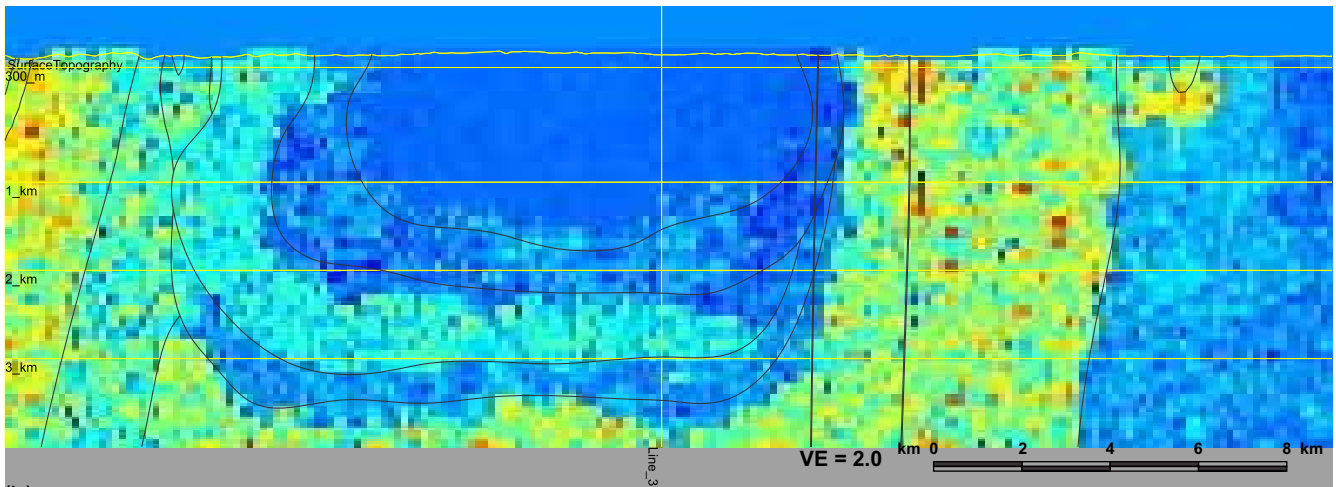
NE



(a)

SW

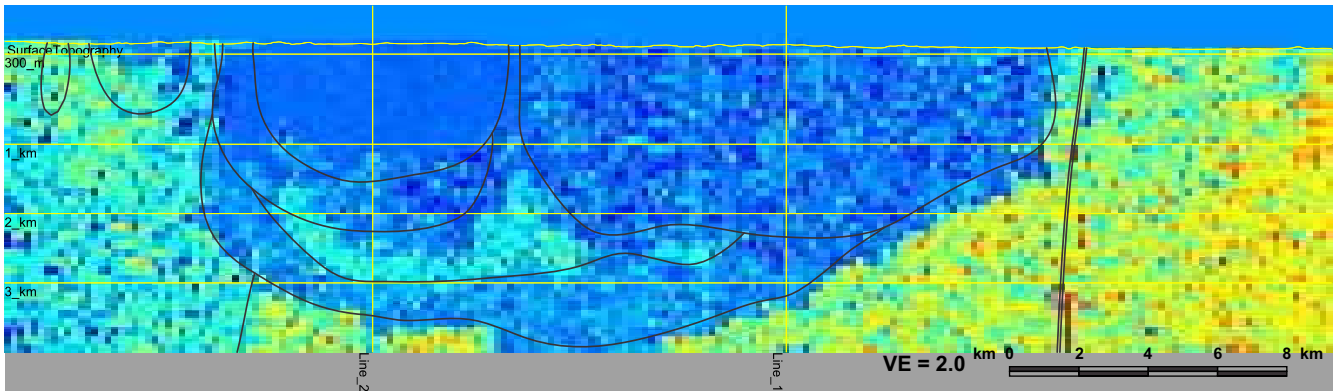
NE



(b)

SE

NW



(c)

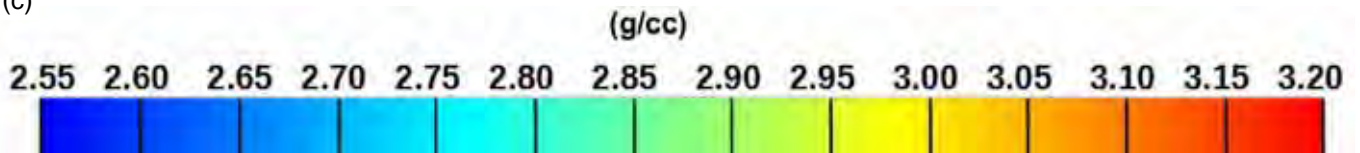
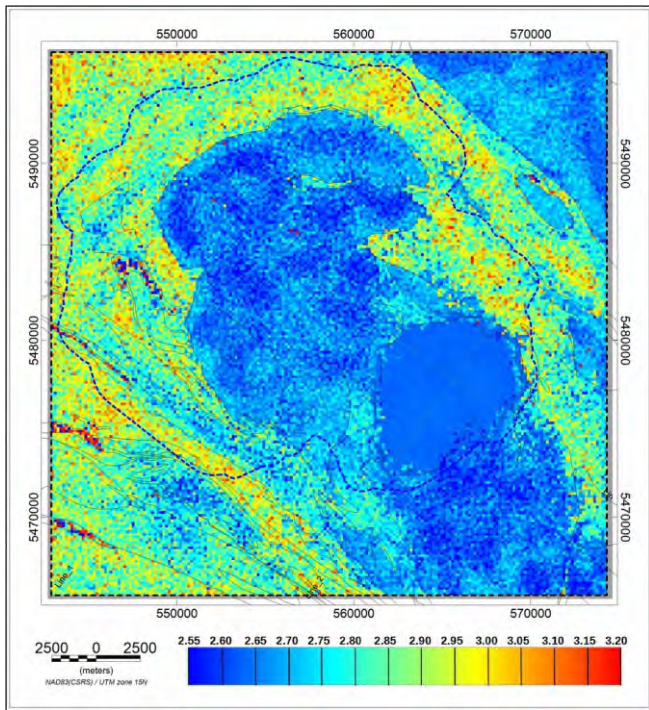
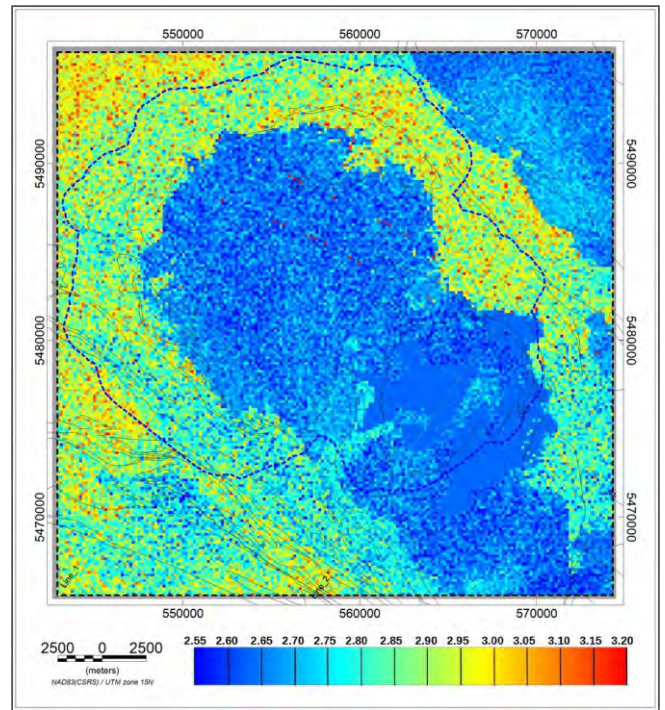


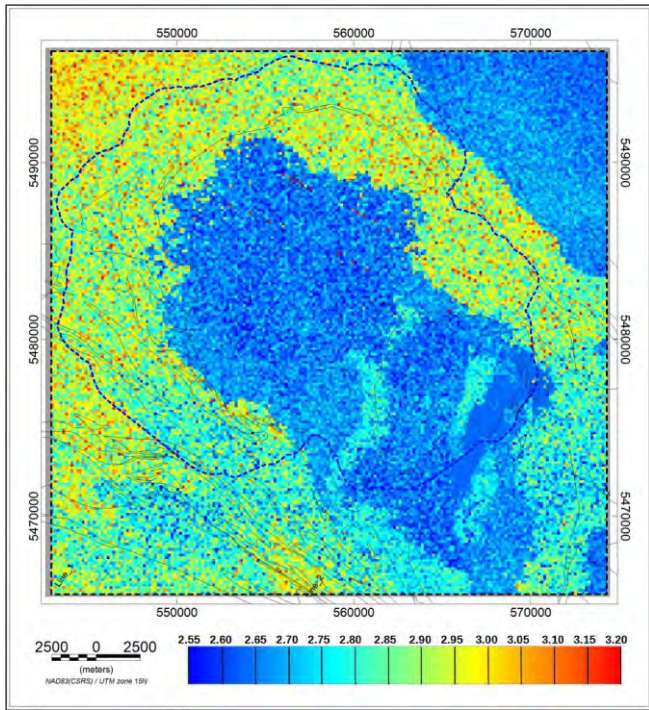
Figure 5.34 Joint gravity and magnetic inversion density variation along (a) Line 1 (b) Line 2 (c) Line 3. Interpolated starting model boundaries and features appear as faint black lines on all images.



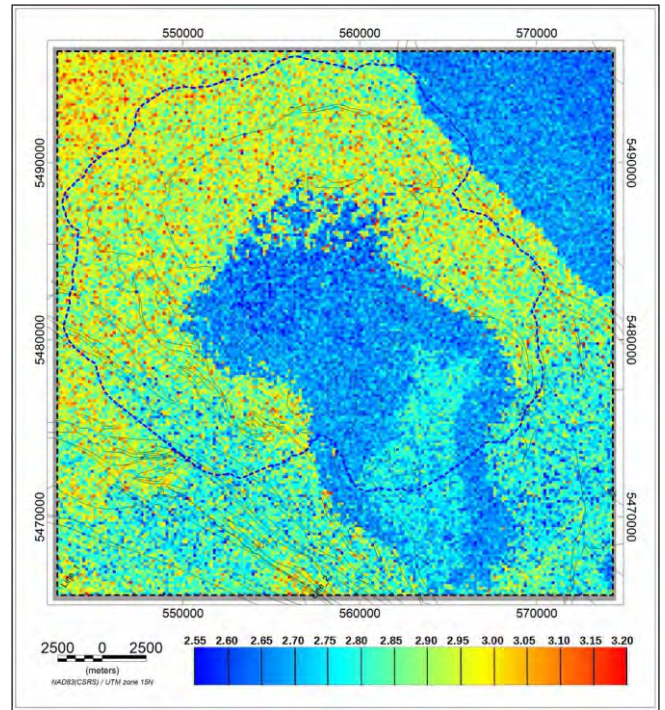
(a)



(b)



(c)

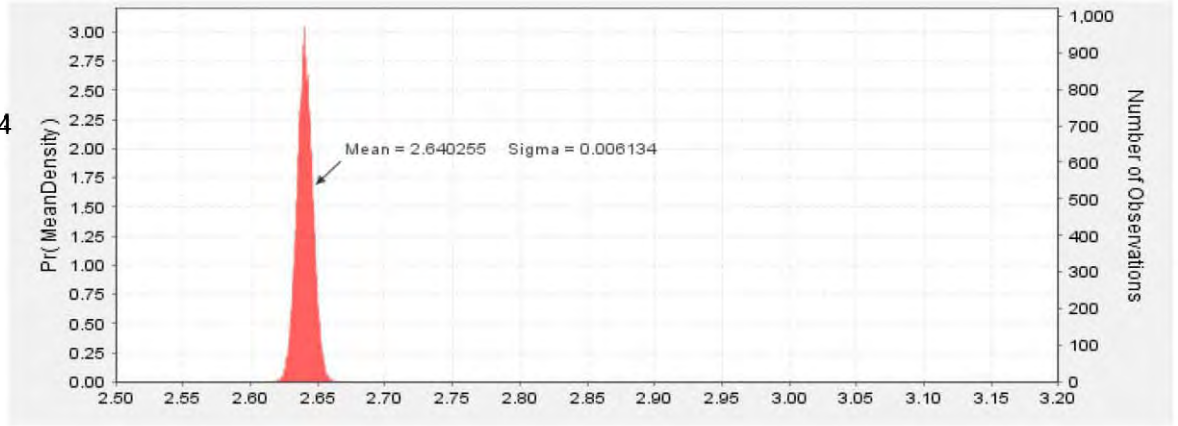


(d)

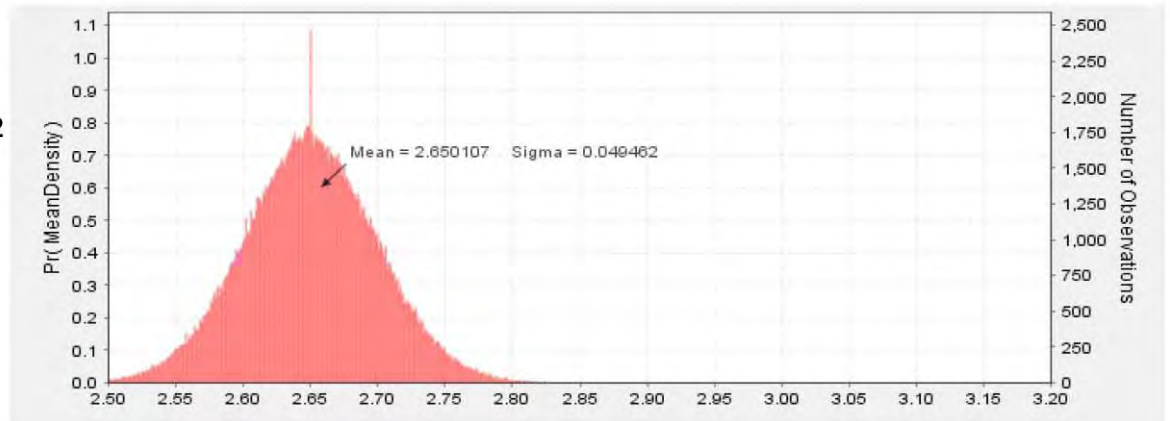
Figure 5.35 Joint gravity and magnetic inversion density distribution results along depth slices at (a) 300 m above MSL (b) 1 km below MSL (c) 2 km below MSL (d) 3 km below MSL. Density units are in g/cc. The dashed blue line marks the LiDAR coverage.

(a) Feldspar Megacryst
Granite

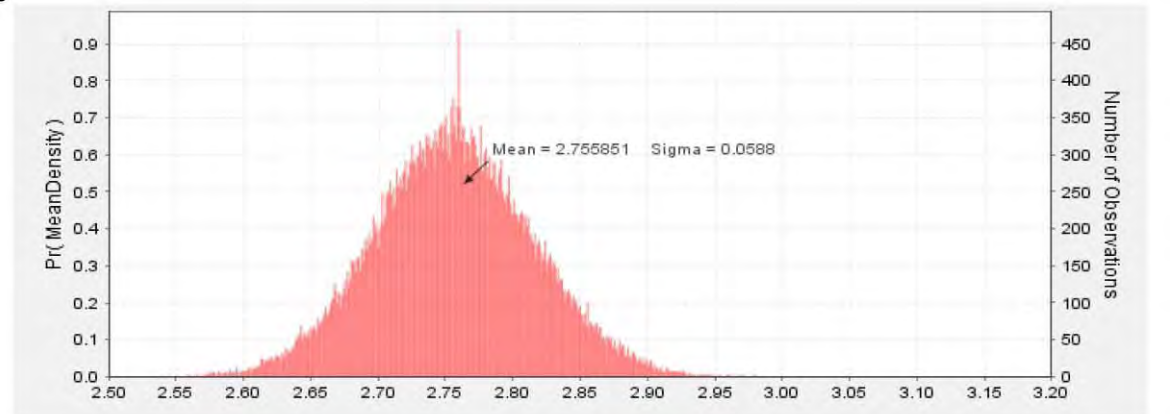
Mean = 2.640255
 Std deviation = 0.006134
 Minimum = 2.594952
 Maximum = 2.793284

(b) Biotite granite to
granodiorite

Mean = 2.650107
 Std deviation = 0.049462
 Minimum = 2.421118
 Maximum = 2.882391

(c) Hornblende tonalite to
granodiorite

Mean = 2.755851
 Std deviation = 0.0588
 Minimum = 2.500856
 Maximum = 2.979242

(d) Biotite tonalite to
granodiorite

Mean = 2.680886
 Std deviation = 0.039363
 Minimum = 2.508806
 Maximum = 2.900322

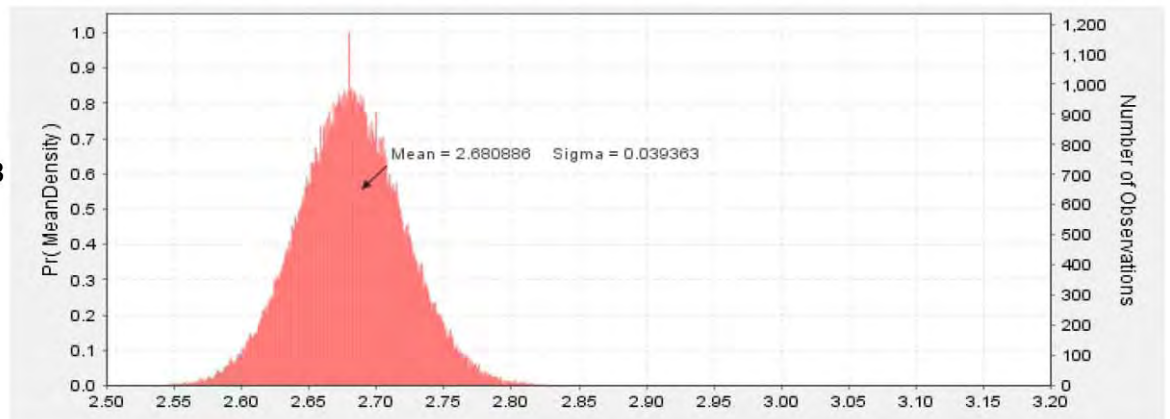
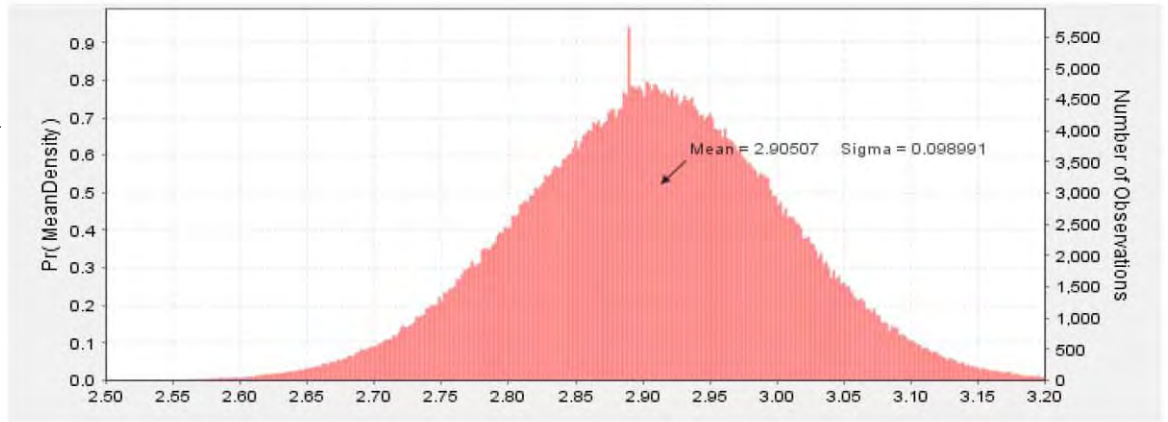


Figure 5.36 Histograms of mean densities of the Revell batholith units from joint inversion with moderate constraint.

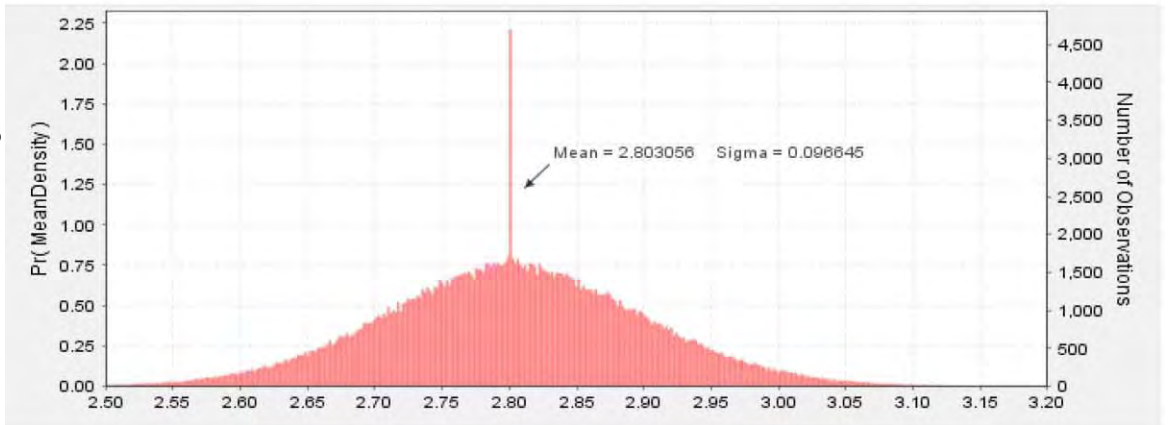
(a) Mafic metavolcanics

Mean = 2.90507
 Std deviation = 0.098991
 Minimum = 2.411355
 Maximum = 3.351071



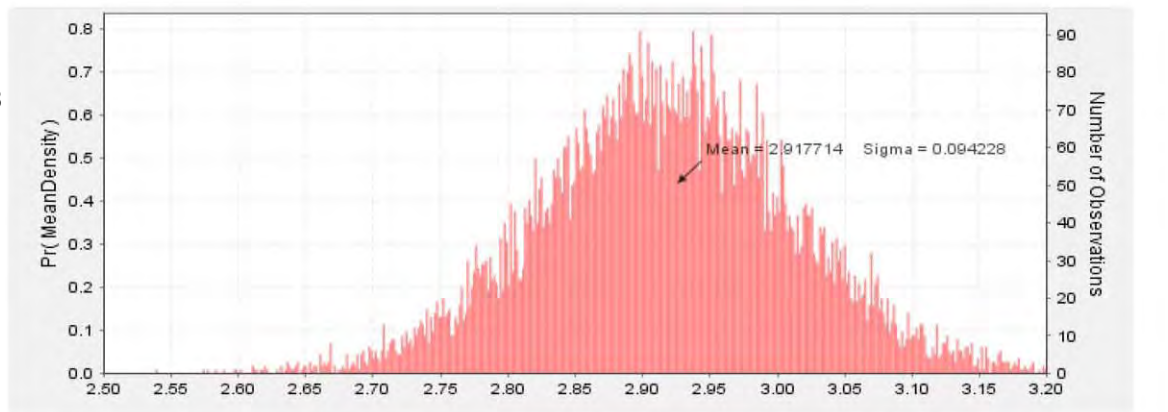
(b) Felsic to intermediate metavolcanics

Mean = 2.803056
 Std deviation = 0.096645
 Minimum = 2.356782
 Maximum = 3.261225



(c) Metasedimentary to Metavolcanics

Mean = 2.917714
 Std deviation = 0.094228
 Minimum = 2.539411
 Maximum = 3.29744



(d) Metasedimentary

Mean = 2.782169
 Std deviation = 0.096031
 Minimum = 2.368281
 Maximum = 3.268261

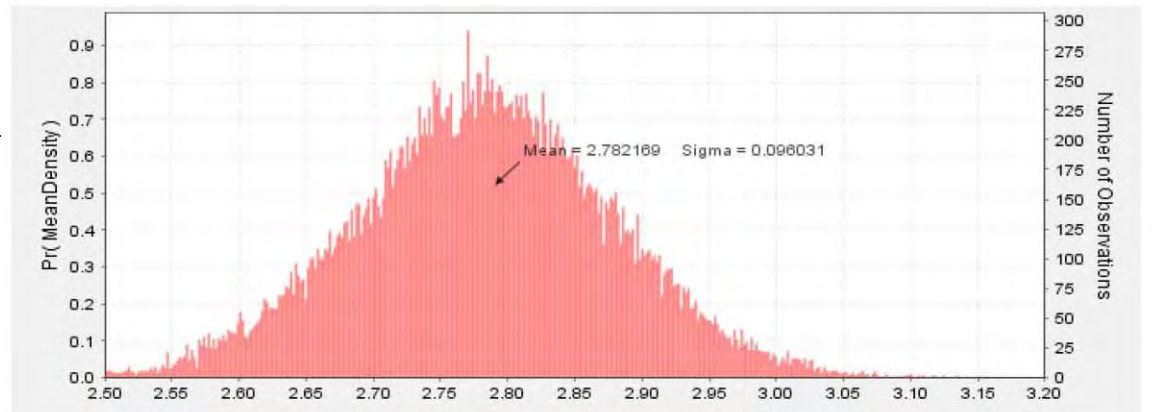
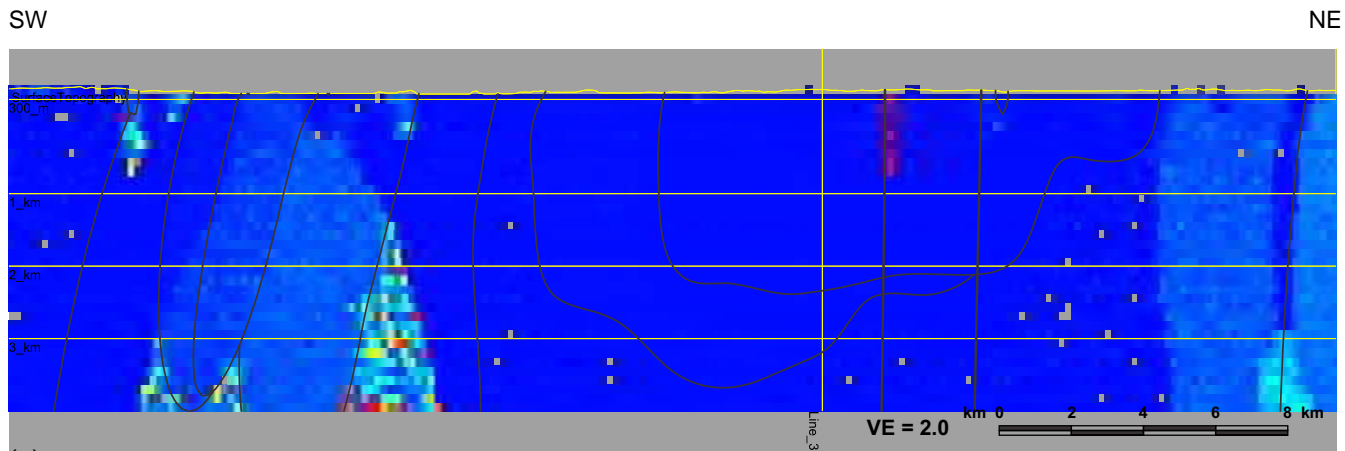
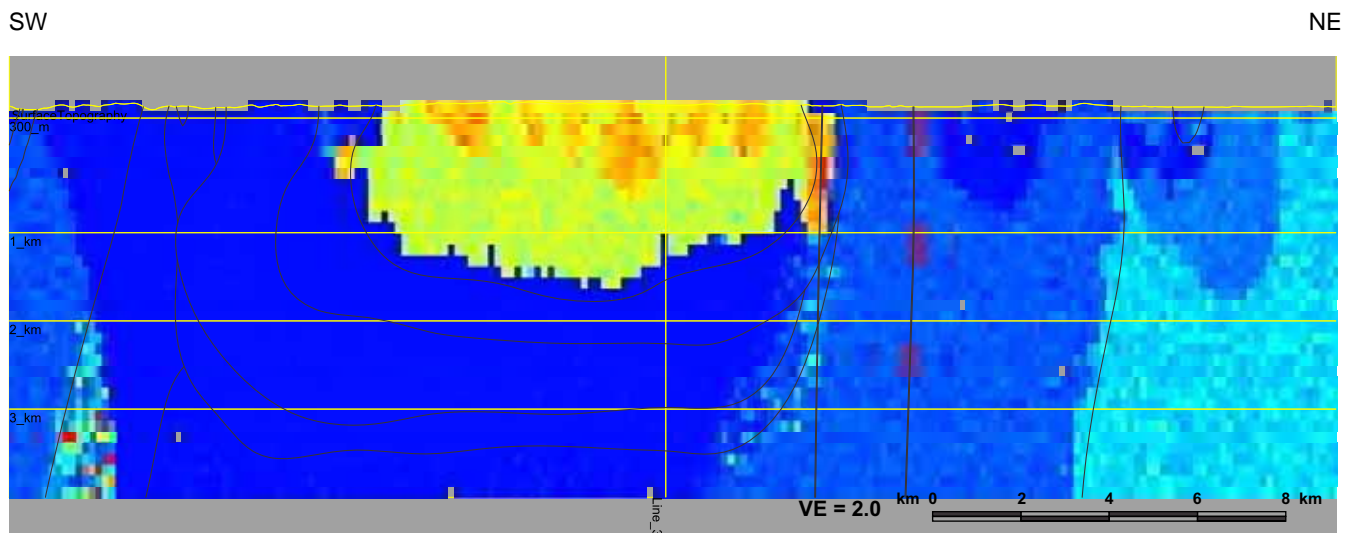


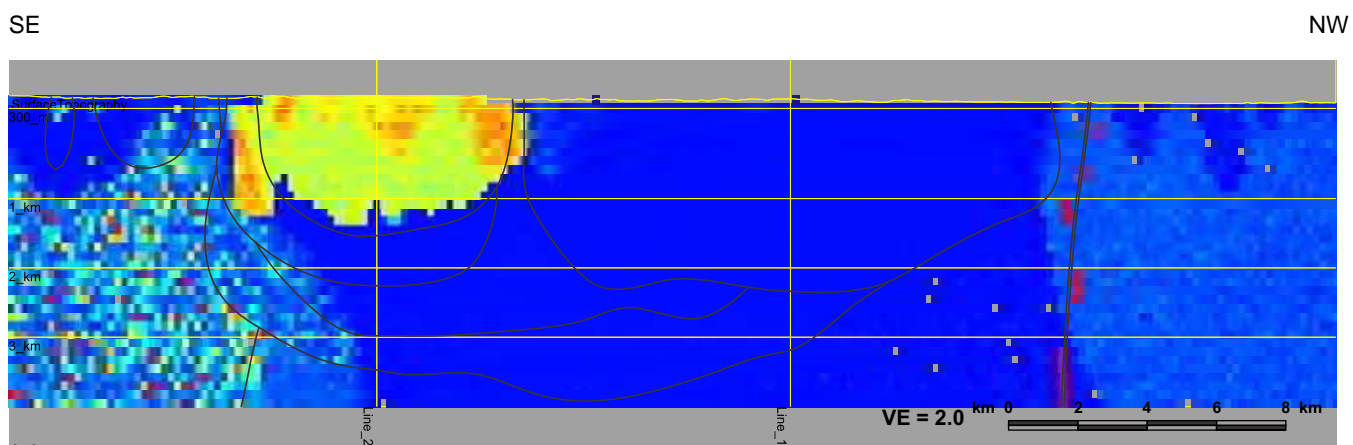
Figure 5.37 Histograms of mean densities of greenstone and other units surrounding the Revell batholith from joint inversion with moderate constraint.



(a)



(b)



(c)

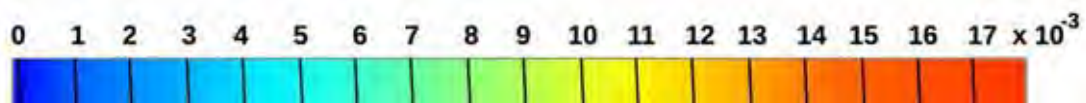
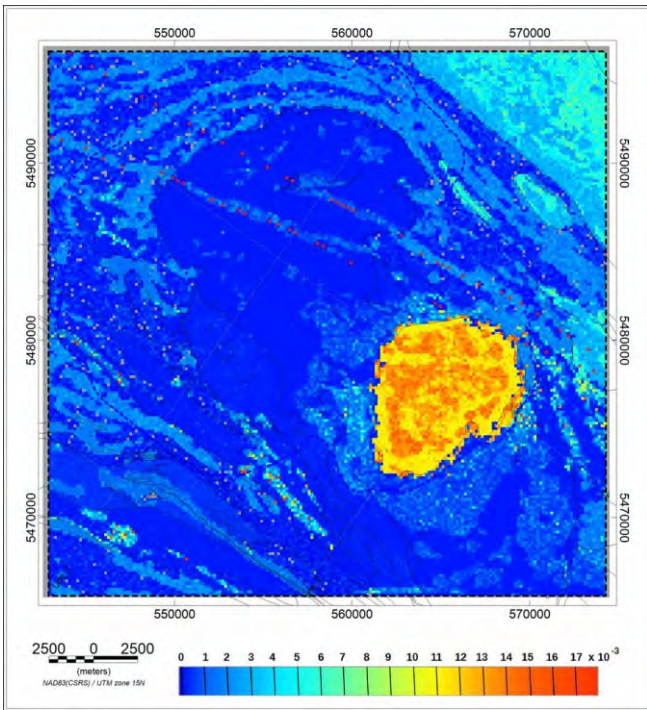
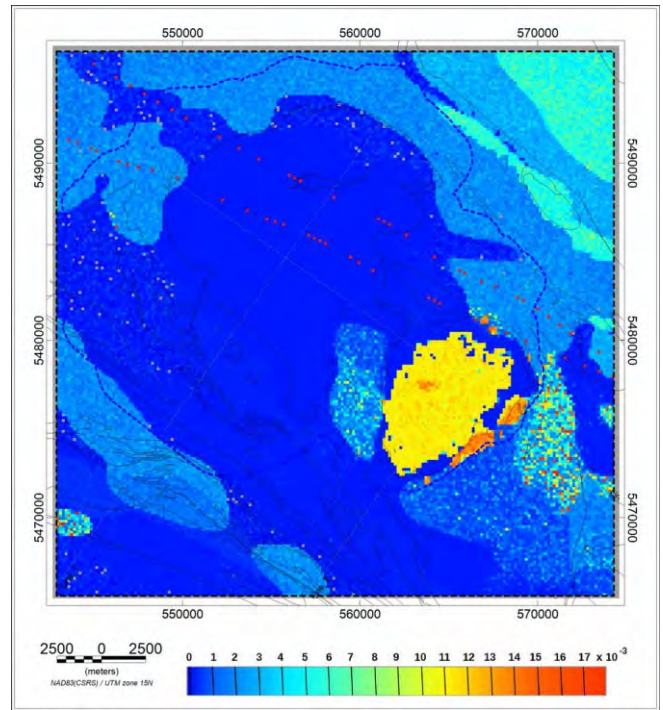


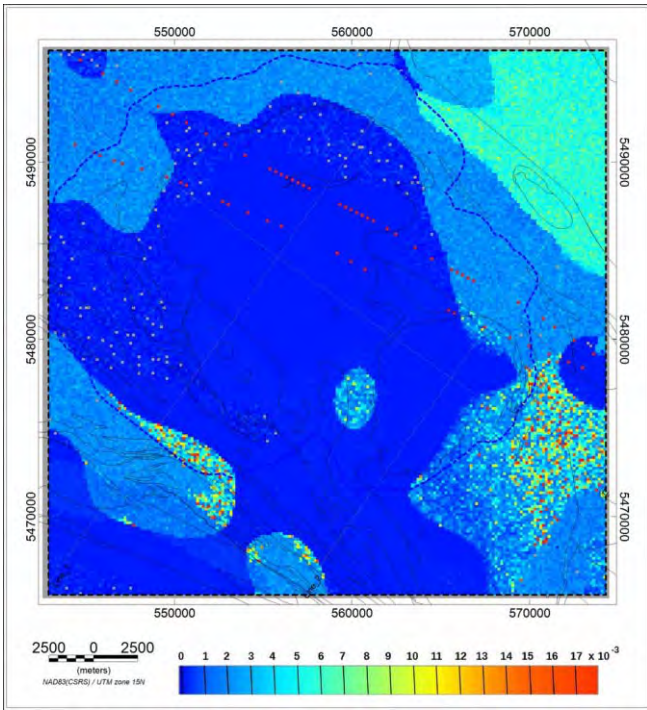
Figure 5.38 Joint gravity and magnetic inversion magnetic susceptibility variation along (a) Line 1 (b) Line 2 (c) Line 3. Magnetic susceptibilities are in SI units. Interpolated starting model boundaries and features appear as faint black lines on all images.



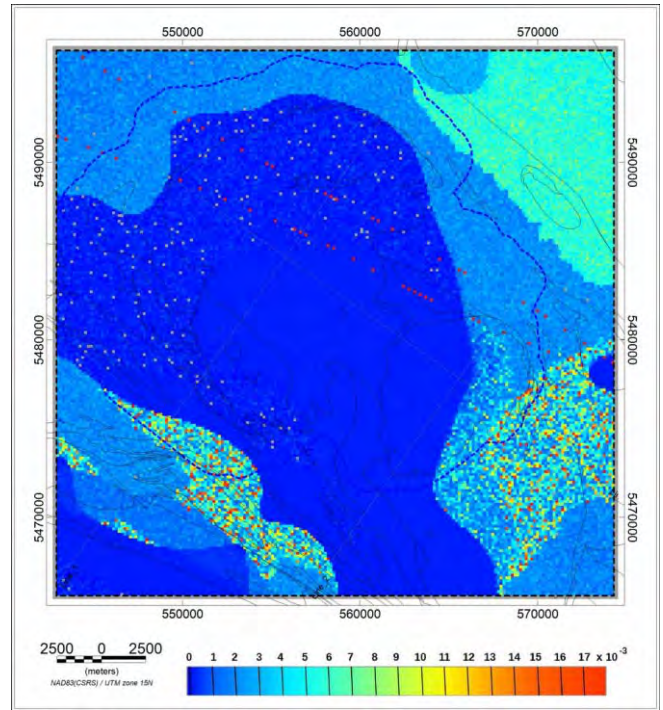
(a)



(b)



(c)

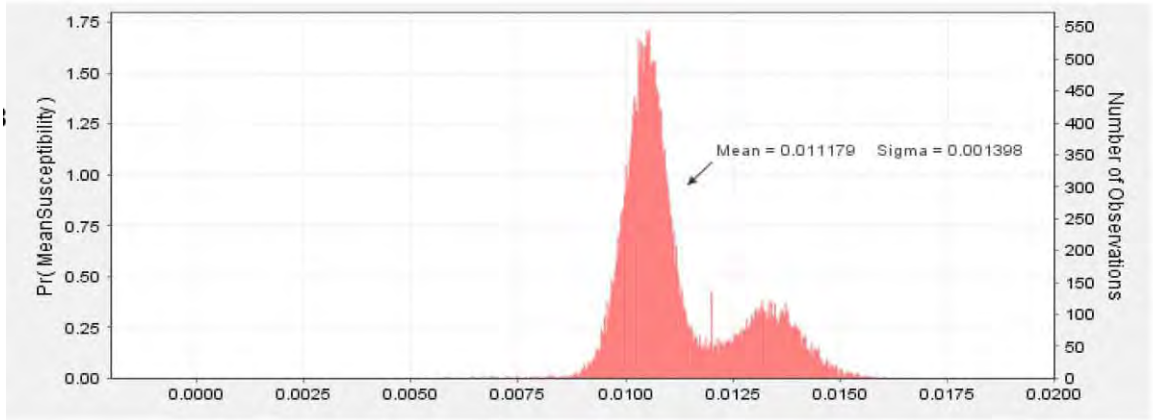


(d)

Figure 5.39 Joint gravity and magnetic inversion magnetic susceptibility distribution results along depth slices at (a) 300 m above MSL (b) 1 km below MSL (c) 2 km below MSL (d) 3 km below MSL. Magnetic susceptibilities are in SI units. The dashed blue line marks the LiDAR coverage.

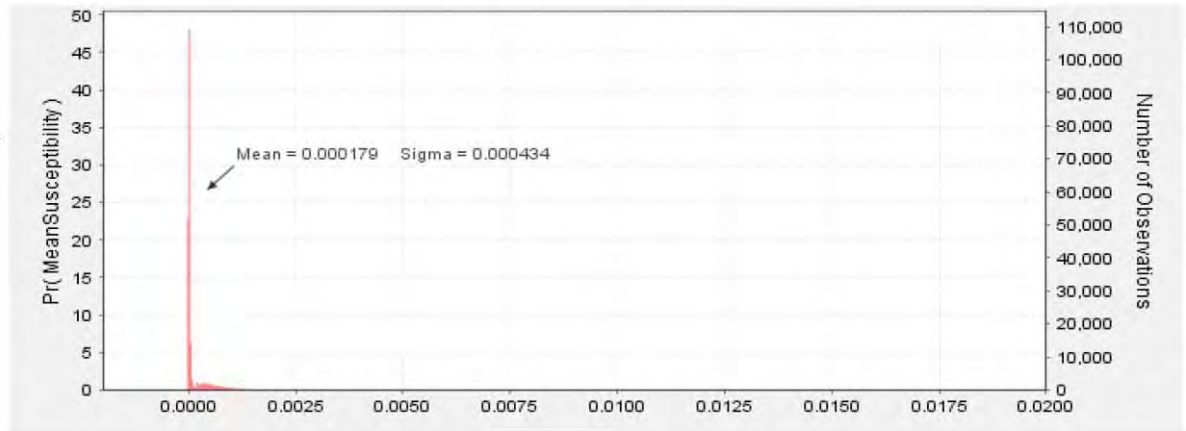
(a) Feldspar Megacryst Granite

Mean= 0.011179
 Stddeviation=0.001398
 Minimum=0.004105
 Maximum =0.017777



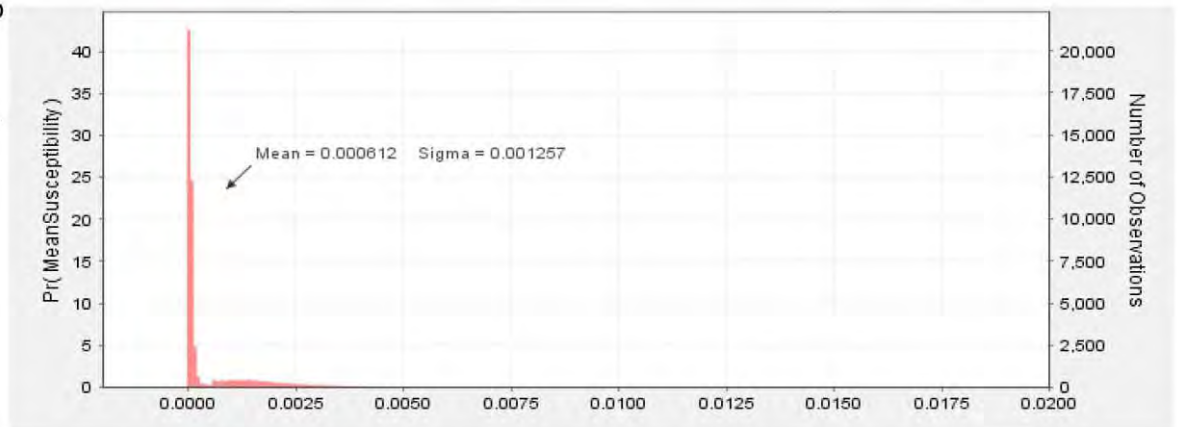
(b) Biotite granite to granodiorite

Mean= 0.000179
 Stddeviation =0.000434
 Minimum=-0.000169
 Maximum =0.015075



(c) Hornblende tonalite to granodiorite

Mean =0.000612
 Stddeviation=0.001257
 Minimum=0.000003
 Maximum=0.036298



(d) Biotite tonalite to granodiorite

Mean =0.000533
 Stddeviation=0.00117
 Minimum =-0.000173
 Maximum= 0.031578

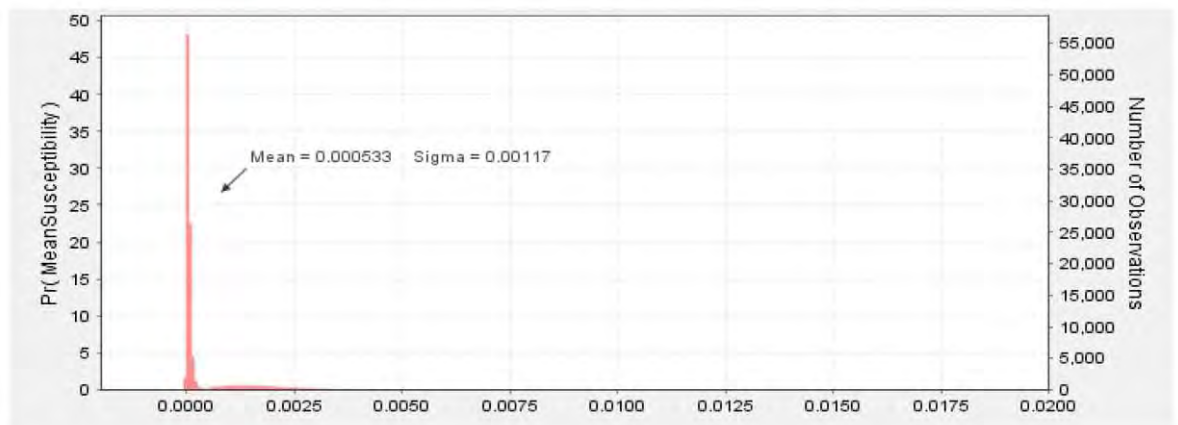
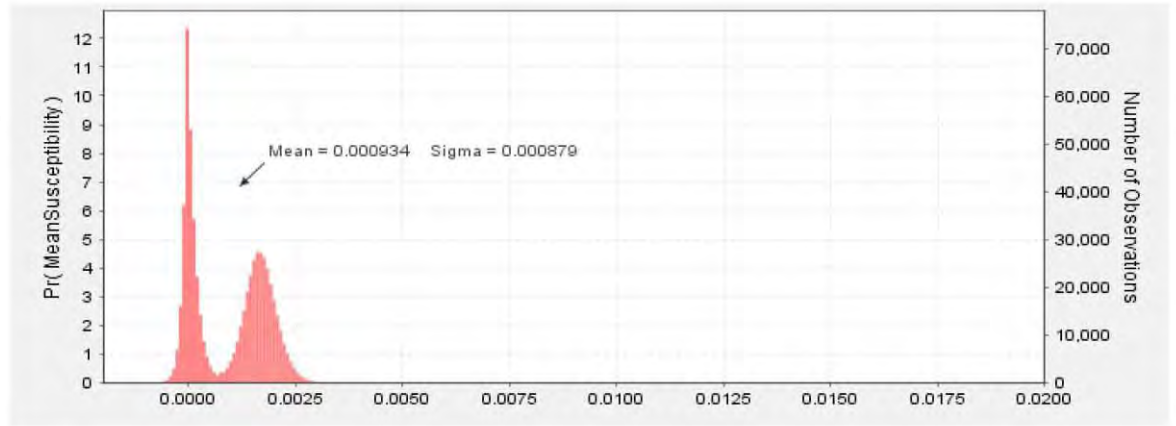


Figure 5.40: Joint inversion model magnetic susceptibility distributions for the Revell batholith units with associated statistics for each rock unit.

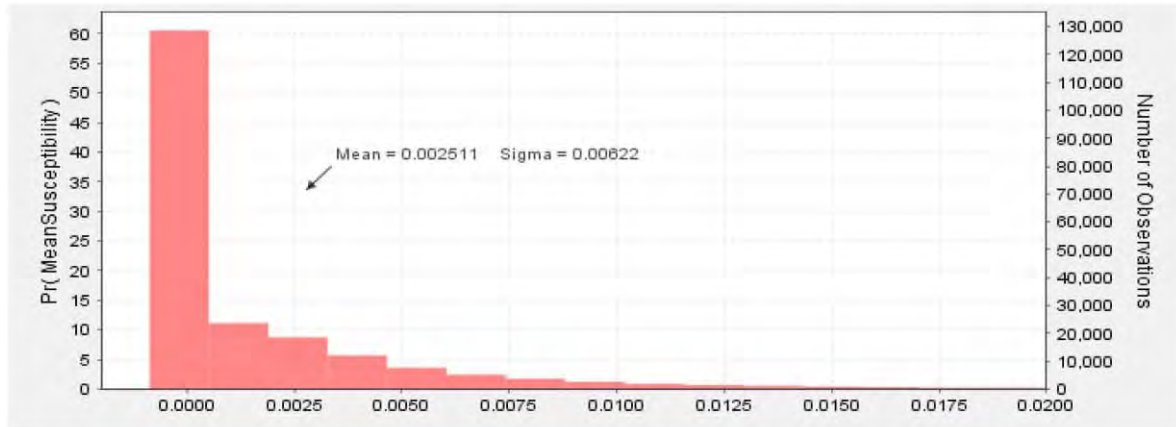
(a) Mafic metavolcanics

Mean = 0.000934
 Std deviation = 0.000879
 Minimum = -0.002219
 Maximum = 0.036713



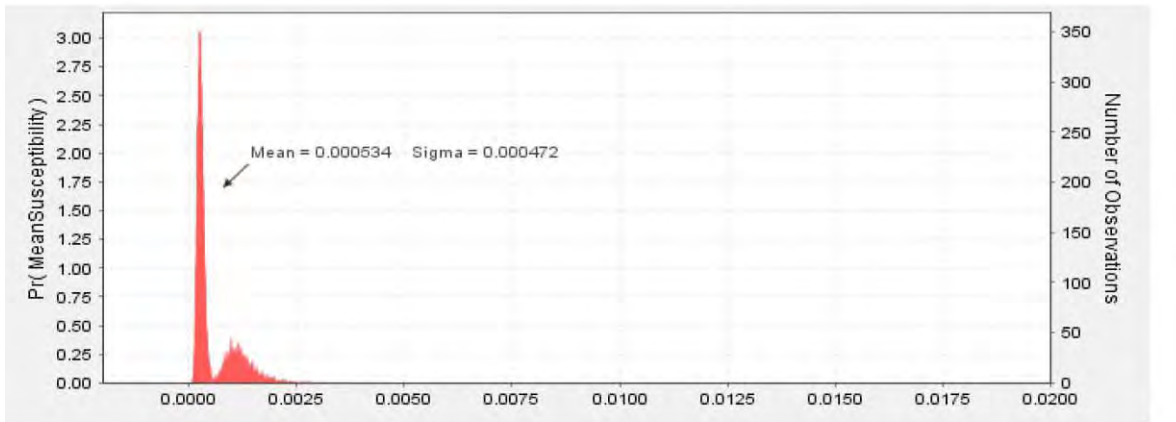
(b) Felsic to intermediate metavolcanics

Mean = 0.002511
 Std deviation = 0.00622
 Minimum = -0.000181
 Maximum = 0.689029



(c) Metasedimentary to Metavolcanics

Mean = 0.000534
 Std deviation = 0.000472
 Minimum = 0.000069
 Maximum = 0.003557



(d) Metasedimentary

Mean = 0.000915
 Std deviation = 0.00534
 Minimum = 0.000056
 Maximum = 0.004907

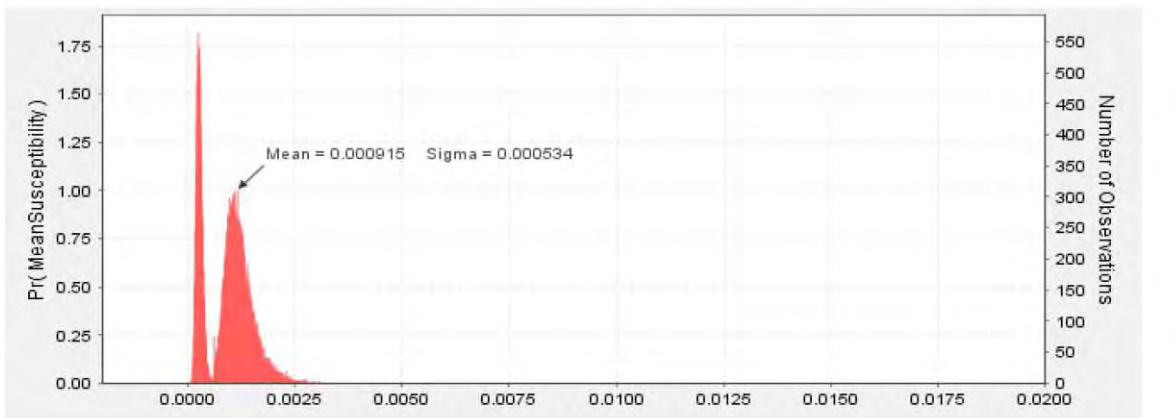
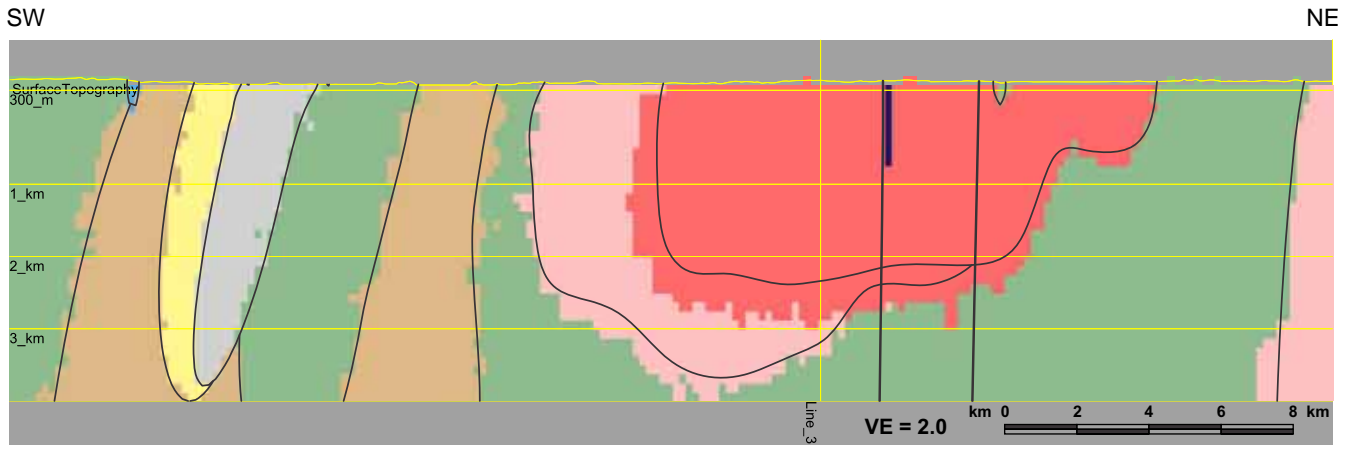
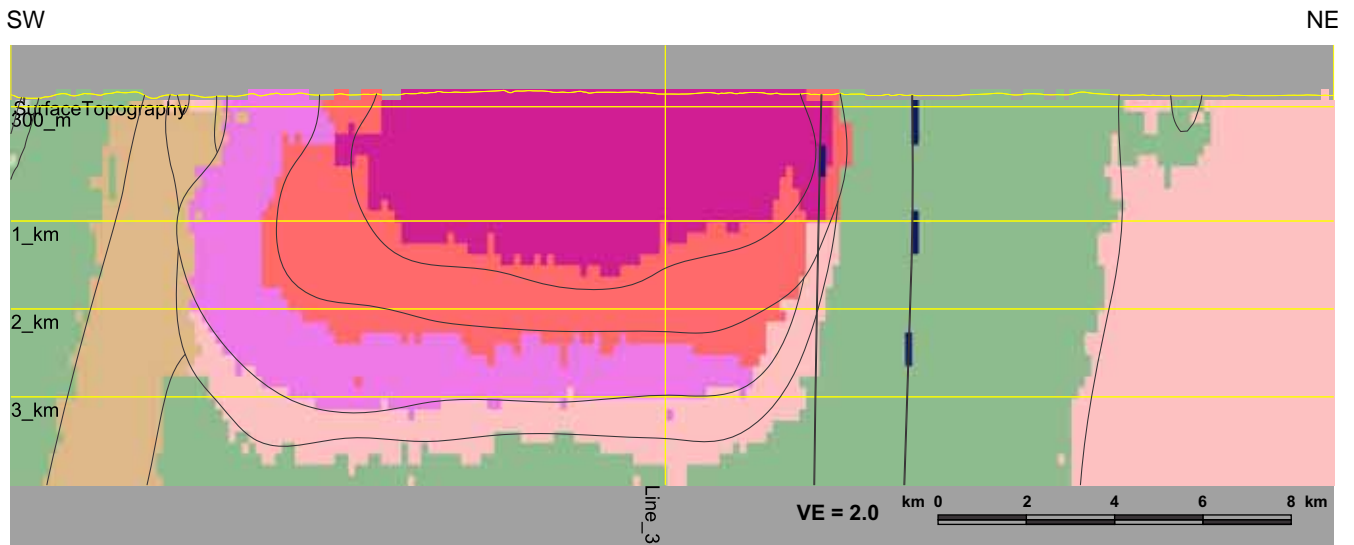


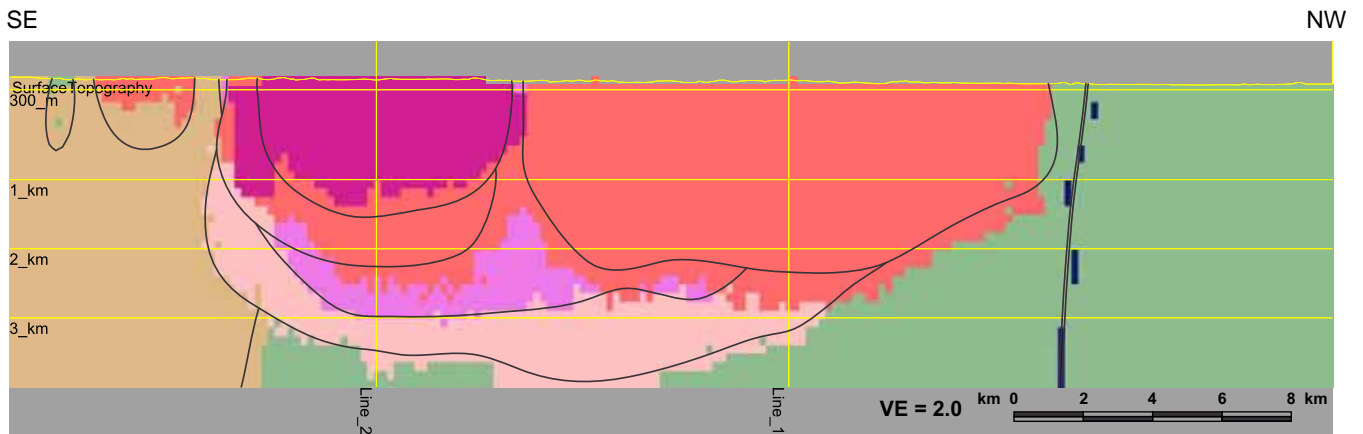
Figure 5.41 Joint inversion model magnetic susceptibility distributions for greenstone and other units surrounding the Revell batholith with associated statistics for each formation.



(a)

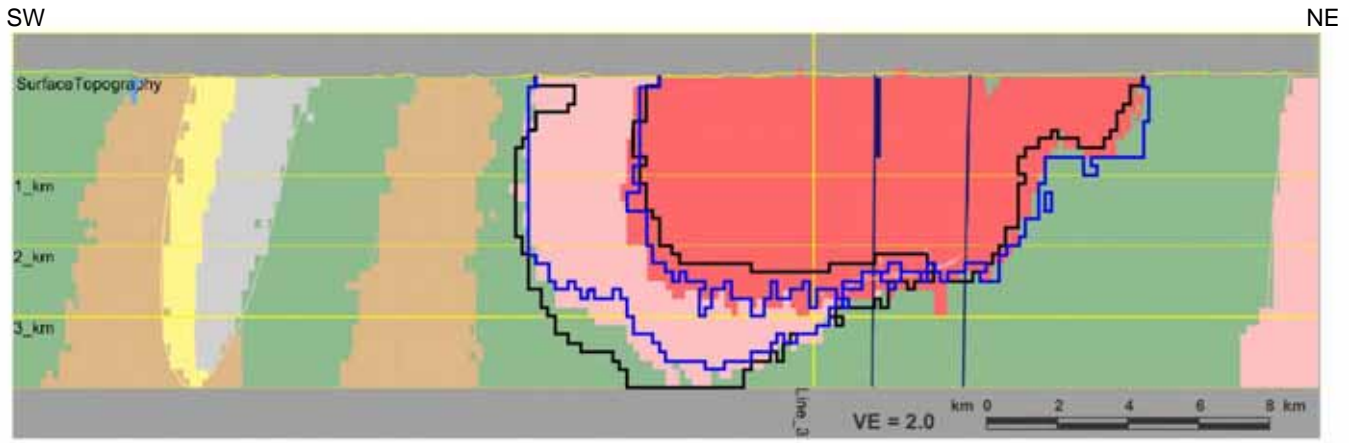


(b)

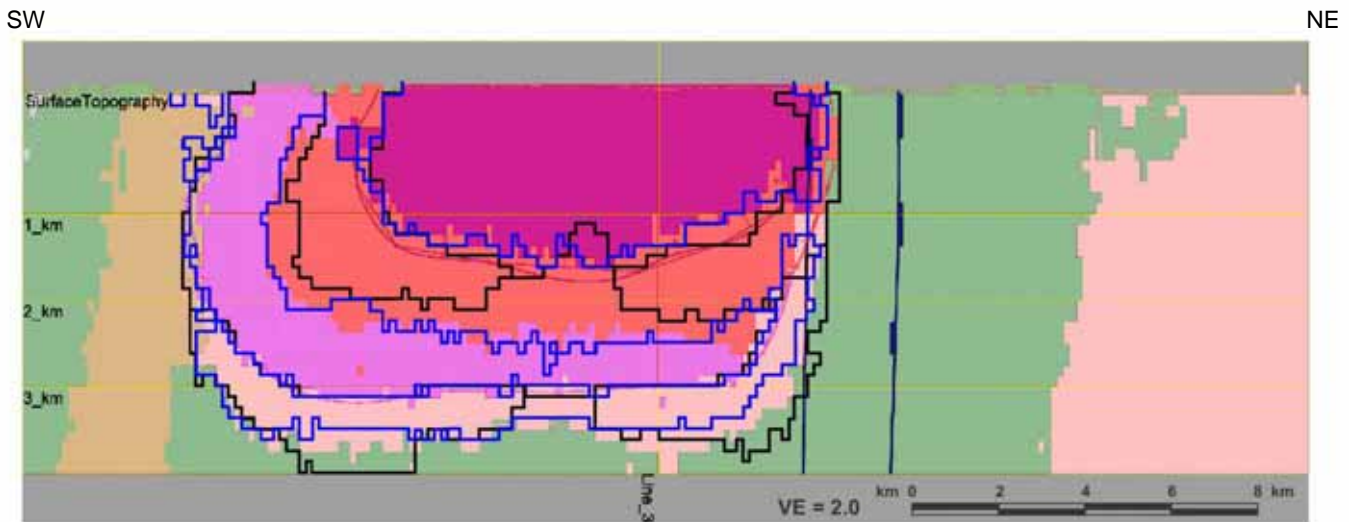


(c)

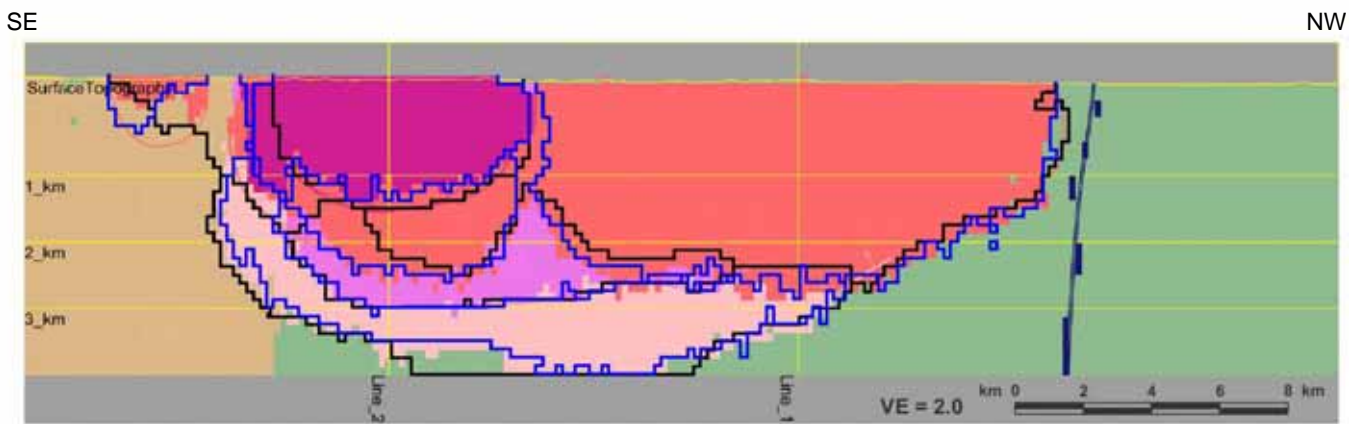
Figure 5.42 Joint gravity and magnetic moderate constraint inversion results in colour in the background along (a) Line 1 (b) Line 2 (c) Line 3. Interpolated starting model boundaries and features appear as faint lines on all images



(a)

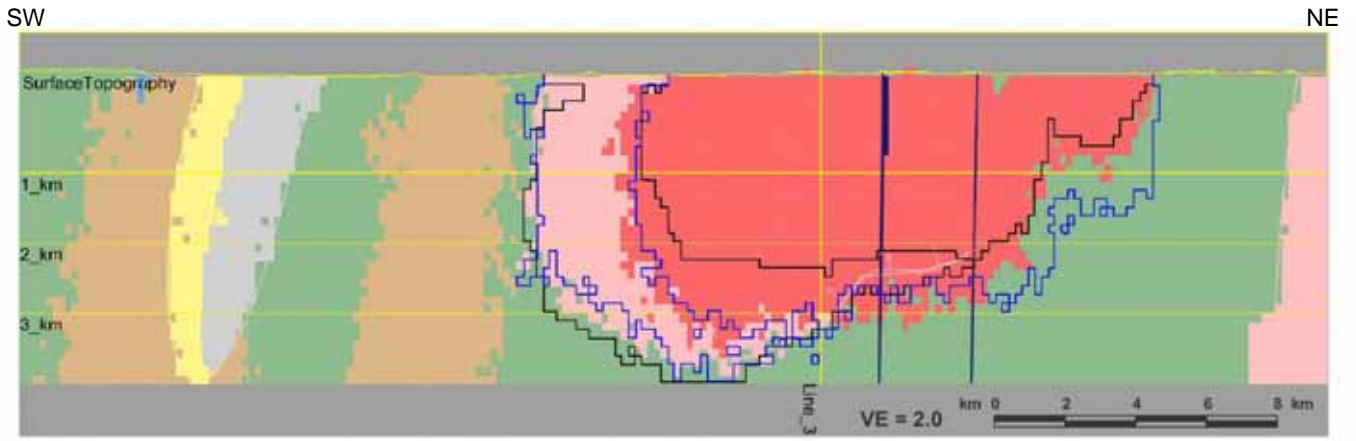


(b)

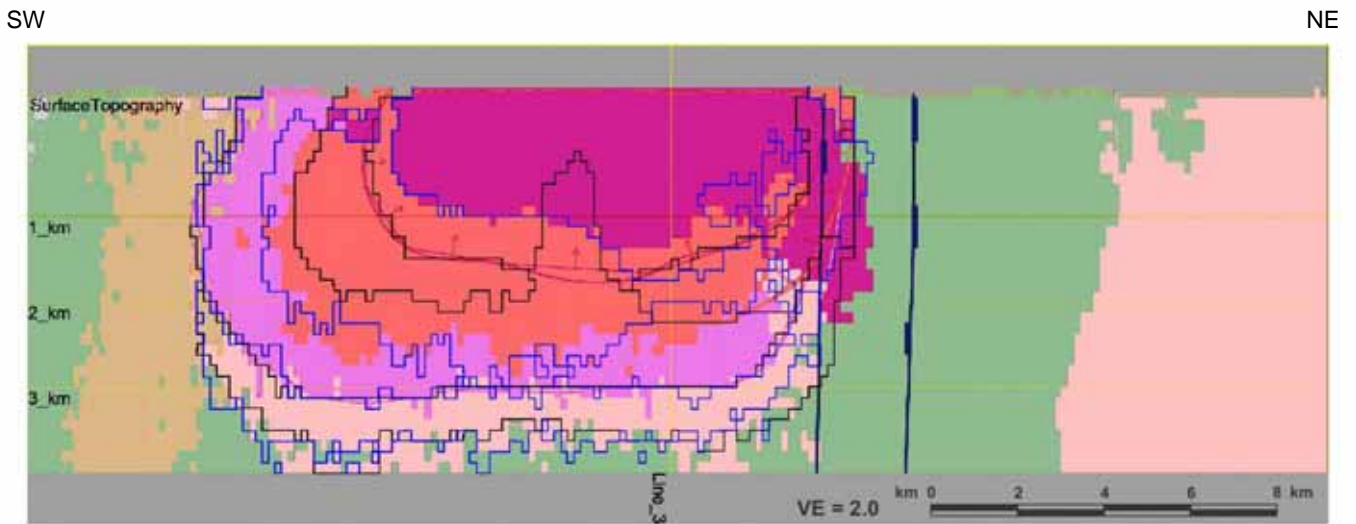


(c)

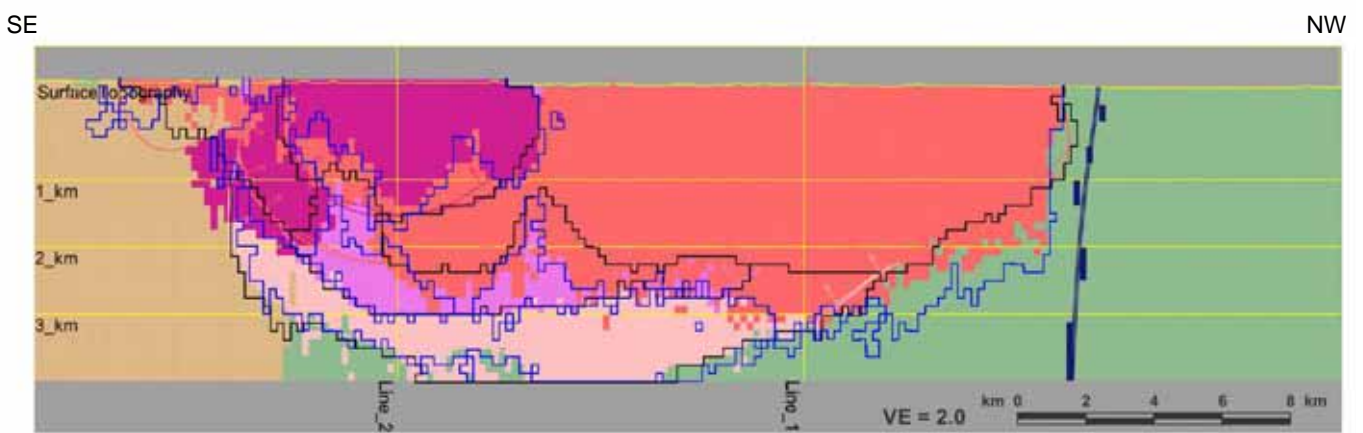
Figure 5.43: Joint gravity and magnetic moderate constraint inversion results in colour in the background along (a) Line 1 (b) Line 2 (c) Line 3. Solid black lines and blue lines are from gravity only inversion and magnetic only inversions respectively with moderate constraint.



(a)



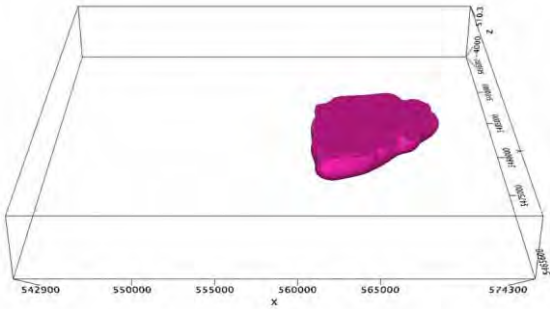
(b)



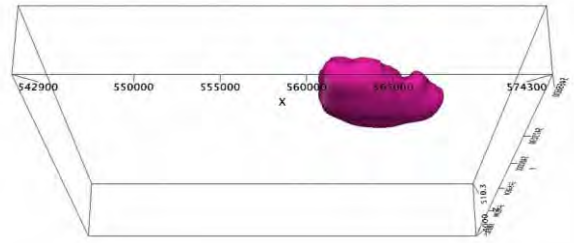
(c)

Figure 5.44: Joint gravity and magnetic loose constraint inversion results in colour in the background along (a) Line 1 (b) Line 2 (c) Line 3. Solid black lines and blue lines are from gravity only inversion and magnetic only inversions respectively with loose constraint.

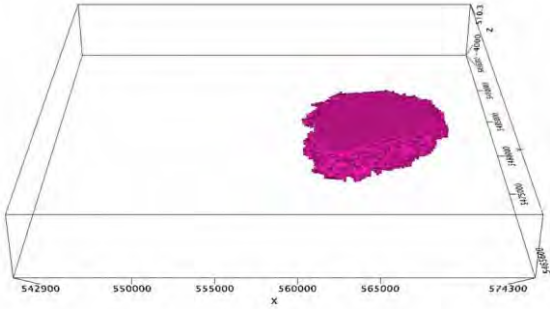
(a) view from above



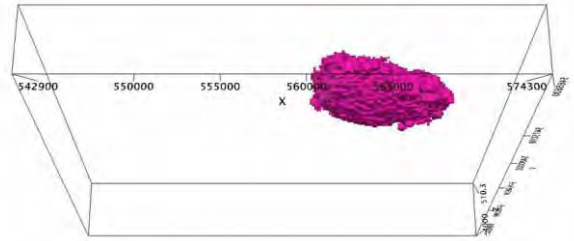
(b) view from below



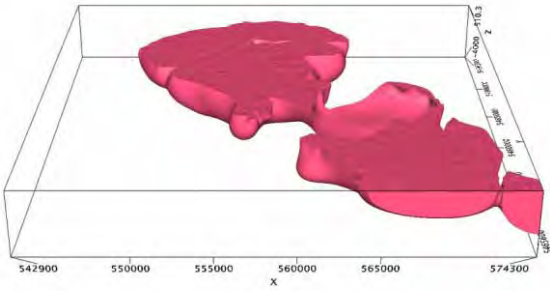
(c) view from above



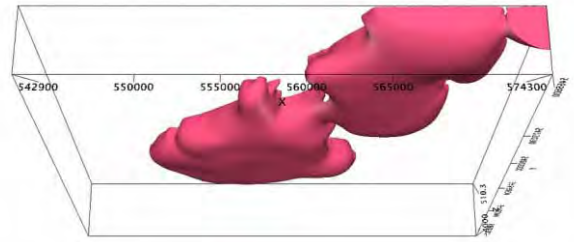
(d) view from below



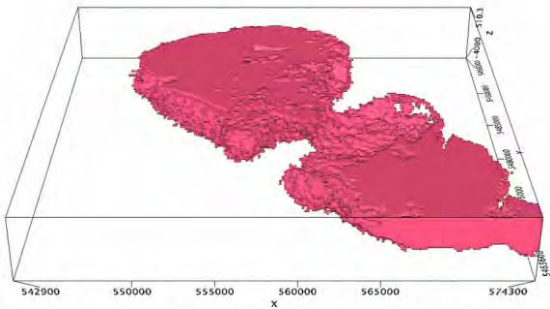
(e) view from above



(f) view from below



(g) view from above



(h) view from below

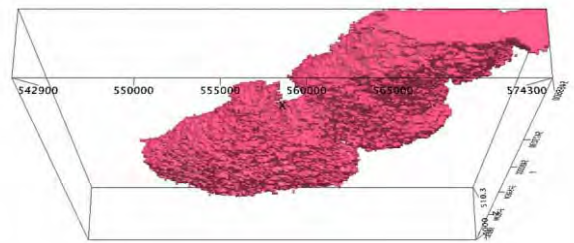
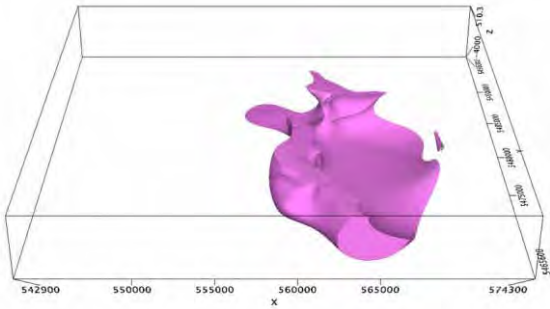
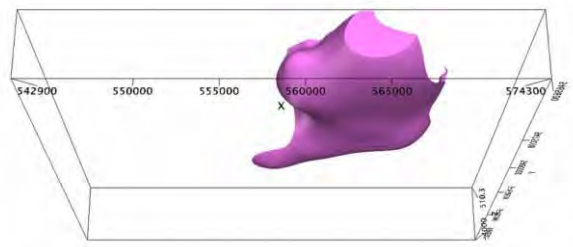


Figure 5.45: Different 3D views of units within the Revell batholith after jointjoint inversion with moderate constraint. The arrows point from starting models to final models. The starting model for the feldspar megacrystic granite unit is shown in (a) and (b), and the final model in (c) and (d). The starting model for the Biotite granite to granodiorite unit is shown in panes (e) and (f), and the final model in (f) and (g).

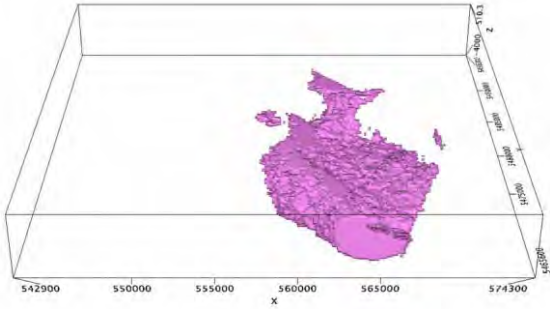
(a) view from above



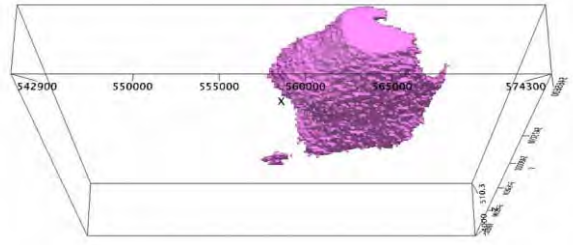
(b) view from below



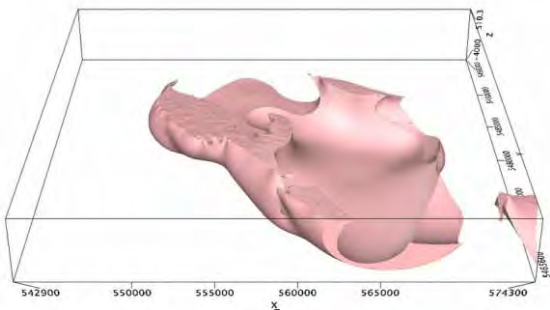
(c) view from above



(d) view from below



(e) view from above



(f) view from below

